KU LEUVEN

ARENBERG DOCTORAL SCHOOL
Faculty of Engineering Science

Pore-scale modeling of hygric properties of hydrophobised building materials

Daan Deckers

Supervisor:
Prof. dr. ir. Hans Janssen
Prof. dr. ir. Evy Vereecken

Dissertation presented in partial fulfillment of the requirements for the degree of Doctor of Engineering Science (PhD): Civil Engineering

17 September 2024

Pore-scale modeling of hygric properties of hydrophobised building materials

Daan DECKERS

Examination committee:
Prof. dr. ir. arch. Herman Neuckermans, chair
Prof. dr. ir. Hans Janssen, supervisor
Prof. dr. ir. Evy Vereecken, supervisor
(KU Leuven and KIK-IRPA, Belgium)
Prof. dr. ir. David Seveno
Prof. dr. ir. arch. Staf Roels
Prof. dr. ir. Ernst Jan de Place Hansen
(Aalborg University, Denmark)
Prof. dr. Tom Bultreys
(Ghent University, Belgium)
Dr. ir. Steven Claes
(VITO-Energyville, Belgium)

Dissertation presented in partial fulfillment of the requirements for the degree of Doctor of Engineering Science (PhD): Civil Engineering

17 September 2024

© 2024 KU Leuven – Faculty of Engineering Science
Uitgegeven in eigen beheer, Daan Deckers, Kasteelpark Arenberg 40, B-3001 Leuven (Belgium)

Alle rechten voorbehouden. Niets uit deze uitgave mag worden vermenigvuldigd en/of openbaar gemaakt worden door middel van druk, fotokopie, microfilm, elektronisch of op welke andere wijze ook zonder voorafgaande schriftelijke toestemming van de uitgever.

All rights reserved. No part of the publication may be reproduced in any form by print, photoprint, microfilm, electronic or any other means without written permission from the publisher.

Acknowledgements

As I am approaching the end of my PhD, I would like to extend my gratitude to everybody who helped me during these last 5 years, both professionally as well as in my private life. Firstly, I would like to thank my promotor Hans Janssen for allowing me to start my PhD, but more importantly, for his excellent guidance throughout these last 5 years. Your constant availability for questions and elaborate discussions as well as your detailed way of commenting on any of my written work helped shape this work to what it is now. The same applies to my co-supervisor Evy Vereecken, who's guidance throughout my master thesis instigated my passion for research in the first place.
Furthermore, I would like to extend this gratitude to all the members of my examination committee for their time to assess this dissertation. I sincerely appreciate our discussions and your valuable input to the final version of this PhD thesis. A special thanks also goes out to Staf Roels for guiding me throughout my master thesis and for allowing me to help in some hygrothermal expertise studies which were a nice distraction from the PhD at times. Also, the Research Foundation - Flanders (FWO) is gratefully acknowledged for their financial support.
Besides the above-mentioned people who have directly contributed to this PhD thesis, I would like to thank all the colleagues of the Building Physics and Sustainable Design Section which I have encountered during the years. Not only for their professional help, but more importantly their social and mental support during my PhD on "bricks", as you so eloquently liked to say. While the "lunch table" was definitely a highlight of my day, it won't be a shock to you all that I enjoyed our "bar table" even more.
Next, I would like to thank my family and friends for their unconditional support and their talent to completely distract me from my work. Special thanks go out to Seppe and An-Sofie for their relentless support.
Finally, I am eternally grateful to my parents who made all of this possible.

Abstract

In the research area of building physics, internal insulation systems receive much interest because they are the sole option for a thermal retrofit in buildings with preservation-worthy facades. One of the key problems of this insulation system is that it induces an increased risk of moisture problems by lowering the overall temperature of the masonry layer while simultaneously reducing its drying potential. As a possible remediation strategy, the application of a water repellent agent on the masonry is often proposed. This product reduces (or eliminates) the absorption of wind-driven rain, while leaving the material vapour open to not impede drying of moisture towards the outside environment. While the hydrophobisation procedure theoretically reduces the risk of moisture problems by removing its main moisture source, there are multiple reports on existing moisture problems worsening or new moisture problems initiating. Some possible reasons for a faulty application are the existence of cracks in the masonry or the use of a water repellent agent which does not suit the building material. The suitability of a certain water repellent agent can be investigated by performing several hygrothermal simulations with the hygric properties of different hydrophobised materials used as input. However, these properties can currently only be acquired through time-expensive experiments which are often not suitable for hydrophobised building materials. As an alternative, the use of pore-scale models for the determination of the hygric properties of hydrophobised building materials is investigated in this thesis.
Previous researchers of the Building Physics and Sustainable Design Section of the KU Leuven have created a pore-scale model, capable of simulating the hygric properties of hydrophilic porous materials. As this model simulates the microscopic moisture storage and transport processes in capillary active (i.e. hydrophilic) pores, rendering the pore walls hydrophobic with the help of a water repellent agent makes the current model unfit. The prime objective of this PhD project is therefore to enable the model to simulate the hygric properties of hydrophobised materials by modifying and validating the currently hydrophilically-oriented pore-scale model. To achieve this main objective, the thesis is divided into three different parts.

The first part of this thesis measures the hygric properties of hydrophobised building materials experimentally, so they can be used to validate the simulated hygric properties derived from the adapted pore-scale model. Since existing experimental techniques are often not capable of measuring the hygric properties of hydrophobised building materials though, both existing as well as newly developed experimental methods are applied. While the cup tests remain viable for vapour permeability measurements on hydrophobised materials, the steady state centrifuge experiment and adapted cup tests are created to quantify the moisture storage properties and liquid permeability, respectively. This section concludes that the hydrophobised materials store very little moisture under normal atmospheric conditions, causing moisture flow to be dominated by vapour transport.
The second part investigates the microscopic moisture behaviour in hydrophobised materials at the pore level. When the water repellent agent enters the pore network of a material, it renders the pore walls hydrophobic. However, the smallest pores in the pore network can remain hydrophilic if the water repellent agent is too big to enter. This part of the thesis therefore focuses on locating these hydrophilically-oriented pores. Afterwards, the moisture storage and transport processes in both hydrophilic and hydrophobised elements are investigated. For this microscopic investigation, samples are preconditioned to different saturation states after which the moisture distribution in the individual elements is imaged using X-ray computed tomography images and/or nuclear magnetic resonance relaxometry. These experimental techniques showed that almost all pore bodies and throats of the materials became hydrophobised, but that moisture storage in some of the corners of these hydrophobised elements remains possible. These storage sites are scattered throughout the network, though, and hence no continuous liquid flow path through the material exists after hydrophobisation. Vapour flow is thus the dominant transport phenomenon. These conclusions are further used to adapt the hydrophilically-oriented pore-scale model.
The final part of this thesis then adapts the existing hydrophilically-oriented pore-scale model using the conclusions drawn from the microscopic investigation of the moisture behaviour. The hygric properties of hydrophobised porous materials, simulated with this adapted pore-scale model, are subsequently validated using the experimentally measured hygric properties of hydrophobised materials. This successful adaptation illustrates the possibilities of the pore-scale modeling approach for the hygric property determination of hydrophobised building materials. Further validation of the model using other (fully and partially) hydrophobised materials though remains necessary. The adapted pore-scale model is subsequently used to simulate the moisture behaviour in hydrophobised materials in which increasing amounts of pores remain hydrophilic to represent imperfect hydrophobisation applications. By using the

simulated hygric properties from this model to replicate capillary absorption experiments, the need for a suitable water repellent agent, which is tailored towards the building material and hence sufficiently reduces moisture absorption, is highlighted. Choosing the best water repellent agent therefore requires prior knowledge about the material's pore size distribution as well as the water repellent agent's emulsion droplet sizes to make sure sufficient amounts of pores become hydrophobised.

Beknopte samenvatting

Binnenisolatie systemen genieten veel interesse in het onderzoeksgebied van de bouwfysica omdat ze typisch de enige optie zijn voor een thermische renovatie van gebouwen met beschermde gevels. Één van de belangrijkste problemen van dit type isolatiesysteem is het verhoogd risico op vochtproblemen, wat veroorzaakt wordt door de verlaagde temperatuur van de metselwerkwand te combineren met een verminderde droogpotentiaal. Om dit soort vochtproblemen tegen te gaan wordt er vaak voorgesteld om een hydrofoberingsmiddel aan te brengen op de buitengevel. Dit product vermindert (of elimineert) de absorptie van regen, terwijl het materiaal dampopen blijft om het drogen van vocht naar de buitenomgeving niet te belemmeren. Hoewel dit hydrofoberingsmiddel het risico op vochtproblemen theoretisch vermindert door de belangrijkste vochtbron te verwijderen, zijn er meerdere meldingen van bestaande vochtproblemen die verergeren of nieuwe vochtproblemen die ontstaan. Enkele mogelijke oorzaken van zulke foutieve toepassingen van hydrofoberingsmiddelen, zijn de aanwezigheid van scheuren in het metselwerk of het gebruik van een hydrofobiseringsmiddel dat niet geschikt is voor het bouwmateriaal. De geschiktheid van een bepaald middel kan worden onderzocht door verschillende hygrothermische simulaties uit te voeren met de hygrische eigenschappen van de materialen, gehydrofobeerd met verschillende middelen, als input. Deze hygrische eigenschappen kunnen momenteel echter alleen worden verkregen met tijdsintensieve experimenten die vaak zelfs niet geschikt zijn voor gebruik op gehydrofobeerde bouwmaterialen. In deze PhD thesis wordt daarom onderzocht of poriënschaalmodellering kan dienen als alternatief voor de bepaling van de hygrische eigenschappen van gehydrofobeerde bouwmaterialen.
Onderzoekers van de afdeling Bouwfysica en Duurzaam Bouwen hebben een poriënschaalmodel ontwikkeld dat in staat is om de hygrische eigenschappen van hydrofiele poreuze materialen te simuleren. Aangezien dit model de microscopische vochtopslag- en transportprocessen in capillair actieve (d.w.z. hydrofiele) poriën simuleert, zal het hydrofoberen van de poriewanden met behulp van een hydrofoberingsmiddel dit huidige model onbruikbaar maken. Het belangrijkste doel van deze thesis is daarom om dit model in staat te stellen

om de hygrische eigenschappen van gehydrofobeerde materialen te bepalen door het huidige hydrofiel georiënteerde poriënschaalmodel aan te passen en te valideren. Om dit hoofddoel te bereiken, is de thesis verdeeld in drie verschillende delen.

Het eerste deel van deze thesis bepaalt de hygrische eigenschappen van gehydrofobeerde bouwmaterialen experimenteel, met als doel ze te gebruiken om de hygrische eigenschappen, die voortkomen uit het aangepaste poriënschaalmodel, te valideren. Aangezien bestaande experimentele technieken vaak niet in staat zijn om de hygrische eigenschappen van gehydrofobeerde bouwmaterialen te bepalen, worden zowel bestaande als nieuw ontwikkelde experimentele methoden toegepast. Hoewel de cup tests bruikbaar blijven voor het meten van de damppermeabiliteit van gehydrofobeerde materialen, worden de steady state centrifuge test en een variant op de cup tests ontwikkeld om respectievelijk de vochtopslag en vloeistofpermeabiliteit te kwantificeren. Deze sectie concludeert dat de gehydrofobeerde materialen onder normale atmosferische omstandigheden zeer weinig vocht opslaan, waardoor vochttransport wordt gedomineerd door damptransport.

Het tweede deel van deze thesis richt zich op het onderzoeken van het microscopisch vochtgedrag in gehydrofobeerde materialen op het niveau van de poriën. Wanneer het hydrofoberingsmiddel het poreuze netwerk van een materiaal binnendringt, maakt het de poriewanden hydrofoob. De kleinste poriën in het poreuze netwerk kunnen echter hydrofiel blijven als de polymeren van dit hydrofoberingsmiddel te groot zijn om binnen te dringen. Dit deel van de thesis richt zich daarom op het (mogelijks) lokaliseren van zulke hydrofiel georiënteerde poriën, waarna de vochtopslag- en transportprocessen in zowel hydrofiele als gehydrofobeerde elementen onderzocht worden. Voor dit microscopische onderzoek worden materialen vooraf geconditioneerd tot verschillende verzadigingsgraden, waarna de vochtverdeling in de afzonderlijke poriën wordt gevisualiseerd met behulp van X-ray computed tomography of nuclear magnetic resonance relaxometry. Deze experimentele technieken tonen aan dat bijna alle poriën van de materialen werden aangetast door het hydrofoberingsmiddel, maar dat vochtopslag in sommige hoeken van deze gehydrofobeerde poriën mogelijk blijft. Deze opslagplaatsen zijn verspreid over het netwerk, wat betekent dat er geen continue vloeistofstroom door het materiaal bestaat na hydrofobering. Damptransport blijft hierdoor het dominante transportverschijnsel. Deze conclusies worden verder gebruikt om het hydrofiel georiënteerde poriënschaalmodel aan te passen.

Het laatste deel van deze thesis past het bestaande hydrofiel georiënteerde poriënschaalmodel aan volgens de conclusies die voortkomen uit het microscopisch onderzoek van het vochtgedrag. De hygrische eigenschappen van gehydrofobeerde poreuze materialen, gesimuleerd met dit aangepaste poriënschaalmodel, worden vervolgens gevalideerd met behulp van de experimenteel

gemeten hygrische eigenschappen. Het succesvol aangepaste model toont de modelijkheden van de poriënschaalmodellering voor de bepaling van hygrische eigenschappen van gehydrofobeerde bouwmaterialen. Verdere validatie van het model voor andere (gedeeltelijk en volledig) gehydrofobeerde bouwmaterialen blijft wel nog nodig. Een verder onderzoek met dit model naar de impact van een toenemende hoeveelheid hydrofiele poriën in gehydrofobeerde materialen benadrukt ook de noodzaak van een geschikt hydrofoberingsmiddel dat is afgestemd op het bouwmateriaal. Het succesvol aanbrengen van hydrofobering vereist dus voorafgaande kennis van de poriegrootteverdeling van het materiaal en de afmeting van de polymeren van het hydrofoberingsmiddel.

Nomenclature

The acronyms and abbreviations, listed below, are limited to the variables which are used multiple times throughout the dissertation. Information about variables, only used at specific locations in the text, can be found there.

Roman

A	Cross-section	[m^2]
A_{cap}	Capillary absorption coefficient	[$kg/m^2s^{0.5}$]
g_{ij}	Conductance between pore bodies i and j	[kg/sPa]
g_l	Liquid conductance	[kg/sPa]
g_v	Vapour conductance	[kg/sPa]
G	Shape factor	[-]
K	Moisture permeability	[kg/msPa]
M(t)	Magnetic signal in function of time	[dB]
p_c	Capillary pressure	[Pa]
$p_{c,thres}$	Threshold capillary pressure	[Pa]
p_v	Vapour pressure	[Pa]
r	Pore radius	[m]
r_{hydr}	Hydrophobic radius	[m]
R_v	Gas constant	[J/kgK]
S_c	Volume fraction of corner islands	[-]
T	Temperature	[°C]
T_2	Transverse relaxation time	[s]
$T_{2,\ bulk}$	Bulk tansverse relaxation time	[s]
$T_{2,\ surface}$	Surface transverse relaxation time	[s]
$T_{2,\ diffusion}$	Diffusion-induced transverse relaxation time	[s]
TE	Inter-echo spacing	[s]
w_{cap}	Capillary moisture content	[kg/m^3]
w_{sat}	Saturated moisture content	[kg/m^3]

Greek

α	Regularization parameter	[-]
δ_{a}	Vapour permeability	[kg/msPa]
θ	Contact angle	[°]
μ	Vapour diffusion resistance factor	[-]
ρ_2	Surface relaxivity	[m/s]
ρ_{l}	Density of liquid water	[kg/m^3]
ω	Radial velocity	[rad/s]

Acronyms and abbreviations

CPMG	Carr-Purcell-Meiboom-Gill
DLS	Dynamic light scattering
ILT	Inverse Laplace transform
IP	Invasion percolation
LM	Laboratory made
MIP	Mercury intrusion porosimetry
NMR	Nuclear magnetic resonance
NTC	No throat corner islands
PNM	Pore network model
PSD	Pore size distribution
RH	Relative humidity
RPM	Revolutions per minute
SEM	Scanning electron microscopy
SNR	Signal-to-noise ratio
XCT	X-ray computed tomography

Contents

Abstract iii

Beknopte samenvatting vii

Contents xiii

1 Introduction 1
- 1 Problem statement . . . 1
- 2 Research objectives . . . 3
- 3 Dissertation outline . . . 4

2 Introduction to hydrophobised building materials 7
- 1 The physical principles of water repellent agents . . . 8
- 2 The types of water repellent agents . . . 9
  - 2.1 Metal-bearing compounds . . . 9
  - 2.2 Organic materials . . . 9
  - 2.3 Silicon-bearing compounds . . . 9
- 3 Properties of hydrophobised building materials . . . 11
  - 3.1 Penetration depth . . . 11
  - 3.2 Hygric properties . . . 12
  - 3.3 Macroscopic moisture behaviour . . . 15
- 4 Building materials and water repellent agents used in this PhD thesis . . . 17
  - 4.1 Materials . . . 17
  - 4.2 Water repellent agents . . . 19
- 5 Summary . . . 21

3 Introduction to pore-scale modeling 23
- 1 Applications of pore-scale modeling . . . 24
- 2 Different types of pore-scale modeling . . . 27
- 3 Pore network characterisation . . . 29

3.1 Direct imaging . . . 30
3.2 Statistical reconstruction . . . 31
3.3 Process-based approach . . . 32
3.4 Stochastic pore network generation . . . 32
4 Pore network model used in this thesis . . . 33
4.1 Pore network characterisation . . . 34
4.2 Moisture storage in pore network elements . . . 35
4.3 Moisture transport in pore network elements . . . 38
5 Summary . . . 40

4 Experimental determination of the macroscopic hygric properties 45
A Hygric property determination of hydrophilic porous materials 46
A.1 Introduction . . . 46
A.2 Description of the steady state centrifuge experiment . . . 48
A.3 Design of the laboratory steady state centrifuge . . . 51
A.4 Validation of the steady state centrifuge experiment . . . 62
A.5 Application of the steady state centrifuge experiment . . . 69
A.6 Discussion . . . 72
A.7 Summary . . . 74
B Hygric property determination of hydrophobised porous materials 75
B.1 Introduction . . . 75
B.2 Materials . . . 75
B.3 Moisture retention curve . . . 76
B.4 Vapour permeability . . . 79
B.5 Liquid permeability . . . 83
B.6 Discussion . . . 86
B.7 Summary . . . 89

5 Investigation of the microscopic moisture behaviour 91
A Microscopic moisture behaviour in hydrophilic porous materials 92
A.1 Introduction . . . 92
A.2 Theory of nuclear magnetic resonance experiments . . . 94
A.3 Materials and methods . . . 105
A.4 Results . . . 111
A.5 Discussion . . . 120
A.6 Summary . . . 122
B Microscopic moisture behaviour in hydrophobised porous materials 124
B.1 Introduction . . . 124
B.2 Materials and methods . . . 126
B.3 Results . . . 133
B.4 Location of hydrophilic pore bodies and throats . . . 138
B.5 Summary . . . 141

6 Pore network modeling of hygric properties **143**
A Pore network modeling in hydrophilic porous materials 144
A.1 Introduction 144
A.2 Materials and methods 145
A.3 Results 148
A.4 Recommendations for possible model improvement . . . 155
A.5 Discussion 161
A.6 Summary 164
B Pore network modeling in hydrophobised porous materials . . . 165
B.1 Introduction 165
B.2 Adaptation of the hydrophilically-oriented PNM 166
B.3 Macroscopic validation of the adapted PNM 168
B.4 Discussion 180
B.5 Summary 182

7 Conclusions and outlook **187**
1 Summary and discussion 187
1.1 Chapter 4: Experimental hygric property determination 187
1.2 Chapter 5: Investigation of microscopic moisture behaviour 190
1.3 Chapter 6: Pore network modeling of hygric properties . 192
2 Conclusions 195
3 Limitations and future work 197

Bibliography **201**

Curriculum **223**

List of publications **225**

Chapter 1

Introduction

1 Problem statement

Moisture control in built structures is known to be essential in maintaining a durable, sustainable, healthy and comfortable built environment. Nevertheless, a dependable assessment of the hygrothermal behaviour is frequently overlooked when constructing and/or renovating buildings. As a result, moisture problems occur widely throughout the existing building stock. This is demonstrated in a 2009 study by the World Health Organization [1], which concluded that 18% of the EU population was still confronted with building-dampness-related problems.

When driving rain is the moisture source of concern, proper shielding of the exterior facades, via a roof overhang or an external render, may form a suitable solution. In case these exterior facades are worthy of preservation though, like for historic buildings, altering the exterior appearance is not allowed, and (more) invisible solutions are required. To that end, the application of a water repellent agent, to reduce the driving rain absorption, is becoming more and more popular over the last decade [2–9]. This becomes specifically relevant when these preservation-worthy exterior facades are thermally retrofitted, typically to render the building more sustainable with respect to energy consumption. As exterior alterations are not permitted, often only internal insulation can be applied to that aim. However, this internal insulation may significantly increase the moisture damage risk due to lower temperatures in the original facade as well as reduced drying rates to both the inside and outside environments, which generally leads to higher moisture contents [10,11].

Recently several studies [10,12–15] as well as a H2020 project (RIBuild) [16] on internal insulation of masonry walls have been conducted, all with the aim of diminishing the risk at potential moisture problems. These investigations

conclude that the occurring moisture damage is predominantly caused by the driving rain load. They therefore suggest that the application of a water repellent agent may be beneficial for the success of such thermal retrofit through internal insulation, if applied correctly [4,12–15]. Such hydrophobisation should however be applied with caution, as it does not only reduce the driving rain absorption but also decreases the drying to the outside environment. Rain absorption is diminished by eliminating spontaneous liquid storage and transport in the hydrophobised pores of the facade material, but that effect also minimises or eradicates the first drying phase, which is typically responsible for the largest share of drying [5,8,17].

These contradicting consequences of water repellent treatments result in some faulty applications where new moisture problems occur or existing moisture problems worsen. Possible reasons for such faulty applications are moisture absorption through cracks in the hydrophobised masonry [18–21] or choosing the wrong water repellent agent for a certain application [5,6,18]. Not only is the suitability of a water repellent agent in masonry walls heavily case-dependent [12–14,22], different water repellent agents also impact the hydrophobised material's moisture behaviour differently [5,6,18]. Deciding whether such a hydrophobisation application is recommended as well as choosing the correct water repellent agent therefore requires detailed simulations with Heat, Air and Moisture transfer models of hydrophobised walls. These hygrothermal simulations require input on the moisture storage and transport properties of hydrophobised materials. However, the experimental determination of such hygric properties is lengthy, imprecise and sometimes even impossible with the currently available methods [8]. This is caused by the reduction or elimination of moisture absorption in these hydrophobised samples, which hinders the preconditioning of the samples as well as severely retards the moisture transport throughout the experiments.

As an alternative, pore-scale modeling of the moisture storage and transport inside the pore structure of the hydrophobised materials could provide a potential solution to that cumbersome experimental approach. In such pore-scale models, the microscopic moisture storage and transport processes are simulated at the pore level (i.e. in every pore of the material). This information is subsequently upscaled towards the sought macroscopic hygric properties. Pore-scale modeling for the hygric property determination has previously been applied with success on hydrophilic materials [23–27]. However, models in literature handling hydrophobised building materials [28,29], assume very simple representations of the pore structure and make severe assumptions on the distribution of the water repellent agent in the pores of the material as well as the microscopic moisture behaviour in such hydrophobised pores. Both Lal et al. [28] and Namoulniara et al. [29] for example assume that hydrophobised pore bodies and throats are perfectly hydrophobised, which means that no moisture storage

is possible in these elements and that they only allow vapour transport. Also, pore bodies and throats are labelled as hydrophobic via a random generator [28] or according to their pore radii [29]. These assumptions are not based on prior research, but on unproven hypotheses. **The primary goal of this project is thus to develop a more correct pore-scale modeling approach for the hygric property determination of hydrophobised building materials in which the water repellent agent's distribution throughout and the moisture behaviour in the hydrophobised material's pore structure is evidence-based.**

2 Research objectives

Previous research of the KU Leuven Building Physics and Sustainable Design Section has produced a pore-scale model that allows determining the hygric properties of hydrophilic materials [23]. As this model simulates the microscopic moisture storage and transport processes in capillary active (i.e. hydrophilic) pores, rendering the pore walls hydrophobic with the help of a water repellent agent makes the current model unfit. **The prime objective of this project is to enable the existing model to simulate the hygric properties of hydrophobised materials by modifying and validating the currently hydrophilically-oriented pore-scale model.** By doing so, the lengthy and/or difficult experimental determination of these hygric properties can be replaced with more efficient and effective pore-scale modeling.
To accomplish this prime objective, two sub-objectives, which each make up a chapter of this dissertation, are established. Firstly, adapting the hydrophilically-oriented pore-scale model for moisture storage and transport simulations in hydrophobised materials requires knowledge about the interaction between moisture and hydrophobised pore surfaces at the pore-level. **Sub-objective 1 therefore entails the investigation of the microscopic moisture behaviour at the pore level in hydrophobised porous materials.** Once the pore-scale model is adapted using the conclusions of sub-objective 1, hygric properties of hydrophobised materials can be simulated. These simulation results still require validation to justify the implementation of the adapted pore-scale model. To this aim, hygric properties of hydrophobised porous materials are determined experimentally for comparison with the simulation results. Since not all commonly used experimental methods are applicable to hydrophobised materials, this requires the development of several new methods. **Sub-objective 2 therefore concerns the experimental determination of macroscopic hygric properties of hydrophobised porous materials using both existing and newly developed experimental techniques.** Completion of these sub-objectives is necessary for the realisation of the prime objective.

3 Dissertation outline

In order to achieve the research objectives put forward in previous section, this dissertation is divided into several chapters. To start with, **Chapter 2** provides the reader with an introduction to the use of water repellent agents on building materials. First, the physical principles behind such a hydrophobisation application are explained and an overview is given of the vast spectrum of commercially available products. Next, the influence of such water repellent agents on the moisture behaviour of building materials is illustrated. Finally, the materials and water repellent agents, around which this thesis is centered, are described and the choice for these materials is justified.

Chapter 3 then provides the reader with the knowledge on pore-scale modeling, as required to understand the choices made in this dissertation. Since this technique is widely used throughout different research domains, this chapter starts by illustrating some of its applications. Next, the different approaches towards pore-scale modeling are discussed and the reasoning behind the use of quasi-static pore network modeling in this thesis is explained. This pore network modeling approach requires the pore network of a material as input, which is why the different types of pore network characterisation are reviewed. The final part of this chapter focuses on the hydrophilically-oriented quasi-static pore network model of Islahuddin and Janssen [23], which will be adapted for hygric property determination of hydrophobised building materials in Chapter 6.

After providing the reader with the information required to understand the research performed in this thesis, the next chapters address the two sub-objectives as well as the prime objective, as formulated in Section 2. **Chapter 4** focuses on the experimental determination of hygric properties of hydrophobised materials, which will be used for the validation of the adapted pore-scale model. The first part of this chapter develops and validates a new experimental method, called the steady state centrifuge technique, for the moisture retention curve determination of porous materials. To do so, results obtained with this new method for several hydrophilic materials are compared with the outcomes of more common experimental techniques. After its successful validation, this technique is applied for the moisture retention curve determination of the hydrophobised materials in the final part of this chapter. Additionally, other experiments are also used to measure both the vapour and liquid permeability of hydrophobised materials.

Next, **Chapter 5** focuses on the investigation of the microscopic moisture behaviour at pore level in hydrophobised porous materials. In this chapter, the information required for the adaptation of the existing hydrophilically-oriented pore-scale model is gathered. This microscopic investigation is based on two different experimental techniques: nuclear magnetic resonance relaxometry and X-ray computed tomography imaging. The first part of Chapter 5 applies

these techniques to hydrophilic materials to assess their applicability for the microscopic study in this dissertation. The competent technique(s) are subsequently used for the microscopic investigation of the moisture behaviour in hydrophobised materials.

Subsequently, **Chapter 6** focuses on the pore-scale modeling of hygric properties of hydrophobised building materials. Since the existing hydrophilically-oriented pore-scale model has only been validated macroscopically in [23] using experimentally determined hygric properties, the first part of Chapter 6 provides a microscopic validation of the model using the results of the microscopic investigation of hydrophilic materials in Chapter 5. Based on this microscopic validation, the existing model is slightly adapted. Next, the outcomes of the microscopic investigation of hydrophobised materials in Chapter 5 are used to adapt the hydrophilically-oriented pore-scale model for hydrophobised materials in the final part of Chapter 6. Simulation results obtained from this adapted pore-scale model are subsequently validated using the experimentally measured hygric properties of hydrophobised materials, obtained in Chapter 4.

After completing the prime objective in Chapter 6, **Chapter 7** reiterates the most important conclusions obtained in this PhD thesis and highlights the limitations of the current work. Based on these limitations, an outlook for follow-up research is also provided.

Chapter 2

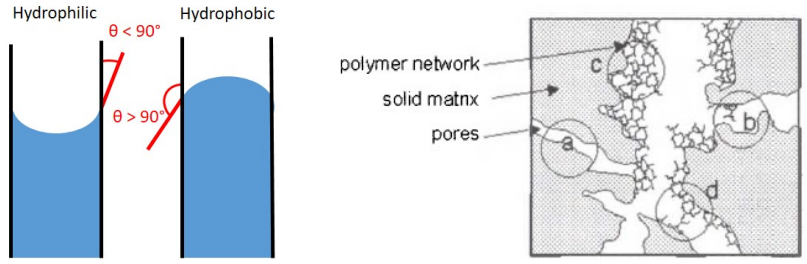
Introduction to hydrophobised building materials

Water repellent agents are typically applied to building materials to render them hydrophobic. This limits their rain water uptake and effectively reduces the risk at moisture problems. There is a vast array of commercially available products which claim to do just that, however, some water repellent agents have shown to perform better than others [5], while still others worsen existing moisture problems or even create new ones [18,21]. Choosing the correct water repellent agent in a certain situation is therefore crucial to guarantee a successful application. This chapter therefore aims at introducing the reader to the working mechanism of a hydrophobisation application and to the vast gamma of commercially available water repellent agents in Sections 1 and 2, respectively. Next, the impact of these water repellent agents on a material's hygric properties and moisture behaviour is discussed in Section 3. Subsequently, the porous materials and water repellent agents, around which this thesis is centered, are described and motivated in Section 4. Finally, Section 5 reiterates the most important takeaways of this chapter.
Section 4 is largely adopted from paper 2.1 below.

Paper 2.1: D. Deckers, Y. Zhu, E. Koos, H. Janssen. Microscopic localisation of hydrophilically oriented pore bodies and throats in hydrophobised porous materials. Transp. Porous Media, 151: 773–793, 2024. doi: 10.1007/s11242-024-02069-w

1 The physical principles of water repellent agents

When a building material is being hydrophobised, the water repellent agent is transported through the material's pore network. Regardless of the type of water repellent agent, it is typically composed of molecules with a polar head and a non-polar tail. Inside the pore network, the polar heads attach themselves to the polar pore surfaces, hereby creating a thin surface coating with their non-polar tails directed towards the bulk of the pores. These non-polar tails actively repel the polar water molecules [18,30,31] and hereby change the interaction between water and hydrophobised pore surfaces. Pores are assumed hydrophobic when the contact angle at the water/air interface is larger than 90°, as shown in Figure 2.1 (a), which can be interpreted as the affinity of the water molecules towards each other becoming larger than their affinity towards pore surfaces. In such hydrophobised pores, spontaneous absorption of water is assumed to be impossible.



(a) (b)

Figure 2.1: Illustration of the contact angle (θ) of water in hydrophilic and hydrophobic capillaries (a) and the polymer network of a water repellent agent in the pore network of a porous material (b) [30].

Since only the thin surface coating has hydrophobic properties, the bulk of the pore volume remains accessible to water vapour particles and hence vapour transport should not be affected significantly [30–32]. However, when the size of the pores is smaller than or of a similar size as the particles of the water repellent agent, they experience difficulty trying to penetrate these fine pores. In this case, it is speculated that these pores can become blocked (a in Figure 2.1 (b)), clogged (d in Figure 2.1 (b)), or remain partially to fully hydrophilic (b in Figure 2.1 (b)) [30,32]. These blocked or hydrophilically-oriented pores have not yet been directly visualised, however, and their existence is currently only proven through indirect evidence, examples of which are given in Section 3.

2 The types of water repellent agents

Commercially available water repellent agents typically belong to either of the following three categories: silicon-bearing compounds, metal-bearing compounds or organic materials [6,18]. Recently, the introduction of nanotechnology in mixtures with existing water repellent agents also showed promising results [33,34]. More research, however, is required before they can be readily used. These compounds are therefore not further discussed in this thesis. Of the other three categories, the silicon-bearing compounds are most widely used for hydrophobisation of building materials [6], which is why these are emphasised most below.

2.1 Metal-bearing compounds

The most popular metal-bearing compounds are typically based on aluminum stearate, in which the polar aluminum head attaches itself to the polar pore surfaces while the stearate tail provides the hydrophobicity [6,18]. Some other metal-bearing compounds, such as titanium stearate, can also be found mixed in with silicon-bearing compounds [18]. Overall, these water repellent agents are not very durable [35] and typically not effective for hydrophobisation of masonry [6,18]. They can be used as admixtures in mortars (combined with other types of agents) [36], but since the focus of this thesis lies on the hydrophobisation of existing structures, this technique is not further discussed.

2.2 Organic materials

The water repellent agents composed of organic materials are typically based on acrylics, polyurethanes and perfluoro-polyethers and can either be used as stand-alone water repellent agents or in mixtures with silicon-bearing compounds [6,18]. These materials are often used as consolidants which simultaneously give a water repellent character to the affected materials [18].

2.3 Silicon-bearing compounds

Silicon-bearing compounds, most often used for the hydrophobisation of building materials, can be divided into three different groups: silanes, siloxanes and silicone resins [18,37,38]. All compounds are similarly composed of a repeating Si-O-Si backbone, however, the number of repeating connections determines the polymer chain length, and thus classifies the product as a silane, a siloxane or a silicone resin. While silanes possess the shortest chains and hence the lowest molecular weight, silicone resins are longest and consequently have the highest molecular weight. Attached to these backbones are several alkyl (e.g. methyl) and alkoxy (e.g. methoxy) groups. The latter reacts with water to connect the

compounds to the pore surfaces of the building materials and form a thin pore surface coating as in Figure 2.1 (b). The former provides the hydrophobic effect. For further details regarding the chemical reactions that cause the molecules to attach themselves to the pore surfaces, the reader is referred to literature [18,37,38].

Water repellent agents based on silanes, siloxanes and silicone resins are typically used in different applications. Silanes, which can penetrate deep into materials due to their low viscosity and low reactivity, are often used for the hydrophobisation of alkaline substrates such as concrete [6,37]. Siloxanes, which are more reactive, are typically used for the hydrophobisation of natural stones and bricks, since their high reactivity results in a small penetration depth in the alkaline concrete [37,38]. Silicone resins consist of an elaborate 3D network of Si-O-Si connections and they are hence the most stable compounds. Due to their stability, these resins are most often used as admixtures in paints and plasters [37].

The commercially available water repellent agents, used for the hydrophobisation of building components, are typically mixtures of both silanes and siloxanes, with their ratio tailored towards the building material [37]. These compounds originally required mixing with organic solvents (e.g. white spirit) prior to application, however, due to environmental concerns most products are currently provided as water-borne solutions (i.e. water repellent agent/water emulsions) [37–39]. More recently, these silicon-bearing compounds have been developed as creams or pastes as complement to the current liquid versions [38–40]. Besides the formulation and used diluent, there are other factors which distinguish between different commercially available water repellent agents. For example, the percentage of active ingredient (i.e. silicon-bearing compounds) in the water/water repellent agent emulsion can vary. Feng et al. [8] have shown that there is a critical concentration above which the hydrophobisation application is deemed effective at limiting the water uptake, but this is explained in more detail in the next section. For other differences between silicon-bearing compounds (e.g. the type of alkyl group), the reader is referred to the literature [6,39].

3 Properties of hydrophobised building materials

Due to the presence of the hydrophobic polymers on the pore surfaces, the material's interaction with moisture completely changes. This section discusses the existing research on this changing moisture behaviour. It should be mentioned that the term moisture encompasses both liquid water and vapour in this dissertation. First, research towards the penetration of water repellent agents in different materials is summarised. Next, the changes these agents impose on the hygric properties of materials are reviewed. Finally, the macroscopic moisture behaviour of these hydrophobised materials in two commonly used experiments (capillary absorption and drying experiments) is investigated. This section focuses on materials hydrophobised with silicone-bearing compounds, since these are most often used to hydrophobise building components. It will be shown that even within this category of water repellent agents, there are many products which influence material properties differently.

3.1 Penetration depth

When a water repellent agent is applied on a building material, it is transported through the material's pore network, where the polymers attach to the pore surfaces and render them hydrophobic. The distance these agents can penetrate in such materials is typically referred to as the penetration depth. Previous studies have investigated this penetration depth, mostly on laboratory samples, by comparing the rate of water penetrating in hydrophobised and hydrophilic parts of the sample. This is either done by cutting a hydrophobised sample lengthwise (i.e. perpendicular to the hydrophobised surface) and visually assessing the absorption of water droplets deposited on the cut surface (illustrated in Figure 2.2) [5,6,17,41] or by tracking the moisture inside a material during an absorption experiment using more elaborate techniques like gamma ray attenuation [3], nuclear magnetic resonance imaging [42] or X-ray computed tomography [19,41]. Since the absolute penetration depth of water repellent agents into building materials is heavily dependent on the building materials, the water repellent agents, the application procedure (i.e. spraying or brushing the agent), the applied amount of water repellent agent and many other factors [5,6,42], it is difficult to discuss the penetration depths measured in literature in terms of absolute distances. A general conclusion, however, is that the material is most hydrophobic near the surface where the agent is applied and gradually remains more hydrophilic deeper into the material [41–43]. This gives rise to fully and partially hydrophobised zones which are characterised by almost no water penetration and delayed water penetration, respectively. An example of both zones can be found on Figure 2.2. Soulios et al. [6] have noted that the water repellent agent migrates into the material long after it has been applied, which eventually results in large partially hydrophobised zones. It is

also interesting to note that most of the studies on penetration depth focus on lab-scale isolated or composite samples rather than real full-scale masonry walls. Deckers et al. [41] have shown that these laboratory experiments do not necessarily match the penetration of the same water repellent agents in actual masonry.

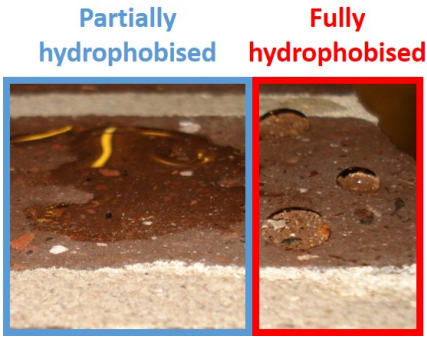


Figure 2.2: Droplets deposited on a hydrophobised masonry wall with both the fully and partially hydrophobised zones denoted [41].

3.2 Hygric properties

This section elaborates on the existing research concerning hygric property measurement of hydrophobised materials. The experimental techniques, which have been used in literature to measure the hygric properties of hydrophobised building materials, are briefly described here, however, for more elaborate descriptions of these experiments, the reader is referred to literature (e.g. [44]).

3.2.1 Moisture storage properties

The measurement of the moisture storage properties of hydrophilic building materials is often based on several well-known experimental techniques (e.g. mercury intrusion porosimetry, pressure plates, hygroscopic desiccators). These techniques are typically combined to construct the moisture retention curves of hydrophilic materials as illustrated in Figure 2.3. They have previously also been applied to hydrophobised materials, however, with mixed success.
Multiple studies have used the mercury intrusion porosimeter to measure the change in the porosity and pore size distribution of hydrophobised materials [6, 8,9,32]. In this experiment, mercury is forced into the material in incrementally increasing pressure steps and the recorded mercury intrusion in function of the applied pressure is used to determine the material's pore size distribution and

moisture retention curve. The existing literature on hydrophobised materials [6,8,9,32] notes a slight decrease in porosity (and hence in vacuum saturation content) and a reduction of the amount of small pores after the treatment. This is attributed to the clogging or blocking of the smallest pores by the water repellent agents [8,9,32], see Section 1.

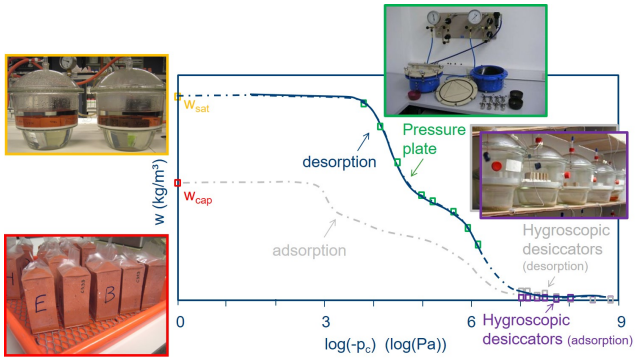


Figure 2.3: The adsorption and desorption moisture retention curves and the experimental techniques used to measure them [45].

In the capillary region, the pressure plates often contribute to the composition of the moisture retention curves. In this test, samples are placed on a saturated ceramic plate in a closed pressure vessel. The air pressure in this vessel above the sample is incrementally increased to guarantee various pressure differences over the sample. These pressure differences force moisture out of the sample through the ceramic plate and this moisture outflow is monitored for every pressure step. When no more moisture is expelled, the sample has reached its moisture equilibrium at a specific applied pressure. At that point, the sample's moisture content is gravimetrically determined, and together with the pressure difference across the sample, it contributes a data point to the construction of the moisture retention curve. Feng and Janssen [8] applied these pressure plates to different porous materials, all hydrophobised with a silicon-bearing compound. Treated ceramic brick and sintered glass filters retained more moisture than their untreated counterpart, which is unreasonable given the water repellent nature of the agents. This is attributed to a possible loss of hydraulic contact between the hydrophobised samples and the ceramic plate in the pressure plate test set-up, rendering this technique unreliable for hydrophobised building materials [8]. Other attempts at determining the moisture retention curve of hydrophobised materials using the pressure plate test set-up are lacking in the literature, probably due to these being unsuccessful. To the author's knowledge, no other viable experimental techniques exist which allow composing the moisture retention curves of hydrophobised materials in this capillary region.

In the hygroscopic region, several studies compare sorption isotherms of hydrophilic and hydrophobised materials, measured with the hygroscopic dessicators [8,9,30,32,46]. Samples are placed in these dessicators, which are preconditioned to different relative humidities with saturated salt solutions, until they reach moisture equilibrium. These equilibrium moisture contents, together with the measured relative humidities (transformed to capillary pressures), then contribute to the construction of the moisture retention curves. The studies on hydrophobised materials [8,9,30,32,46] all conclude that the hygroscopicity of treated materials is reduced since they retain less water. This is a logical outcome of the water repellent nature of the hydrophobised pore walls. Nevertheless, the moisture stored in the hygroscopic region is not completely eliminated and hence (little) moisture storage in these treated materials remains possible.

3.2.2 Moisture transport properties

The vapour permeability of materials is typically measured using cup tests, wherein the vapour flow through a sample, placed between two climate controlled environments, is measured. Using the vapour flow rate, the sample's dimensions and the climatic conditions in the two environments, the vapour diffusion resistance factor is calculated according to the ISO 12572 norm [47]. Since the vapour permeability depends on the relative humidity conditions, the cup test is typically performed twice, on materials positioned between two environments preconditioned to a low relative humidity (dry-cup; e.g. 12%-54% RH) and two environments preconditioned to a high relative humidity (wet-cup; e.g. 84%-97% RH) [8]. Due to the capillary condensation in the smaller pore bodies and throats at high relative humidities (and the formation of water islands in pore corners), the wet-cup typically results in lower vapour diffusion resistance factors than the dry-cup [48,49].

The cup test has shown to remain applicable to hydrophobised building materials, and multiple studies have therefore reported on the change of the vapour diffusion resistance factor after hydrophobisation [3,5,6,8,9,17,30,32,50,51]. Generally, these factors remain unaltered or present a slight increase. This is typically attributed to the clogging and/or blocking of some of the pores which reduces the pore network's connectivity [9,32]. Most studies which perform both dry-cup and wet-cup still note the dependency of the vapour diffusion resistance factor on the relative humidity [6,8,32]. However, Li et al. [9] note that the results of the dry-cup and wet-cup are more similar since capillary condensation in smaller (hydrophobised) pores is hindered.

Measuring the liquid permeability has proven to be much more difficult for hydrophobised building materials. Only a single study, performed by Feng and Janssen [8], reports on a value measured by the falling head water column test. In this experiment, a preconditioned sample is positioned under a water column, which forces liquid water to flow through the material. The moisture flow rate,

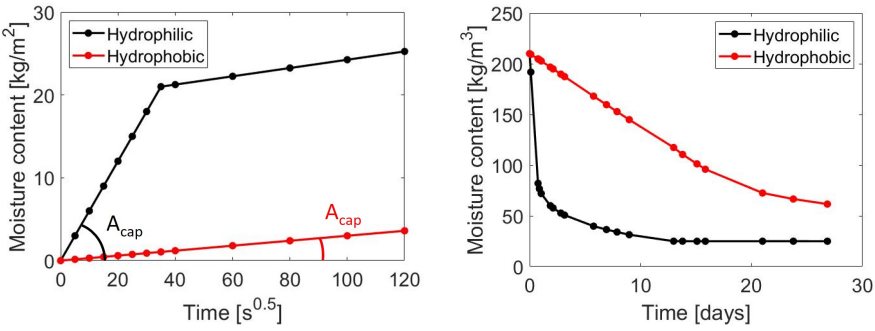
derived from the decreasing height of the water column, is then used to calculate the liquid permeability using Darcy's law. Feng and Janssen [8] show only slightly reduced liquid permeabilities for hydrophobised materials, however, it should be noted that only measurements between capillary and saturated moisture content were performed, since preconditioning of hydrophobised samples to lower moisture contents remains problematic. This means that samples are preconditioned to vacuum saturation and hence all hydrophobised pores are therefore forcibly water-filled [8]. These vacuum conditions do not occur in reality and unsaturated liquid permeabilities at lower moisture contents are therefore desired, yet unavailable in the literature.

3.3 Macroscopic moisture behaviour

3.3.1 Capillary absorption experiment

The main aim of a hydrophobisation application is the reduction of wind-driven rain absorption of building components. This is why capillary absorption experiments are often performed to estimate the application's effectiveness. In such absorption experiments, the hydrophobised surface of samples is placed in water and the rate of absorption is tracked by periodic weight measurements. The increase in mass, representative of the amount of moisture absorbed, is subsequently plotted in function of the square root of time as illustrated in Figure 2.4 (a). Hydrophilic samples typically display two linear stages. The capillary absorption coefficient is calculated as the slope of the first, fast stage and it represents the ease with which samples can spontaneously absorb water. The application of a water repellent agent reduces this capillary absorption coefficient [5,50], as illustrated in Figure 2.4 (a), and the degree of this reduction is often used as a measure of the obtained hydrophobicity.

Despite being the main goal of a hydrophobisation procedure, the reduction of the capillary absorption coefficient is not always successful. Hansen et al. [5] performed several experiments on ceramic brick and lime mortar, both hydrophobised with 16 different water repellent agents, ranging from silicon-bearing compounds to compounds based on nanotechnology, some of which are diluted to different concentrations. These samples are fully immersed in water and their weight increase is noted after 20 hours. Results showed that some hydrophobised materials absorbed equally much moisture while others absorbed less than 1 % of the moisture of their hydrophilic counterparts [5]. Although this is not a typical capillary absorption experiment due to the full submersion of samples, it does show the need for a correct fit between building material and water repellent agent.



(a) (b)

Figure 2.4: Illustration of the moisture content evolution in capillary absorption (a) and drying experiments (b) in hydrophilic and hydrophobic building materials.

In most studies, where the water repellent agents are tailored towards the building materials, capillary absorption coefficients are reduced by at least 80 % [9,32,51], and usually even more [6,8,17,30,43,46,50]. Such applications are typically described as successful when reductions of at least 95-97 % are obtained [6,30]. Besides finding the water repellent agent which tailors best towards a certain building material, some other factors have proven to influence the measured capillary absorption coefficients. Firstly, an increase in the percentage of active ingredient (i.e. amount of water repellent agent in the applied water/water repellent agent emulsion) seems to render the application more effective until the active ingredient's critical concentration is reached [8,43]. Further increasing the concentration beyond this critical concentration no longer reduces water absorption notably. Secondly, Soulios et al. [6,7] have found that the capillary absorption coefficient further reduces when the experiment is repeated several times. They attribute this to the fact that the first iterations wash away the emulsifiers in the water repellent agent after which it becomes more effective. Finally, Zhao and Meissener [43] prove that cleaning the materials' surfaces before application of the water repellent agent and waiting a sufficiently long time after materials are exposed to the agent to allow all chemical processes to finish (i.e. a sufficiently long curing time), are also necessary for a successful hydrophobisation application. Hence, not only the choice of the water repellent agent, but the manner in which it is applied to materials needs to be tailored towards the building material.

3.3.2 Drying experiment

In a one-dimensional drying experiment, all surfaces of a saturated sample, besides its top surface, are covered with vapour tight tape and they are placed in a climate controlled chamber. The samples are allowed to dry through their one uncovered surface and the weight decrease is tracked via periodic weight measurements. The drying behaviour of many hydrophilic materials is characterised by a fast, first drying stage followed by a much slower, second drying stage as illustrated in Figure 2.4 (b). The drying rate in the first drying stage is limited by the evaporation rate at the top surface since the supply of moisture to this surface occurs through fast liquid water transport. In the second, slower stage, moisture is supplied to the surface via much slower vapour diffusion since there is no continuous liquid flow path towards this top surface anymore. This causes the drying rate to be limited by the supply of moisture to the evaporation surface.
In a hydrophobised building material, where liquid water transport is diminished or even completely eliminated, this fast, first drying stage does not occur (or has a much reduced rate) as illustrated in Figure 2.4 (b). Any moisture which evaporates at the sample's top surface must therefore be supplied via vapour diffusion. This phenomenon has been noted in multiple studies [5,8,17,52]. The removal of this first drying stage explains why the drying rate of hydrophobised materials is much slower, even though their vapour permeabilities are hardly altered. The degree to which this drying process is delayed once again depends on the building materials and water repellent agents as illustrated by the multiple drying experiments in Hansen et al. [5].

4 Building materials and water repellent agents used in this PhD thesis

This PhD is centered around two porous materials and three water repellent agents. These are all described in this section and some relevant information is repeated throughout the thesis when these materials and agents are used.

4.1 Materials

The two porous materials used in this thesis, Vandersanden Robusta ceramic brick and ROBU P100 sintered glass filter, are both well-documented in our research section [8,44]. The Vandersanden Robusta brick [53] is a ceramic brick with a density and porosity of $1818 \pm 32\,\mathrm{kg/m^3}$ and $32.6 \pm 0.4\%$ respectively. It has a relatively high permeability compared to other ceramic bricks, which is illustrated by its capillary absorption coefficient of $0.61\ \mathrm{kg/m^2 s^{0.5}}$ [54]. This

brick is composed of pores in both the micro- and nanometer ranges as shown on Figure 2.5.

Parts of this thesis focus on imaging the pore network of materials with X-ray computed tomography, which has a spatial resolution limit of about 1 µm. This means that the nanoscale porosity of the ceramic brick (i.e. all pores with radii smaller than 1 µm) cannot be visualised and resultantly, the moisture behaviour in these pores cannot be investigated. To this aim, a P100 sintered glass filter from ROBU [55], with density and porosity of $1414 \pm 15\,\mathrm{kg/m^3}$ and $36.5 \pm 0.7\%$ respectively, and pores with radii ranging from 5 µm to 75 µm, is used, despite it not being a typical building material. This sintered glass' entire pore network can be captured by X-ray computed tomography images with a spatial resolution of 2.5 µm [56] and the pore size distribution of this material, derived from these images, is shown on Figure 2.5.

Lime mortar, which typically also becomes hydrophobised in a real masonry wall, is not studied in this dissertation even though it has a greater share of nanoscale porosity and is more hygroscopic than the ceramic brick and/or sintered glass. Further studies on such hygroscopic building materials remain future work.

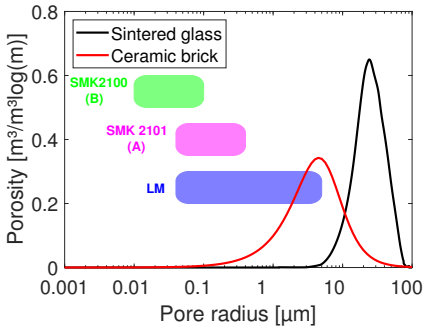


Figure 2.5: The pore size distributions of Vandersanden robusta ceramic brick and sintered glass, extracted from mercury intrusion porosimetry measurements and X-ray computed tomography images, respectively, together with the emulsion droplet sizes of the three different water repellent agents.

4.2 Water repellent agents

The aforementioned materials are hydrophobised with two commercially available water repellent agents from Wacker: SILRES BS SMK 2101 (water repellent agent A) and SILRES BS SMK 2100 (water repellent agent B). Both of these water repellent agents are water-borne silicon-bearing compounds (i.e. water repellent agent/water emulsions). Water repellent agents A and B are composed of 90%/10% and 50%/50% silanes/siloxanes, respectively [6], and they are both diluted with water to a 90%/10% water/agent emulsion before being applied to the materials. The application of these agents in this concentration has shown to be suitable for the chosen materials and hence sufficiently limit water absorption rates [6,8]. In the prepared water/water repellent agent emulsion, the polymer chains curl up to guarantee the least amount of contact between the polymer chains' hydrophobic tails and water molecules and they form emulsion droplets as shown in Figure 2.6. Since the ability of the agents to enter (and hence hydrophobise) certain pores is governed by these emulsion droplet sizes [30], the hydrodynamic radii of these emulsion droplets of all three water repellent agents are measured using a dynamic light scattering (DLS) setup (LS Spectrometer, LS Instruments) at 20 °C and at a scattering angle of 90°. This hydrodynamic radius represents the amount of physical space the emulsion droplets occupy in the water/agent emulsions. They are shown together with the pore size distributions of sintered glass and ceramic brick in Figure 2.5.

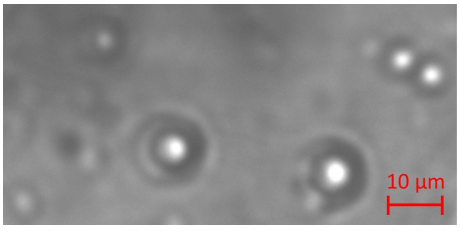
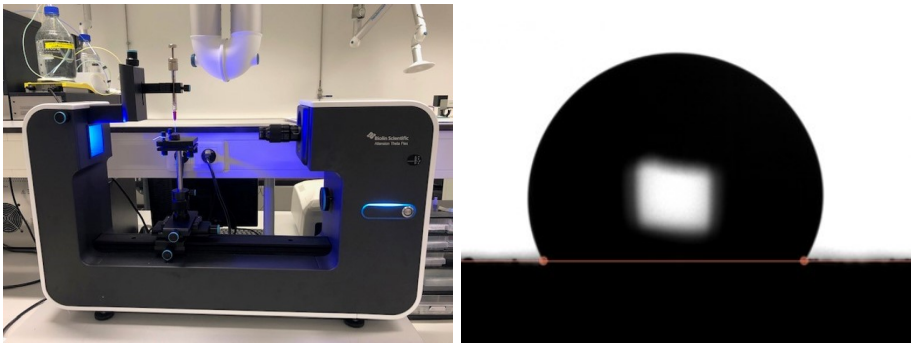


Figure 2.6: A microscopic picture of a water repellent agent in emulsion.

These commercially available water repellent agents are typically applied on building materials like ceramic brick, which have smaller pores than sintered glass as shown in Figure 2.5. Multiple sources state that the size of the emulsion droplets determines which of the building material's pores cannot be entered and hence remain hydrophilic or become blocked or clogged (and inaccessible for moisture) as displayed in Figure 2.1 (b) [6,30]. Using the commercial water repellent agents on these larger pores of sintered glass, however, will probably cause less or no pore blocking. Therefore, a third water repellent agent, composed of emulsion droplets with larger hydrodynamic radii, is created

in cooperation with the Soft Matter, Rheology and Technology (SMaRT) section of the KU Leuven. The recipe of the agent is inspired by [57], but the different products used and the detailed preparation are discussed here.
In a typical preparation of 10 g of the lab-made water repellent agent, 0.45 g of hexadecyltrimethylammonium bromide (CTAB, 99.0%; purchased from Fluka) is dissolved with 2.85 g of Milli-Q water in a 5 mL glass vial. 6.65 g of silane (purchased from TCI Chemicals) is weighed in a 25 mL capped PP plastic cup, followed by 0.05 g of polyethylene glycol stearylamine (POE, n=approximately 15; purchased from TCI Chemicals) and mixed using a dual asymmetric centrifuge mixer (SpeedMixer DAC 150.1 FVZ-K) at 3500 RPM for 5 min. After this initial mixing, the dissolved CTAB aqueous solution and 100 µL of N-octylamine (99.0%; purchased from Merck) are added to the plastic cup. A second round of mixing is done at 3500 rpm for 15 min. Finally, the content in the plastic cup is further dispersed using an ultrasound probe (BRANSON Digital Sonifier model 250) for 15 s at 10% amplitude with cycles of 0.5 seconds on and 9.5 seconds off. The final product is a viscous white cream-like emulsion. This laboratory made water repellent agent is henceforth named water repellent agent LM. It is composed of emulsion droplets with hydrodynamic radii between 0.04 µm and several micrometers, which is larger than the commercial water repellent agents as indicated in Figure 2.5.
To hydrophobise the materials, one cleaned surface of the samples is placed upright in the water/water repellent agent emulsion to allow complete capillary absorption of the product. A surplus of agent is always provided and samples are never too thick (maximum of 3 cm) to make sure that the sample is uniformly hydrophobised. This results in fully hydrophobised samples, without a partially hydrophobised zone like in Figure 2.2. Although this thesis focuses on fully hydrophobised materials, further extension of this work towards partially hydrophobised materials is discussed as an important future research subject in Chapter 7. After the hydrophobisation process, samples are kept in a humid chamber (i.e. 86 % RH) for at least two weeks of curing since previous research has shown that a sufficient curing period is required [43]. Afterwards, the contact angles between deionised water droplets and hydrophobised materials are measured using the contact angle goniometer on a drop volume tensiometer (Attension Theta Flux, Biolin Scientific) shown in Figure 2.7 (a), using the static sessile drop method. A blunt-end stainless steel syringe needle with an internal diameter of 0.25 mm (7018336, Nordson) is used for all measurements. The contact angle is measured on three different samples for every water repellent agent and on each sample four droplets are imaged to account for sample heterogeneity. An example of such a contact angle measurement is shown in Figure 2.7 (b). For water repellents A, B and LM, respectively, this results in contact angles of $117.6° \pm 7.1°$, $109.7° \pm 7.7°$ and $120.3° \pm 3.6°$ for sintered glass and contact angles of $134.6° \pm 8.6°$, $120.4° \pm 10.6°$ and $122.3° \pm 5.7°$ for

ceramic brick.



(a) (b)

Figure 2.7: The contact angle goniometer (a) and an example of a contact angle measurement with the baseline, used for the measurement, indicated (b).

5 Summary

This section provides the reader with an introduction to water repellent agents in order to give a sufficient background for the remainder of this thesis. In the first part of this chapter, the physical principles of the process of hydrophobisation are explained and a concise overview of the vast spectrum of commercially available water repellent agents is given. The differences between water repellent agents based on silicon-bearing compounds, metal-bearing compounds and organic materials are discussed and the most used products (i.e. silicon-bearing compounds) are defined in more detail.
Next, the hygric properties of hydrophobised building materials are discussed. It is shown how the penetration of the water repellent agent into building materials creates a fully hydrophobised zone, with the highest degree of hydrophobicity, and a more extensive partially hydrophobised zone, where the influence of the water repellent agents is less pronounced. In these hydrophobised materials, the hygric properties change due to the modified interaction between pore surfaces and pore moisture. The common experimental techniques for hygric property determination largely fail in characterising these hydrophobised materials. Especially the moisture storage properties and the liquid permeabilities of hydrophobised materials are difficult or even impossible to measure with existing techniques. Literature on the vapour permeabilities, measured with the cup test, show that the hydrophobisation application hardly alters vapour transport and the reported sorption isotherms do show a reduced hygroscopicity.

The reduced interaction between hydrophobised materials and moisture also influences capillary absorption and drying experiments. The capillary absorption experiment is often used to estimate the efficiency of an application since it directly quantifies the primary goal of a hydrophobisation application (i.e. limiting the wind-driven rain absorption). In the existing research, it is mostly highlighted that choosing a suitable water repellent agent for a certain building material is imperative in guaranteeing a sufficient reduction of the capillary absorption coefficient. Other factors, such as the percentage of the active ingredient, the cleaning of the surface prior to hydrophobisation and sufficient curing time can also affect the rate of water absorption in a capillary absorption experiment. While a reduction or elimination of water absorption is the water repellent agent's main goal, it has its disadvantages. In drying experiments, the limited liquid water transport has shown to prevent the fast, first drying stage of occurring, meaning that the overall drying process is significantly delayed even though the material's vapour permeability is hardly affected.
The final part of this chapter introduces the different building materials and water repellent agents around which this thesis is centered. The properties of the Vandersanden Robusta ceramic brick and the ROBU P100 sintered glass filter are given and it is explained that the latter is required in this thesis since its entire pore network can be visualised with (the often applied) X-ray computed tomography. Two commercially available water repellent agents from WACKER, both silicon-bearing compounds with different silanes/siloxanes compositions, are used in this thesis. However, a third laboratory made water repellent agent, composed of larger polymer droplets, also proves necessary. This last agent is created in cooperation with the Soft Matter, Rheology and Technology (SMaRT) section of the KU Leuven.

Chapter 3

Introduction to pore-scale modeling

Pore-scale modeling of fluid transfer in porous media has been around for several decades. One of the first pore-scale models, targeting fluid transfer in rock and soil, was developed by Fatt et al. [58] in 1956, and numerous other models have followed since. In such models, the (inter)action of different liquids and gases is simulated in the material's individual pores, after which this simulated microscopic information can be used to gain understanding of fluid and gas transfer on the macroscopic level. This chapter provides a background on pore-scale modeling, as required to help the reader understand the further use of this modeling approach throughout this dissertation. Since this PhD thesis targets unsaturated moisture flow (i.e. both liquid and vapour flow) in porous materials, this chapter mostly focuses on pore-scale models describing the interaction between gas (i.e. air and water vapour) and liquid (i.e. liquid water), rather than gas-gas or liquid-liquid interactions.
First, Section 1 describes several applications of pore-scale models. It hereby focuses on the research areas which are most in line with the contents of this PhD thesis. Section 2 then handles the different types of pore-scale modeling in literature and substantiates the choice for the quasi-static pore network modeling approach to be used throughout this thesis. Subsequently, Section 3 focuses on the different manners to characterise the pore network of a material. These pore networks are simplified representations of the materials' true pore structures, serving as input to pore network models. Next, Section 4 provides a detailed methodology of the pore network model used in this thesis. And finally, Section 5 repeats the most important conclusions.

Parts of this chapter are derived from paper 3.1 stipulated below.

Paper 3.1: D. Deckers, H. Janssen. Microscopic validation of a pore network model for hygric properties of porous materials. Transp. Porous Media, 151: 119–140, 2024. doi: 10.1007/s11242-023-02035-y

1 Applications of pore-scale modeling

Pore-scale modeling has previously been shown to be a useful and reliable tool to study the behaviour of liquids and gases in the research areas of building physics [23,24,28,29,59], earth sciences [60–62], petroleum engineering [63,64], and many others. This section describes some interesting applications, with focus on the studies required to understand the choices made in this PhD thesis. First, a brief overview is given of research in earth sciences and petroleum engineering, since these research areas provide some overlap with building physics, especially when studying moisture flow in porous rocks. Next, the existing research on pore-scale modeling in building physics is summarised and the biggest obstacle for building materials is further elaborated. Finally, since this PhD is centered around hydrophobised building materials, the last part of this section handles the development of pore-scale models with varying wettabilities. There are countless other applications of pore-scale modeling though, for which the reader is referred to literature.

In the research areas of earth sciences and petroleum engineering, a lot of effort has gone into developing pore-scale models capable of simulating the extraction of oil from reservoirs by waterflooding the reservoir rocks with brine [62,63,65,66]. Bultreys et al. [63] for example imaged the imbibition process of brine displacing decane in water-wet quarry stones and compared these images to the fluid flow simulated with a pore-scale model. Besides these models, which target the modeling of liquid-liquid displacement, other applications describing moisture flow into air-filled materials, like moisture permeability calculations of water in various rocks [67], are also investigated. It should be mentioned that pore-scale modeling has been more extensively studied in these research areas and hence their developed models often serve as inspiration for the models simulating moisture behaviour in building materials. For a more complete summary of the developed pore-scale models in these research areas the reader is referred to the literature (e.g. [68]).

Pore-scale models targeting moisture transfer in porous building materials are often used for the determination of the materials' hygric properties [23,59], such as moisture permeability and moisture retention curves. Alternatively, they can be applied for detailed investigation of important moisture processes, such as the drying of saturated materials [28]. Regardless of their goal, they

are much less present in literature. This is often due to the fact that these building materials comprise a multiscale pore network, with pores spanning from the nanometer to the millimeter range. The issue with these types of multiscale pore networks is twofold. Firstly, common visualisation methods, like X-ray computed tomography imaging or scanning electron microscopy, only allow visualising part of the pore structure due to their spatial resolution limits. This leaves the finest pores difficult, if not impossible, to visualise experimentally [56,59]. Secondly, both experimental and simulational studies on porous materials have shown that small-scale processes (e.g. corner flow) heavily influence fluid flow [23,69,70]. Therefore, pore networks of building materials should be sufficiently detailed to account for these small-scale processes while still being sufficiently large to be representative of the material. Extracting such large, but detailed, multiscale pore networks from building materials is hence not straightforward.

Xu et al. [71,72] and Carmeliet et al. [59] were amongst the first to attempt creating such multiscale pore networks for building materials. Xu et al. [71,72] relies on the superposition of several generated pore networks at different scales to compose their multiscale pore network. Carmeliet et al. [59] on the other hand generate several pore networks with increasing levels of magnification and combine results from simulations on all these pore networks to acquire the material's hygric properties. While pore-scale simulations of the hygric properties in both studies [59,71,72] acquire reasonable agreement with experimentally determined material properties, their generated multiscale networks are based on multiple assumptions like structured network topologies, volumeless pore bodies, ...

Other multiscale pore networks of building materials mostly focus on creating networks of cementitious materials to use in pore-scale models which target these materials' permeabilities [24,73,74]. Here, networks are typically composed separately at different scales (e.g. different networks for the capillary pores and the gel pores), by for example simulating the cement hydration kinetics or the cement particle packing [24,74]. These different networks are then combined to a multiscale pore network by connecting them in a simplified way [24,74]. These studies make equally grave assumptions in order to create the multiscale pore networks of cementitious materials.

To avoid the grave assumptions made in existing studies, Claes and Janssen [75] and Shi et al. [76] are currently developing a stochastic generator which allows creating more detailed multiscale pore networks of building materials based on pore network properties derived from visualisation methods at different scales. The principle behind this stochastic generator is further described in Section 3.4. Even though this summary on multiscale pore networks limits itself to building materials, it should be noted that these types of multiscale networks have also been investigated in other research areas. For more information, the

reader is referred to literature [25,77,78].
When the pore structure of building materials can be characterised, it can be used as input into pore-scale models for hygric property determination. Islahuddin and Janssen [23], for example, developed a pore network model for hygric property determination of hydrophilic materials and validated it macroscopically using experimentally determined hygric properties. It is currently only validated on academic materials, particularly a sintered glass filter, for which the monoscale pore network can be imaged in its totality via X-ray computed tomography. As explained before, extraction of multiscale pore networks of actual building materials is currently ongoing [75,76]. This pore network model of Islahuddin and Janssen [23], explained in detail in Section 4, will be adopted and adapted in this thesis for the hygric property determination of hydrophobised building materials.
Since this thesis is centered around hydrophobised materials, the literature is also reviewed for any pore network models which incorporate varying wettabilities in their pore structure. The impact of wettability on fluid flow has been documented extensively in the research areas of earth sciences and petroleum engineering [79] and several pore-scale models exist which take this mixed wettability into account [66,80,81]. The models in these studies are often based on the same physical principles as the one used in this thesis, which is described in Section 4. However, the alteration of the wettability in the pore structure of building materials by the water repellent agent occurs differently and hence needs further investigating in this thesis. This pore-dependent wettability alteration is investigated in Chapter 5.
In building physics, research towards the pore-scale modeling of moisture flow in hydrophobised materials is very limited [28,29]. Lal et al. [28] developed a pore-scale model for the drying of a hydrophobic macroporous asphalt. They take into account evaporation of water from corner flows by calculating the amount of time required for some elements to empty. Due to these computationally demanding calculations, however, the computational domain (i.e. the simulated pore structure) remains quite small. The pore structure is also significantly simplified to pore bodies positioned on a cubic lattice and hence always connected to 6 neighbouring pore bodies, all with constant triangular cross-sections. The hydrophobised elements are assumed to be empty at the start of the simulation and remain empty throughout. This requires only vapour transport to be modeled in the hydrophobised elements. Namoulniara et al. [29] simulated moisture transport through a hydrophobised concrete sample. Similar to Lal et al. [28], however, hydrophobised pore network elements are simply assumed to be completely filled with the water repellent agent and hence they do not participate in moisture transport. To the author's knowledge, other research on pore-scale modeling of moisture transfer in hydrophobised building materials does not exist in literature.

A successful implementation of both liquid and vapour transport in hydrophobised pore bodies and throats of building materials is still missing from literature. This thesis therefore focuses on the creation of a pore-scale model capable of simulating all moisture processes in both hydrophilic and hydrophobised pore network elements. This pore-scale model will eventually be used to simulate the hygric properties of the hydrophobised materials by applying it to pore networks of both the sintered glass and ceramic brick described in Chapter 2.

2 Different types of pore-scale modeling

In literature, different types of pore-scale modeling exist. All models can typically be subdivided into different categories based on the degree to which they simplify both space and time in their simulations. In this section, the most common approaches in pore-scale modeling are explained and their aforementioned handling of space and time is discussed. Based on this discussion, the final part of this section elaborates on the model used in this thesis for the hygric property determination of building materials.

Starting off with the representation of space in simulations, there mainly are two different approaches: direct pore-scale modeling [82,83] and pore network modeling [23,63,69,70,82]. Direct pore-scale modeling approaches solve the Navier-Stokes equations directly in the complex pore structure of materials [78]. Since the geometry of the pore space can be very complex, these simulations are typically computationally expensive and hence mostly applicable to small volumes. For example, small-scale processes, such as water flow in pore corners, have shown to significantly impact moisture flow through materials. Therefore, the pore structure should be sufficiently detailed to allow modeling the moisture behaviour in these corners. Several types of direct pore-scale modeling, which all aim to solve the Navier-Stokes equations (or simplifications hereof), exist in literature. The most well-known approach in building physics is the lattice-Boltzmann method [84] which solves the discretized Boltzmann equations of fluid particle distributions moving and colliding on a regular lattice [78,85]. For a more detailed explanation of this and other direct simulation methods, the reader is referred to the literature [78,85].

Pore network modeling on the other hand simplifies the pore structure to a stick-and-ball pore network consisting of pore bodies and throats with simplified geometries. It subsequently models the microscopic moisture storage and transport processes in the different pore bodies and throats separately. An optional next step is then to extract information on the macroscopic fluid behaviour from the pore-level simulations on sufficiently large networks, representative of these materials [78]. Depending on the model's level of detail, the geometry of pore network elements can be represented by different shapes, from elements with only circular cross-sections [24] to a mix of elements with

triangular, rectangular and circular cross-sections [23]. An example of such a simplified pore network is given in Figure 3.1 where the spherical pore bodies are connected by cylindrical pore throats. Construction of such a pore network, which is representative of the pore structure, is not straightforward. It often requires some arbitrary decisions [86] to divide the continuous pore space into individual pore bodies and throats and as a result multiple different pore networks can be extracted from the same pore structure [87]. Research has shown that tailoring these pore networks to some measured parameters (e.g. porosity, moisture retention curves) can help in creating a reliable pore network, capable of simulating hard to measure properties, such as moisture permeability curves [88–90].

Both within the direct modeling [91] and pore network approaches [78,85,92], models can be classified as quasi-static or dynamic, depending on their approach towards the time scale of the simulations. The main difference between the two is that dynamic models take into account the time-dependency of moisture storage and transport, while quasi-static models do not. For example, in quasi-static pore network models, elements can become capillary filled when their threshold capillary pressure is reached. When this happens, the elements are assumed to be filled immediately. In dynamic pore network models, however, water is allowed to enter a certain element when its threshold capillary pressure is reached and the simulated rate of water displacement determines how fast the filling occurs. This, for example, allows simulating dynamic effects which have shown to notably influence the hygric properties in a previous experimental study by Janssen et al. [93]. On the other hand, the inclusion of dynamic moisture storage and transport processes naturally comes at the expense of a higher model complexity and longer computational time. Since this PhD focuses on the modeling of (static) hygric properties of building materials, without the inclusion of dynamic effects, quasi-static modeling is the preferred (and least computationally demanding) modeling option. Future research towards dynamic modeling with the aim of investigating dynamic moisture storage and transport processes in building materials, however, is also ongoing in the research section.

The computational demand and complexity of the simulations using a pore network model are significantly lower than for direct pore-scale modeling due to the simplifications inherent to pore network modeling [82]. These simplifications evidently result in a less detailed representation of the pore space, which might impact the simulated moisture behaviour in the elements. However, previous validations of pore network modeling of quasi-static [23] and dynamic [63] moisture transfer in porous media establish that the simplifications do not necessarily impact the reliability of the intended outcomes if the pore networks are carefull extracted. This pore network approach is moreover a necessity in relation to unsaturated hygric properties of building materials, given the complex nature of the pore spaces of these materials. Building materials often comprise

pores with sizes covering multiple orders of magnitudes, from the nanometer to the millimeter range [75], which are all relevant for moisture storage and transport [94]. The correct consideration of large pores necessitates a sufficiently large volume to maintain representativeness, while the correct consideration of fine pores requires a sufficient resolution to maintain the level of detail. Applying direct pore-scale modeling on the complex pore structures of building materials would thus require an excessive computing capacity (concerning both memory and processing). This leaves the simplified - but often still sufficiently accurate - pore network modeling as the only viable option at the moment.
In this PhD, an existing pore network model, previously macroscopically validated for hygric property determination of hydrophilic materials [23], will be rendered capable of doing the same for hydrophobised materials. This pore network model, which is based on the quasi-static modeling approach, is explained in detail in Section 4. The rest of this chapter and the thesis therefore focuses on quasi-static pore network modeling in porous materials. Further research on the dynamic pore network modeling approach for building materials is currently ongoing within the framework of a different PhD project.

3 Pore network characterisation

A preparatory step for any pore network model is the extraction of a material's pore network. This network should accurately represent both topological (e.g. coordinates and connections of pore network elements) and geometrical (e.g. radii, volumes and shapes of different elements) information of the material's pore structure. To do so, there are four common approaches in literature [95]. Firstly, the direct imaging approach acquires 3D images of the material via imaging techniques, like X-ray computed tomography, and extracts the pore network from these images using pore network extraction programs [96,97], which are further described in Section 3.1. This approach is only applicable if the spatial resolution and field of view limits of the visualisation methods allow capturing the material's entire pore network in a representative manner. Secondly, the statistical reconstruction approach uses statistical information, gathered from a detailed 2D slice of a material, to generate a stack of 2D slices representative of the material's 3D image. Subsequently, the pore network is extracted from the generated 3D image of the pore structure [98–102]. Thirdly, the process-based approach simulates the formation of the material in order to acquire images of the pore structure. This is done by recreating the packing of grains and other geological processes such as sedimentation or diagenesis [103,104]. Subsequently, the pore network is extracted from the resulting 3D image. Finally, the stochastic generation approach uses predetermined frequency distributions of - and correlations between - pore network parameters, to stochastically recreate the material's pore network. In this approach hence,

the pore network is generated directly, and no actual extraction from images of the pore structure is required. An overview of existing research handling these four approaches is given in the following sections.

3.1 Direct imaging

In direct imaging, the pore network is extracted from segmented 3D images of the material's pore structure. These images are acquired from a visualisation technique, such as X-ray computed tomography, after which they are segmented into pore and solid voxels. An example of this extraction procedure is shown in Figure 3.1. The pore bodies and throats in this figure are simplified to spheres and cylinders for illustration purposes, however, in reality they are represented by more complex shapes (e.g. triangular or rectangular). Of course, this technique is limited by the image's spatial resolution and field of view, but with the development of new techniques, these limits are being stretched continuously. The pore network from these images is typically extracted using any of three main techniques: the maximal ball algorithm [67,96,97,105–107], the medial axis algorithm [97,108–111] and the watershed algorithm [97,112].

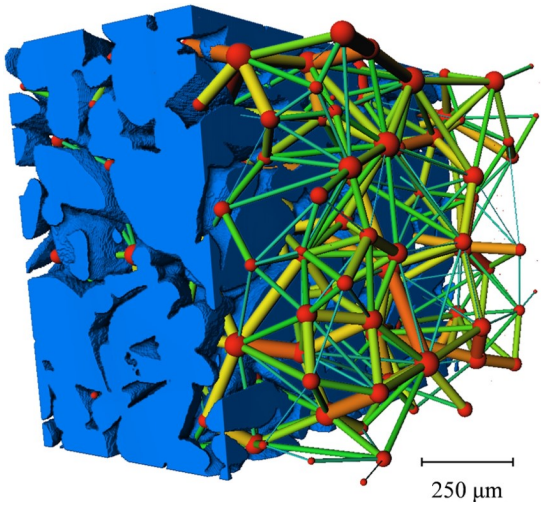


Figure 3.1: Illustration of the extraction of a pore network from a material's 3D image [76].

In the maximal ball algorithm, for each pore voxel, the maximal sphere centered in that voxel, not containing any solid voxels, is determined. All spheres are then ordered according to a certain hierarchy where the biggest spheres generally have the highest priority. Using this hierarchic structure, pore bodies and throats are classified and all voxels are assigned to a single pore network element. From that assignment, the network properties, like pore location, volume, shape, ..., are calculated. The first versions of this algorithm performed adequately, but required a lot of computer memory. This only allowed its use for small computational volumes [67,105,106]. Subsequent studies have therefore focused on making the algorithm more efficient as well as less error-prone [96,97,107].
The medial axis algorithm first extracts the skeleton of the pore network using thinning or pore space burning algorithms, and then identifies the pore bodies (i.e. nodes of the skeleton) and throats (i.e. connectors of the nodes of the skeleton). Next, maximum inscribed spheres are used to retrieve information about the geometry of the individual pore network elements. The main downside to this algorithm is the computed skeleton's susceptibility to noise which distorts the air/pore interface after image segmentation [78,109–111].
The watershed algorithm calculates the solid surface distance map, describing the distance of every voxel to the nearest solid surface. Next it finds the ridge lines (i.e. the local minima in this distance map) which divide the pore space in several different pore bodies with connecting pore throats in between. Using this distance map, all geometrical information of the elements can be calculated. Just like the medial axis algorithm it is sensitive to image noise which distorts the air/pore interface after image segmentation [112].
The pore network extraction code used in this PhD thesis is the program PNextract developed by Raeini et al. [97], which is an enhanced version of the well-known algorithm of Dong and Blunt [96]. This PNextract algorithm uses a combination of a thinning algorithm, to compute the skeleton of the network, as well as a maximal ball algorithm to calculate the size of the elements. For more information, the reader is referred to [97]. As mentioned before, the characterisation of pore networks using such extraction algorithms is non-unique and the resulting network is influenced by any assumptions made in the algorithm itself [86,87].

3.2 Statistical reconstruction

Building materials often comprise pores with sizes covering multiple orders of magnitudes, from the nanometer to the millimeter range [75], which all contribute significantly to moisture storage and transport processes [94]. Acquiring 3D images of the pore network of these materials is therefore sometimes impossible, or at least very time-consuming. A single, sufficiently accurate 2D slice is, on the other hand, easier to obtain and takes less time. Using statistical information acquired from this single 2D slice, a stack of 2D slices, comprising a

3D image, can be created [101,102]. To do so, different types of statistics, such as one-point, two-point [98–100] or multiple-point statistics [101,102], are used. For example, the two-point probability statistic is a function which describes the possibility that two pixels, located at a distance r from each other, belong to the same phase (i.e. pore or solid phase). This statistic can be calculated from the available 2D slice and subsequently used to compose related 2D images. For more information about the workflow and details of the statistical reconstruction of pore structures, the reader is referred to the literature [98–102]. After this statistical reconstruction, a 3D image is available from which the pore network needs to be extracted using any of the pore network extraction techniques explained in section 3.1.

3.3 Process-based approach

In the process-based approach, the sedimentation, compaction and diagenesis processes, which create certain (soil- and rock-like) materials, are simulated in a simplified manner to recreate the material's pore structure [103,104]. A simple example of such a modeled process is compaction of spherical grains. The grain coordinates are simply moved closer together along one (compaction) axis without changing their shape. As a result, some of the spherical grains overlap. In [103], it is simply assumed that the material in these overlapping spheres has dissolved under pressure and is removed from the material. The first implementations of this process-based approach only simulated processes starting from identical spherical grains [103], however, this was later adapted to account for different-sized spherical grains measured during a particle size analysis [104]. This technique is predominantly used in geology where the processes which form materials are well-studied. After the recreation of the pore structure, a pore network can be extracted using any of the techniques described in Section 3.1.

3.4 Stochastic pore network generation

The previous three techniques focused on obtaining a representative 3D image of a material's pore structure and subsequently extracting a pore network from it using a pore network extraction program. Geometric and topological properties are therefore established by these images. Often, building materials exist of pore network elements with sizes ranging over different orders of magnitude (i.e. nano-, micro- and even millimeter scale) and information must typically be gathered via different imaging methods, each targeting a specific spatial scale. A different way to approach the pore network extraction of such complex materials is to stochastically generate the pore network, rather than extracting it from pore structure images, based on statistical information gathered at these different scales. This entails extracting frequency distributions of several pore

network properties, like pore body and throat radii, pore body coordination numbers (i.e. the amount of connections to other pore bodies), ..., from images made at different spatial scales, and combining them to stochastically generate a pore network representative of the material's entire pore structure.
The early versions of such networks were rather simple, with pore bodies placed on cubic lattices, connected to a maximum of 6 neighbouring elements via pore throats, all confined to regular shapes (e.g. rectangular or circular cross-sections) [60,61]. Research has shown, however, that the accuracy of pore network simulations depends heavily on the degree to which the pore networks are representative of the true pore structure [61,96,110,113,114] in terms of pore body coordinates, element radii, shapes and volumes, and many more. Further improvements on these pore networks are therefore provided by Claes and Janssen [75] and Shi et al. [76,115] who developed a stochastic generator capable of creating pore networks which match a predefined set of pore network properties. This stochastic generator requires frequency distributions of different pore network properties and information about the correlations between these different properties as input. Next, a number of pore bodies is generated at locations determined via Sobol sequences, with properties sampled from the frequency distributions. Finally, the pore network is iteratively adapted until the pore network properties match the predefined frequency distributions. This process can result in various generated pore networks with the same statistical properties. Existing stochastic generators have shown promising results on monoscale pore networks [76,116], and therefore further research into multiscale pore networks is ongoing [25,75,77].
Studies have found reasonable agreement between pore networks extracted from images and these stochastically generated networks when sufficient geometrical and topological information is gathered [61,75,117]. The stochastic generator, developed by Claes and Janssen [75] and Shi et al. [76,115] currently does require some trial and error in order to obtain pore networks that simulate the material's hygric properties satisfactorily. When direct imaging of the material's complete pore network is not possible due to spatial constraints, however, this stochastic generation can be a worthwhile alternative.

4 Pore network model used in this thesis

The quasi-static pore network model (PNM) for hygric property simulation, used in this thesis, is developed by Islahuddin and Janssen [23], and has previously been macroscopically validated using measured hygric properties of (monoscale) porous materials. This model simulates the moisture storage and transport processes on a pore level in a sufficiently large pore network with the aim of eventually obtaining the material's macroscopic hygric properties (i.e. the moisture retention and permeability curves). A detailed explanation

and illustration of this PNM as well as its macroscopic validation can be found in Islahuddin and Janssen [23], however, the most important elements are explained in this section.
Before the PNM can be used, the pore networks of the materials, used in this thesis, need to be extracted or generated as explained in Section 4.1. With these pore networks as input, the PNM can simulate moisture behaviour in two steps. In step one, the storage of moisture in the individual pore bodies and throats is simulated for a range of boundary conditions (i.e. different capillary pressures). Using this information, the moisture retention curve can be composed. In step two, the transport of moisture through these individual pore bodies and throats is simulated with the aim of composing the moisture permeability curve. This step requires knowledge about the distribution of moisture throughout the individual elements of the pore network, which is acquired in the first step. Sections 4.2 and 4.3 describe these two steps, respectively.

4.1 Pore network characterisation

Prior to the use of the PNM, the networks of the two materials around which this PhD is centered (ROBU sintered glass filter and Vandersanden ceramic brick) need to be characterised since these networks serve as input parameters to the PNM. Depending on the material, a different pore network characterisation approach is used. Since the pore network of the sintered glass filter can be imaged in its totality with X-ray computed tomography, it can be extracted via the direct imaging approach. This means that the images are segmented into pore and solid phases, after which the PNextract program from Raeini et al. [97] extracts the pore network. More information about the segmentation of images and the pore network extraction using PNextract is provided in subsequent chapters.
Since the ceramic brick comprises a multiscale pore network with pore body and throat dimensions spanning several orders of magnitude [75], extraction of the entire pore network via X-ray computed tomography imaging is not feasible. Stochastically generating a pore network based on statistical information is thus chosen to recreate its pore network. This stochastic generation is explained in the relevant chapters since it depends on information gathered from executed experiments.
The pore networks of sintered glass and ceramic brick contain lists of the individual pore bodies and throats with their geometrical and topological information. The geometrical information consists of radii, volumes, shape factors and lengths of both pore bodies and throats. The topological information contains coordinates, lists containing all inlet and outlet pore bodies and throats and all information regarding connections between different elements (which pore bodies are connected to each other and the specific throats which connect them). These lists of individual elements serve as input to the PNM. Other

input parameters, which are required for the PNM, are a single contact angle (see Chapter 6) and the temperature (293.15 K).

4.2 Moisture storage in pore network elements

This first step of the PNM simulates the amount of moisture (i.e. both liquid water and vapour) present in all pore network elements at different capillary pressures. In hydrophilic elements, moisture can be stored in such elements in three ways: in capillarily filled elements if above the element's threshold capillary pressure, or alternatively, once below that pressure, adhered as water islands in pore corners or as water films on pore surfaces, as illustrated in Figure 3.2. The PNM first establishes whether elements are filled or empty at a certain capillary pressure using an invasion percolation algorithm. The amount of moisture stored in the corners and on the pore surface of the empty elements is subsequently calculated using semi-empirical expressions. By summing up the simulated amount of moisture in all individual elements, the moisture content in the material at a certain capillary pressure is calculated. This calculation is repeated for a range of capillary pressures to allow composing the moisture retention curve. The following explains this first step in more detail.

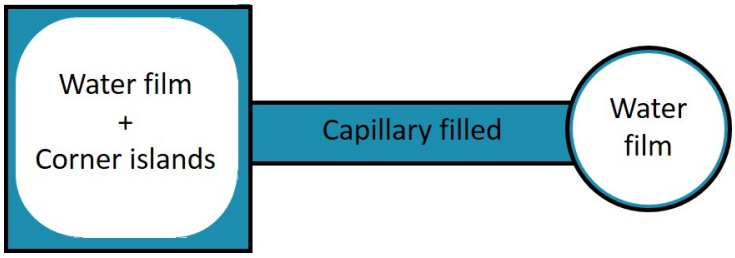


Figure 3.2: The three possible storage mechanisms in hydrophilic pore bodies and throats.

When the pore networks are acquired via the PNextract program of Raeini et al. [97] or via stochastic generation, a list of pore bodies and throats with their topological (e.g. positions and connections) and geometrical (e.g. radii, volumes, shape factors) information serves as input for the PNM. An important geometric variable is the element's shape factor G [-] defined as the cross-sectional area A [m^2] of the element divided by its perimeter squared p^2 [m^2]. This shape factor classifies elements as having round, square or triangular cross-sections over their entire length. Note that this simplified representation of the pores' cross-section causes the pore network to be less representative of the true pore structure of a material, however, as explained before, these simplifications are necessary to limit the computing expense in the large pore networks of building

materials. Using the element's inscribed radius and shape factor, its threshold capillary pressure $p_{c,thres}$ [Pa] at which it drains during the drying process is calculated with [104]

$$p_{c,thres} = \frac{-(1 + 2\sqrt{\pi G})\, \sigma\, cos(\theta)}{r} \tag{3.1}$$

where σ [N/m] is the surface tension of water ($= 72.5 * 10^{-3}$ N/m at 20°C), θ [°] is the solid/water contact angle and r [m] is the radius of the pore network element. Here we assume the simplified case of perfect wetting and hence the contact angle equals 0°. Chapter 6 elaborates further on this assumption of perfect wetting. For simplicity, the following explanation focuses on a drying sequence where the air and vapour phase displaces the liquid phase, but the same workflow is followed in a wetting sequence.

After acquiring the pore network and calculating the threshold capillary pressures of each element, the second step of the PNM is to determine which pore network elements are empty/filled at different capillary pressures. Rather than using direct simulations to follow the drying front, the drying sequence is represented by an invasion percolation algorithm which mimics the drying process. In Islahuddin and Janssen [23], four different percolation algorithms are defined which all describe a different method of moisture invasion or withdrawal: adsorption, desorption, imbibition and drainage. These four algorithms are described in Appendix 3.A. The drainage (or drying) algorithm, used in this thesis, is also explained here in more detail and the necessary changes, applied to this algorithm, are highlighted.

The invasion percolation algorithm attempts to replicate the drainage process by stepwise emptying the different elements in the pore network. In every step, only the elements connected via a continuous airway to the air boundary (dotted line in Figure 3.3) are candidates to be emptied next. In other words, pores 1 and 2 in Figure 3.3 are candidates to be emptied first. Whenever there are multiple candidates, the element with the largest threshold capillary pressure, as calculated by Equation 3.1 (i.e. often the largest element), empties. This results in pore 1 in Figure 3.3 emptying in the first step of the algorithm. This first step is subsequently characterised by pore 1's threshold capillary pressure ($p_{1,thres}$). In other words, the algorithm remembers which pores are filled at this capillary pressure for further calculations. Since element 1 empties, element 5 becomes viable to be emptied next. If its threshold capillary pressure is even larger than $p_{1,thres}$, it is also emptied in step 1 and element 11 becomes viable to be emptied next. If the threshold capillary pressure of element 5 is smaller than $p_{1,thres}$, it is not emptied in step 1, but simply added to the list of candidates to be emptied in step 2. This drainage algorithm continues until full desaturation. This is a simplified representation of the true drainage process, however, since its accurate simulation is not an option, this simplification is unavoidable.

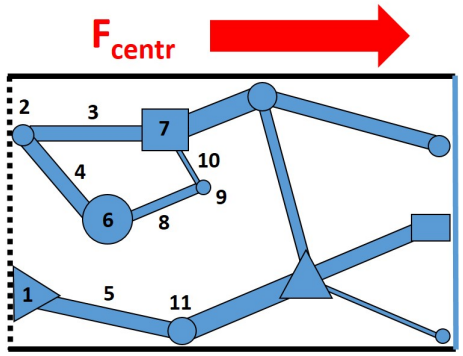


Figure 3.3: Illustration of the percolation algorithm in which the air boundary is represented by the dotted line and the blue line represents the outflow surface.

This discussion describes the drainage algorithm as developed in Islahuddin and Janssen [23]. In this thesis, however, samples are often desaturated in a centrifuge test setup. From the study regarding this centrifuge setup [118], it is known that moisture is forced outward in the direction of the centrifugal force (F_{centr}) and that it expels from the sample at the right surface, indicated by the blue line. The other surfaces are covered with vapour tight tape to eliminate moisture evaporation. Due to imperfect contact between the tape and the sample, some air can still penetrate the left surface, indicated by the dotted line. In case drainage is governed by the centrifugal force, the algorithm is slightly changed to only allow elements to desaturate in the direction of the centrifugal force. This prohibits water movement against the direction of the driving force. Element 9, which has no connecting throats in the direction of this centrifugal force therefore does not empty.
After the percolation algorithm, the emptying sequence of elements is known. In other words the model knows which elements are capillary filled at different values of the capillary pressure. The empty elements can still store moisture, as water films on pore surfaces and as water islands in pore corners. The latter is only possible when their cross-section is classified as triangular or rectangular. The thickness of the adsorbed water film (t_f [m]), which depends on the reigning capillary pressure, is calculated according to Bradley's statistical thickness [119]

$$t_f(p_c) = K_1 + K_2 * ln(-\frac{p_c}{\rho_l R_v T}) \tag{3.2}$$

in which K_1 [-] and K_2 [-] are experimentally determined parameters, which equal $0.385*10^{-9}$ and $-0.189*10^{-9}$ respectively for silicate materials, ρ_l [kg/m^3] is the density of liquid water (= 1000 kg/m^3), R_v [J/kgK] is the gas constant (= 462 J/kgK) and T [K] is the temperature (= 293.15 K). This equation is derived

from adsorption experiments on several silicate materials (i.e. several Portland cements), but for more information the reader is referred to [119]. Although the measurements are performed on such silicate materials, these experimentally determined parameters are still used to model the surface adsorption in the materials used in this thesis, under the assumption that the thickness of such surface films in building materials does not vary much.
The volume of water present in a pore corner is represented as a volume fraction (S_c [-]), which represents the fraction of the element's total volume occupied by water in its corners and is hence limited to 1. It is calculated from the imposed capillary pressure as well as the elements' geometrical properties

$$S_c = \begin{cases} \frac{(4-\pi)\, r_c(p_c)^2}{A} & \text{square} \\ (1 - 4\pi G)(\frac{r_c(p_c)}{2Gp})^2 & \text{triangular} \end{cases} \tag{3.3}$$

with $r_c(p_c)$ [m] the water/air interface curvature as calculated from equation 3.1 for the imposed capillary pressure. The expressions in both Equations 3.1 and 3.3 are an extension of the well-known Mayer-Stowe-Princen method [120–122]. After these steps, the model knows where moisture is stored at different values of the capillary pressure, both in filled elements, corner islands and water films. The total amount of moisture is then easily calculated at these different capillary pressures and the moisture retention curve can be composed.

4.3 Moisture transport in pore network elements

The second step of the PNM entails the calculation of the material's permeability at different capillary pressures to compose the moisture permeability curve. To this aim, a 1 Pa pressure difference is imposed over the network, and the resulting moisture flow is calculated. This flow is then translated to the moisture permeability K [kg/msPa] via Darcy's law

$$Q = K \Delta p_c \frac{A_n}{L_n} \tag{3.4}$$

in which Q [kg/s] is the total moisture flow rate into or out of the pore network, Δp_c [Pa] is the imposed capillary pressure difference over the network and A_n [m^2] and L_n [m] are the cross-section and length of the pore network. The two last variables are predefined by the pore network's dimensions and the capillary pressure difference over the network is taken equal to 1 Pa. This calculation is performed at the same capillary pressures as in step 1. At each of these capillary pressures, the distribution of moisture throughout all individual elements is known. This means that for each calculation at a different capillary pressure, the distribution of moisture in the elements and the resulting element conductances change, as explained below, while the rest of the calculation remains identical. The only unknown in the Darcy equation is the moisture flow Q into or out

of the pore network. The flow from one pore body to another is determined by the conductance (g_{ij}) between these two pore bodies and their capillary pressure difference. Calculating the capillary pressures in the individual pore bodies of the pore network relies on composing and solving a set of mass balance equations in every pore body i, connected to pore bodies j, by assuming mass conservation

$$\sum_i g_{ij}(p_{c,j} - p_{c,i}) = 0 \tag{3.5}$$

in which g_{ij} [kg/sPa] is the conductance between pore bodies i and j and $p_{c,i}$ [Pa] and $p_{c,j}$ [Pa] are the capillary pressures in the pore bodies i and j, respectively. After solving this set of equations, the capillary pressure in each element is known. The moisture flow Q into or out of the network, required to solve the Darcy equation, is then easily obtained by summing all moisture flows in the pore throats connecting all boundary pore bodies (k), positioned at the outlet of the pore network, with the outlet (o) itself

$$Q = \sum_k g_{ko}(p_{c,o} - p_{c,k}) \tag{3.6}$$

The previous equations still require a quantification of the conductances between the pore bodies. To do so, first, the individual conductances of each element (i.e. both pore bodies and throats) have to be calculated. After the percolation algorithm, the distribution of moisture throughout the pore network is known at the different capillary pressures considered. The algorithm therefore knows which elements are filled (and hence only transport moisture through liquid flow) and which elements are empty with liquid corner islands and surface films (and hence transport moisture both in vapour and liquid form). The next step is to calculate the moisture conductance of each element, for which liquid and vapour flow are assumed to be two parallel processes. This means that, in empty elements with liquid flow in corner islands and surface films, the vapour g_v [kg/sPa] and liquid g_l [kg/sPa] conductances are calculated separately and summed up to form the total element conductance g_{tot} [kg/sPa]. In reality, these transport processes will interact [70], however, simulations with much higher complexity and increased computation time are required to take this into account. The vapour g_v [kg/sPa] and liquid g_l [kg/sPa] conductances are calculated based on Fickian diffusion processes and Hagen-Poiseuille flow, respectively

$$g_l = \frac{c_G \rho_l G A^2}{\mu L} \tag{3.7}$$

$$g_v = \frac{1}{1 + K_N} \frac{\delta_a p_v}{\rho_l R_v T} \frac{A^*}{L} \tag{3.8}$$

$$K_N = \frac{\lambda}{2r} \quad \text{with} \quad \lambda = \frac{RT}{\sqrt{1 + (M_v/M_a)\,\pi N_a((d_v + d_a)/2)^2 P}} \tag{3.9}$$

with c_G [m^2] a constant dependent on the shape factor [123], ρ_l [kg/m^3] the density of water, μ [Pa s] the dynamic water viscosity, L [m] the length of the element, δ_a [kg/msPa] the air vapour permeability, p_v [Pa] the vapour pressure calculated using Kelvin's law, A* the element's cross-section which is reduced to account for the adhered water films and possible corner islands, R_v [J/kgK] the vapour constant, T [K] the temperature, λ[m] the mean-free-path length, M_v (18 g/mol) and M_a (29 g/mol) [g/mol] the molar masses of water vapour and air, N_a [1/mol] the Avogadro constant and d_v (0.27 nm) [m] and d_a (0.37 nm) [m] the collision diameters of vapour and air.
Once the conductances of all elements (both pore bodies and throats) are known, the pore body (i) to pore body (j) conductances g_{ij} are calculated by assuming that the conductances of half of pore body i, the entire pore throat between i and j and half of pore body j are placed in series. The total pore body to pore body conductance is then calculated by reciprocal addition of these three conductances

$$g_{ij} = \left(\frac{1}{g_{p,i}} + \frac{1}{g_{t,ij}} + \frac{1}{g_{p,j}} \right)^{-1} \tag{3.10}$$

in which $g_{p,i}$ and $g_{p,j}$ are half of the pore conductances of pores i and j, respectively, and $g_{t,ij}$ is the throat conductance. Assume pore i is empty and pore j and throat ij are filled with water, then $g_{p,j}$ and $g_{t,ij}$ are the liquid conductances of these last two elements, calculated as Hagen-Poiseuille flows using Equation 3.7. $g_{p,i}$ then equals the sum of the vapour conductance in the bulk of the element (calculated as a Fickian diffusion process using Equation 3.8) and the liquid conductance in the corner and surface flows (calculated as Hagen-Poiseuille flow using Equation 3.7).

5 Summary

This chapter provides the reader with information regarding pore-scale modeling, which is required to understand the use of this modeling approach in this PhD thesis. First, several applications of pore-scale modeling in relevant research areas are discussed to illustrate the possibilities and limitations of these types of models. Here it is shown that there are no models describing all moisture processes in hydrophobised pore bodies and throats without making grave assumptions. This furthermore highlights the need for this PhD thesis. Next, a discussion of the different types of pore-scale modeling is provided. In this part, it becomes clear that quasi-static pore network modeling is currently

the only viable option for simulations of moisture processes in the extensive multiscale pore networks of building materials. To use such pore network modeling approaches, the pore network, which is a simplified representation of a material's pore structure, first needs to be obtained. The four most common approaches for pore network characterisation are therefore described. Finally, the quasi-static pore network model for hygric property simulation, on which this thesis is based, is described in detail in the last section of this chapter.

Appendix 3.A: Invasion percolation algorithms

The original model by Islahuddin and Janssen [23] contains four different algorithms (adsorption, desorption, imbibition and drainage), which all describe a different fluid flow process. The basic principles of these percolation algorithms remain the same, while the boundary conditions vary. In such invasion percolation algorithms, the wetting or drying sequence of the pore bodies and throats is determined in a stepwise manner and the capillary pressures at which these elements become empty or filled are saved for further calculations. The four algorithms are illustrated in Figure 3.4 using a simple 2D network, where the drying or wetting order of the first ten elements is indicated with the numbers 1 to 10. It should be mentioned that in reality, 3D networks are studied and hence there are two more boundaries which cannot be shown in Figure 3.4.

In the adsorption algorithm, all pores, positioned on any of the four boundaries, are classified as boundary pores. Any of the elements, connected via a continuous air path to the boundaries is viable to be filled in the following step. This means that all pores in the pore network can be filled in the first step, where the entire network is empty. At that point, the element with the smallest threshold capillary pressure (i.e. often the smallest element) is filled first. This filling occurs at the pore's threshold capillary pressure ($p_{c,thres,1}$), which is remembered for future calculations with the PNM. Next, pore 2 has the smallest capillary pressure and it is hence filled at its threshold capillary pressure ($p_{c,thres,2}$). This continues until the pore network is fully saturated. It is important to mention that this algorithm can be used with or without air entrapment. If air entrapment is simulated, pores, which are no longer connected to boundary pores via a continuous air path, will not become filled and hence remain empty at the end of the simulation. If air entrapment is not taken into account, all empty pores in the network are viable to become filled in the next step and hence the filling sequence simply arranges the pores according to an increasing threshold capillary pressure.

The desorption algorithm is the reverse of the adsorption algorithm. All pores are filled at the beginning of the simulation and all pores, positioned on the four boundaries of the network, are classified as boundary pores. All the elements, which are connected via an air path to these boundary pores, are viable to be emptied in the next step. This means that only the boundary pores can empty in step 1 at which point the element with the largest threshold capillary pressure (i.e. often the largest element) is emptied. When pore 1 empties, its connecting throat (throat 7) is now connected to the boundary via an air path and it becomes a candidate to be emptied next. This continues until the network is completely desaturated.

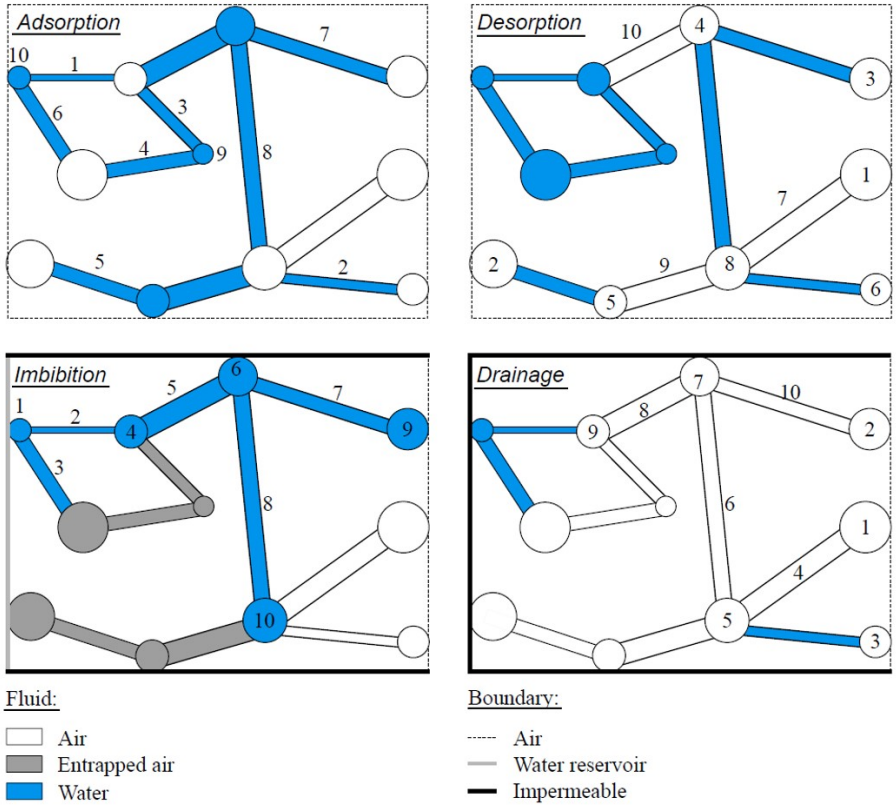


Figure 3.4: Illustration of the four different invasion percolation algorithms implemented in the model of Islahuddin and Janssen, with the numbers showing the first ten invasion orders [23].

In the imbibition algorithm, the upper and lower (black) boundaries become impermeable, the left (grey) boundary is exposed to a free water surface and the right (dotted) boundary is exposed to air. Elements are now viable to be filled when they are connected to the water boundary via a continuous water path and if air can escape via a continuous air path to the air surface. Hence, in step 1, only the pores on the left boundary can be filled and the element with the smallest threshold capillary pressure (i.e. often the smallest element) is chosen. This filling occurs at the threshold capillary pressure of pore 1 ($p_{c,thres,1}$). If the connecting elements' threshold capillary pressures are smaller than $p_{c,thres,1}$, they also become filled in the same step. Assuming that $p_{c,thres,2}$ and $p_{c,thres,3}$ are smaller than $p_{c,thres,1}$, all three of these elements (pores 1,2,3) are filled

at the same step. The algorithm then remembers that these three elements became filled at $p_{c,thres,1}$. In the next step, pore 4 can be filled since it is now connected to the free water surface. After filling pore 4, there is a grey cluster of elements in Figure 3.4 which is no longer connected to the air boundary via a continuous air path. Since air can no longer escape these pores and be replaced by water, these element remain empty. This process continues until the pore network is completely saturated, apart from the elements filled with entrapped air.

In the drainage algorithm, all boundaries are assumed impermeable apart from the right (dotted) air boundary. The network starts fully saturated after which all elements, connected to this air boundary via a continuous air path, are viable to be emptied. If there are multiple candidates, the pore with the largest threshold capillary pressure (i.e. often the largest pore) is emptied. As can be seen in Figure 3.4, the first three elements which can be emptied are the three boundary pores. When such an element empties, the connecting elements (e.g. throat 4 when pore 1 empties) become viable to be emptied next. If this element has a larger threshold capillary pressure, it is emptied immediately. For example, when throat 4 empties at $p_{c,thres,4}$, the larger pore 5 (with larger $p_{c,thres,5}$) also empties immediately. The algorithm then remembers that both throat 4 and pore 5 empty at $p_{c,thres,4}$. This process continues until full desaturation.

Chapter 4

Experimental determination of the macroscopic hygric properties

This chapter focuses on the experimental determination of hygric properties of building materials. These hygric properties can be divided into moisture storage properties (i.e. the moisture retention curve) and moisture transport properties (i.e. liquid and vapour permeability). The main goal is to characterise the moisture storage and transport properties of hydrophobised materials, so that these measured properties can be used to validate the adapted pore network model in Chapter 6. The literature review in Chapter 2 has made clear that the commonly known cup tests can still be used for the vapour permeability measurement of such hydrophobised materials, while measurement of the moisture storage properties and liquid permeability is more difficult (if not impossible) with existing experimental methods. For the measurement of the moisture storage properties of hydrophobised building materials, the steady state centrifuge technique is developed. Before applying this technique to hydrophobised materials, however, it requires validation. Therefore, Subchapter A first describes the design and validation of this steady state centrifuge technique using hydrophilic materials, after which Subchapter B applies this technique to hydrophobised materials. Furthermore, Subchapter B also measures the vapour permeability of the hydrophobised materials using the commonly known cup tests and slightly adapts these cup tests to assess the contribution of the liquid permeability to the overall moisture permeability.

Subchapter A is largely based on paper 4.1 displayed below.

Paper 4.1: D. Deckers, H. Janssen. Development and validation of the steady state centrifuge experiment for the moisture retention curve of porous building materials. J. Build. Physics, 47(1): 36-61, 2023. doi: 10.1177/17442591231178778

A Hygric property determination of hydrophilic porous materials

A.1 Introduction

The accurate determination of hygrothermal material properties has become increasingly important over the last few years, due to the development of more powerful Heat, Air and Moisture transfer models. These models allow simulating the hygrothermal behaviour in building components, hereby facilitating the analysis and design of hygrothermal performances of building components. As stated in Chapter 1, when discussing the possible application of a water repellent agent, these types of hygrothermal simulations are crucial to not only justify such an application, but also decide which commercially available water repellent agent is most suitable for that building component. These simulations do require accurate hygric properties of the hydrophobised building components as input, since they can heavily influence the simulation results [124–128]. Chapter 2 has shown, however, that existing experimental techniques are not capable of reliably measuring these hygric properties of hydrophobised materials and hence new methods need to be developed. This subchapter therefore focuses on the development of the steady state centrifuge experiment, well-established in soil physics [129–132], for measurement of the moisture storage properties of porous building materials. This technique is first validated in this subchapter with the help of three well-characterised hydrophilic materials after which Subchapter B applies it to hydrophobised materials. The moisture transport properties of these hydrophobised materials are also discussed in subchapter B.

Although the main motivation for this technique's development is its use on hydrophobised building materials, research on new experimental techniques for the measurement of the moisture storage properties of hydrophilic building materials also remains of major importance (e.g. [133]). Especially since existing experimental methods for these moisture storage properties can be time-consuming, inaccurate and often only applicable to part of the desired measuring range [134]. The pressure plate test, for example, mainly focuses on the capillary region and requires about 2 months [8] of testing. While mercury intrusion porosimetry (MIP) provides the full-range moisture retention

curve in a matter of days, the use of environmentally damaging mercury as well as its inability to start from the (more realistic) capillary water content, constitute its challenges. The steady state centrifuge experiment, developed in this section, therefore also aims to improve on the shortcomings of hygric property measurement of hydrophilic materials.

In the centrifuge experiment, the moisture in a saturated sample is expelled during centrifugation at its outermost boundary under influence of the centrifugal force. This centrifugation produces a capillary pressure in a sample which, combined with the measured moisture content of the sample, can be used to compose the material's moisture retention curve. Two different centrifuge experiments are commonly used for moisture storage characterisation; steady state [130,131,135–137] and transient centrifugation [129,138–141]. In steady state centrifugation, saturated samples are rotated until they reach their equilibrium moisture content. Theoretical calculations of the capillary pressure combined with weight measurements of the moisture content then constitute data points of the moisture retention curve. This technique has been validated for soil and rock samples (e.g. [130,135,142]), however, only a limited amount of studies have indicated its relevancy for building materials [143]. An elaboration and optimization of the test sequence dedicated to porous building materials is therefore still lacking.

In transient centrifugation, the dynamic drainage process is registered. This requires measurements of the moisture outflow from samples and/or the distribution of moisture contents and capillary pressures in samples during centrifugation. By minimizing the difference between measured and simulated variables, the moisture storage and transport properties of the materials can be inversely characterised [144]. Contrary to steady state tests, it is no longer required to complete the full equilibration process [137] which reduces the total measuring time. Additionally, the moisture permeability of the materials can be obtained simultaneously [129,132]. Šimůnek and Nimmo [129] were the first to use moisture sensor measurements of the evolution of the moisture content distribution inside the sample to determine the water retention and permeability curves. Their results show good agreement with steady state centrifuge experiments on the same Oakley sand [129]. Further validation of the transient centrifuge technique is provided by studies on different soils and by comparison with results obtained from other more commonly used experimental techniques such as pressure plate tests [140,141].

While transient centrifugation has shown to be suitable for various soil samples, several sources [140,143] have proven that only measuring the moisture outflow in a transient experiment can result in moisture retention curve determination, but will lead to inaccurate moisture permeability measurement. At least one sensor (preferably more) [140],which measures either moisture distributions or capillary pressures distributions across the sample, must be embedded inside

the sample to also measure moisture permeabilities during transient centrifuge experiments. Not only do these embedded sensors require an accurate (and expensive) in-flight data acquisition system, but the installation of sensors in rigid porous building materials requires breaking the material and destroying the pore structure. These disadvantages make (the much simpler) steady state centrifugation the preferred option for the determination of the moisture storage properties of general building materials.
Subchapter A therefore focuses on the development of a laboratory centrifuge and the validation of the steady state centrifuge experiment for determination of the moisture retention curve of hydrophilic building materials. The moisture transport properties of the hydrophilic building materials, used for comparison with the properties of hydrophobised materials in Subchapter B, are already well-characterised in previous work [8,44], and these transport properties are therefore not measured here. First, the physics behind centrifuge testing and a further elaboration on the experimental methodology is given in Section A.2. Next, the development of the laboratory centrifuge is explained, problems experienced are described, and construction guidelines are provided in Section A.3. Subsequently, Section A.4 validates the steady state centrifuge experiment using a common building material and formulates guidelines for the most efficient workflow of the experiment. These guidelines are subsequently followed in Section A.5 to illustrate that this technique is also applicable to other building materials. Finally, a discussion of the steady state centrifuge test and the main conclusions of this subchapter are provided in Sections A.6 and A.7, respectively.

A.2 Description of the steady state centrifuge experiment

A.2.1 Physics of steady state centrifugation

In steady state centrifuge experiments, typically moisture saturated samples (capillary or vacuum saturated) are placed in a centrifuge and spun with a certain radial velocity. Under the influence of the pressures induced by the centrifugal force, water is directed outwards and expelled at its outer surface (i.e. the outflow surface). The process continues until the sample reaches its equilibrium moisture content. Since the centrifugal force is a body force, which acts on water in all pores simultaneously, the samples are expected to equilibrate faster than in protocols where they are subjected to external forces (e.g. pressure plates). During the experiment, the one-dimensional moisture transfer can be described by the modified Richard's equation [129]

$$\frac{\partial \mathrm{w}(\mathrm{r_{rad}})}{\partial \mathrm{t}} = \frac{\partial}{\partial \mathrm{r_{rad}}}\left(\mathrm{K}\left(\frac{\partial \mathrm{p_c}}{\partial \mathrm{r_{rad}}} - \Delta\rho\omega^2\mathrm{r_{rad}}\right)\right) \tag{4.1}$$

where w [kg/m^3] is the moisture content, $\mathrm{r_{rad}}$ [m] the radial distance from the center of rotation, t [s] the time, K [kg/msPa] the moisture permeability, $\mathrm{p_c}$ [Pa]

the capillary pressure, $\Delta\rho$ [kg/m^3] the density difference between the invading (i.e. air) and the defending (i.e. water) fluid and ω [rad/s] the radial velocity. Once the samples reach equilibrium, the capillary pressure distribution inside the sample can be calculated as a function of the distance from the rotational axis (r_{rad}) as [145]

$$p_c(r_{rad}) = \frac{\Delta\rho\omega^2}{2}(r_2^2 - r_{rad}^2) \tag{4.2}$$

where r_2 [m] is the distance from the rotational axis to the outflow surface of the sample as shown in Figure 4.1. This figure shows an example of the capillary pressure distribution at equilibrium, theoretically calculated using equation 4.2, for a 4 cm long sample, rotated at 500, 750 or 1000 revolutions per minute (RPM), and with its outflow surface located 20 cm from the rotational axis. The variables indicated on the figure match the ones in Equations 4.1 and 4.2. Equation 4.2 results in a quasi-linear capillary pressure distribution in most of the sample, with a sudden transition to 0 Pa when r_{rad} approaches r_2 near the outflow surface. The capillary pressure of 0 Pa implies that the outer surface of the sample must remain completely saturated throughout the experiment, which is proven further in the text. Otherwise, the derivation of Equation 4.2 from Equation 4.1, which assumes a fully saturated outflow surface, is no longer valid.

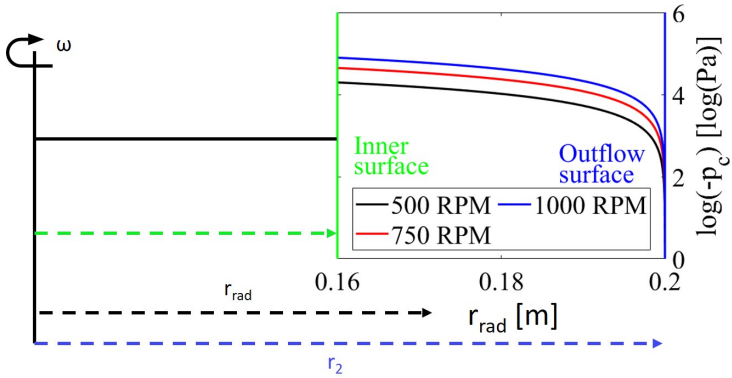


Figure 4.1: Equilibrium capillary pressure distribution of a 4 cm long sample rotated at 500, 750 or 1000 RPM.

A.2.2 Methodology of steady state centrifugation

In the steady state centrifuge experiment, moist samples are rotated until periodic weight measurements indicate that they have reached their equilibrium moisture content. By combining this moisture content (w) with the theoretically calculated average capillary pressure (using Equation 4.2), the sample contributes one data point ($\log(-p_c)$,w) to the moisture retention curve. Varying the boundary conditions (i.e. the radial velocity and/or the sample's position and/or length) in subsequent tests allows manipulating the capillary pressures and moisture contents in the samples to retrieve information over the relevant range of the moisture retention curve.

Figure 4.1 shows that the capillary pressure distribution inside the samples is highly non-linear near the outflow surface of the sample though. This non-linear portion of the curve significantly affects the calculation of an average capillary pressure over the entire sample. As a solution, the sample, which measures 4 cm in Figure 4.1, is divided in two subsamples; a smaller part located at the outflow surface (grey area in figure 4.2) and the rest of the sample. Although this smaller part measures 1 cm in length in Figure 4.2 (a), its length can vary as long as it contains the highly non-linear descent of the capillary pressure to 0 log(Pa). To improve hydraulic continuity, a moist filter paper is placed between both samples. As shown in Figure 4.2 (a), the sudden decline of the capillary pressure towards 0 Pa now occurs in the grey part of the sample. Since the different parts of the sample can be weighed separately, it is possible to omit the small part from the analysis. The capillary pressure distribution across the larger sample is quasi-linear over its entire length and the average capillary pressure resultantly does not diverge much from the value at its center (indicated by the red mark in Figure 4.2 (a)).

In an attempt to further optimize the experiment, the target sample can be divided into smaller subsamples still, connected to each other by moist filter papers (e.g. 3 x 1 cm like in Figure 4.2 (b)). Since every subsample contributes one data point ($\log(-p_c)$,w) to the moisture retention curve, the division into three subsamples now provides three data points per experiment. The capillary pressures at equilibrium for these three samples are illustrated by the red markers in Figure 4.2 (b). Despite obtaining more data points for every experiment, the hydraulic resistance of the filter papers slows down the moisture transport and most likely increases the necessary centrifugation time before equilibrium is reached. These contradicting effects on equilibration time require a further assessment of the impact of sample division on the overall test duration.

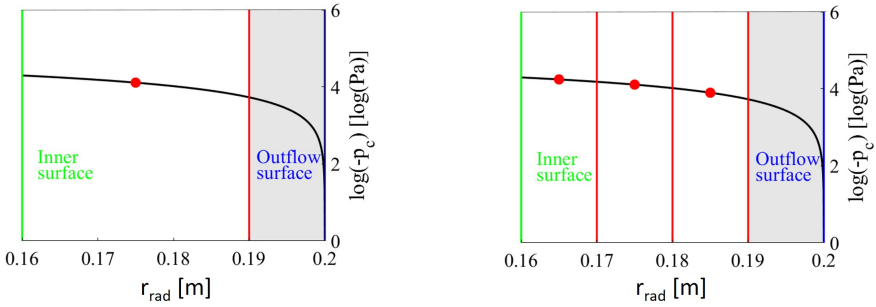
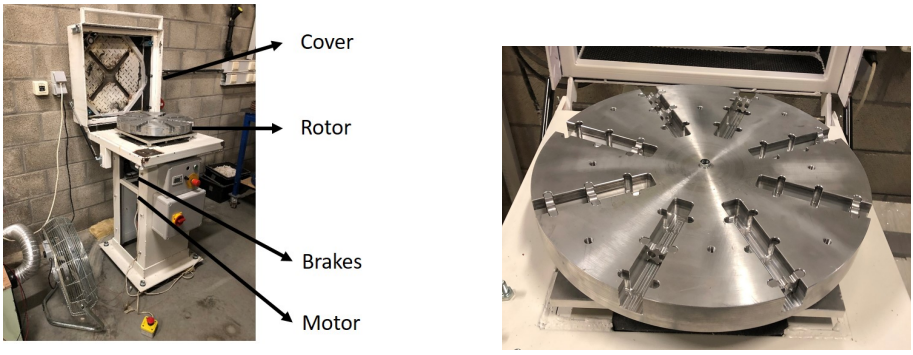


Figure 4.2: The division of a 4 cm long sample in 2 parts (a) and 4 parts (b) where the grey area represents the sample to be omitted because of its non-linear capillary pressure distribution. The red lines represent the filter papers and the red markers represent the central/average capillary pressures of the individual parts.

A.3 Design of the laboratory steady state centrifuge

The laboratory centrifuge is composed of four noteworthy parts all shown in Figure 4.3 (a): the motor, the rotor, the cover and the brakes. These parts are all supported by the white metal column, which provides additional safety to the operator as well. During the experiment, samples are placed in the rotor, the rotation of which is controlled by the motor which has a theoretical maximum velocity of 6000 RPM. Since rotating solid materials at high speeds involves several risks, user safety is guaranteed by the cover, which shields the rotor from its surroundings. Figure 4.3 shows both the centrifuge in its totality (a) and a close-up view of the rotor (b). This section focuses on the description of the different components and discusses the problems that were experienced and resolved during the centrifuge's design. The choice to develop a centrifuge rather than to buy a commercially available one allows more freedom in both the initial design as well as future adaptations to the centrifuge.



(a) (b)

Figure 4.3: The centrifuge in its totality (a) and a close-up view of the aluminum rotor (b).

A.3.1 Designing the motor

In order to measure the moisture retention curve over the desired capillary pressure range, the capillary pressures, induced in the sample by the centrifugation, have to be easily adaptable for different iterations of the experiment. As shown by Equation 4.2, this is possible by varying either the sample's length, the sample's position and/or the rotational velocity. The first two factors are governed by the design of the rotor as shown in the next section and are hence limited by practical constraints. The rotational velocity, however, depends entirely on the motor.

With this in mind, Equation 4.2 was used in the design stage to obtain the necessary rotational velocities for a rotor with an outer radius of 0.2 m. This radius has been established early in the design process since it is limited by the physical room in the laboratory. For this project, a synchronous motor (Type: CM3C71S-60A-K/BZ/PK/RH1M/KK from SEW Eurodrive [146]) with a maximal rotational velocity of 6000 RPM has been deemed sufficient. For 2 cm and 4 cm long samples, located at the maximum distance of 0.2 m from the rotational axis, this motor allows inducing capillary pressures of 6.16 log(Pa) (99% RH) and 6.45 log(Pa) (98% RH), respectively. This allows measuring the entire moisture retention curve of most (if not all) commercial ceramic bricks as well as many other building materials. Compared to the pressure plates, which allow maximum capillary pressures of 6.18 log(Pa) [8], this technique guarantees a similar or more extensive measuring range. For hydrophilic materials which require even higher capillary pressures (or lower RH), other complementary techniques are well-established (e.g. ad- and desorption desiccators) [8].

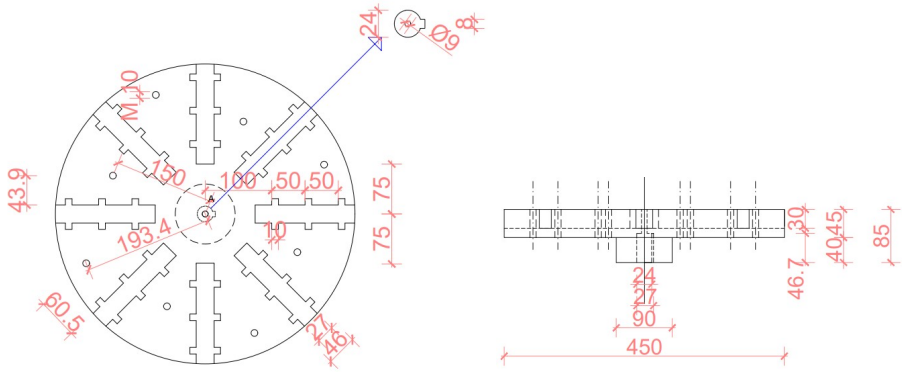
In practice, this rotational velocity of 6000 RPM has been proven unattainable

for the current centrifuge setup for two reasons. Firstly, the combination of the centrifuge setup with the floor has its first natural frequency around 2000 RPM. Therefore, performing experiments between 1750 RPM and 2250 RPM is discouraged to avoid vibration damage to other sensitive equipment in the vicinity. Secondly, the heat generated by the motor significantly increases the temperature of the air inside the cover and resultantly the surface temperature of the rotor. As a result, unwanted evaporation from the sample's surfaces is induced. As remedying measures, holes are drilled in the top of the cover to allow heat to be extracted from the vicinity of the rotor while a ventilator produces a cross-flow across the motor to extract a part of the produced heat at its source. Both of these measures can be seen in Figure 4.3.
After application of both measures, the air temperature within the protective encasing equilibrates to 23°C - 24°C for a rotational velocity of 1500 RPM, which causes the rotor's surface temperature to stay below an acceptable 22.5°C. Since the motor was initially overdimensioned, these radial velocities prove sufficient for the application in this dissertation. Higher rotational velocities require a further reduction of the heat at the source by for example replacing the current motor with a water-cooled or oil-cooled one. However, one should be aware that the mechanical load experienced by the samples at these higher velocities due to centrifugation can become a bigger problem than heat generation. Despite introducing these heat reducing measures, water evaporation remains a sensitive issue, which is why other preventive measures (vapour tight tape and specific sample holders) are elaborated further below in this subchapter.

A.3.2 Designing the rotor

A close-up picture of the rotor is displayed in Figure 4.3 and its specific dimensions are displayed in Figure 4.4. As stated before, the diameter of the rotor is limited by the physical room in the laboratory, however, larger (and hence heavier) rotors are not recommended due to stability issues at high velocities. Higher capillary pressures are more easily obtained by varying the rotational velocity, as can be deduced from Equation 4.2. The rotor contains 8 channels in which samples can be placed against an aluminum plate at a distance of 10 cm, 15 cm or 20 cm from the center of rotation, which results in maximal sample lengths of 2 cm, 7 cm or 12 cm, respectively. This allows freedom in both the position and dimension of each sample. The aluminum plate is perforated to create two holes to allow moisture outflow from the samples. The channels have a cross-section of 2.7 x 2.7 cm^2, which is designed to house samples measuring 2.5 x 2.5 cm^2. To maximise the volume of the samples, rectangular samples are used instead of cylindrical ones, which are often used in literature [129,136,139]. This rectangular shape also simplifies the design of the sample holders, shown in Section A.3.4. The smaller cylinder, attached to the bottom of the rotor and visible in Figure 4.4 (b), forms the connection

between rotor and motor shaft. Originally, an aluminum top plate (to secure the samples) was bolted to the rotor, the screw holes for which are shown in Figure 4.4 (a). However, this plate proves to be unstable during centrifugation due to slight variations in the force with which the screws are tightened. Since its only purpose is to provide additional safety, the removal was not detrimental to the execution of the test given that the cover provides a sufficient degree of security already.
To guarantee the structural integrity of the rotor at 6000 RPM, a finite element analysis is performed with the program Ansys to calculate the stresses and strains. The maximal stresses, which evidently occur at 6000 RPM, have a magnitude of 179 MPa. This remains well below the yield strength of 386 MPa of the aluminum alloy 6061-T651 used for the construction of the rotor. Since experimentation has shown that 6000 RPM is unattainable with the current setup, implying that the experiments are all executed at lower radial velocities, failure of the rotor is highly unlikely.



(a) (b)

Figure 4.4: The dimensions of the rotor in top view (a) and side view (b) [mm].

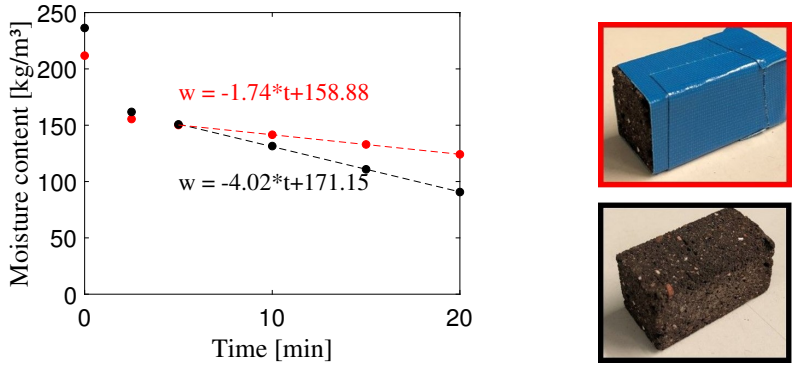
A.3.3 Designing the brakes

When the centrifuge is stopped and the centrifugal forces are removed, the moisture inside the sample redistributes under influence of the capillary pressure gradient across the material. Because the sample is weighed in its entirety, moisture redistribution within a sample does not influence its weight. When moisture redistributes between different subsamples in a composite sample, however, the weight of the different subsamples is influenced as well. Since any moisture flow governed by other forces than the centrifugal force renders equation 4.2 not applicable, moisture redistribution in composite samples is

unwanted. Therefore, the time between stopping the centrifuge and weighing the samples should be minimized. This necessitates sufficiently strong brakes which allow quickly halting the test. In this design, regenerative brakes (typically used in electric vehicles) are used with the slight difference that brake energy is not stored in a battery, but dissipated in a shunt resistor. These brakes allow stopping the centrifuge in less than 10 seconds for rotational velocities up to 1500 RPM. The next section shows that this braking time is negligible compared to the time required to weigh all the samples.

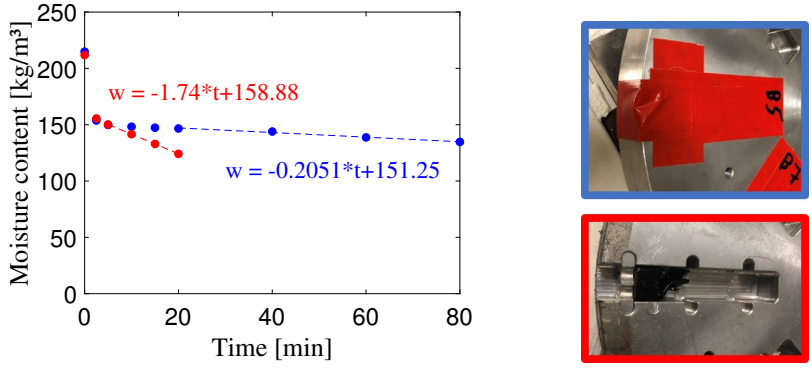
A.3.4 Designing the sample holders

The first, exploratory measurements are performed on fully saturated samples, placed directly in the channels of the rotor. These samples quickly desaturate over time, however, due to both the large (unwanted) evaporation flux from the sample's surfaces exposed to the air and the liquid moisture outflow in the radial direction driven by the centrifugal force. To reduce the contact between samples and air and resultantly the unwanted evaporation of moisture, all surfaces, apart from the outflow surface, are covered with vapour tight tape. Figure 4.5 shows the moisture content in function of time for two different 2 cm long samples, one of which is packaged in vapour tight tape. They are simultaneously rotated at 1000 RPM. The initial rapid decrease of the moisture content is attributed to the moisture outflow due to the centrifugal forces, while the following slow decrease is governed by the combination of the centrifugal force and the unwanted evaporation of moisture from the exposed sample surfaces. The latter proves to be the dominant factor since certain measures aimed at eliminating evaporation from the sample also eliminate this slow second stage as shown further in this subchapter. This second stage is therefore described as the evaporation stage, characterised by the evaporation flux. As shown in Figure 4.5, this evaporation flux reduces from 4.02 kg/m^3min to 1.74 kg/m^3min due to the vapour tight tape. A further reduction to 0.21 kg/m^3min is obtained by also covering the top and front of the channel in the rotor like in Figure 4.6.



(a) (b)

Figure 4.5: Comparison of the moisture content evolution in time for a 2 cm long sample rotated at 1000 RPM between samples with and without tape (a) and an example of these samples (b).



(a) (b)

Figure 4.6: Comparison of the moisture content evolution in time for a 2 cm long sample, with its surfaces covered by tape, rotated at 1000 RPM with and without the addition of extra tape on the rotor surface (a) and an example of these samples (b).

Although the evaporation stream is severely reduced by the vapour tight tape, several problems remain. Firstly, the tape on the aluminum rotor only adheres sufficiently well for radial velocities of 1000 RPM or lower. At higher speeds, the tape releases mid-flight, hereby damaging the sound insulation attached to

the inside of the cover. Other types of tape with better adhesive qualities (e.g. airtight tape) experience the same issues and prove even harder to remove. Secondly, the literature on soil samples reveals that the moisture content first decreases rapidly after which moisture is expelled during a slow, second stage that can take hours up to days [137]. Any evaporation stream, no matter how small, therefore influences this second stage and hence the true equilibrium moisture content. In an attempt to further reduce evaporation from the sample, sample holders are created to prevent contact between samples and the surrounding air.

Sample holder without direct water contact. A first type of sample holder, shown in Figure 4.7, encompasses both the sample, which is positioned against a perforated plate, as well as a porous material at the other side of this plate. The porous material, which was either paper or calcium silicate insulation during these tests, absorbs the water expelled by the sample. At low rotational velocities, when the sample expels little water, the material is preconditioned with a small amount of water prior to placing it in the sample holder. This measure maintains a high relative humidity throughout the experiment and hereby minimizes the evaporation flux. Although the evaporation stream of samples inside the holder reduces to 0.04 kg/m^{3}min at 1000 RPM, it is not completely eliminated from the measurements. Additionally, due to the limited storage capacity of the porous material, it can become saturated at high rotational velocities due to the vast amount of moisture expelled from the samples. A pool of water is then collected inside the holder, which flows back in to the target sample after stopping the centrifuge.

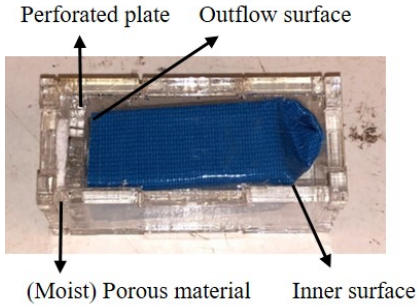
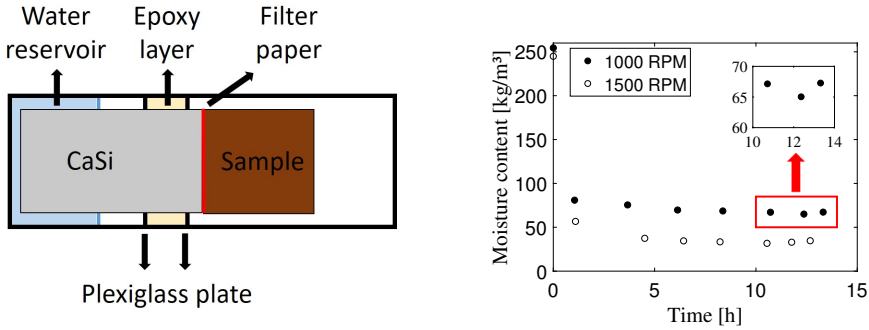


Figure 4.7: The sample holder without direct water contact.

Sample holders with direct water contact. In soil physics, the evaporation flux is sometimes eliminated by guaranteeing contact between the sample and a fully saturated material [130,131,137]. This is replicated by connecting the material of interest with a saturated piece of calcium silicate insulation, which in its turn is in direct contact with a water reservoir. An example of this holder is given in Figure 4.8 (a). Connections between different materials are always formed by a moist filter paper to improve the hydraulic continuity. Due to the small pores of the calcium silicate insulation, the material is not desaturated at the rotational velocities used in this dissertation.



(a) (b)

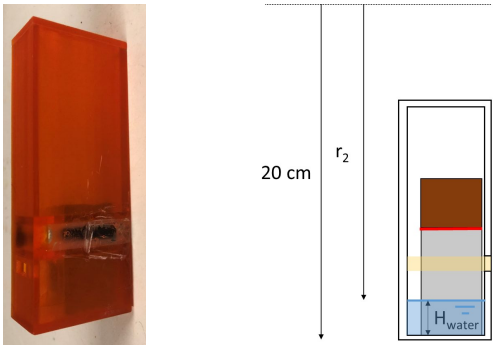
Figure 4.8: The sample holder containing the saturated calcium silicate (CaSi) insulation in contact with a water reservoir (a) and the moisture content evolution in time for two samples rotated at 1000 RPM and 1500 RPM (b).

Figure 4.8 (a) is the top view of a horizontal cut through the sample holder. The water reservoir is separated from the sample of interest by two plexiglass plates with a layer of epoxy in between. The calcium silicate insulation is in contact with a water reservoir on the one side and the sample, which is tested, on the other side. The epoxy layer makes sure there is no contact between the water reservoir and the sample of interest. During construction of the sample holder, the part of the calcium silicate insulation between the two plexiglass plates is wrapped in a plastic sleeve before epoxy is poured on the material. Due to the epoxy's low viscosity, a small amount sporadically reaches the calcium silicate insulation and penetrates it, hereby filling part of the pore system and slowing down water transport during centrifugation. Therefore, some sample holders were made with more viscous silicone instead of epoxy. Although this solves the problems with respect to contamination, the silicone cannot withstand the pressures associated with high rotational velocities and the sample holders resultantly break. Epoxy therefore remains the solution for the construction of the holders and in case of contamination, the holder is discarded.

When calculating the capillary pressure distribution in these sample holders, equation 4.2 remains valid with the slight difference that r_2 is replaced by the distance from the rotational center to the free water surface as shown in Figure 4.9 (b). Without any direct contact between sample and liquid water, evaporation could desaturate the sample's surface at r_2 hereby nullifying the assumption of a fully saturated outflow surface ($p_c = 0$ Pa). In this sample holder, however, this is guaranteed by the free water surface.

Using these sample holders reduces the evaporation flux to a degree where it becomes negligible. Figure 4.8 (b) shows two samples rotated at 1000 RPM and 1500 RPM. There is a distinct fast, first stage where most of the moisture is expelled after which the slow, second stage further reduces the moisture content to its equilibrium. The fluctuation of the moisture content at the end of the measurement is attributed to sample handling, to slight fluctuations in the water reservoir level (and r_2) and corresponding variations in calculated capillary pressures, and to water transfer from the calcium silicate insulation to the sample when the centrifuge is stopped. The latter is discussed in the next section. The equilibrium moisture content is calculated as the average of the last three weight measurements.

Finally, some problems arise when using the sample holders in Figure 4.8 (a) at high rotational velocities. Since the entire holder consists of plexiglass pieces glued together, high pressures seem to force water out through the connections. The water level in the reservoir, and hence the corresponding capillary pressure distribution, therefore fluctuates. In extreme circumstances (weak holders and/or high velocities), water reservoirs can empty completely when they are not refilled on a regular basis (e.g. overnight). This causes the calcium silicate insulation to desaturate and absorb water from the sample. Therefore, the actual final holders are 3D-printed to remove these connections. These final sample holders, capable of bearing rotational velocities up to 1250 RPM, are shown in Figure 4.9 (a).



(a) (b)

Figure 4.9: An illustration (a) and a representation (b) of the 3D-printed sample holders.

Moisture redistribution. After stopping the centrifuge, it takes some time before all samples are weighed. Since the samples, placed in all 8 channels of the rotor, can exist of multiple subsamples connected to each other with filter paper and wrapped in vapour tight tape, the weighing process can take 10 to 20 minutes. In this waiting period, moisture redistribution between and moisture evaporation from subsamples can pose a problem. To investigate their influence, samples, with a length of 2 cm or 2 x 1 cm, connected with a filter paper, are preconditioned in the centrifuge at either 350 RPM or 1000 RPM for an hour, after which they are removed and weighed at regular intervals. During this weighing process, samples are either taken out of the holder and completely covered in vapour tight tape (A), left in the holder directly on the saturated calcium silicate insulation (B) or left in the holder with a piece of plastic between brick and insulation to prohibit contact with the calcium silicate insulation (C). An example of all three storage methods can be found in Figure 4.10.

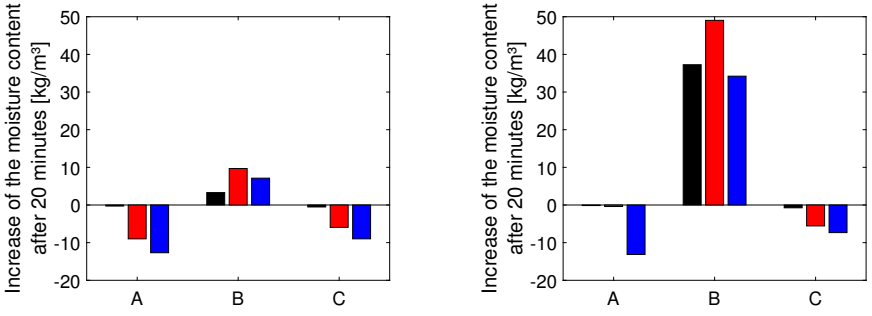
Figure 4.11 shows the change in moisture content of the samples after 20 minutes of storage according to any of the three different storage methods. The results are the average of 2 samples per storage method. Since results of individual samples were very similar, only averages are displayed. When samples consist of 2 parts, the bottom sample refers to the one in contact with the calcium silicate insulation during rotation. As shown, method B should be avoided at all cost since the direct contact with the calcium silicate insulation allows a lot of moisture to be absorbed, especially when much moisture is expelled during centrifugation (at high rotational velocities). The evaporation/redistribution of moisture in methods A and C is of similar magnitude. The major disadvantage of method A is that the samples should first be wrapped with extra tape to

reduce air/material contact. This significantly delays the weighing process and allows more moisture to evaporate. For this reason, method C is used in all further measurements.



(a) (b) (c)

Figure 4.10: The three ways in which samples can be stored between measurements; Outside of the sample holder and completely covered with vapour tight tape (a), inside the sample holder in contact with the saturated calcium silicate insulation (b) and inside the sample holder without contact with the saturated calcium silicate insulation (c).



(a) (b)

Figure 4.11: The change of the moisture content in the samples measuring 2 cm (black), 2x1 cm (top sample; red) and 2x1 cm (bottom sample; blue) after 20 minutes, for samples which were initially preconditioned at 350 RPM (a) or 1000 RPM (b). During these 20 minutes, the samples are stored as shown in Figure 4.10 (i.e. A, B or C).

Figure 4.12 shows the evolution of the moisture content in time for the samples which are stored according to method C. Contrary to the composite samples,

the 2 cm long samples experience hardly any moisture evaporation. By first weighing the composite samples (i.e. 2x1 cm) and by keeping the weighing process below 15-20 minutes, moisture evaporation will have a limited effect on the true equilibrium moisture content. This investigation is of course material-dependent since moisture redistribution will be more significant in permeable materials. Nevertheless, it is assumed that storage method C remains the optimal solution for other materials as well.

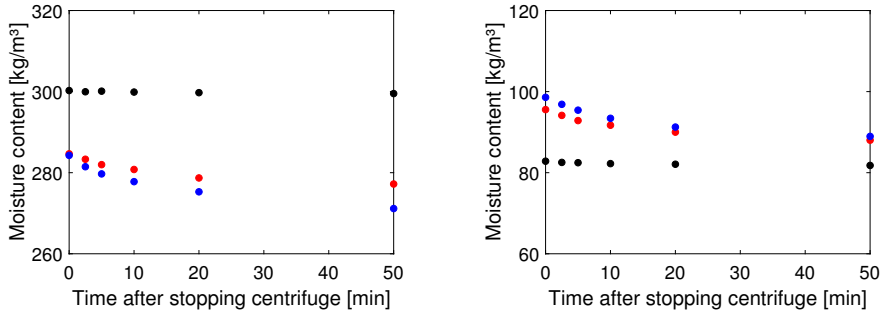


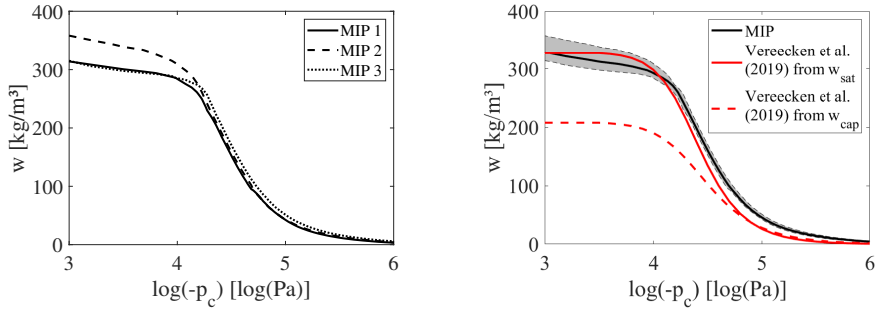
Figure 4.12: The evolution of the moisture content in time for the samples which are stored according to method C and preconditioned at 350 RPM (a) or 1000 RPM (b). The samples measuring 2 cm, 2x1 cm (top sample) and 2x1 cm (bottom sample) are respectively displayed in black, red and blue.

A.4 Validation of the steady state centrifuge experiment

A.4.1 Materials

In this section, the steady state centrifuge experiment is validated using Robusta bricks produced by Vandersanden, a material that has been extensively investigated by Feng and Janssen [8] and which is described in detail in Chapter 2. In this section, the moisture retention curve of the brick is derived from new MIP measurements on 3 samples, cut from the same bricks as the samples used in the centrifuge experiments. These measurements are performed using an Autopore IV mercury porosimeter from Micromeritics. The pressures increased gradually from 0 to 2×10^8 Pa and the moisture retention curves, displayed in Figure 4.13 (a), are derived from the mercury intrusion curves using the Washburn equation with a mercury/solid contact angle of 130°. For the post-processing of these MIP measurements, the densities and saturated moisture contents of the samples are derived from the MIP measurements themselves. The differences between the three samples are notable, and the average moisture

retention curve (full line) as well as a shaded area encompassing all curves are shown on further figures. The moisture retention curve of the Robusta brick has previously been determined by other experimental techniques (e.g. pressure plates) by Feng and Janssen [8]. In this paper, the MIP results showed to be representative of the moisture retention curve of this material over the capillary pressure range studied in this dissertation. Due to this similarity, only the results from the MIP are shown to guarantee readability of the figures, and the reader is referred to Feng and Janssen [8] for the other experiments.
The same brick has also been used in a previous transient centrifuge experiment by Vereecken et al. [143], in which the moisture storage properties were determined from the recorded moisture outflow. The results from this paper for both capillary and vacuum saturated samples are displayed in Figure 4.13 (b). In the paper, two vacuum saturated samples are tested, but only one result is shown due to the similarity between both curves. Since the moisture retention curve of both the MIP and the centrifuge test on vacuum saturated samples are very similar, the latter will be omitted from further figures to improve readability.



(a) (b)

Figure 4.13: The desorption moisture retention curves determined from 3 different MIP measurements (a) and a comparison of MIP results with the transient centrifuge experiment by [143] both from vacuum as well as capillary saturation (b).

A.4.2 Desorption moisture retention curve from vacuum saturation

In order to validate the steady state centrifuge experiment, three different sample compositions, shown in Figure 4.14, are tested. Two sample compositions consist of a single sample with a cross-section of 1.5 x 2.5 cm^2 and a length of either 2 cm or 1 cm. The other is a composite sample composed of two subsamples with cross-sections of 1.5 x 2.5 cm^2 and a length of 1 cm connected to each other

with a moist filter paper. All surfaces of the samples, besides the one in contact with the calcium silicate insulation, are covered with vapour tight tape before being placed in the sample holders and two duplicates of each composition are tested. The composite samples provide two data points per test while the single samples only provide one. Since the moist filter paper, which also loses moisture throughout the test, provides a hydraulic resistance, it is uncertain in which way these composite samples influence the necessary equilibration time. This section targets answers to this question.

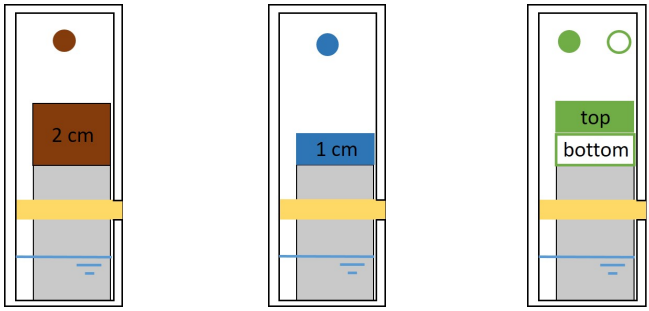


Figure 4.14: The three sample compositions used for the validation of the steady state centrifuge experiment and the symbols used in the visualisation of the results.

The centrifuge experiment is performed for 6 different rotational velocities: 350 RPM, 500 RPM, 625 RPM, 750 RPM, 1000 RPM and 1250 RPM. Figure 4.15 shows the results obtained from the centrifuge tests for all rotational velocities, wherein the different symbols represent each sample composition. All the results are obtained for samples which have been rotated in the centrifuge for at least 4 days (or more if equilibrium is not reached at that point) to make sure that the slow second stage, shown in Figure 4.8, has finished completely. Overall, the results from the three compositions do not show any substantial differences while agreeing well with the moisture retention curve obtained from the MIP measurements. However, the composite samples display more outliers (A and B). Outlier A is caused by failure of a sample holder. Water from the water reservoir was allowed to reach the bricks, as shown by the completely wet sample surface after testing. This explains the higher moisture content and hence these results can therefore be omitted.

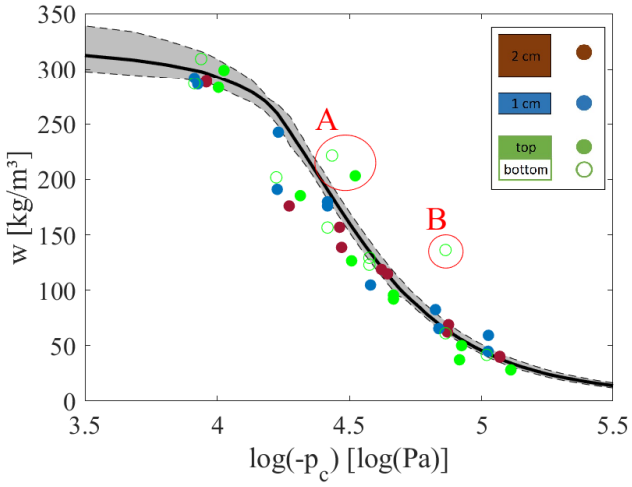
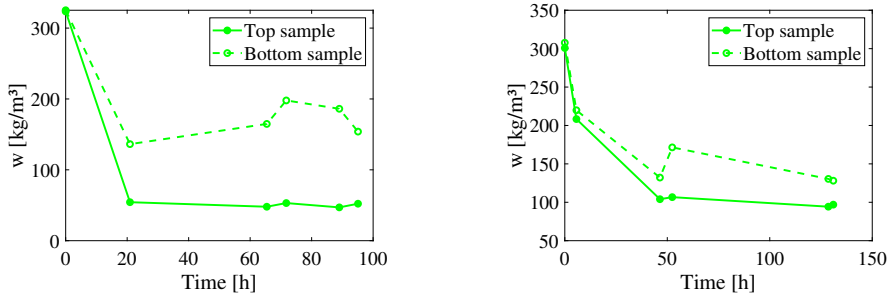


Figure 4.15: The desorption moisture retention curve obtained using the three sample compositions in the centrifuge test for vacuum saturated samples compared with the MIP results (black).

The explanation for outlier B is more difficult and for now hypothetical. The evolution of the moisture content in function of time for this outlier and for the corresponding top part of the composite sample are shown in Figure 4.16 (a). After an initial fast decline, the moisture content in the bottom sample (outlier B) increases significantly while its corresponding top sample equilibrates. It is believed that it has somehow come into contact with water. In Figure 4.16 (b), the top and bottom part of a different composite sample show the same behaviour albeit to a lesser degree. After a sharp decline, the bottom sample somehow absorbs water before desaturating again until it obtains its equilibrium moisture content. This kind of behaviour is solely seen in the composite samples which leads to believe that the water could come from the filter paper where it was stored after leaving the top sample. Following this reasoning, a longer centrifugation time would have allowed outlier B to equilibrate as well. The filter paper provides more resistance to moisture outflow than expected due to it also desaturating during rotation. Figure 4.16 shows equilibration periods of more than 4 to 6 days and prematurely stopping the experiment will result in a grave overestimation of the equilibrium moisture content. Based on this information and the fact that the other samples equilibrate much faster (as shown further below), composite samples do not increase the efficiency of the experiment and are omitted from further experimentation.



(a) (b)

Figure 4.16: The moisture content in function of time for outlier B in Figure 4.15 together with the corresponding top part of this composite sample (a) and a different example of such a composite sample (b).

As shown in Figure 4.8 (b), the samples experience a fast first stage wherein most of the moisture is expelled, followed by a slow second stage in which they further desaturate. This second stage, however, only accounts for a small amount of the total moisture loss. Therefore, it could be questioned whether reaching the true moisture equilibrium is necessary. For this reason, a different set of samples is rotated for a maximum of one day, causing some samples to not reach complete equilibrium. Results are compared with the experiments in figure 4.15, which were allowed to reach true moisture equilibrium and hence rotated for 4 to 8 days. To limit experimentation time, these tests are only performed for rotational velocities of 350 RPM, 500 RPM, 750 RPM and 1000 RPM using all three sample compositions. Figure 4.17 shows these results together with the ones already shown in Figure 4.15, disregarding outliers A and B. Since all samples reacted similarly, the figure does not distinguish between different compositions to improve its readability. Even though the weight measurements show that only samples rotating at low rotational velocities (350 RPM and 500 RPM) fully reach their equilibrium, the differences between the results in Figure 4.17 are so small that it is believed to be up to common experimental variation and material heterogeneity. This shows that if the moisture content has progressed somewhat into the second stage, it sufficiently approaches its true moisture equilibrium. Experiments can hence be stopped if two subsequent weight measurements show similar moisture contents (e.g. less than 5 kg/m^3 apart). It has to be mentioned that this is currently only valid for the Vandersanden ceramic brick, which is why Section A.5 applies the steady state centrifuge experiment to other materials.

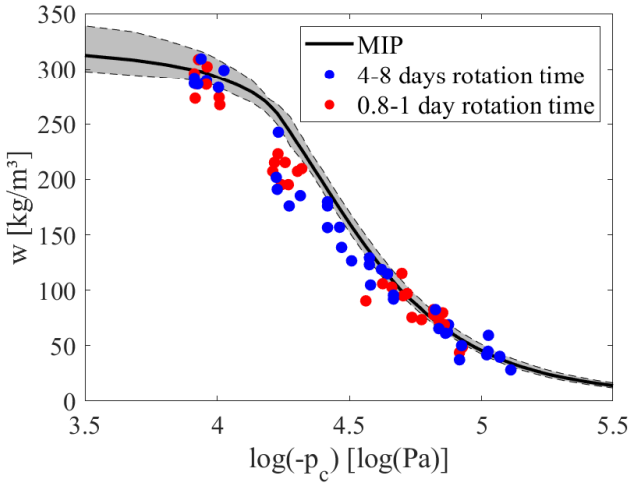


Figure 4.17: The results from the centrifuge experiment on Vandersanden ceramic bricks for which samples were rotated 0.8-1 days or 4-8 days.

From Figure 4.17, it can be concluded that the experiment can be stopped when subsequent weight measurements are not too far apart. It would be practical, however, if this equilibration time can be estimated beforehand. With this in mind, the experiments, used to constitute Figure 4.17, are reanalysed. Finding this equilibration time, however, proves to be very difficult because the decrease in moisture content is heavily sample dependent. To illustrate, Figure 4.18 shows two identical samples being rotated for a day. While one sample reaches its equilibrium after 6 hours, the other requires more than 24 hours. This could possibly be due to sample heterogeneity or a bad contact between the sample and the calcium silicate insulation inside the sample holder during rotation. Drawing conclusions on necessary equilibration time is therefore difficult.
Rather than estimating the necessary centrifugation time, the following practical approach is advised. The centrifuge experiment is started at the end of a day after which it is allowed to rotate throughout the night. The next day, the samples are weighed in the morning and evening. If the two measurements show little change in moisture content (e.g. less than 5 kg/m^3, depending on the wanted accuracy), a new experiment starts. For low rotational velocities (e.g. 350 RPM, 500 RPM), it is even possible to finish the experiment in a matter of hours making it more efficient to start the low velocity tests in the morning and weigh the samples around midday and at night. The high velocity tests can be started before the weekend to account for their longer equilibration period. Doing so, it becomes possible to measure an entire moisture retention

curve in 1 to 2 weeks. This is significantly faster than more common protocols (e.g. pressure plates). The only experimental technique that provides a quick complete curve determination (i.e. in one day) is mercury intrusion, which requires expensive and toxic mercury. It should be mentioned that the MIP measurements on the Vandersanden bricks are more accurate and show less variation as can be seen in Figures 4.15 and 4.17. A more detailed comparison with these experimental techniques is provided in Section A.6.

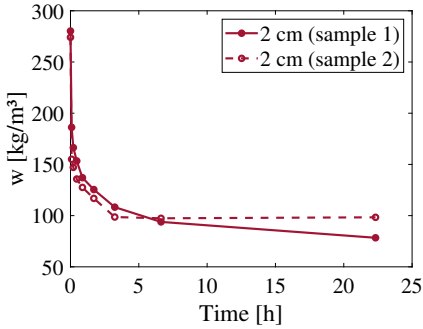


Figure 4.18: The moisture content in function of time for two samples with a length of 2 cm rotated at 750 RPM.

A.4.3 Desorption moisture retention curve from capillary saturation

Determining the full desorption moisture retention curve starting from capillary saturation within a limited timeframe is difficult (if not impossible) with any of the well-known experimental protocols. The MIP experiment for example only allows the moisture retention curve determination from vacuum saturation while the pressure plates require 2 months of testing. With the steady state centrifuge experiment however, this becomes possible. The workflow remains the same as for vacuum saturated samples with the difference that samples are initially capillary saturated. These experiments are once again performed on Robusta ceramic bricks, but only samples with a length of 2 cm are tested. The results are shown in Figure 4.19 together with the moisture retention curve derived from MIP measurements. The moisture retention curve from Vereecken et al. [143], derived from a transient centrifuge experiment on the same capillary saturated bricks, is also added to the figure. There is a good agreement with the moisture retention curve from Vereecken et al. [143] and at higher capillary pressures, the moisture retention curve derived from MIP measurements is also approached. The good agreement between the different techniques validates this steady state centrifugation experiment once more.

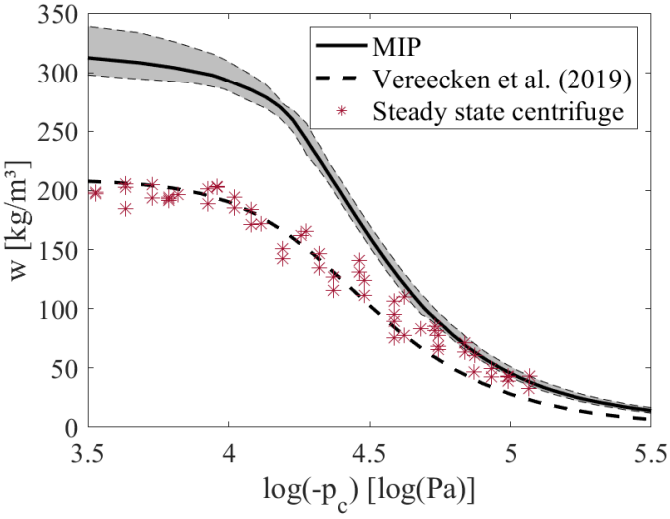


Figure 4.19: The results from the centrifuge experiment starting from capillary saturated samples compared with the results from MIP as well as with the results from a centrifuge experiment by [143].

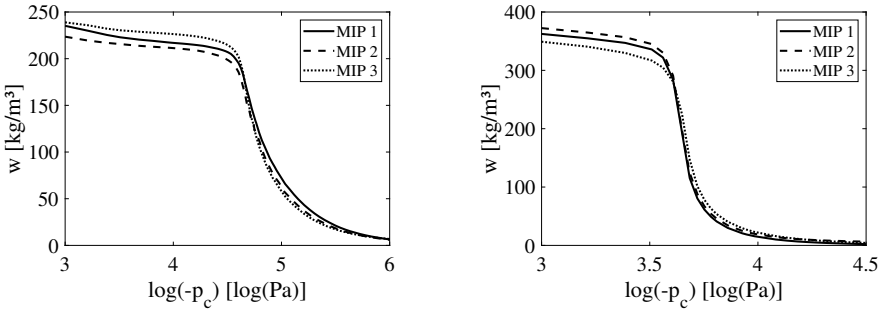
A.5 Application of the steady state centrifuge experiment

After the validation of the steady state centrifuge experiment, two other materials are characterised to further illustrate the applicability of the steady state centrifuge technique to different materials. The practical approach, discussed in Section A.4.2, is used. Preconditioned samples are placed in the centrifuge and rotated overnight. The following day, weight measurements are performed in the morning and in the evening. If these do not differ by more than 5 kg/m^3, the samples are deemed to have reached equilibrium. The results are subsequently compared to moisture retention curves extracted from MIP measurements on the same material.

A.5.1 Materials

The first material is a different type of brick, previously used in the EC HAMSTAD project [147], which has previously been characterised extensively with common experimental techniques. The measured saturated and capillary moisture contents equal 240 kg/m^3 and 149 kg/m^3. In this PhD thesis, new MIP measurements are performed to account for any changes between bricks produced in different batches. The measurements are made with the same

apparatus as used for the Robusta Vandersanden bricks in section A.4.1. Three different samples are tested and their results are shown in Figure 4.20 (a). The second material is the sintered glass filter from ROBU (type P100) which has been extensively discussed in Chapter 2. This material has a saturated and capillary moisture content of 365 kg/m^3 and 272 kg/m^3, respectively. Three samples are once again subjected to MIP measurements and their results are shown in Figure 4.20 (b).



(a) (b)

Figure 4.20: The desorption moisture retention curves determined from three different MIP measurements on HAMSTAD bricks (a) and the sintered glass filter (b).

A.5.2 Moisture retention curves

Figures 4.21 (a) and (b) show the results gathered from the steady state centrifuge experiment together with the results from the MIP experiment for the HAMSTAD brick and sintered glass filter, respectively. The results for the HAMSTAD brick are collected from 7 different experiments, in which samples with a 2 cm thickness are rotated at 250 RPM, 350 RPM, 600 RPM, 750 RPM, 850 RPM, 1000 RPM and 1250 RPM. The first two rotational velocities are omitted in the case of capillary saturated bricks since no moisture is expelled from the sample in this case. The results for the sintered glass filter are gathered from 6 experiments, in which samples are rotated at 150 RPM, 200 RPM, 225 RPM, 250 RPM, 300 RPM and 350 RPM. During every experiment at least three samples are tested, except for the lowest rotational velocities where little to no moisture is expelled.

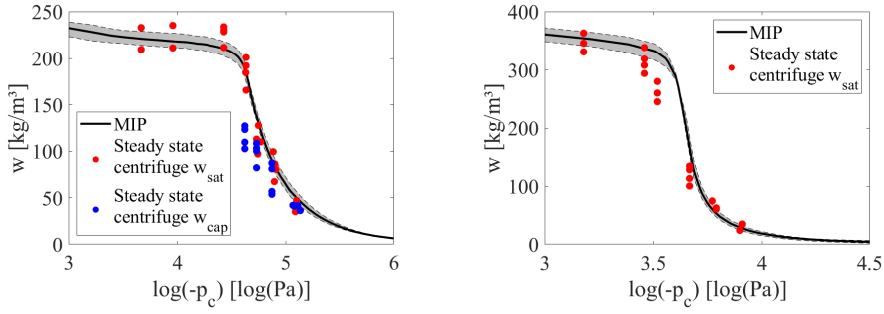


Figure 4.21: The results from the centrifuge experiment starting from saturated and capillary moisture content compared with the results from MIP for both HAMSTAD bricks (a) and sintered glass (b).

The steady state centrifuge results agree well with MIP measurements for both (vacuum saturated) materials. Although the accuracy of MIP measurements still remains somewhat superior as can be seen from the small variability between individual measurements. Preconditioning of the HAMSTAD brick to its capillary saturation also shows a good comparison at the higher absolute capillary pressures. The sintered glass samples, however, could not be preconditioned to their capillary moisture content. Whenever these samples came into contact with water, they absorbed enough water to (nearly) become vacuum saturated. This is possibly caused by the small size of the centrifuge samples as well as the relatively large size and high connectivity of the pores in the sintered glass' pore network, which eliminate air entrapment. Testing larger samples, which can be preconditioned to their capillary moisture content as previous experiments have shown, is unfortunately not possible with the current design of the centrifuge. Finally, for the PhD research of a visiting scholar (Lukas Weber) from FH Münster, moisture retention curves of gypsum boards, both starting from vacuum and capillary saturated moisture content, have been measured with the centrifuge and compared to MIP results. From this validation, the same conclusions as for previous materials can be drawn and hence the validation was also successful. The outcomes will be published in the future by the visiting scholar.

A.6 Discussion

This subchapter has shown the successful development and validation of steady state centrifugation for the determination of the moisture retention curve of porous building materials. In this discussion, the comparison is made with other more common protocols for moisture retention curve determination in this capillary pressure range, i.e. pressure plates and mercury intrusion. In doing so, the advantages and disadvantages of this centrifuge technique with regards to these existing techniques are discussed. Before going into this comparison however, a remark is made about the current design of the centrifuge and how it could be adapted to measure at higher rotational velocities (and corresponding larger absolute capillary pressures).

To allow successful measurements at higher rotational velocities, two problems require solving. Firstly, the heat generated by the motor should be reduced in order to not elevate the sample's temperature during rotation. In the current setup, cooling the motor with a ventilator and providing air flow openings in the protective cover proves sufficient to perform tests at normal temperatures (i.e. maximum air temperatures of 23-24 °C). However, higher velocities will require a water- or oil-cooled motor to extract more heat at the source. Secondly, the sample holders in this report, which are proven to eliminate evaporation, are currently limited to rotational velocities of 1250 RPM. Higher velocities require fabricating them out of a stronger material (e.g. aluminum) to avoid failure during centrifugation. An additional benefit to these strong holders is that samples can be glued inside these holders to allow redistributing part of the mechanical pressure, induced by rotation, to the holder itself. This way, the initiation of cracks or complete destruction of the samples, which have shown to occur at high rotational velocities, can be minimised. Using both these measures, measurements at higher rotational velocities are expected to be possible as long as samples do not compress or break under the induced pressures. Testing of samples which are deformed during centrifugation is out of the scope of this work.

The validation of steady state centrifugation, shown in previous sections, puts emphasis on the limited experimentation time of the technique. Using steady state centrifugation, a full moisture retention curve can be obtained in 1 to 2 weeks. Compared to pressure plates, which require about 2 months, this is significantly faster. On top of that, the pressure plates are more labor intensive than the centrifuge experiment, which only requires weighing the samples once or twice a day. Mercury intrusion, on the other hand, can handle several samples per day. Even though the three different measurements in Figure 4.13 show that multiple tests are required to take into account sample heterogeneity, it is therefore still faster than the centrifuge experiment. The validation has also shown that MIP measurements remain superior in terms of accuracy, however, it should be mentioned that necessary assumptions (e.g. contact angle between

mercury and pore walls) can significantly influence results [148]. Moreover, this technique is destructive and requires the use of expensive and toxic mercury.
Besides time and accuracy, the cost of an experimental setup is often a determining factor in whether or not a technique is adopted widely and/or used regularly. As explained before, the centrifuge setup, designed for this project, is laboratory made. Since very little of the design process has been outsourced, the total cost of the centrifuge is kept low and amounts to €6000. This is significantly less than both a mercury intrusion porosimeter or the pressure plate test setup. This only holds for a self-made centrifuge, however, and does not take into account the time spend to design this centrifuge. If a commercial centrifuge would be purchased, it would cost significantly more than the noted amount. This once again highlights the importance of the elaborate description of this (cost-effective) design given above, which can be easily replicated.
The main advantage of steady state centrifugation is the ability to measure the moisture retention curve from capillary saturated samples within a limited timeframe. It is widely acknowledged that the capillary moisture content is the maximum moisture content occurring in real applications. It is therefore often required in hygrothermal models. Until now, however, no experimental technique allowed a fast measurement of this moisture retention curve from capillary saturation. Pressure plates still require about 2 months to equilibrate while mercury intrusion can only measure moisture retention curves starting from vacuum saturation. The latter is also only applicable to standard hydrophilic building materials due to the necessary estimation of the contact angle between pore walls and mercury. Once the building materials are hydrophobised and the interaction between mercury and material changes, however, MIP becomes unable to measure the material's moisture retention curve while the steady state centrifuge technique remains applicable. For such hydrophobised materials, MIP measurements can only be used to measure pore size distributions and porosities as displayed in literature [6,8,9,32]. The centrifuge technique, developed in this subchapter, therefore provides a wider range of potential applications, which will be elaborated on in Subchapter B.
A final advantage of steady state centrifugation is its easy handling. The practical approach, described previously, only requires two weight measurements per day and defines a clear moment at which the centrifuge can be stopped. The post-processing of the experimental data (i.e. the calculation of the capillary pressure) is also easily understood, contrary to mercury intrusion, where necessary assumptions (e.g. contact angle between mercury and pore walls) can have great impact on the reported moisture retention curves [148].
To sum up, steady state centrifugation allows a relatively fast and sufficiently accurate determination of the moisture retention curves, both from vacuum and (the more realistic) capillary saturation. The main downside to the current centrifuge design is that it limits the rotational velocity to 1250 RPM.

By implementing the previously mentioned design changes, however, higher rotational velocities are expected to not pose problems. Extension of the current steady state centrifuge setup to measure other hygric properties, such as adsorption moisture retention curves or moisture transport properties, requires significantly adapting the existing design of the centrifuge and is therefore out of the scope of this PhD. Examples of such adapted centrifuge setups from the research area of soil sciences, however, can be found in [129] and [132] amongst others.

A.7 Summary

This subchapter handles the development and validation of the steady state centrifuge experiment for the determination of the desorption moisture retention curve of porous building materials. The first part describes the design of the laboratory centrifuge and highlights the difficulties encountered during construction. Solutions to these difficulties (as well as failed measures) are provided. Seeing as the cost of the final design is significantly less than other common protocols (i.e. pressure plates and mercury intrusion), its detailed description is valuable for others who wish to adopt this technique. Especially the development of sample holders, which eliminate evaporation during centrifugation, shows to be very important to eliminate unwanted moisture evaporation from the samples. It is important to mention that the final design only allows measurements for rotational velocities up to 1250 RPM. Higher velocities require measures to reduce heat generation at the source by using a water- or oil-cooled motor.
The second part of this subchapter successfully validates the steady state centrifuge technique by determining the desorption moisture retention curves from two ceramic bricks and one sintered glass filter, starting from both vacuum and capillary saturation, and comparing them with results from mercury intrusion porosimetry. Subchapter B further focuses on using this technique to measure the currently unknown moisture retention curves of hydrophobised building materials.

B Hygric property determination of hydrophobised porous materials

B.1 Introduction

This section experimentally characterises the hygric properties of the hydrophobised materials, so that they can be used in the validation of the adapted pore network model in Chapter 6. Chapter 2 has shown that current experimental techniques have had mixed success when measuring hygric properties of such hydrophobised materials. While the measurement of the vapour permeability remains possible with the widely-known and well-established cup tests, quantifying the liquid permeability and moisture retention curve proves much more difficult, if not impossible. For a detailed description of the existing research on hygric property measurement of hydrophobised materials, the reader is referred to Chapter 2. This section uses a combination of existing and novel experimental methods to compose the hygric properties of both hydrophobised sintered glass and ceramic brick.
Section B.2 first reiterates which materials are used and how they are hydrophobised with the chosen water repellent agents. Next, section B.3 captures the moisture retention curves with the help of the newly developed steady state centrifuge experiment, of which the design and validation have been discussed in Subchapter A. Subsequently, Section B.4 measures the vapour permeabilities of the different hydrophobised materials with the well-known cup tests. The liquid permeabilities of these materials are then quantified in Section B.5 using an adapted version of the well-known cup tests. Finally, Section B.6 discusses the measured hygric properties and Section B.7 summarises the most important conclusions.

B.2 Materials

This PhD thesis is centered around 2 materials: the P100 sintered glass filter from ROBU and the Robusta ceramic brick from Vandersanden. Both materials have been described in detail in Chapter 2 as well as in Subchapter A above, and hence their description is not repeated here. They have also been well-documented previously in our research section and the hygric properties of these hydrophilic materials are thus already well-defined [8,44]. These hygric properties are used throughout this part of the thesis to compare with the hygric properties measured for the hydrophobised materials.
Both sintered glass and ceramic brick are hydrophobised with two commercial water repellent agents (agent A and B) and one laboratory made water repellent agent (agent LM). All water repellent agents are silicon-based emulsions with different mixtures of silanes and siloxanes. Once more, the reasoning behind

the choice for these water repellent agents as well as a detailed description can be found in Chapter 2.
All water repellent agents are mixed with water to form a 90%/10% water/water repellent agent emulsion prior to being applied to the building materials. The bottom surface of variously sized samples is then brought into contact with the emulsion after which it is capillarily absorbed. A surplus of water repellent agent emulsion is always provided and samples are never thicker than 3 cm to make sure that the entire sample is homogeneously hydrophobised and no partially hydrophobised zones, like illustrated in Chapter 2, are present. Next, they are placed in a climate chamber with 86 % RH for at least 2 weeks of curing. Afterwards, the static contact angles between deionised water and hydrophobised materials are measured using the static sessile drop method on three different samples for every water repellent agent, and on each sample four droplets are imaged to account for sample heterogeneity. This results in contact angles of $117.6° \pm 7.1°$, $109.7° \pm 7.7°$ and $120.3° \pm 3.6°$ for sintered glass samples hydrophobised with water repellent agents A, B and LM, respectively, and contact angles of $134.6° \pm 8.6°$, $120.4° \pm 10.6°$ and $122.3° \pm 5.7°$ for Robusta ceramic brick samples, hydrophobised with water repellent agents A, B and LM, respectively.

B.3 Moisture retention curve

Since existing techniques fail at measuring moisture retention curves of hydrophobised materials, the steady state centrifuge experiment was designed and validated in Subchapter A and guidelines for its use were formulated. In short, samples, preconditioned to their saturated moisture content, are placed in the centrifuge and rotated until they reach their equilibrium moisture content. To limit testing time, it is advised to remove samples from the test setup once two subsequent weight measurements, spaced several hours apart, show moisture contents within 5 kg/m³ from each other. Exploratory measurements on hydrophobised samples prove that this is not possible due to these samples' much longer equilibration times. Figure 4.22, for example, shows the evolution of the moisture content of two hydrophobised sintered glass samples in the centrifuge. There is a rapid first desaturation stage after which a significant amount of moisture is still expelled in the much slower second desaturation stage. The moisture in the hydrophobised pore bodies and throats, which do not empty in this first stage, needs to be transported through the largely emptied hydrophobised pore network in the second desaturation stage. The high flow resistance provided by the hydrophobised surfaces of the empty elements explains why this second stage occurs at a much lower rate. Stopping the experiment when two subsequent weight measurements indicate moisture contents within 5 kg/m³ of each other, as proposed in the practical approach developed for hydrophilic materials, would result in equilibrium moisture contents of around

70 kg/m³, while the true equilibrium moisture contents are closer to 10 kg/m³. It is therefore imperative to keep the samples sufficiently long in the centrifuge to approach the true equilibrium moisture content. This is assumed to occur when three subsequent weight measurements show fluctuating weight and the average of these last three measurements is then seen as the equilibrium moisture content. As a result, measuring the moisture retention curves for hydrophobised materials now requires several months of testing, rather than 1 week as was the case for their hydrophilic counterparts.

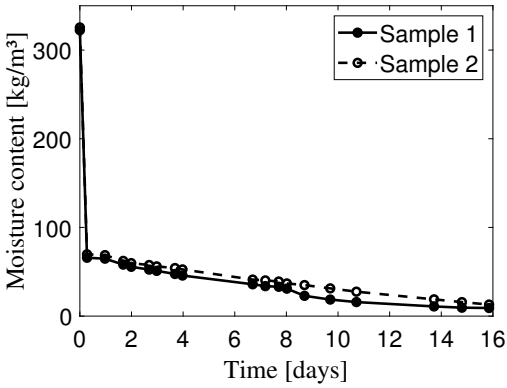


Figure 4.22: The measured moisture content in function of centrifugation time for two hydrophobised sintered glass samples.

The moisture retention curves of both sintered glass (a) and ceramic brick (b), hydrophobised with all three water repellent agents, are shown in Figure 4.23. The results obtained from the steady state centrifuge experiment are represented by the individual markers. Some of the measurements, represented by the hollow markers, unfortunately did not reach moisture equilibrium in a reasonable amount of time. These experiments are therefore stopped when the moisture content has progressed significantly in the slow desaturation stage. Figure 4.22, however, shows that this does not mean that the equilibrium moisture content is reasonably approached. Since a longer centrifugation time evidently would result in lower moisture contents, the hollow markers represent an upper limit for the true moisture retention curve. The moisture retention curves of the hydrophilic materials, extracted from MIP measurements, are also displayed on the same figure. These MIP results were previously obtained in Subchapter A, but here, they are represented by the average of the three MIP measurements (bold line) and the shaded area encompassing all MIP results. In the steady state centrifuge experiment, saturated hydrophobised samples, measuring 15 x 25 x 10 mm^3, are rotated at different rotational velocities.

For hydrophobised sintered glass and ceramic brick, samples are subjected to rotational velocities between 125-350 RPM and 200-1000 RPM, respectively. All samples are preconditioned via vacuum saturation since alternative forms of preconditioning, like capillary absorption, are not possible due to the materials' hydrophobic nature.

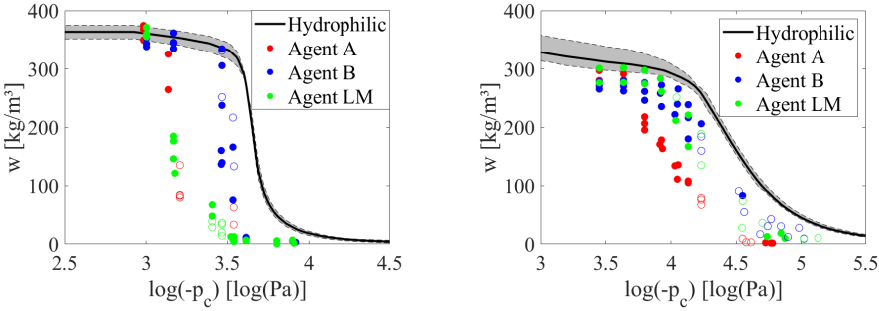


Figure 4.23: The moisture retention curves of the sintered glass (a) and ceramic brick (b), hydrophobised with the 3 water repellent agents, obtained using the steady state centrifuge experiment and the moisture retention curve of the hydrophilic materials as derived from MIP measurements.

The most obvious effect of the hydrophobisation procedure is the horizontal displacement of the moisture retention curves to smaller absolute capillary pressures. This can be understood as follows. The hydrophobisation application causes pore surfaces to become hydrophobic and hence their affinity towards water is changed. These pore network elements now rather repel water than attract it. During a desorption process, these hydrophobised elements will therefore expel water under influence of smaller liquid-gas pressure differences (i.e. capillary pressures) and the moisture retention curves are therefore moved to smaller absolute capillary pressures. This effect is more pronounced when the hydrophobised pore walls have less affinity with the water. The amount to which the moisture retention curves are moved is therefore an indication of the hydrophobised materials' degree of hydrophobicity, as quantified by the water/material contact angles. The static contact angles, measured using the sessile drop method, as explained in Chapter 2, equal $117.6° \pm 7.1°$, $109.7° \pm 7.7°$ and $120.3° \pm 3.6°$ for sintered glass samples hydrophobised with agents A, B and LM, respectively. In other words, the strongest hydrophobic effect is the result of a hydrophobisation with agents A and LM ($\theta_B < \theta_A \approx \theta_{LM}$). This is reflected by the moisture retention curves in Figure 4.23 (a). The same analysis for the ceramic brick samples, displaying

contact angles of $134.6° \pm 8.6°$, $120.4° \pm 10.6°$ and $122.3° \pm 5.7°$ for agents A, B and LM ($\theta_B \approx \theta_{LM} < \theta_A$), respectively, shows that the slightly more hydrophobic effect of agent A displaces the moisture retention curve in Figure 4.23 (b) the most.
Although the moisture retention curves are moved to smaller absolute capillary pressures, they also show that a certain rotational velocity is required to start the desaturation of these hydrophobised samples. For sintered glass and ceramic brick, these threshold rotational velocities equal 150 RPM and 300 RPM (for 1 cm thick samples), respectively. Any velocities below that will not change the moisture content in the saturated materials. In other words, moisture transport only initiates when the induced pressures are large enough to conquer a certain moisture flow resistance. This resistance is much smaller than in hydrophilic materials and it prevents these samples from emptying completely under influence of the smallest amounts of centrifugal pressures. Maybe, the imperfect hydrophobisation of the pore walls still provide some hydrophilic parts to which the moisture can adhere to. The existence of such hydrophilic storage sites in the hydrophobised pore network is proven in the microscopical investigation of Chapter 5. This possible cause for the existence of the threshold rotational velocity, however, remains speculation at the moment.
Important to mention is that the ceramic brick, contrary to the sintered glass, does not necessarily empty completely under the influence of the rotational pressures to which it is subjected. The design of the steady state centrifuge setup, discussed at length in Subchapter A, currently limits the rotational velocities (and corresponding capillary pressures) to 1250 RPM (and 5.1 log(Pa)). A further investigation at these higher velocities is therefore not possible. Unfortunately, at these higher velocities, the smallest pore network elements, which are most likely to remain hydrophilic in the hydrophobised materials, as explained in Chapter 2, tend to empty. It is therefore possible that these smaller elements have remained hydrophilic in the hydrophobised materials, causing them to empty at the same rotational velocities (and corresponding capillary pressures) as in hydrophilic samples. Figure 4.23 (b) does show, however, that these hydrophilically-oriented pores constitute maximum moisture contents of 10-15 kg/m³, which is (almost) negligible with regards to moisture contents which occur in real-life applications.

B.4 Vapour permeability

Vapour permeability of materials is typically measured via the well-known cup tests, which follow the ISO 12572 standard [47]. In this test, a material is placed between two environments with different relative humidities and the vapour flow through the sample is measured. Because the vapour permeability is dependent on the relative humidity, various cup tests are performed in which the sample is placed between different salt solutions (and hence different relative humidities)

to mimic dry (e.g. 12%-54% RH) and wet (e.g. 86%-94% RH) conditions. This dependency is caused by the existence of water islands in the pore network of the material at wet conditions. These water islands facilitate moisture transport through the material by inducing fast liquid transport. In hygroscopic materials (e.g. wood-based or cementitious materials [149]) this can have a significant effect on the measured water vapour permeability. In other building materials, such as ceramic brick or sandstone (i.e. less-hygroscopic materials), the impact is limited.

The cup tests in this project, both under dry-cup and wet-cup conditions, are performed according to ISO 12572 [47]. The dry-cup setup employs a 54 % RH (using a saturated $Mg(NO_3)_2.6H_2O$ salt solution) in the climate chamber and 12 % RH (using a saturated LiCl salt solution) in the cup. The wet-cup is exposed to 86 % RH (using a saturated KCl salt solution) in the climate chamber and 94 % RH (using a saturated KNO_3 salt solution) in the cup. Both ceramic brick and sintered glass, hydrophobised with the two commercial water repellent agents (agents A and B), are subjected to the cup tests and for each combination of building material/water repellent agent, three samples are tested. The cup tests are not performed on samples hydrophobised with the laboratory made water repellent agent (agent LM), to save some of the expensive sintered glass for other experiments. Also, as will be shown further in this section, all other tested samples agreed with previous conclusions drawn in literature and hence no surprises are expected for the samples hydrophobised with the laboratory made water repellent agent. All tested samples have a cross-section of 90 x 70 mm^2 and a thickness of 30 mm. The shape and dimensions of the cross-section are fixed by the shape of the cup.

Figure 4.24 shows the cups used in this project, which are inspired by Feng et al. [48]. The cups comprise a glass container and a plastic detachable lid. This setup allows performing the dry-cup and wet-cup tests on the same samples by simple removing the detachable lid and replacing the salt solution in the glass container. This further limits the use of the expensive sintered glass. To attach the samples to the lid, a hole is made and a plexiglass box is glued into the lid. Before samples are glued to the plexiglass box, a small amount of epoxy resin is rubbed on the side of the samples with a brush. When this epoxy resin hardens, it renders the sides of the sample impermeable. Next, the sample is placed in the plexiglass box and it is fastened with silicone sealant around its bottom edges (see Figure 4.24). Finally, the space between the plexiglass box and the smaller sample is filled with epoxy resin. Because the sides of the sample have previously been rendered impermeable, further absorption of epoxy resin is limited. In this cup design, there is no masked edge present and a correction is therefore not necessary. The plexiglass box, which extends a little higher than the sample itself, hinders the air flow over the sample and hence slightly increases the vapour transfer resistance at the top of the sample

to 2.4 * 10^7 m^2sPa/kg. This value is derived from a drying experiment on a saturated calcium silicate sample with a similarly obstructed air flow. The transfer resistance as well as the resistance provided by the air layer between the salt solution and the sample inside the cup are both taken into account in the calculation of the vapour diffusion resistance factor (μ[-]).

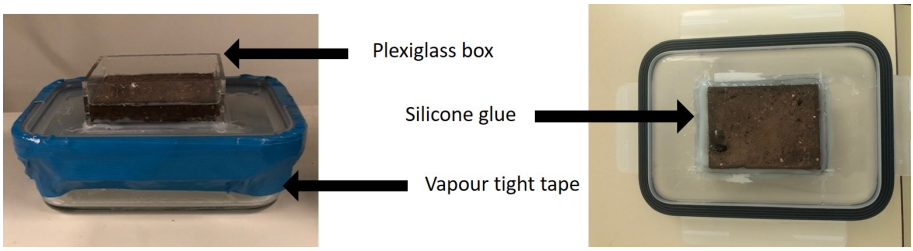


Figure 4.24: An example of the cups in the climate chamber.

The cups are placed in the climate chamber for about 1.5 months and periodic weight measurements are made on a balance with a resolution of 0.001 g. When at least 5 measurements, spaced approximately 3 days apart, show a constant moisture flow rate out of or into the cups, the tests are stopped. Previous experiments at the research section have shown that some of the saturated salt solutions only guarantee the prescribed relative humidity inside the cups if the correct water to salt ratio is used. In this study, the most stable salt solutions, whose relative humidities depend least on the water to salt ratio, are therefore chosen. Nevertheless, the relative humidity inside the cups is measured whenever a cup test is completed. This is done by removing the lid and sealing the (open) cup in a plastic bag together with a relative humidity sensor. After an equilibration period, this sensor displays the relative humidity in the cup. Inside the climate chamber, a HOBO sensor measures temperature and relative humidity throughout the entire test.
The vapour diffusion resistance factors for sintered glass (a) and ceramic brick (b), calculated according to the ISO 12572 [47] standard, are shown in Figure 4.25 together with values measured on hydrophilic samples. The latter are adopted from different studies [8,44], however here, the relative humidity in the cups was not measured after completion of the test. Therefore, only results, calculated with the salts' relative humidities as provided by the manufacturer, can be shown. The vapour diffusion resistance factors of both materials seem to increase slightly when they are hydrophobised. This agrees with various sources in literature [5,6,9,32,50]. It is however notable that results only seem slightly (or not at all) dependent on the relative humidity. The already limited hygroscopic behaviour of the hydrophilic materials seems to be (almost) completely removed when they are hydrophobised. This is due to the prevention of liquid water

storage (and fast liquid flow) in the hydrophobised pore network. This conclusion is previously mentioned in literature [6,9] as well, however, it is not generally accepted [6,8,32]. It is also interesting to note that the results of the wet-cup are much more variable than the dry-cup. This is because the salt in the wet-cup (KNO_3) is assumed to result in 94 % RH while measurements after the cup tests show $96\% \pm 1.3\%$ RH. This small difference has a more pronounced effect on the narrow relative humidity range of the wet-cups (i.e. 86%-94%) and hence small measurement errors more significantly influence the resulting µ-values. Performing cup tests on hygroscopic materials (e.g. lime mortar) before and after the hydrophobisation application in the future are required to validate this possibly reduced hygroscopicity. Unfortunately, the experiments on already less-hygroscopic materials (i.e. ceramic brick and sintered glass) are not enough to draw conclusions in the hygroscopic region.
After the cup tests, a surplus of epoxy resin was poured over the samples to render them completely vapour tight and the cups were once more placed in the climate chamber (54% RH) with LiCl (12% RH) inside the cups. Since the sample was rendered completely vapour tight, the recorded moisture flow into the cup quantifies the magnitude of the possible leakage flow through the lid. This moisture flow was less than 1% of the total recorded moisture flow during the experiments and it is hence deemed insignificant.

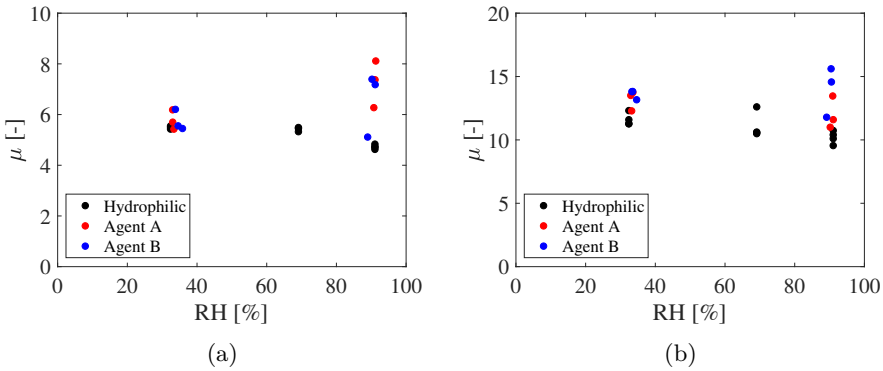


Figure 4.25: The vapour diffusion resistance factors measured on the hydrophilic and hydrophobised sintered glass (a) and ceramic brick (b) using the measured relative humidities.

B.5 Liquid permeability

While the vapour permeability of hydrophobised materials is easily quantified using well-known cup tests, their liquid permeability is rarely measured independently. Instead, the capillary absorption coefficient is often used as a measure of the hydrophobised materials' ability to transport moisture (both in vapour and liquid form). From the many different water repellent agent/building material combinations tested in literature [6,8,17,30,43,46,50], it becomes clear that the amount of moisture absorbed during such capillary absorption experiments is heavily reduced, but never completely eliminated. The question is whether moisture transport in these samples occurs through combined liquid and vapour transport or via vapour transport alone. This section investigates the moisture flow rate through a sample when it is allowed to capillary absorb moisture in adapted cup tests.

The adapted cup test is a combination of the well-known cup test and capillary absorption experiment wherein the salt solution inside the cup of Section B.4 is replaced by a water reservoir in direct contact with the sample. This test setup is sketched in Figure 4.26. These cups, three for each material/water repellent agent combination, are placed in a climate chamber with a controlled relative humidity of 54 % and the entire cup is weighed periodically for at least 1 month. The amount of moisture, transported from inside the cup, through the sample, and into the climate chamber is derived from weight measurements. The goal of these experiments is to compare this moisture flow to the theoretically calculated vapour flow. If the moisture flow rate out of the cup (and through the sample) is not notably larger than the vapour flow rate, liquid transport of water does not occur in these hydrophobised samples. Just like the original cup tests, this experiment is only performed on the sintered glass and ceramic brick samples, hydrophobised with the commercial water repellent agents A and B. When the test is stopped and the detachable lid is removed, the bottom of the sample is checked to guarantee that the sample remained into contact with the water reservoir throughout the entire test.

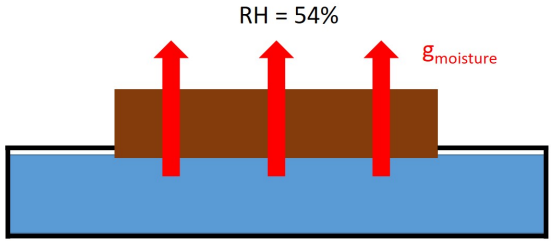


Figure 4.26: A sketch of the adapted cup tests.

Calculating the theoretical vapour flow through the sample can be done using Equation 4.3 in which A [m^2] is the cross-section of the sample, $p_{v,bottom}$ [Pa] and $p_{v,top}$ [Pa] are the vapour pressures in the cup and the climate chamber, respectively, d_{mat} [m] is the thickness of the sample, δ_a [kg/msPa] is the vapour permeability of air ($1.9*10^{-10}$ kg/msPa) and Z_{si} [m^2sPa/kg] is the vapour transfer coefficient at the sample's top surface (assumed to be equal to $2.4*10^7$ m^2sPa/kg as measured in Section B.4)

$$g_{vapour} = A\frac{(p_{v,bottom} - p_{v,top})}{d_{mat} * \mu/\delta_a + Z_{si}} \tag{4.3}$$

in which the vapour pressure in the cup equals the saturated vapour pressure at 23 °C while the vapour pressure in the climate chamber is calculated from this saturated vapour pressure and the measured relative humidity. For the vapour diffusion resistance factor, both the minimum and maximum values, measured in Section B.4, are used and hence both minimum and maximum theoretical vapour flows are calculated. For sintered glass and ceramic brick, the minimum and maximum vapour diffusion resistance factors are equal to 5-7.5 and 11.5-16, respectively.

The moisture loss over time, both measured during the adapted cup test and calculated theoretically using Equation 4.3, is shown in Figure 4.27 for both sintered glass (a) and ceramic brick (b). The theoretical vapour flow is calculated using both the minimum and maximum μ-values, represented on the figure by the grey zone. The samples of both materials, hydrophobised with agent B, show moisture flow rates equally large as the theoretically calculated vapour flow rate. In these samples, there is simply no significant liquid flow and all moisture transport occurs through the much slower vapour flow.

The samples, hydrophobised with agent A, however, show periods of fast moisture loss interchanged with periods in which moisture transport seems to be governed solely by vapour transport. This is clarified in Figure 4.28 in which the moisture flow rate, calculated from the weight measurements in Figure 4.27, is shown for sintered glass (a) and ceramic brick (b), hydrophobised with agent A. After the sudden loss of moisture, the moisture flow rates of the ceramic brick samples quickly evolve towards the theoretically calculated vapour flow rate. For sintered glass, there are periods of rapid moisture loss, after which the vapour flow rate is once more approached.

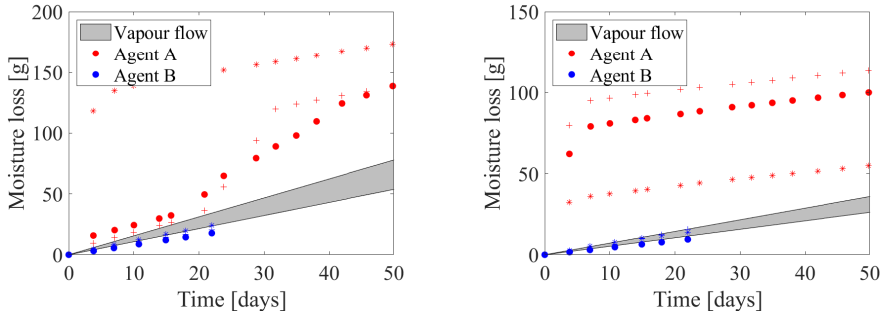


Figure 4.27: The moisture loss in function of time measured during the adapted cup tests on sintered glass (a) and ceramic brick (b), hydrophobised with agent A and agent B and the theoretically calculated vapour flow through the same samples.

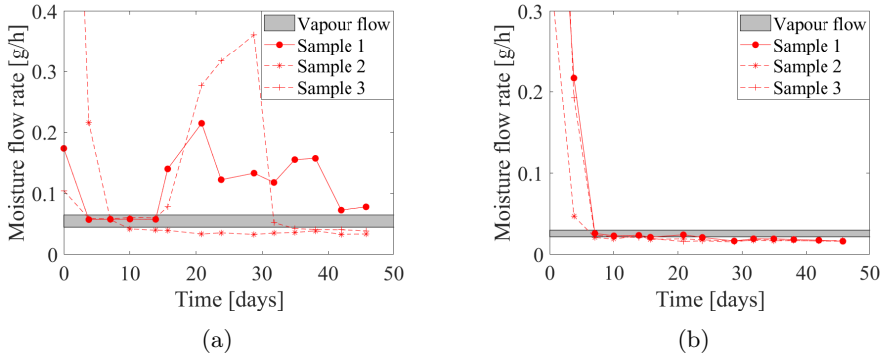
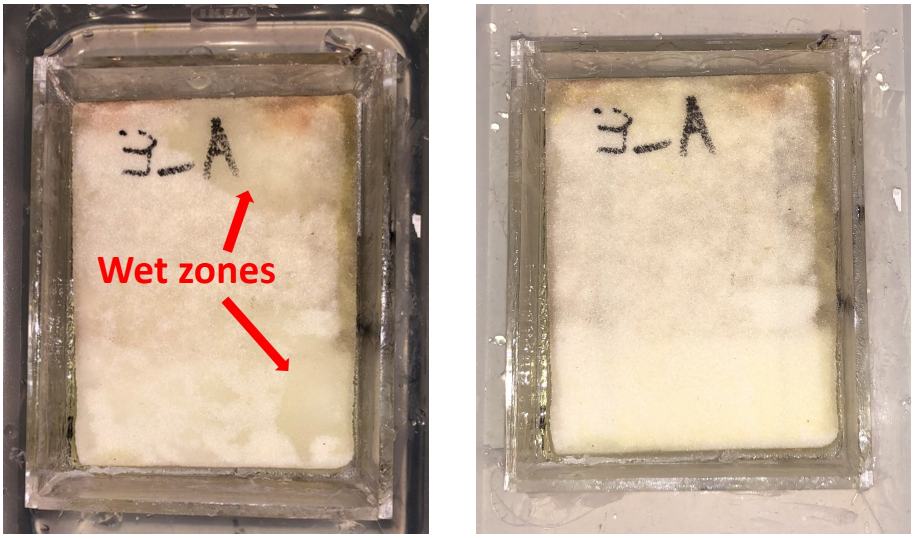


Figure 4.28: The moisture flow rate in function of time measured during the adapted cup tests on sintered glass (a) and ceramic brick (b) samples, hydrophobised with agent A, and the theoretically calculated vapour flow through the same samples.

Figure 4.29 shows sintered glass sample 3 of Figure 4.28 (a) after 10 days of measuring (a) and at the end of the adapted cup tests (b). This sample shows some areas where the water has been able to breakthrough and be absorbed in the pore network. This stored water temporarily induces fast liquid flow and hereby increases the moisture flow rate. Over time, it evaporates towards the climate chamber, as proven by the dry sample at the end of the test, and the measured moisture flow rate once more approaches the theoretically calculated

vapour flow rate as shown in Figure 4.28. At this point, moisture is only transported through vapour flow. Possible reasons for this temporary storage of water (and increased moisture flow rate) are given in the discussion below.



(a) (b)

Figure 4.29: Sintered glass sample 3 after 10 days (a) and at the end (b) of the adapted cup test.

B.6 Discussion

In this subchapter, the hygric properties of hydrophobised sintered glass and ceramic brick have been measured using both existing and novel experimental techniques. For both the moisture retention curve as well as the liquid permeability, existing experimental techniques proved inadequate for hydrophobised materials and new experiments are developed and applied. The vapour permeability, on the other hand, is measured using the well-known cup test which was proven suitable for hydrophobised materials in previous studies [5,6,9,32,50].

The steady state centrifuge experiment, used for moisture retention curve determination, is previously developed and validated in Subchapter A on hydrophilic materials. Due to its successful validation, it is used for the moisture retention curve determination of both hydrophobised sintered glass and ceramic brick. The hydrophobisation application mainly causes the moisture retention curves to move towards smaller absolute capillary pressures and this displacement

is dependent on the hydrophobic strength (i.e. the contact angle) of the material. Higher degrees of hydrophobicity make the materials more water repellent, causing them to expel moisture from their pores at smaller absolute capillary pressures. It should be noted that all moisture retention curves are determined from initially vacuum saturated samples in which hydrophobised pores are forcefully filled with water. These vacuum conditions never occur in reality. One could therefore argue the representativeness of these moisture retention curves for real-life applications, especially since hydrophobised materials hardly absorb any moisture spontaneously under normal circumstances, as shown in Section B.5. Unfortunately, preconditioning hydrophobised samples to lower moisture contents, which do occur in reality, proves impossible at the moment with the existing techniques.

The measurement of the vapour diffusion resistance factor of hydrophobised materials remains possible using cup tests and hence no newly developed experiments are necessary. Two interesting conclusions, which both agree with other experiments performed in literature [5,6,9,32,50], are derived in this thesis. Firstly, the vapour diffusion resistance factor increases slightly after the hydrophobisation application. The presence of the water repellent agent on the pore surfaces has been known to influence the vapour permeability by reducing the cross-section of the pores through which the vapour can be transported as well as by blocking some elements which thus reduces the pore network connectivity [9,32]. Both of these consequences intuitively imply an increase of the vapour resistance. Secondly, the hydrophobised pores' reduced affinity towards water reduces or eliminates the storage of moisture in the pore network. The removal of fast liquid water transport in this stored water further reduces the hygroscopicity of the already non-hygroscopic materials and resultantly also reduces the difference between dry-cup and wet-cup results. The vapour diffusion resistance of these hydrophobised materials is therefore hardly dependent on the relative humidity. In literature, this further reduction of the hygroscopicity has been noticed, both in hygroscopic dessicators [8,9,30,32,46] as well as cup tests [6,9]. Other studies still measure a lower vapour diffusion resistance factor under wet conditions [6,8,32], albeit only slightly. The reduced amount of moisture stored in the pore network of hydrophobised materials will be confirmed in the microscopic study of Chapter 5.

Finally, quantifying the liquid permeability via existing experimental techniques proved impossible. This is mainly due to the fact that the liquid transport in hydrophobised materials is heavily reduced (or even eliminated) which makes its quantification very difficult. Adapted cup tests are therefore developed in which moisture can be transported both by vapour as well as liquid flow. By comparing the measured moisture flow rate (both liquid and vapour) with the theoretically calculated vapour flow rate, the magnitude of the liquid flow rate is estimated. For both materials, a hydrophobisation with water repellent agent

B completely eliminates any liquid flow and hence all moisture is transported as vapour. When materials are hydrophobised with agent A, however, the samples have finite periods in which the moisture flow rate exceeds the calculated vapour flow rate. In these periods, some liquid water is absorbed and stored in the material, which temporarily induces fast liquid water transport and increases the moisture flow rate through the sample. However, this stored liquid water evaporates during the cup tests and the samples once more return to their dry state where vapour transport remains the only transport phenomenon in the hydrophobised materials.

There are several possible reasons for the temporarily induced liquid flow in the samples hydrophobised with agent A. The most likely one has been derived from the work of Soulios et al. [6,7]. They noticed a decrease of the capillary absorption coefficient in subsequent capillary absorption experiments and dedicated it to the washing away of emulsifiers in the water repellent agent. Removal of these emulsifiers increases the polymer's ability to repel water which hereby lowers the measured capillary absorption coefficient. When water penetrates the samples in the adapted cups, as in Figure 4.29, it temporarily provokes fast liquid water transport. It is possible that some of the emulsifiers in the applied agent are washed away in the process. This in turn increases the water-repellency of the hydrophobised pores which makes the further absorption of moisture much harder (if not impossible). This could explain why the moisture flow rate returns back to the vapour flow rate after the fast moisture loss. Although this reasoning is purely hypothetical, the return of the moisture flow rate to the theoretically calculated vapour flow rate does show that under normal working circumstances, the hydrophobised materials solely permit vapour transport. In real-life applications, the wind-driven rain aids at washing away those emulsifiers [6,7] and hence vapour transport should be the only transport phenomenon in correctly hydrophobised materials. This theory is supported by capillary absorption tests on the samples used in centrifuge experiments. Since these samples are repeatedly vacuum saturated, any emulsifiers which might be present in the pore network are already washed away. During these tests, no notable moisture absorption occurred which means that there cannot be a liquid flow path in the sample. Liquid transport in these samples is hence eliminated.

It should be mentioned that all previous experiments are performed on fully hydrophobised materials. The literature review in Chapter 2 has shown that the hydrophobisation application causes the existence of a fully hydrophobised zone near the outside surface and a partially hydrophobised zone deeper into the material. The conclusions in this section are therefore only applicable to this fully hydrophobised zone. The investigation of the partially hydrophobised zone, both in terms of its penetration depth and hygric properties, still requires a future in-depth study.

B.7 Summary

This section focuses on the hygric property determination of sintered glass and ceramic brick, hydrophobised with three different water repellent agents, using a mixture of existing and newly developed experimental techniques. The moisture retention curve is measured using the steady state centrifuge experiment, developed and validated in Subchapter A. These experiments shows that hydrophobised materials expel moisture under the influence of smaller absolute capillary pressures due to the interaction of moisture with the hydrophobised pore surfaces. This results in a displacement of the curves towards smaller absolute capillary pressures, which is more pronounced for water repellent agents that display a higher degree of hydrophobicity (i.e. larger contact angles).

Next, the vapour diffusion resistance factors are measured using the well-known cup tests. These experiments show slightly elevated vapour diffusion resistance factors which are less dependent on the relative humidity. Overall, this agrees with already existing literature. These cup tests were slightly adapted to quantify the liquid permeability in the hydrophobised materials by allowing direct water contact inside the cup and measuring the moisture flow rate through the sample. This rate is compared to the theoretically calculated vapour flow rate which only takes into account vapour flow through the sample. While the materials, hydrophobised with agent B, show only a vapour flow through the sample, the materials, hydrophobised with agent A, show periods in which both vapour and liquid transport is combined. Liquid water is stored in these materials which temporarily induces a liquid flow. Once the stored moisture is evaporated, however, moisture flow is solely governed by vapour flow once more. This temporary storage of moisture is possibly attributed to the presence of emulsifiers in the water repellent agent which hinder the water repellent effect. The evaporation of this stored moisture washes away these emulsifiers, however, and further increases the water-repellency. In normal working circumstances, it can therefore be concluded that hydrophobised materials only transport moisture through vapour flow.

Chapter 5

Investigation of the microscopic moisture behaviour

This chapter investigates the microscopic moisture behaviour in hydrophilic and hydrophobised porous materials. The main aim of this chapter is to acquire sufficient information to adapt the existing hydrophilically-oriented pore network model for hygric property determination of hydrophobised materials. Two experimental techniques are used to examine this microscopic moisture behaviour: X-ray Computed Tomography (XCT) imaging and Nuclear Magnetic Resonance (NMR) relaxometry. As explained in Chapter 2, the spatial resolution limits on XCT imaging prohibit visualising pore networks of common building materials (e.g. ceramic brick). To this aim, NMR relaxometry, capable of characterising water in pore bodies and throats of both micro- and nanometer scale [43,150], is investigated as a possible solution for this problem. Since NMR relaxometry is relatively unknown, however, validating this experimental technique is necessary. Subchapter A therefore uses both experimental techniques to investigate the microscopic moisture behaviour in hydrophilic sintered glass. In doing so, XCT imaging and NMR relaxometry are compared and their capabilities and shortcomings are identified. Subsequently, Subchapter B studies the moisture behaviour in the hydrophobised materials using the most suitable method(s). Its conclusions will serve as input for the adaptation of the hydrophilically-oriented pore network model toward the hygric property determination of hydrophobised porous materials in Chapter 6.

Subchapter A is based on papers 5.1 and 5.2 and Subchapter B is based on paper 5.3, all stipulated below. Parts of the text are adopted directly from these works, while others are rewritten to clarify their contribution to the research objectives of this thesis.

Paper 5.1: D. Deckers, H. Janssen. Microscopic validation of a pore network model for hygric properties of porous materials. Transp. Porous Media, 151: 119–140, 2024. doi: 10.1007/s11242-023-02035-y

Paper 5.2: D. Deckers, H. Janssen. Microscopic Moisture Localisation in Unsaturated Materials Using Nuclear Magnetic Resonance Relaxometry. J. Build. Physics, 2024. doi: 10.1177/17442591231219931

Paper 5.3: D. Deckers, Y. Zhu, E. Koos, H. Janssen. Microscopic localisation of hydrophilically oriented pore bodies and throats in hydrophobised porous materials. Transp. Porous Media, 151: 773–793, 2024. doi: 10.1007/s11242-024-02069-w

A Microscopic moisture behaviour in hydrophilic porous materials

A.1 Introduction

The detection of moisture in construction materials has always been a strongly researched topic, due to moisture's potentially damaging influence on building structures. Most experimental techniques focus on measuring macroscopic moisture contents in samples though, and do not readily target the microscopic distribution of moisture in the material's individual pores. Such information can however be valuable to better understand pore-scale (and hence also material-scale) moisture storage and transport processes. In the research area of hydrophobisation, for example, materials are rendered hydrophobic to reduce rain water absorption. Multiple studies have shown, however, that some water repellent agents restrict the water uptake more strongly than others [5], and this is often allocated to the different interaction between water repellent agent and material pore structure [8,30,32]. Understanding which pores can still store and transport moisture after application of the water repellent agent will therefore help to better understand how the different agents penetrate and influence the materials' pore network. This information is moreover required to adapt the hydrophilically-oriented pore network model in Chapter 6.

When studying the microscopic moisture behaviour in porous building materials, one of the main problems is that these materials typically comprise a multitude of pores at different spatial scales [75,151] which all contribute significantly to moisture storage and transport [94]. Popular experimental techniques like XCT imaging are not capable of visualising these types of networks, let alone the moisture stored in them, due to limits on their spatial resolution. Knowing this, NMR relaxometry becomes an interesting option. This is a non-destructive experimental technique which measures the relaxation of hydrogen nuclei excited by external magnetic fields. Since this relaxation is mainly governed by the interaction between the hydrogen nuclei and the pore walls, the measured signal can be transformed into a size distribution of the various water islands inside a material [152,153], both in capillary filled pores or in absorbed pore corners. This technique is theoretically capable of measuring the signal generated by hydrogen nuclei in both micrometer (1-1000 µm) and nanometer (1-1000 nm) scale pores [43,150].

NMR relaxometry has shown to provide valuable insights in several applications where moisture plays an important role, such as petroleum research [154], building preservation [42,155], mortar hydration [150,156] and many more. In porous building materials, the focus typically lies on fully saturated materials and the investigation of the pore structure of these materials [157] or on the determination of saturation profiles (and hence overall moisture contents) in unsaturated materials [158–160]. Studies on unsaturated samples with the aim of locating which pores contain moisture and how moisture is stored in these elements is still largely missing. Munsch et al. [161] is a scarce example investigating the microscopic distribution of water in screed (preconditioned to different saturation states) and observing the presence of water in capillary filled pores as well as in pore corners. A validation of the results with other experimental techniques, however, is not provided. This subchapter therefore uses NMR relaxometry on unsaturated porous materials with the aim of locating the water islands stored in capillary filled pores and absorbed pore corners. This is done by transforming the recorded magnetic signals into water island size distributions which represent the size of water islands both in these capillary filled pores and absorbed pore corners.

The main aim of this section is to assess the applicability of NMR relaxometry to investigate the microscopic moisture behaviour in unsaturated porous materials. To do so, results obtained from the NMR measurements are compared to information extracted from XCT imaging. Experiments are therefore all performed on the hydrophilic ROBU P100 sintered glass filter whose pore network can completely be visualised with XCT imaging. By comparing results from NMR relaxometry with results derived from XCT imaging, it is possible to discuss both its capabilities and limitations. A successful validation of the NMR technique allows extending the NMR relaxometry to Vandersanden ceramic

brick, consisting of nano- and micrometer scale pore bodies and throats [75]. In this case, NMR relaxometry also becomes interesting to investigate the moisture behaviour in both hydrophobised sintered glass as well as hydrophobised ceramic brick in Subchapter B.
This subchapter starts with an explanation of the physical principles behind NMR relaxometry and the extraction of the water island size distributions from the recorded magnetic signals in Section A.2. Next, the materials and methodology used in this subchapter are explained in more detail in Section A.3. Subsequently, Section A.4 describes and compares the results from NMR relaxometry and XCT images. Finally, the applicability of NMR relaxometry to investigate the moisture behaviour in unsaturated porous materials is discussed and the most important conclusions are reiterated in Sections A.5 and A.6, respectively. Based on these conclusions, the suitable techniques are used to investigate the microscopic moisture behaviour in hydrophobised materials in Subchapter B.

A.2 Theory of nuclear magnetic resonance experiments

This section focuses on the physical principles of NMR relaxometry. The explanation is simplified and only contains the information necessary for this application. For a more in-depth explanation of NMR testing, the reader is referred to the literature [152,153,162].

A.2.1 Physical principles

When a nucleus with an odd number of protons (^{1}H nucleus in this study) is placed in an environment containing a static magnetic field (B_0), the nuclear spin precesses around this magnetic field. The net magnetization vector $\overrightarrow{M}(t)$ [dB] of the material is determined by summing up the individual nuclear moments of all ^{1}H nuclei in the tested sample. During an NMR experiment, this magnetization vector is manipulated by applying two separate magnetic fields. A constant magnetic field (B_0) and a time varying magnetic field which typically consists of short magnetic pulses. In the absence of the magnetic pulses, the magnetization vector is oriented parallel to the static magnetic field. The individual pulses cause the net magnetization vector to rotate away from this parallel direction over an angle β. Once the pulse is removed, the magnetization vector returns to its original state. The rate at which the magnetization returns back to its original state is governed by the transverse relaxation time T_2 [s]. For one idealised (cylindrical) pore, the change of the magnetization vector over time is described as follows

$$\overrightarrow{M}(t) = M_0 * \sin\beta * \exp(-t/T_2) \tag{5.1}$$

with M_0 [dB] the initial magnetic amplitude and β [°] the angle over which the magnetization vector is initially rotated. A more detailed explanation of these basic principles can be found in [152], amongst others. The transverse relaxation time represents the time constant of the rate at which the magnetic signal declines. It therefore depends on how energy is transferred from the ^{1}H nuclei to their surroundings. Research has shown that there are three different ways of transferring energy [153,163], which all contribute to the overall transverse relaxation time

$$\frac{1}{T_2} = \frac{1}{T_{2,bulk}} + \frac{1}{T_{2,surface}} + \frac{1}{T_{2,diffusion}} \tag{5.2}$$

The bulk relaxation time ($T_{2,bulk}$ [s]) results from the molecular interaction amongst hydrogen nuclei. It is often measured in a container large enough to ignore the interaction with the container edges. For water, a bulk relaxation time of three seconds is a good estimation [153]. The surface relaxation ($T_{2,surface}$ [s]) reflects the molecular interaction between the hydrogen nuclei and the pore surfaces. This term can be calculated with [163,164]

$$\frac{1}{T_{2,surface}} = \rho_2 * \left(\frac{S}{V}\right) = \rho_2 * \left(\frac{c}{r}\right) \tag{5.3}$$

where S/V [1/m] represents the surface-to-volume ratio of the pore. Under the assumption of idealised pores, this term can be simplified to c/r, where r [m] is the pore radius and c [-] is the shape factor equal to 1, 2 or 3 for planar, cylindrical or spherical pores, respectively [164]. ρ_2 [m/s] is the surface relaxivity of the material. This is a factor reflecting the strength of the relaxation due to the interaction at the fluid-solid interface. A more elaborate explanation of this factor can be found further in this subchapter.

Finally, the diffusion-induced relaxation time ($T_{2,diffusion}$ [s]) is caused by internal magnetic field gradients which cause protons to dephase because they move into an area where the magnetic field is slightly different [153]. The factors contributing to the non-uniformity of the magnetic field across a sample are outlined in the literature [152,153,165]. The most important one in this study is the presence of magnetic impurities (e.g. iron oxides [166]). When large amounts of these impurities are present, the diffusion-induced relaxation time dominates the total transverse relaxation time. This factor is estimated via

$$\frac{1}{T_{2,diffusion}} = \frac{D(\gamma * g * TE)^2}{12} \tag{5.4}$$

with D [m^2/s] the molecular diffusion coefficient of water (equal to 2500 μm^2/s at 30 °C [167]), g [G/m] the magnetic field strength gradient and TE [s] the inter-echo spacing. The latter is a factor inherent to the NMR measuring

sequence and it is explained further in the chapter. Combining all these factors, the total transverse relaxation time can be written as

$$\frac{1}{T_2} = \frac{1}{T_{2,bulk}} + \rho_2 * \left(\frac{c}{r}\right) + \frac{D(\gamma * g * t_e)^2}{12} \tag{5.5}$$

The equation relates the total transverse relaxation time to the geometry of the water-filled pores (c/r). Typically, it is simplified with the help of three assumptions [168]. Firstly, it is assumed that the measurements are made in the fast-diffusion regime, which means that the dimensions of the pores are small enough for the protons to come into contact with the pore surface multiple times before returning to their original state. This causes the relaxation at the fluid-surface interface to be more impactful than the bulk relaxation of the water. The latter then becomes negligible. This fast-diffusion regime is assumed to be valid when this condition is satisfied [167]

$$\kappa = \rho_2 * \frac{a}{D} = \rho_2 * \frac{r}{3 * D} \ll 1 \tag{5.6}$$

In this equation, a [m] is the mean distance a proton needs to travel before reaching the pore surface. In a spherical pore, this distance is often assumed to be equal to the radius of the spherical pore (r) divided by three [167]. The material used in this PhD has pores with radii ranging between 5 µm and 75 µm and an average surface relaxivity of 11.4 µm/s (see Section A.4.2). This means that 95 % of the pores has a κ smaller than 0.1 which is assumed to be in the fast-diffusion regime [169]. The slightly higher κ of 0.11 for the largest pores of sintered glass is also assumed to remain sufficiently small to maintain the fast-diffusion regime.

The second assumption handles the connectivity of different pores. The pioneering work of Brownstein and Tarr [163] that led to Equation 5.5, is based on isolated (cylindrical) pores. The analysis of the results is therefore only truly correct when pores are not (or weakly) connected to each other. The second assumption is therefore that of weak diffusional coupling. This is only valid if the protons remain within the same pore during the timeframe of the NMR measurement [168]. If not, Ghomeshi et al. [170] have shown that a strong coupling between pores causes a cluster of well-connected pores to be interpreted as one large element. The discussion section elaborates on the applicability of weak diffusional coupling in this PhD.

The third assumption can be allocated to the diffusion-induced relaxation rate caused by internal magnetic field gradients. Initially, it is assumed that this term has a limited influence on the measured transverse relaxation time. This results in a homogeneous magnetic field across the material, something which is typically found in materials with a low percentage of paramagnetic impurities. The purity of the sintered glass, used in this PhD, renders this assumption valid as discussed further in Sections A.3.1 and A.4.2. Taking into account these three

assumptions, Equation 5.5 is simplified to Equation 5.7 and a direct relationship between the relaxation time in a pore and the pore size is established

$$\frac{1}{T_2} = \rho_2 * \left(\frac{S}{V}\right) = \rho_2 * \left(\frac{c}{r}\right) \tag{5.7}$$

It is known from Equation 5.1 that the magnetic signal in every pore decays mono-exponentially with a rate governed by this transverse relaxation time. In a material with multiple pores hence, the measured magnetic signal decays multi-exponentially. Equation 5.1 should thus be transformed into Equation 5.8 where $T_{2,k}$ represents the pore dependent relaxation times belonging to the k different pores

$$M(t) = M_0 * \sum_k \exp\left(-\frac{t}{T_{2,k}}\right) \tag{5.8}$$

To measure the magnetic signal, commonly the Carr-Purcell-Meiboom-Gill measuring sequence (CPMG) is used [171]. This sequence consists of a constant magnetic field and a predefined number of pulses. The amplitude of the magnetic signal can be measured after every pulse and hence the amount of pulses (N) and the time between pulses determine the length of the measured signal. This should be sufficiently long to measure the full magnetic decay. The sequence of N pulses is repeated for a predefined number of times and every recorded decay signal is called a scan. The final magnetic signal is the average of these different scans and the amount of scans governs the signal-to-noise ratio (SNR). The three experimental parameters (the inter-echo time, the number of echoes and the number of scans) are further investigated in Section A.4.2. For more information about the CPMG sequence, the reader is referred to the literature [152,153,162].

After measuring the magnetic signal, it is transformed into a transverse relaxation time distribution. This represents the distribution of pore dependent relaxation times throughout the pore network. The algorithms developed for this purpose are shown in the next section. Using Equation 5.7, the relaxation time distributions can subsequently be transformed into pore size distributions if the surface relaxivity ρ_2 is known. This surface relaxivity reflects the strength of relaxation caused by the interaction between fluid and pore surface. Even though it is often assumed to be a constant value within one material, in reality the surface relaxivity varies on a pore to pore basis due to the influence of several pore-dependent factors [168,172]. One significant pore dependent factor, for example, is the mineralogy inside the pores. A surplus of paramagnetic species in a certain pore results in higher relaxivity factors due to more significant interactions between water protons and pore walls. For the application in this report, it is assumed that the surface relaxivity is constant for all pores. In practice it is typically calculated by fitting the measured relaxation time

distribution of a saturated sample to its pore size distribution determined via either MIP or XCT imaging.

A.2.2 Inversion of the measured magnetic decay signal

The previous section has shown that the relaxation times are directly linked to the distances these protons need to travel before they can interact with the pore walls. In a capillary filled pore body or throat, the relaxation times can hence be linked to the pore radius. Therefore, when the material is fully saturated, the pore size distribution is extracted from the calculated transverse relaxation time distribution. For a water island in an element corner, however, not the pore radius, but the water island radius is linked to these relaxation times. Therefore, in unsaturated materials, where both capillary filled elements and water islands in element corners coexist, the transverse relaxation times are transformed into water island size distributions, which contain both the water islands in filled elements and in pore corners. Determining these water island size distributions from XCT images and NMR measurements is the main goal of this section.
The goal of the post-processing software of NMR measurements is to first determine the relaxation time distribution from the measured magnetic signal, as illustrated by Figure 5.1, after which it can be transformed into the water island size distribution. This section first explains the theory behind the inverse determination of this transverse relaxation time distribution from the measured magnetic decay. Next, the developed inversion programs are validated with the help of artificially created NMR signals and the programs' capabilities and limitations are highlighted.

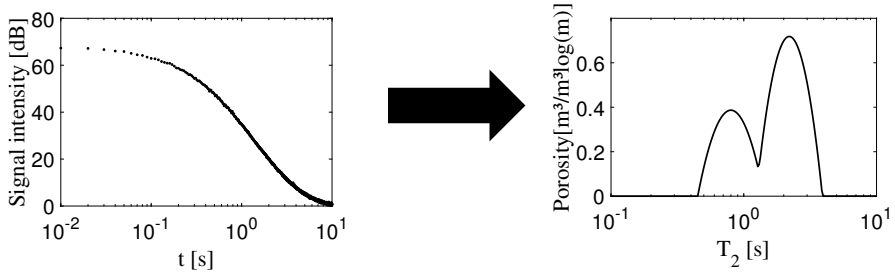


Figure 5.1: Example of the transformation from the measured magnetic signal to the transverse relaxation time distribution.

Regularization theory. The goal of the inversion program is to extract the distribution of T_2 values from the measured magnetic signal using Equation 5.8. Since every pore is characterised by its pore-dependent $T_{2,k}$ this translates to a set of equations with k unknowns. Porous materials can consist of thousands or more pores and hence solving problems with that many unknowns is not feasible. Therefore, M predefined T_2 values are chosen for which the set of equations will be solved. This results in the following problem to be addressed

$$M(t_j) = \sum_{i=1}^{M} f_i * \exp\left(-\frac{t_j}{T_{2,i}}\right) = A * f \qquad j = 1, 2, ..., N \tag{5.9}$$

$$A = \begin{bmatrix} \exp\left(-\frac{t_1}{T_{2,1}}\right) & ... & \exp\left(-\frac{t_1}{T_{2,M}}\right) \\ ... & ... & ... \\ \exp\left(-\frac{t_N}{T_{2,1}}\right) & ... & \exp\left(-\frac{t_N}{T_{2,M}}\right) \end{bmatrix} \tag{5.10}$$

$$f = [f_1\ f_2\ f_3\ ...\ f_M]^T \tag{5.11}$$

with $M(t_j)$ [dB] the measured magnetic amplitudes at N different times t_j, $T_{2,i}$ [s] the M predefined transverse relaxation times and f_i [-] the weights belonging to these predefined $T_{2,i}$. The latter are the unknowns in this equation. Solving this system of equations requires calculating the inverse of the kernel matrix A. It is widely known that this is an ill-posed problem, meaning that the solution is significantly influenced by measurement errors [173,174]. Since these errors cannot be completely avoided, there is no exact solution to the problem and an infinite number of solutions with the same degree of accuracy exist [173,174]. Such a problem is known as an inverse Laplace transform (ILT) and it occurs in various areas of research. In literature, a wide variety of methods is developed to solve such ill-posed problems. For a complete review, the reader is referred to [174,175], amongst others. In this PhD, three inversion algorithms, all based on regularization theory, are used. In regularization theory, the following objective function is minimised

$$\min\left(\|A * f - M\|_2^2 + \alpha * \|\text{Regularization term}\|_2^2\right) \tag{5.12}$$

in which α [-] is the regularization parameter. The first part of this equation contains the residual norm which represents the goodness-of-fit between the calculated signal (A*f) and the measured signal (M). The second part contains the regularization term which renders the solution less susceptible to noise. An optimal choice of α is required to provide a solution which on the one hand resembles the "true" solution and on the other hand is not affected too much by

measurement noise, and is discussed further below. The regularization term can take different forms depending on the type of regularization used. In this PhD, Tikhonov regularization [173], the maximum entropy method [176–178] and the CONTIN program [173] are used as inversion methods. Tikhonov regularization and the maximum entropy method minimise the objective functions in Equations 5.13 and 5.14, respectively

$$\min\left(\|A * f - M\|_2^2 + \alpha * \|f\|_2^2\right) \tag{5.13}$$

$$\min\left(\|A * f - M\|_2^2 + \alpha * \sum_i f_i * \ln(p_i * f_i)\right) \tag{5.14}$$

where p_i [-] is a weighted vector, with all its elements equal to exp(-1) * 1000. This vector is added to amplify the influence of the short relaxation times to the residual norm and hereby remove possible high tilted tails at these small relaxation times [178]. While both regularization terms are different, their aim remains to suppress the influence of noise on the calculated relaxation time distribution. Studies comparing both techniques have shown that Tikhonov regularization has the tendency to oversmooth the solution [178,179] while the maximum entropy principle can result in unnecessarily narrow peaks [180]. Since all techniques have their advantages and disadvantages, using multiple inversion algorithms is required to nuance results. These two inversion algorithms are coded in MATLAB.

The third inversion technique, based on the CONTIN method, is developed by Bruker who supplied the NMR apparatus used in this study. This method is a popular inversion tool based on Tikhonov regularization [173]. Since the source code is unavailable and the determination of influential calculation parameters (e.g. the regularization parameter as explained in the next paragraphs) can therefore not be checked, solely using this inversion algorithm is not possible. Because it is a professionally developed code, however, it can benefit the analysis by eliminating doubts introduced by potentially faulty coding in the other inversion algorithms.

An important aspect of the regularization methods is the choice of the optimal regularization parameter (α). A large α renders the regularization term more important, which means that it favors the rigidity of the solution at the expense of an increase in the residual norm. A small α reduces the misfit between measured and estimated signal while making the solution more susceptible to the measurement noise. The parameter hence depends on the amount of noise in the measured signal. Noisy signals will require larger regularization parameters to prevent the solutions being dominated by this noise.

Different methods exist in literature for the choice of the optimal regularization parameter. There is no single best method since all have their advantages

and disadvantages. In this PhD, only the S-curve technique is used. For other existing methods, the reader is referred to the extensive literature on the subject [181]. In the S-curve technique, the logarithm of the residual norm ($\xi = \|\mathrm{A} * \mathrm{f} - \mathrm{M}\|_2^2$) is plotted against the logarithm of the regularization parameter as shown in Figure 5.2. The optimal regularization parameter is chosen as the biggest α that satisfies

$$\frac{\mathrm{dlog}(\xi)}{\mathrm{dlog}(\alpha)} < \mathrm{tol} \tag{5.15}$$

where $0 < \mathrm{tol} < 1$ [175,178]. In other words, the optimal regularization parameter is located on the S-curve just before the residual norm significantly increases. This technique does require calculating the solution for different values of α before the optimal parameter can be chosen. This can increase the computation time if the initial values are badly chosen.

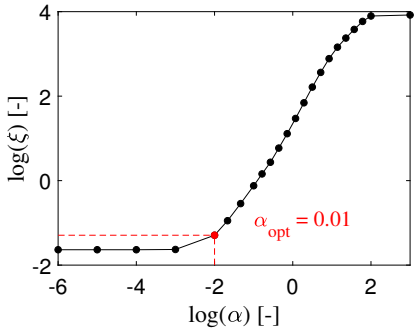


Figure 5.2: Illustration of the S-curve method.

Validation of the inversion methods. As explained before, the ill-posed inversion problem used to calculate the relaxation time distribution is a widely known problem without an optimal solution. Therefore, three different inversion algorithms are used in this PhD, all with their advantages and disadvantages. Before they are used to post-process measured magnetic signals, a validation of the three algorithms is performed. In this thesis, this is done by generating transverse relaxation time distributions of different shapes, transforming them into 'measured' magnetic decay signals using Equation 5.9, adding different levels of noise to this 'measured' signal and then using the inversion algorithms to once again calculate the transverse relaxation time distribution. The workflow, illustrated in Figure 5.3, is often used in literature to assess the performance of such inversion algorithms [178,180]. The noise added to the signals is Gaussian noise with a SNR of 0.1 dB, 10 dB or 30 dB. The fictive transverse relaxation

time distributions are divided into unimodal or bimodal distributions to account for a wide array of shapes.

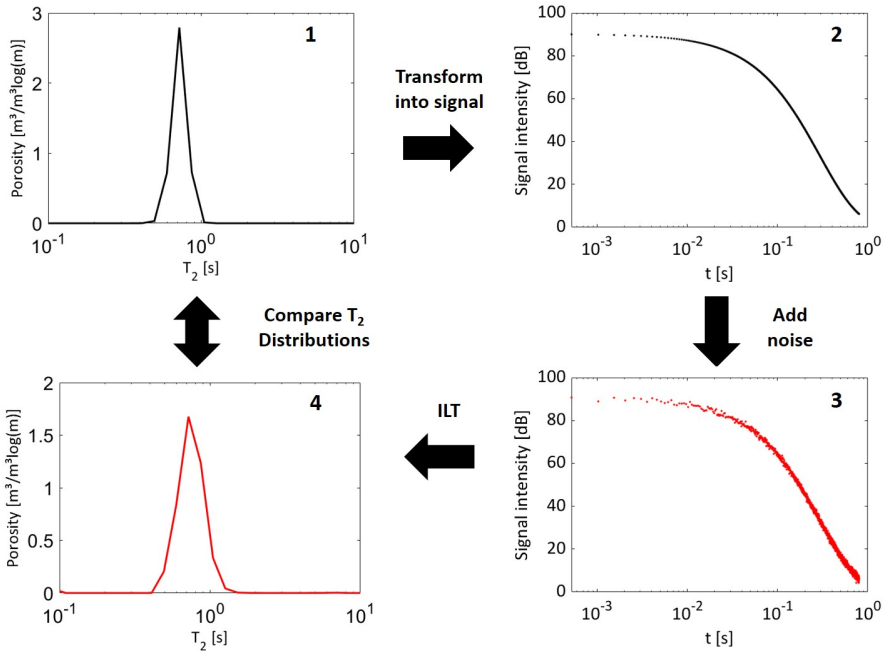
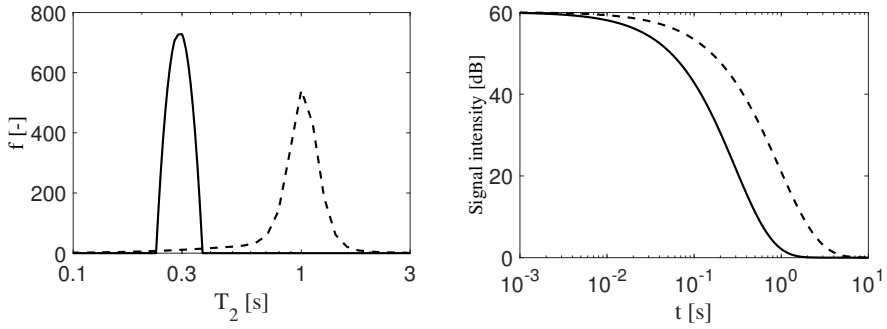


Figure 5.3: Workflow of the validation of the models developed to calculate the ILT.

Figure 5.4 shows the unimodal transverse relaxation time distributions and the magnetic signals derived from these distributions. There is a symmetric distribution and a distribution with a long tail towards smaller T_2 values. They are both modeled after initial measurements of transverse relaxation time distributions acquired from two types of sintered glass. One of these glass types (ROBU sintered glass type P100) is used in the experimental part of this subchapter and described in detail in the materials section A.3.1 while the other one is used as a test material for the NMR apparatus and will not be further discussed. All following distributions are scaled to make sure the area under the curve equals 100 %. As a result, the peak values slightly differ.



(a) (b)

Figure 5.4: The T_2 distribution (a) and the magnetic decay signal without noise (b) for the unimodal distributions.

Figure 5.5 shows the T_2 distributions calculated with the Tikhonov (a), maximum entropy (b) and CONTIN methods (c) for the signals of the unimodal distributions with SNR's of 0.1 dB, 10 dB and 30 dB together with the original distribution. It is evident that increasing the SNR allows the solutions to better approximate the original distribution. The non-symmetrical distribution with the long tail at small relaxation times, however, proves a lot more difficult to reproduce even for high SNR's. None of the inversion algorithms are able to replicate it well. Only the position of the peak is accurate, the rest of the distribution is approximated. This is important to keep in mind when analysing results from the experiments in following sections. Out of all the inversion methods, a visual assessment of the results shows that the CONTIN algorithm performs best, although the differences are minimal.

After the unimodal distributions, some bimodal distributions are simulated. Figure 5.6 shows both the transverse relaxation time distributions as well as the magnetic decay signals without added noise. One of the bimodal distributions has two separated peaks with an equal peak magnitude while the other distribution exists of two connected peaks with a magnitude ratio of 35/65 %. The other combinations (two separated peaks with a peak magnitude ratio of 35/65 % and two connected peaks with equal peak magnitudes) are also investigated, but they resulted in the same conclusions as given here. They are therefore omitted from the discussion.

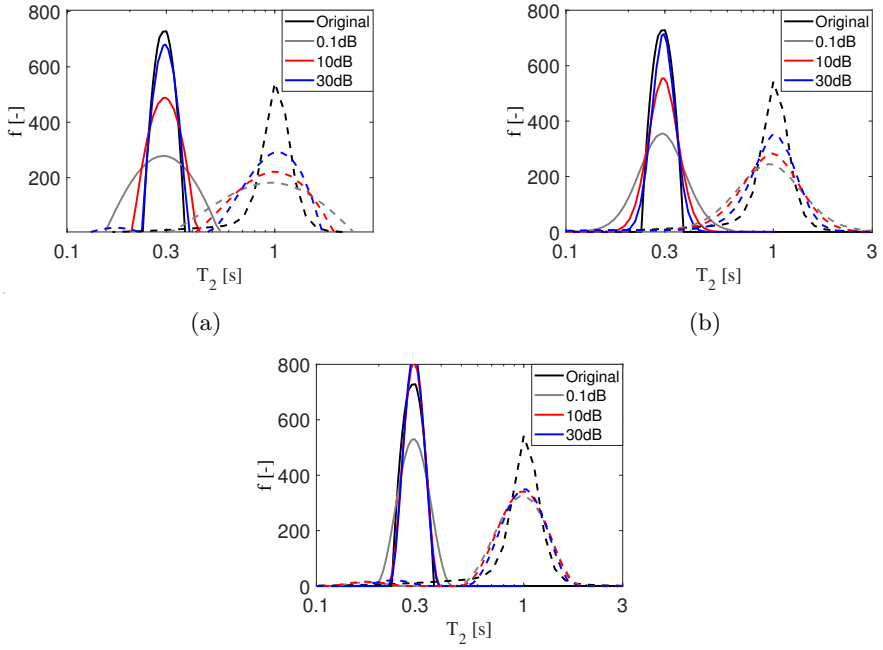


Figure 5.5: The T_2 distributions calculated with the Tikhonov (a) maximum entropy (b) and CONTIN methods (c) for the signals of the unimodal distributions with SNR's of 0.1 dB, 10 dB and 30 dB.

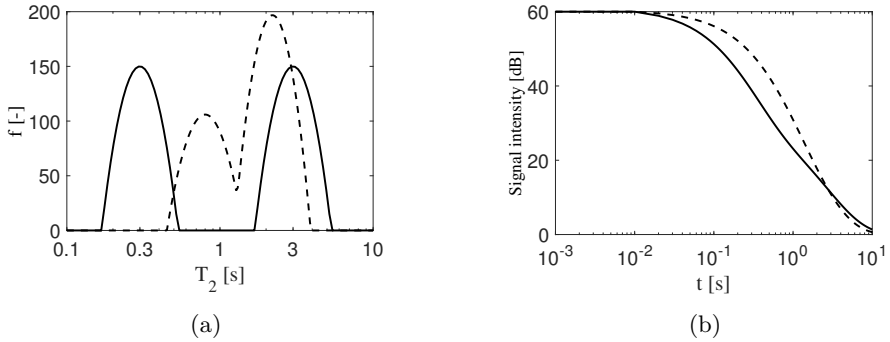


Figure 5.6: The T_2 distribution (a) and the magnetic decay signal without noise (b) for the bimodal distributions.

The T_2 distributions calculated with the Tikhonov, maximum entropy and CONTIN methods for the bimodal distribution with connected peaks are shown in Figure 5.7. The results for the separated peaks can be found in appendix 5.A.1 since they show the same behaviour. The most important conclusion is that an insufficient SNR causes the bimodal distributions to transform into a unimodal distribution regardless of which inversion method is used. Higher SNR's do however allow capturing the bimodal behaviour, which stresses the need for signals with minimal noise levels. Out of all three methods, the CONTIN algorithm provides the best results once more. Unfortunately, its source code is not available. Only the M amount of T_2 values, for which the algorithm performs the calculation, need to be predetermined. The algorithm subsequently returns the calculated solution and does not comment on the used regularization value (α). Therefore, the degree of regularization cannot be estimated. Since not all details are known about the calculation of the distribution, this algorithm cannot be used solely in this study. Further post-processing of experimentally determined magnetic signals is therefore done with all three inversion methods.

A.3 Materials and methods

A.3.1 Material

The experiments in this subchapter are performed on a P100 sintered glass filter from ROBU [55] with density and porosity of $1414 \pm 15 \text{kg/m}^3$ and $36.5 \pm 0.7\%$ respectively, and with pore radii ranging from 5 µm to 75 µm. As explained in the introduction of this section as well as in Chapter 2, this material is used here since its pore network can be completely visualised using XCT images with a spatial resolution of 2.5 µm. These XCT outcomes are used in following sections to possibly validate the results obtained via NMR.
The sintered glass is typically used as a filter material and hence a high degree of purity is provided. This is required for the NMR measurements since the presence of paramagnetic impurities (e.g. iron oxides or aluminum oxides [166]) distorts the relaxation time distributions as shown by Equation 5.4. Technical information provided by ROBU [55] shows less than 2.5 % of these impurities in the sintered glass. They will therefore have a limited effect on the NMR measurements. Further proof is provided in Section A.4.2.

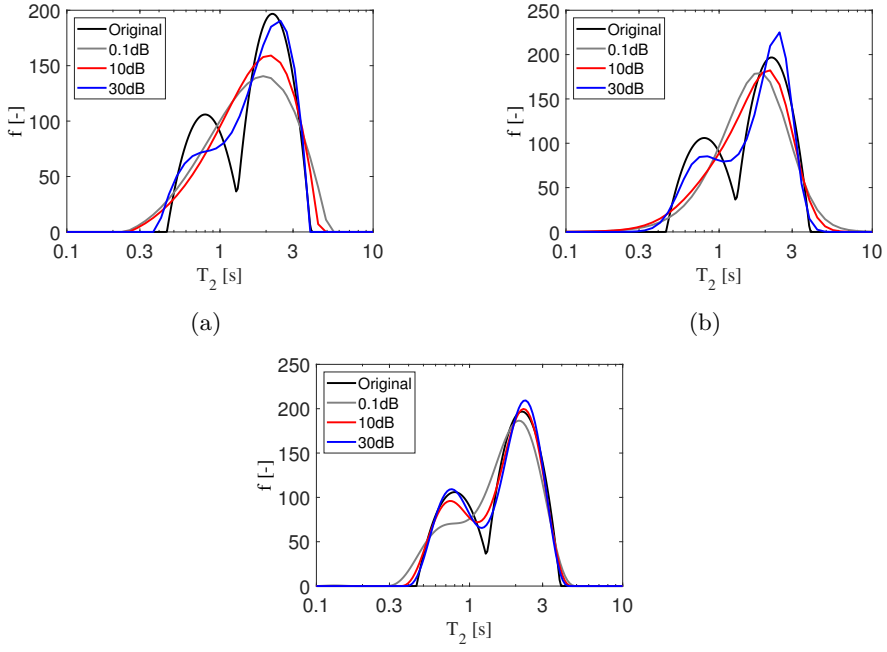


Figure 5.7: The T_2 distributions calculated with the Tikhonov (a) maximum entropy (b) and CONTIN methods (c) for the signals of the bimodal distributions with connected peaks with SNR's of 0.1 dB, 10 dB and 30 dB .

A.3.2 Methodology

The NMR experiments in this subchapter are performed on both saturated and unsaturated samples, and their results are compared to information acquired from XCT imaging. It is important to keep in mind that the magnetic signals, measured during NMR measurements, stem from the excitation of hydrogen nuclei. Air-filled pores will therefore not contribute to the signal. This means that the transverse relaxation time distributions are solely related to the water islands in the pores. Since all pores are filled with water in saturated materials, the distributions obtained from these samples represent the material's pore size distribution.

In unsaturated materials, the interpretation of the distributions obtained from NMR experiments becomes more complex. In such unsaturated materials, water is typically found as water layers adsorbed to pore walls or as water islands in absorbed pore corners or capillary filled pores [23]. Examples of these storage

mechanisms are given in Figure 5.8. The magnetic signal measured in an NMR experiment is hence governed by the hydrogen nuclei stored in one of these three ways. The nuclei present in water films relax too quickly to measure with the NMR apparatus used in this study [182]. Also, the spatial resolution limits of the XCT apparatus make it impossible to visualise these films. Since they typically do not contribute much to moisture storage in sintered glass [23], their omission is justifiable. The transverse relaxation time distributions, inversely calculated from the measured magnetic signals, therefore represent the size of the water islands in capillary filled pores as well as in absorbed pore corners. Their radii are indicated on Figure 5.8. After transformation from the relaxation time domain to the pore radii domain using Equation 5.7, the distributions quantify the water island sizes and they are henceforth called the water island size distributions.

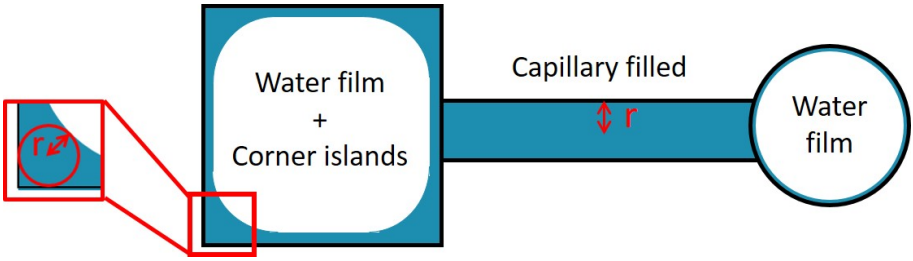


Figure 5.8: The three storage mechanisms occurring in porous materials with indication of the water island radii.

Water island size distributions are extracted from NMR relaxometry and XCT imaging on two unsaturated samples with gravimetrically determined moisture contents of 65 kg/m³ and 135 kg/m³. The main aim of this subchapter is to assess whether the NMR technique is applicable for the investigation of the moisture behaviour in unsaturated porous materials. This is examined by comparing the extracted water island size distributions with distributions obtained from XCT imaging. To this aim, the samples are moved from the NMR apparatus to the XCT device to acquire the images. However, more samples are subjected to XCT imaging to gain insight about moisture storage over the entire saturation range. The following sections describe the preconditioning process and the extraction of the water island size distributions from both NMR measurements and XCT imaging.

Sample preconditioning. The samples are each preconditioned to a different moisture content with the help of the centrifuge, designed in Chapter 4. The three samples from which the XCT images are acquired, are preconditioned to 18 %, 37 % and 63 % of the material's saturated moisture content as determined by weight measurements. This equals 65 kg/m^3, 135 kg/m^3 and 230 kg/m^3, respectively. The two samples with the lowest moisture content are subjected to both XCT imaging and NMR measurements, while the sample with the highest moisture content is only used in XCT imaging. It has to be noted that weight measurements indicate no moisture loss during transport from the NMR device to the XCT apparatus.

XCT imaging. The XCT images are acquired on the GE Nanotom S at KU Leuven's XCT Core Facility [183], where sample and detector are located 10 mm and 200 mm from the source, respectively. The electron beam is generated with a voltage and current of 80kV and 130 mA, and is focused on a diamond-tungsten target. This results in a voxel and focal spot size of 2.5 µm and 2.46 µm, respectively. The X-rays pass through a 0.1 mm thick aluminum filter to reduce beam hardening effects. A single scan, which takes 1.5 hours, results in a cubic volume of 1200^3 voxels (i.e. 3^3 mm^3) from approximately the middle of the sample. An example of a single slice of such a scan is shown in Figure 5.9. Distinguishing between water and air in the scans of the unsaturated samples proved difficult at first, and a proper segmentation of the images was therefore initially challenging. To enhance the contrast between water and air, deionized water is replaced by a 2%/98% KI/deionized water solution, which has been successfully used in previous studies [63,184,185]. This low concentration of KI results in a negligible change of the water/solid contact angle [186].
Segmentation of the acquired images is performed using the 3D trainable WEKA algorithm implemented by Arganda-Carreras et al. [187] in the ImageJ/FIJI program. This is a machine learning algorithm which requires training on a subset of a sample before applying it to the total volume. This training is a semi-supervised, iterative process of manually selecting voxel regions belonging to the three phases (air, water and glass) after which the algorithm trains itself, using certain selected image features, to correctly characterize these regions. This training process continues until the segmentation of the training set is deemed satisfactory after which the other XCT images are segmented using the trained algorithm. After segmentation, the images are visually assessed to ensure that the trained algorithm was successful. An example of a single slice before and after segmentation is shown in Figure 5.9. All images shown in the rest of this dissertation also adhere to the color code in this figure.

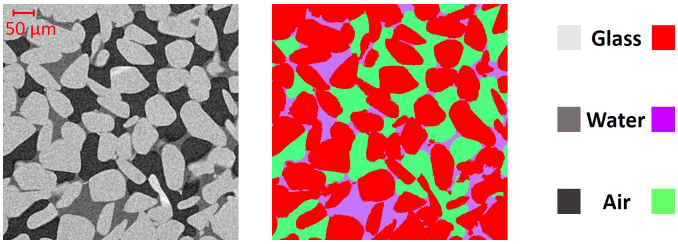


Figure 5.9: Example of an XCT image before and after segmentation using the 3D trainable WEKA algorithm.

Although the trainable WEKA algorithm successfully segments the images, it requires a lot of computer memory. This limits the size of the computational domain to a cube measuring 1.5^3 mm^3 (i.e. 600^3 voxels) for a computer with 128 GB of RAM memory. The volume acquired from the XCT scan, measuring 3^3 mm^3, is therefore divided into eight subvolumes of 1.5^3 mm^3. Both the water island size distributions as well as the moisture contents, acquired by counting the amount of water voxels in the segmented images, are calculated for all eight of these subvolumes. In order to investigate whether this subvolume size of 1.5^3 mm^3 is still representative of the material, progressively larger cube volumes are extracted from 4 sets of XCT images and the calculated porosities of these cube volumes in function of the cube side length are shown in Figure 5.10. The porosity evolves toward a constant value for cubic volumes of 1.25^3 mm^3 - 1.5^3 mm^3. Therefore, the subvolume size of 1.5^3 mm^3, which is the maximum volume that the trainable WEKA algorithm can segment on a computer with 128 GB of RAM memory, is on the limit of being a representative elementary volume with regards to the porosity.

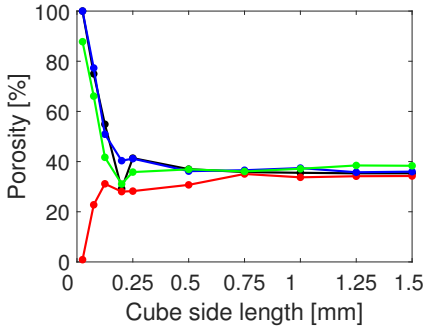


Figure 5.10: The porosity in function of the cube side length of four extracted subvolumes.

After segmentation, all image voxels are classified as glass, water or air voxels. The water phase is then easily isolated from the images by adjusting these images so that the glass and air voxels belong to the same phase (i.e. the glass matrix) and the water voxels belong to a different phase (i.e. the pore space). These images, are then used as input to the pore network extraction program PNextract, developed by Raeini et al. [97], to extract a network of the water phase (i.e. the pore space in the images). This algorithm uses a combination of a thinning algorithm, to compute the skeleton of the network, as well as a maximal ball algorithm to calculate the size of the elements, and it is an enhanced version of the well-known algorithm of Dong and Blunt [96]. The results, generated with PNextract, include topological (e.g. positions and connections) and geometrical (e.g. radii, volumes, shape factors) information about the water islands, since the pore space in the images only represent this water phase. Using all water islands' radii and volumes, which contain the liquid islands both in the capillary filled pores and in absorbed pore corners, displayed in Figure 5.8, the water island size distribution is composed. The same workflow is followed when the pore network needs to be extracted, rather than the water island network, by simply adjusting the XCT images to make sure both the water and air phases now constitute the (to be extracted) pore space, instead of solely the water phase.

NMR relaxometry. The extraction of transverse relaxation time distributions and pore size distributions from the measured magnetic signal has been explained in Section A.2, however, the most important steps and their application to sintered glass are reiterated here. First, using a CPMG sequence, the magnetic decay signal is measured on the Bruker Minispec MQ20 from the Materials and Constructions section of the KU Leuven [188]. Next, the relaxation time distribution is calculated using the three different inversion methods. As shown by the validation of these models, the highest SNR is preferred. Therefore, the highest possible SNR is obtained by recording the maximum number of scans allowed by the NMR apparatus (i.e. 256 scans) during every CPMG sequence. The optimal values of the other measurement parameters (i.e. the inter-echo time and the number of echoes) are determined in the results section.
After obtaining this transverse relaxation time distribution, Equation 5.16 is used to transform this into distributions of the pore size (saturated samples) or the water island size (unsaturated samples). To do so, the surface relaxivity (ρ_2) has to be known. This value is typically calculated by fitting a transverse relaxation time distribution of a fully saturated sample to its pore size distribution extracted from XCT images or MIP [153]. In this subchapter, transverse relaxation time distributions extracted from five saturated samples are fitted to the pore size distributions extracted from XCT images and this results in a ρ_2 equal to 11.4 ± 4.7 µm/s. When transforming the transverse relaxation time distribution

of an unsaturated sample into a water island size distribution, Equation 5.16 is once again used with a ρ_2 equal to 11.4 µm/s.

$$\frac{1}{T_2} = \rho_2 * \left(\frac{S}{V}\right) = \rho_2 * \left(\frac{2}{r}\right) \tag{5.16}$$

A.4 Results

In this section, the water island size distributions, obtained with both experimental techniques are discussed and compared. Section A.4.1 first shows the water island size distributions extracted from the acquired XCT images after which Section A.4.2 shows the water island size distributions obtained from NMR measurements on unsaturated samples. Finally, Section A.4.3 compares the water island size distributions extracted from XCT imaging and NMR relaxometry on unsaturated sintered glass samples to assess NMR relaxometry's capabilities and limitations.

A.4.1 Water island Size Distributions Measured with XCT

As explained in Section A.3.2, three sets of XCT images are acquired from three samples which are preconditioned with the centrifuge to gravimetrically determined moisture contents of 65 kg/m^3, 135 kg/m^3 and 230 kg/m^3. When the samples reach these equilibrium moisture contents in the centrifuge, they are transferred to the Nanotom S to acquire the XCT images. Figure 5.11 shows an example of such an image. The bottom of the sample is clearly more saturated since water expels from the bottom surface during centrifugation. To avoid edge effects, only the images in the red cube (measuring 3^3 mm^3) are extracted, segmented and post-processed as explained in the methodology. On the right hand side of Figure 5.11 the variation of the moisture content over the height of this extracted cube is shown for the three different samples as well as for a fully saturated sample. There is clearly a distinction between the rather uniform moisture profiles for samples with a low moisture content (i.e. 65 kg/m^3 and 135 kg/m^3) and samples with a high moisture content (i.e. 230 kg/m^3). The following discussion therefore distinguishes between these two categories. The sample with the higher moisture content will further be subdivided into the top and bottom of the sample as illustrated by the different colors in Figure 5.11. For the segmentation of the red cube in Figure 5.11, a further subdivision of this cube measuring 3^3 mm^3 into eight cubes of 1.5^3 mm^3 is necessary to account for the trainable WEKA algorithm's computational requirements. For the sample with the highest moisture content, this results in four subvolumes in the bottom 1.5 mm of the red cube in Figure 5.11 (with an overall higher moisture content) and four subvolumes in the top 1.5 mm (with an overall lower moisture content).

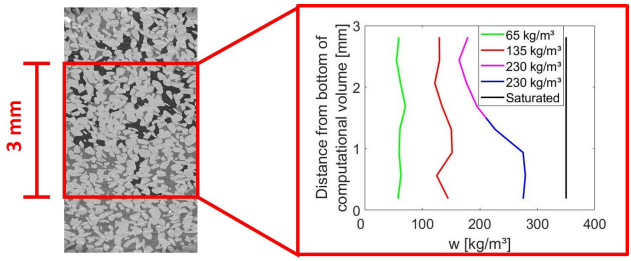


Figure 5.11: Variation of the moisture content over the height of the computational volume for the three samples preconditioned in the centrifuge.

Samples preconditioned to 65 kg/m^3 and 135 kg/m^3. Figure 5.12 shows the water island size distributions of samples with measured moisture contents of 65 kg/m^3 and 135 kg/m^3 and compares them with the pore size distribution of sintered glass. The line denotes the average distribution while the shaded area comprises the distributions of all eight subvolumes. The moisture contents, calculated by counting the water voxels after segmentation, are shown on Figure 5.12 as well. This moisture content is stable over the eight different subvolumes with the exception of subvolume four in the sample with a moisture content of 135 kg/m^3. Since this is the only outlier, it is omitted from further discussion. The stable moisture content over the different subvolumes agrees with the stable moisture content over the computational volume's height, as displayed in Figure 5.11.

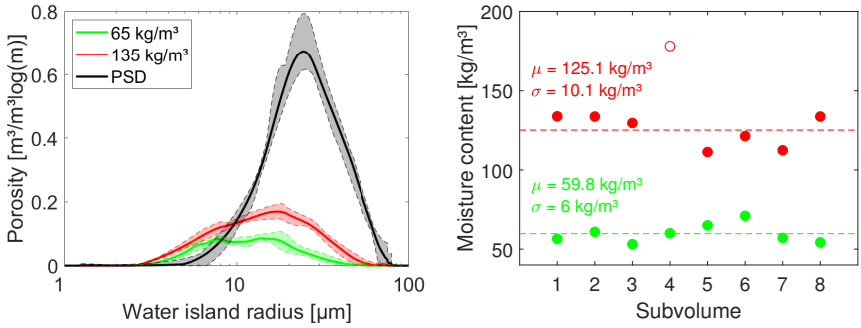


Figure 5.12: The water island size distributions and the moisture contents calculated for the subvolumes of the samples preconditioned to moisture contents of 65 kg/m^3 and 135 kg/m^3.

The moisture content derived from the XCT images is lower than calculated from gravimetric measurements (65 kg/m^3 and 135 kg/m^3) as shown on Figure

5.12, because of several reasons. Firstly, the XCT image represents the middle section of a cylindrical sample with a height of 10 mm and a diameter of 6 mm. During centrifuge drying, the sample desaturates towards its outlet surface (i.e. bottom surface in Figure 5.11) which results in a slight moisture gradient. The moisture content in the middle of the sample could therefore be lower than that from gravimetric measurements due to the higher saturation near the outlet surface of the sample. Secondly, gravimetric measurements before and after XCT imaging have indicated that a small amount of evaporation (i.e. maximum 5 kg/m^3) is possible during the XCT test.
Figure 5.12 shows the appearance of small water islands in the unsaturated samples, with radii approximately between 2 µm and 10 µm, that do not appear in the pore size distribution. When moisture is expelled from the sample and elements are drained, moisture remains absorbed in some of the pore corners. The (large) water islands in the capillary filled elements are hence replaced by smaller corner islands. This translates into a significant amount of small water islands, examples of which can be seen in figure 5.13. It should be mentioned, however, that image noise could have some impact on the smaller water islands near the image resolution of 2.5 µm. However, all images displayed in this dissertation are acquired, segmented and post-processed in the same way. Therefore, this impact of image noise should be similar in all extracted water island size distributions, which allows comparing them to each other.

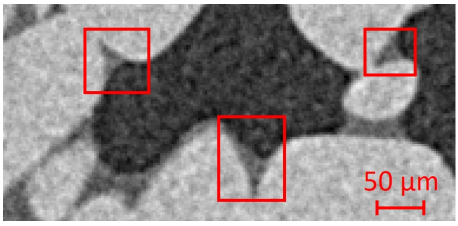


Figure 5.13: Examples of corner islands in unsaturated sintered glass samples.

Sample preconditioned to 230 kg/m^3. As shown in Figure 5.11, the moisture content across the top and bottom 1.5 mm of the computational volume differs significantly. This is caused by the presence of the drying front within this volume for a sample preconditioned to 230 kg/m^3, while it has already passed the computational volume of the samples preconditioned to 65 kg/m^3 and 135 kg/m^3. The results of the four top and four bottom subvolumes are therefore processed separately in the discussion below.
Figure 5.14 shows the water island size distributions and moisture contents of the four top and four bottom subvolumes of the sample with a gravimetric moisture content of 230 kg/m^3. Once again, the average distributions are

shown by the line while the shaded areas encompass all computed distributions. The average moisture content differs significantly between the top and bottom volumes and even within the top and bottom subvolumes there is a lot of variation as indicated by the large standard deviations calculated from the moisture contents. The presence of the smaller water islands are once again indicative of corner islands in emptied elements.

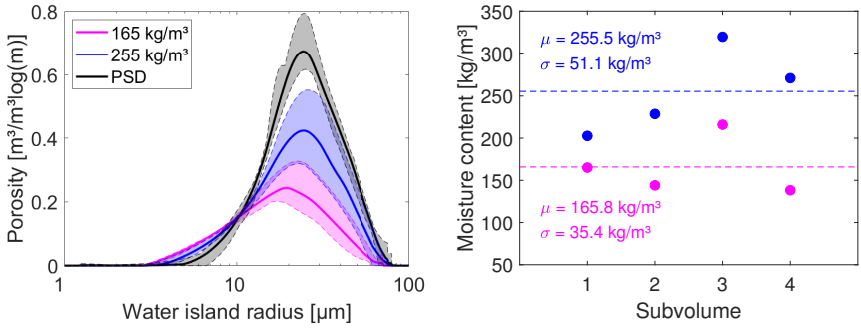


Figure 5.14: The water island size distributions and the moisture contents calculated for the subvolumes of the sample preconditioned to a moisture content of 230 kg/m^3.

A.4.2 Water island Size Distributions Measured with NMR

Saturated samples. All NMR experiments are performed using a CPMG measuring sequence with the maximum amount of scans allowed by the NMR apparatus (256 scans), however, two experimental parameters still require optimising. This CPMG measuring sequence typically applies a number of pulses (or echoes) and measures the amplitude of the signal after every pulse. The amount of pulses and the time between these pulses (i.e. inter-echo time (TE)) therefore need to be established before the measurement. The first measured amplitude is recorded after 1 x TE. Any decay of the magnetic signal before this time is not measured. This inter-echo time should therefore be small enough to measure the initial magnetic decay. A small inter-echo time also requires a sufficient amount of echoes to record the entire decay of the magnetic signal since the combination of the number of echoes and the inter-echo time governs the length of the measured signal (i.e. the acquisition time). For example, suppose the CPMG sequence applies 8000 echoes with an inter-echo time equal to 0.5 ms, 4 s of signal will be recorded. Too many echoes, however, will cause the magnetic coil to overheat and damage the NMR apparatus. Choosing the inter-echo time and the number of echoes should therefore be done carefully. To be on the safe side, a maximum of 8000 echoes is

allowed in this study while the minimum inter-echo time of the NMR apparatus is 0.5 ms.

To investigate the influence of the above-mentioned parameters, the inter-echo time is set to 0.5 ms, 0.7 ms, 1 ms, 1.5 ms and 2 ms and the number of echoes is chosen to make sure that all signals have the same duration (4 s). All measurements are made on the same saturated sample in quick succession and weight measurements show that no moisture evaporated. The recorded transverse relaxation time distributions, inverted using the Tikhonov and maximum entropy methods, are shown in Figure 5.15. The distributions obtained from the CONTIN method are not shown, but they display the same behaviour. Since an equal amount of moisture was present in the samples during all measurements, the initial magnitude of the recorded signal remains the same. The curves are scaled to make sure that the area under the curve equals the sample's porosity of 36.5 %. At first glance, all curves seem equal, however, there is a slight shift to smaller relaxation times when the inter-echo time increases. This is indicative of the presence of paramagnetic impurities [189]. Since the shift is limited, however, these impurities are of little importance in this study. Further results are always obtained with inter-echo times smaller or equal to 0.7 ms to capture the full magnetic decay.

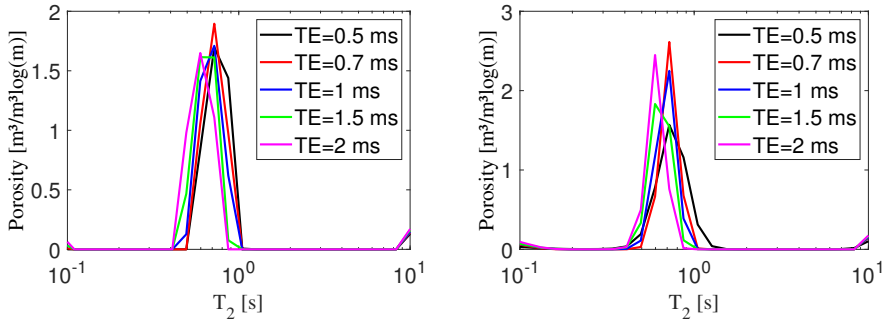


Figure 5.15: The transverse relaxation time distributions, calculated using the Tikhonov (a) and maximum entropy (b) methods for signals measured with different inter-echo times (TE).

Figure 5.16 compares the pore size distributions derived from NMR measurements on fully saturated samples to the pore size distributions extracted from XCT images. The pore size distributions, derived from NMR measurements, are obtained for three different samples and the area under the curve is scaled to represent their sample-dependent porosities equal to 34.8 %, 32.7 % and 32.7 % as calculated from vacuum saturation experiments. Due to the small size of

these samples, small weight fluctuations can significantly alter their calculated porosity which explains why these sample-dependent porosities slightly deviate from the previously mentioned porosity of 36.5 %. The magnetic signals are inversed using the maximum entropy and CONTIN inversion algorithms. The distributions derived using the Tikhonov method are not shown due to their similarity to the maximum entropy method.
The pore size distributions, derived from XCT images, are extracted from images on two different samples. As explained in the methodology, every scan obtained from a single sample is divided into eight subvolumes to allow segmentation using the trainable WEKA algorithm. The distributions are calculated for all eight subvolumes of these scans and hence the results in Figure 5.16 represent the average distribution (full line) and the area within which all results are located (shaded area) for all eight subvolumes of both samples.

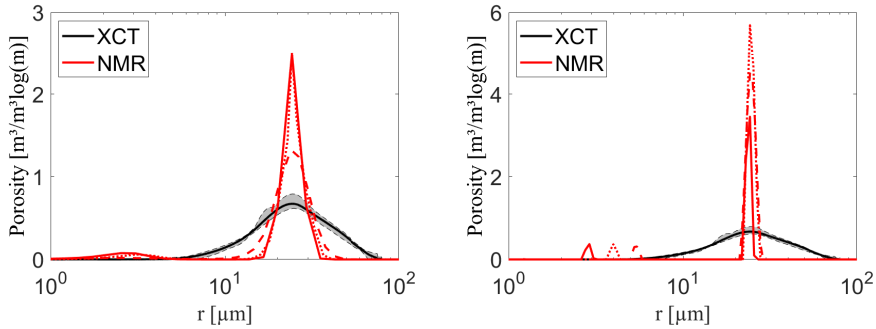


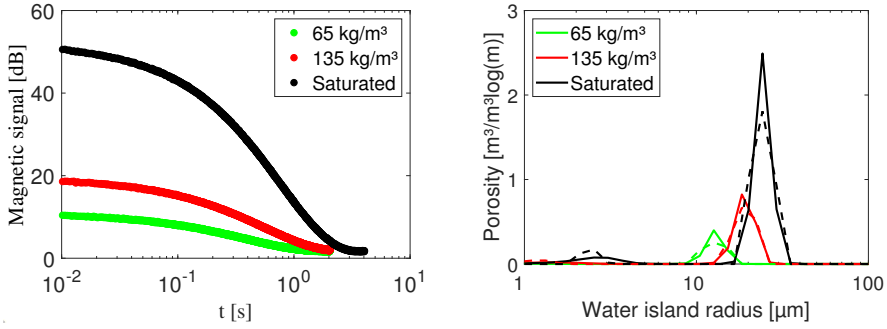
Figure 5.16: The pore size distributions derived from NMR measurements, for which the inversion is done using the maximum entropy (a) and CONTIN (b) methods compared to the pore size distributions calculated from XCT images.

The three samples subjected to NMR measurements show very similar results when the same inversion method is used. The CONTIN method, however, results in very narrow pore size distributions with a single dominant pore size. This is strange since the CONTIN method is a type of Tikhonov regularization which has the tendency to oversmooth solutions [178,179]. The validation of this model in a previous section also did not show this kind of behaviour for the unimodal distributions. It is very difficult to figure out the reason behind these steep peaks since the method's source code is unavailable. Other measurements on both saturated and unsaturated materials kept showing the same steep peaks, which is why further results are obtained only using the Tikhonov and maximum entropy inversion methods.

The results obtained from the NMR measurements using the maximum entropy principle and displayed in Figure 5.16 (a), show three narrow distributions. Their differences are minimal and easily attributed to the ill-posed inversion problem. The distributions are not capable of representing the wide array of pore sizes visualised in the XCT images. The long tail at small relaxation times has been proven to be difficult to recreate in the validation of the models. It is important to mention that the T_2 distributions, obtained for all three samples, are transformed into pore size distributions using Equation 5.16. This means that they are fitted to the pore size distributions obtained from the XCT images. In other words, the peak values of all NMR measurements are forced to align with the peak value of the XCT images. The surface relaxivities (ρ_2) used for this fitting equal $11.4 \pm 4.7 \mu m/s$. These values agree with literature where ρ_2 ranges from 1.5 $\mu m/s$ [161,190] to 50 $\mu m/s$ [167] for various glass materials. The variation on the measured ρ_2 does increase the uncertainty, however, since the positions of the pore size distributions are heavily influenced by this parameter.

Unsaturated samples. In this section, two samples, with porosities of 34.8 % and 32.7 %, are preconditioned to gravimetrically determined moisture contents of 65 kg/m^3 and 135 kg/m^3, after which the water island size distributions are extracted from NMR measurements. The NMR measurements are performed using a CPMG sequence with the smallest possible inter-echo time (TE = 0.5 ms) to capture the fast relaxing hydrogen nuclei in pore corners. During the centrifugation, the biggest pores and throats tend to empty first [23]. Since these largest pores are also characterised by the largest relaxation times, the magnetic signal of the unsaturated samples decays quicker than for saturated samples, as shown on Figure 5.17 (a). A total signal length of 2 s (or 4000 echoes) is therefore deemed sufficient. Due to the smaller amount of hydrogen nuclei in unsaturated samples, the initial signal amplitude is lower than for a saturated sample. This is detrimental to the SNR of the signal [161]. Therefore, the highest amount of scans allowed by the NMR apparatus (i.e. 256 scans) is imposed.

The water island size distributions of the two unsaturated samples and the pore size distribution of a saturated sample, extracted from the NMR measurements, are shown on Figure 5.17 (b). The distributions are scaled to make the area under the curve equal the sample's moisture content. The curve representing the saturated sample is hence scaled to the sample's porosity. Both results from the NMR, obtained using the maximum entropy (–) and Tikhonov inversion methods (- -), are very similar for all saturation states. A shift from larger to smaller water islands for decreasing moisture contents represents the emptying of large elements during a drying sequence.



(a) (b)

Figure 5.17: The recorded magnetic signals (a) and the water island size distributions, extracted using the maximum entropy method (–) and Tikhonov regularization (- -) (b) of the samples preconditioned to 65 kg/m³, 135 kg/m³ and saturated moisture content.

A.4.3 Comparison of results from XCT images and NMR measurements on unsaturated samples

The water island size distributions of the two unsaturated samples, extracted from NMR measurements and XCT images, are shown side by side on Figure 5.18 together with the entire PSD, also extracted from XCT images. The distributions are scaled to make the area under the curve equal the sample's moisture content. The results derived from XCT images and NMR measurements are already discussed in previous sections. The distributions derived from NMR measurements always result in a single narrow peak, while the XCT images show a wider distribution containing a broad range of pore radii. The same was noticed for saturated samples in Figure 5.16. The inversion methods used to transfer the magnetic signal into a transverse relaxation time distribution focus on the dominant size of water-filled pores since these heavily determine the relaxation rate of the magnetic signals. In other words, the distributions calculated from the NMR measurements focus on the capillary filled elements, while the hydrogen nuclei in the pore corners seem to relax too quickly for the NMR to measure.

Figure 5.19 shows the measured magnetic signals of the unsaturated materials together with the fitted magnetic signals. The latter are calculated from the transverse relaxation time distributions, extracted from the measured magnetic signals, using Equation 5.9. The first measured value is larger than the fitted value in both cases. This is either caused by measurement errors or it could indicate that there are hydrogen nuclei in pore corners which are

nearly completely relaxed before the first amplitude is recorded. The latter is consistent with the little literature available on NMR measurements of unsaturated materials [161], albeit on completely different materials. Due to the limit on the smallest possible inter-echo time, however, measuring this initial decay in more detail is not possible.

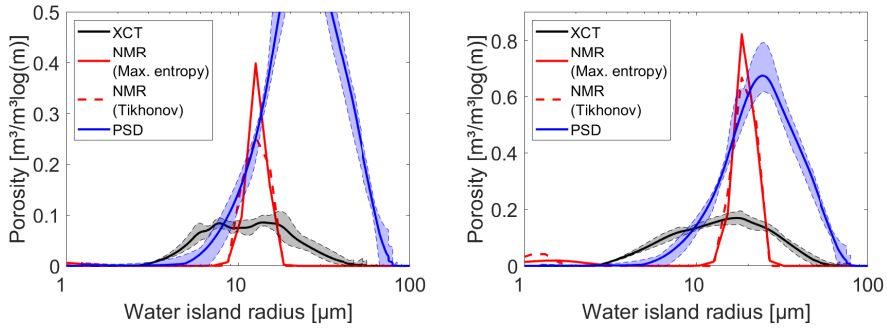


Figure 5.18: The water island size distribution as measured by the NMR and XCT for samples with a moisture content of 65 kg/m^3 (a) and 135 kg/m^3 (b) and the entire PSD extracted from XCT images.

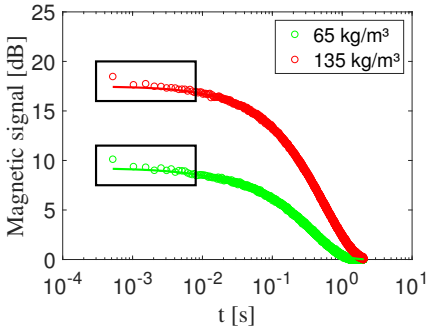


Figure 5.19: The magnetic signals recorded from NMR signals (o) of the unsaturated materials and the fits (-) composed from the calculated transverse relaxation time distribution.

By directly comparing the two NMR relaxation time distributions in figure 5.17 (b), it was already noticed that lowering the moisture content to 65 kg/m^3 results in shifting the peak to smaller water islands that were not (or hardly) observable in the distribution at 135 kg/m^3. This can be interpreted as shifting

the peak to the smaller pores that remain capillary filled while the larger pores empty [23]. Previous research [161] shows the same type of behaviour in screed samples. NMR measurements can therefore be used for a quick estimation of the size of the water-filled pores in a material, but they are not suitable for measuring the size of water islands adhered to pore walls or absorbed in pore corners.
Important to note is that the transition from the relaxation time domain to the pore radius domain is done using Equation 5.16. This equation is only valid for cylindrical pores where S/V equals 2/r. Corner islands are not necessarily shaped this way and hence this equation is no longer valid [191]. This shows that even if NMR measurements are able to measure the signal of hydrogen nuclei in pore corners, translating this to an actual water island radius remains questionable.

A.5 Discussion

In this subchapter, NMR relaxometry is investigated as a possible alternative to the XCT imaging of unsaturated samples. This experimental technique is especially interesting due to its ability to characterise moisture in pores in both the nanometer (1-1000 nm) and micrometer (1-1000 µm) range while the spatial resolution limits of XCT imaging only allow the visualisation of moisture in pores in the micrometer range. A successful validation of the NMR technique would therefore allow using this technique on more common building materials (e.g. lime mortar or ceramic brick), with pore sizes spanning several spatial scales. The use of NMR relaxometry to investigate moisture distribution in unsaturated materials proves difficult, however, and a common theme throughout the process is the uncertainty that goes along with the acquiring and processing of the magnetic signals. Some of the most important factors, which introduce this uncertainty, and their impact on the results, are discussed here.
The first uncertain process is the ill-posed problem of calculating the transverse relaxation time distribution from the magnetic decay signal. This is a problem which returns in several research areas and has multiple solution strategies. Zou et al. [178] for example shows that the maximum entropy regularization principle can cause high tilted tails at small relaxation times. Other studies show that Tikhonov regularization has a tendency to oversmooth solutions [178,179]. Guo et al. [192] combined Tikhonov regularization and the maximum entropy method to benefit from the advantages of both techniques at the expense of increased computational demand. Other techniques besides regularization (e.g. Monte-Carlo inversion [193], singular value decomposition [194], ...) also show good results. The vast array of different inversion methods show that there is not an optimal solution strategy. On top of that, an insufficient SNR significantly influences the results of most methods and can even cause bimodal distributions with closely located peaks to become unimodal [178,179]. In other

words, an inversion method always needs to be tested and understood before using it to calculate relaxation time distributions and even then there is always a degree of uncertainty. Simply using a professionally developed technique, such as the CONTIN algorithm used in this subchapter, does not guarantee correct results.

After obtaining the transverse relaxation time distributions, they can be linked to the pore size distributions with Equation 5.7. This equation is derived for cylindrical pores which are disconnected from each other (i.e. weak or no diffusional coupling) [163]. Ghomeshi et al. [170] investigated strong diffusional coupling of pores and showed its significant influence on the relaxation time distributions. Assessing whether the pore network of a material is well connected or not, however, remains a subjective task. Another heavily researched influence on Equation 5.7 is the presence of paramagnetic impurities [166,189,195]. Since the sintered glass filter is a pure material, the influence of these impurities on the calculation of pore size distributions is limited. When other (more common) building materials, such as ceramic brick, are of interest however, these paramagnetic impurities may become a problem and their impact is not easily removed from the results [166].

A final uncertainty in Equation 5.7 is the determination of the surface relaxivity (ρ_2). This factor is typically established by fitting a transverse relaxation time distribution to the pore size distribution of a material obtained via XCT imaging or mercury intrusion porosimetry measurements. To do so, however, it is assumed that this factor is uniform over the entire material and thus equal in every pore. Several studies [164,168,172] have proven that this is most probably not the case. Benavides et al. [164] for example, used random walk simulations on XCT images of a rock and found an inverse relationship between surface relaxivity and pore size. Saidian and Prasad [172] on the other hand investigated the influence of paramagnetic impurities on the surface relaxivity and found that higher contents of impurities also increase the surface relaxivity. This pore-dependent surface relaxivity, of course, heavily influences the calculated pore size distributions.

All these factors make it very difficult to assess the validity of the results obtained from NMR measurements. This is especially the case when unsaturated samples are of interest, due to the limited research on the magnetic signals generated by corner islands or water films on pore surfaces. Therefore, despite being a promising technique, NMR is not very suitable for the investigation of the moisture distribution in unsaturated materials.

Due to the shortcomings of NMR relaxometry, only XCT imaging remains a feasible option to study moisture behaviour in other hydrophilic and hydrophobised materials. Due to the limits on its spatial resolution, however, experiments on common building materials like ceramic brick are currently not possible. Further study of the microscopic behaviour in hydrophobised materials

in Subchapter B is therefore limited to sintered glass samples.

A.6 Summary

This subchapter investigated the moisture behaviour in hydrophilic sintered glass using both XCT imaging and NMR relaxometry. While the former is a well-established measuring technique, the latter is tested as a possible alternative to XCT imaging. Due to its larger measuring spectrum of both micrometer scale (i.e. 1-1000 µm) and nanometer scale (i.e. 1-1000 nm) pore bodies and throats, NMR relaxometry would provide a way to investigate the moisture behaviour in the smallest pore network elements of common building materials. The first part of the subchapter shows the theory behind NMR measurements and the multiple sources of uncertainty that are inherent to the technique. This uncertainty indicates that performing such NMR experiments and post-processing their results are not straightforward.
The second part of the subchapter measures the water island size distributions using NMR relaxometry and compares them to the results obtained from XCT images. The NMR experiments on unsaturated samples have shown to estimate the size of the largest water islands (i.e. capillary filled pores), but the small water islands in pore corners prove to be out of its measuring range. Additionally, the full distribution of these water-filled pores is not retrieved, only the dominant pore sizes are revealed. It can therefore be concluded that this technique is not suited to a quantitative evaluation of the water islands in unsaturated materials. Investigating the moisture behaviour in the entire pore network of unsaturated building materials, such as ceramic brick, is therefore impossible with existing experimental techniques. The investigation of the moisture behaviour in hydrophobised building materials, explained in the next section, therefore only concerns hydrophobised sintered glass samples.

Appendix 5.A.1 Validation of the inversion programs for bimodal distributions with separated peaks

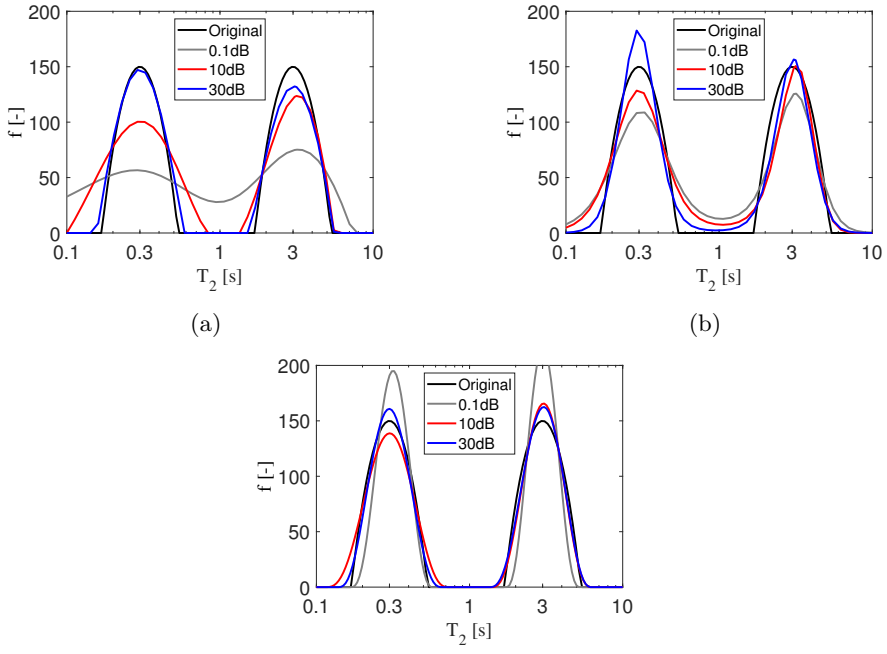


Figure 5.20: The T_2 distributions calculated with the Tikhonov (a) maximum entropy (b) and CONTIN methods (c) for the signals of the bimodal distributions with separated peaks with SNR's of 0.1 dB, 10 dB and 30 dB.

B Microscopic moisture behaviour in hydrophobised porous materials

B.1 Introduction

For the hydrophobisation of masonry walls, silicon-bearing compounds are most commonly used [6]. These compounds, typically supplied as a mixture of silanes, siloxanes and silicone resins, are combined with water prior to their application. In the water repellent agent/water emulsion, polymer chains are formed via polymerisation [196]. Depending on the mixture of silanes, siloxanes and silicone resins, these chains can differ in size. In the water/water agent emulsion, the chains curl up into sphere-shaped emulsion droplets to minimise the exposure of their hydrophobic side groups to water. When the emulsion is applied onto the building facade after mixing, these droplets are transported through the pore network where the agent attaches itself to the pore walls, forming a thin hydrophobic layer. A perfect hydrophobisation application would render all pore walls in the pore structure hydrophobic and therefore remove any liquid transport through or moisture storage in the material. Capillary absorption experiments on such hydrophobised materials, where they are brought into contact with a free water surface, show that spontaneous absorption of moisture is heavily reduced, but not eliminated entirely [6,9,17,32,43,51]. Water is therefore still transported through the material and stored somewhere in its pore network, however, in which elements and in what manner currently remains speculation. It is generally believed that some pore network elements can remain completely hydrophilic when the emulsion droplets are larger than the pore diameter and therefore are denied entry to these elements. The pore surfaces of other (bigger) pores do become either completely or partially covered by a thin hydrophobic layer of the water repellent agent [30,32,197]. Moisture storage is then possible in the elements in which the water repellent agent cannot penetrate as well as at the pore walls in the hydrophobised elements which have remained hydrophilic. Locating these hydrophilically-oriented sites in the pore network of hydrophobised materials is imperative to properly model the microscopic moisture storage and transport processes in the pore network model of Chapter 6.

Besides the presence of such hydrophilically-oriented sites in the pore network, it has been hypothesised that the entry to some of the smallest pore network elements can become blocked by the water repellent agent, rendering them inaccessible to moisture [30,32,197]. This pore blocking reduces the pore network connectivity, which makes it harder for vapour particles to diffuse through the pore system. This might explain the slightly lower vapour permeabilities measured in dry-cup tests on hydrophobised materials [6,9,32,50] or the slight (albeit sometimes negligible) decrease in porosity measured in MIP tests and

vacuum saturation experiments [6,9,32]. Since this effect is overall very limited, as shown by the (only) slight change of porosity and vapour permeability [6,9,32], pore blocking is not investigated further in this PhD project. It should be mentioned that this pore blocking can become much more important when materials with finer pore systems (e.g. lime mortar) are studied and hence an extension of the investigation towards these materials also remains future work.
While the macroscopic hygric properties of hydrophobised materials are heavily researched, their microscopic moisture storage and transport processes are rarely investigated. These processes are especially interesting, however, since they could verify or refute the existence of fully and partially hydrophobised pore bodies and throats. This knowledge can also clarify why some water repellent agents are better suited to certain building materials than others [5], which would make the extensive experimental search for a suitable water repellent agent easier or even redundant. Cnudde et al. [197] have tried imaging the water repellent agent inside a sandstone and a limestone using XCT imaging as well as fluorescent microscopy. They were only capable of visualising pores completely filled by the water repellent agent, but not the thin hydrophobic layers at the pore surfaces. Barnat-Hunek and Smarzewski [198] used scanning electron microscopy (SEM) images to visualise the water repellent agent in hydrophobised ceramic bricks. They noticed a continuous silicon coating on the grains with some cracks where the material possibly remains hydrophilic. Other existing microscopic studies on hydrophobic materials typically image evaporative drying of hydrophobised pore bodies and throats in 2D micromodels [199–201] or sporadically in 3D porous columns [202,203] using XCT imaging. These studies highlight the drying sequence of the pore bodies and throats, but they never discuss any moisture left behind in hydrophilic or partially hydrophobised pore bodies and throats.
This subchapter therefore investigates the presence of (fully) hydrophilic and partially hydrophobised pore bodies and throats in hydrophobised materials which provide sites for moisture storage. The aim of this section is to eventually formulate conclusions and guidelines based on which the existing hydrophilically-oriented pore network model can be adjusted to simulate hygric properties of hydrophobised porous materials in Chapter 6. To do so, hydrophobised porous materials are preconditioned to different moisture contents and the resulting moisture distributions throughout their pore structures are visualised using XCT imaging. These moisture distributions of samples at different saturation stages are subsequently investigated to locate hydrophilic and (partially) hydrophobised pore bodies and throats where moisture storage remains possible. As explained in previous subchapter, this investigation focuses solely on hydrophobised sintered glass due to the spatial resolution limits of XCT imaging. Section B.2 first describes the water repellent agents used to hydrophobise the sintered glass samples and it elaborates on an algorithm designed for the post-processing of

XCT images. Section B.3 then discusses the images acquired from both the hydrophilic as well as the hydrophobised sintered glass. Based on these results, Section B.4 discusses the presence of possible moisture storage sites in both hydrophilic as well as partially hydrophobised pore network elements. Finally, Section B.5 reiterates the most important conclusions of this subchapter, on which the adaptation of the hydrophilically-oriented pore network model in Chapter 6 will be based.

B.2 Materials and methods

This subchapter investigates moisture storage in the pore network of hydrophobised materials. Before the general methodology is explained, a short introduction on the differences in moisture storage in hydrophilic and hydrophobised materials is required. In hydrophilic pore bodies and throats, it is generally known that moisture can be stored in three ways: adhered to the pore surfaces, as absorbed water islands in the corners of empty elements and, when the element's threshold capillary pressure is reached, in capillary filled pores and throats as already illustrated in Figure 5.8. In a perfectly hydrophobised pore, where the entire pore surface is covered with a thin hydrophobic layer (as shown in Figure 5.21 (a)), moisture cannot adhere to any of the pore surfaces and storage is assumed to be implausible under normal circumstances. As explained in the introduction, however, there is a general conviction amongst researchers that some elements of the pore network either remain completely or partially hydrophilic as shown in Figure 5.21 (b) and (c), respectively [30,32,197]. It should be mentioned that water, trapped as a non-wetting phase in the center of the hydrophobised pores (e.g. [79]), is not noticed in the XCT images and this phenomenon is hence not further discussed here.

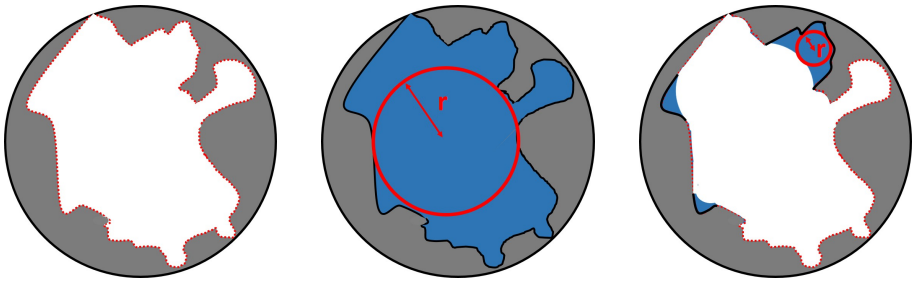


Figure 5.21: Examples of the cross-section of a completely hydrophobised pore (a), a completely hydrophilic pore (b) and a partially hydrophobised pore (c) with the hydrophobised pore surfaces represented by a red dotted line.

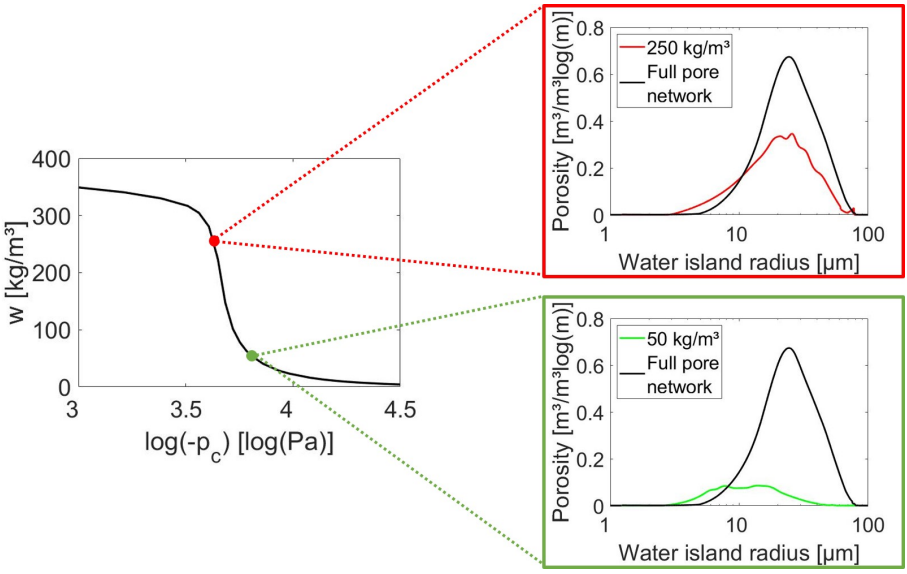


Figure 5.22: Illustration of two water island size distributions of samples, preconditioned to different moisture contents, are shown. These preconditioned moisture contents are also indicated on the illustrative material's moisture retention curve.

The goal of the section is to find the hydrophilic sites in hydrophobised sintered glass samples where water can be stored as in Figure 5.21 (b) and (c). To do so, the same methodology is followed as in Subchapter A. Samples, measuring 10 mm in height and 6 mm in diameter, are preconditioned to different moisture contents in the centrifuge setup, developed in Chapter 4, after which they are transferred to the XCT apparatus for the image acquisition. These images are subsequently segmented using the trainable WEKA algorithm [187] after which the water island network is extracted using PNextract [97]. The extracted data is then used to compose the water island size distributions. This is illustrated in Figure 5.22 where two illustrative samples are preconditioned to different moisture contents. These distributions show where moisture is stored during desorption in a hydrophobised material at various moisture contents. They therefore indirectly give an insight on possible hydrophilic or partially hydrophobised pore bodies and throats where moisture storage remains possible. This detour is necessary since direct visualisation of the water repellent agent has proven to be difficult, if not impossible, with current visualisation techniques [197,198]. This section gives an overview of the water repellent agents used to hydrophobise the sintered glass samples and describes an algorithm which is

developed to distinguish capillary filled elements in the water island network from corner islands. The acquisition, segmentation and post-processing of the XCT images is performed exactly as described in Subchapter A and is hence not repeated here.

B.2.1 Water repellent agents

The sintered glass samples are hydrophobised with two commercially available water repellent agents (SILRES BS SMK 2101 (agent A) and SILRES BS SMK 2100 (agent B)) and one lab-made water repellent agent (agent LM). A detailed description of these water repellent agents as well as the reason for the development of the lab-made water repellent agent can be found in Chapter 2. Only the information relevant for this subchapter is reiterated here. As explained in Chapter 2, all used water repellent agents are silicon-bearing compounds with different compositions of silanes and siloxanes. When added to water, these compounds create polymer chains of different lengths. These chains subsequently form sphere-shaped emulsion droplets in water/agent emulsions to guarantee the least amount of contact between hydrophobic side groups and water atoms. A microscopic image of such emulsion droplets can be found in Chapter 2. The hydrodynamic radius of these emulsion droplets, representing the amount of physical space the droplets occupy in the water/agent emulsions, are measured using a dynamic light scattering (DLS) setup (LS Spectrometer, LS Instruments) at 20 °C and at a scattering angle of 90°. These hydrodynamic radii give an indication of the pores which the emulsion droplets can enter and they are hence shown in Figure 5.23, together with the pore size distributions of sintered glass and ceramic brick.
The commercially available water repellent agents are typically applied on building materials like ceramic brick, which have smaller pores than sintered glass as shown in Figure 5.23. Multiple sources state that the size of the emulsion droplets determines which of the building material's pores cannot be entered and hence remain hydrophilic (or become blocked, and be inaccessible for moisture) [6,30]. Using the commercial water repellent agents on these larger pores of sintered glass, however, will probably cause less or no elements to remain hydrophilic. Therefore, the lab-made agent, composed of emulsion droplets with larger hydrodynamic radii, is created in cooperation with the Soft Matter, Rheology and Technology (SMaRT) section of the KU Leuven. The description and composition of this lab-made agent can be found in Chapter 2.

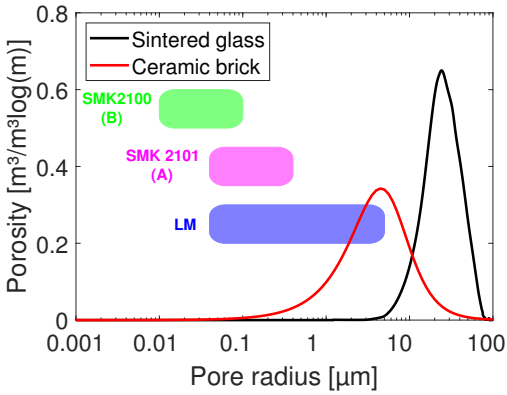


Figure 5.23: The pore size distributions of the sintered glass filter and the ceramic brick as well as the hydrodynamic radii of the water repellent agents as measured by the DLS setup.

All three agents are first diluted with water to form a 90%/10% water/agent emulsion. Next, one surface of the sintered glass samples is placed upright in this emulsion to allow complete capillary absorption of the product. After the hydrophobisation process, samples are kept in a humid chamber (i.e. 86 % relative humidity) for at least two weeks of curing. Afterwards, the contact angles between deionised water droplets and hydrophobised sintered glass are measured using the contact angle goniometer on a drop volume tensiometer (Attension Theta Flux, Biolin Scientific), using the static sessile drop method. A blunt-end stainless steel syringe needle with an internal diameter of 0.25 mm (7018336, Nordson) is used for all measurements. The contact angle is measured on three different samples for every water repellent agent and on each sample four droplets are imaged to account for sample heterogeneity. This results in contact angles of $117.6° \pm 7.1°$, $109.7° \pm 7.7°$ and $120.3° \pm 3.6°$ for sintered glass samples hydrophobised with water repellent agents A, B and LM, respectively.

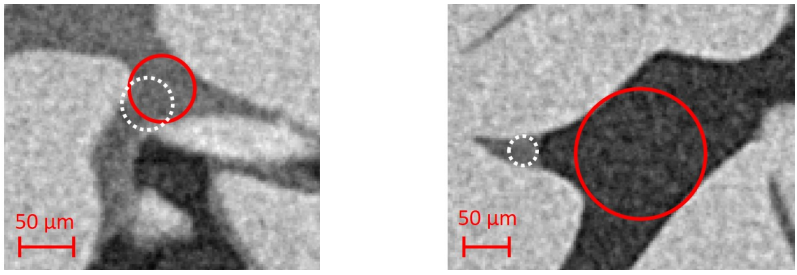
B.2.2 Locating the filled pore bodies and throats in XCT images

In order to develop our understanding of the distribution of water in materials, an algorithm is designed to categorize the water islands, extracted from the XCT images, into capillary filled elements and corner islands. Capillary filled elements are pore bodies and throats which are filled with water, while corner islands exist in corners of pore bodies and throats. Classifying elements as capillary filled requires first dividing the continuum pore space into distinct

pore bodies and throats. The construction of such a network has shown to be a difficult process which involves making some arbitrary decisions [86,87] and can result in several versions of the same pore network with a different division of pore space between individual pore network elements. Therefore, classifying an element as capillary filled is dependent of these pore network extraction algorithms, which is why the same pore network extraction algorithm (PNextract) is used throughout this PhD, with the aim of minimising the influence of the extraction algorithm itself. Nevertheless, misclassification of some water islands is unavoidable when using the algorithm designed in this dissertation, as will be explained further in this section.

The developed algorithm first requires both the pore network and water island network to be extracted from the same set of images. The extracted networks exist of lists of pore bodies and throats with their geometrical (e.g. radius, volume) and topological (e.g. coordinates, connections) properties. If an element is capillary filled, theoretically it can be found in both networks with the same properties. Small variations in the pore network extraction program as well as the segmentation of images, however, can cause the properties in both networks to differ slightly. In other words, the water island network and pore network possess several elements with approximately the same geometrical and topological properties (mainly coordinates, radius and volume) which can be classified as the capillary filled elements. This is exemplified by a capillary filled pore and one with only corner islands in Figure 5.24 where a 2D representation of the extracted pore bodies in both networks is drawn. While the corner island in Figure 5.24 (b) clearly does not represent a filled pore, the capillary filled element in Figure 5.24 (a) will only possess slightly different properties in both water island network (white circle) and pore network (red circle). The goal is to find these elements which are sufficiently similar in both networks and classify them as capillary filled elements. An algorithm is therefore designed to iterate over all water islands and find the element in the pore network with sufficiently similar properties.

The algorithm behaves slightly different for the classification of pore bodies and pore throats. It is first explained for pore bodies, after which the difference with the algorithm for pore throats is clarified. Consider the pore body of the water island network represented by the red element in Figure 5.25 (a). Three properties are used to check whether the elements in the water island network and pore network represent the same pore body or throat. Firstly, the distances between the center of the pore bodies in the water island network and pore network, indicated by the green lines in Figure 5.25 (a), are calculated using the coordinates derived from the pore network extraction. Since a center-to-center distance of 5 µm has a much larger influence on a small pore with a radius of 2 µm than on a large pore with a radius of 30 µm, the distance is normalised with respect to the pore radius and expressed as a percentage. For

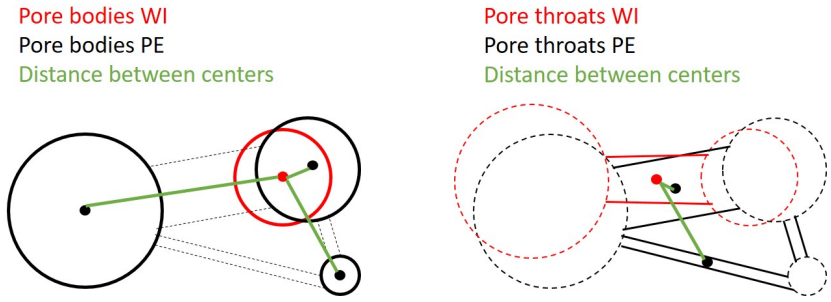


(a) (b)

Figure 5.24: Example of the extraction of a capillary filled element (a) and a water island in a pore corner (b) in the pore network (red line) and the water island network (white dotted line).

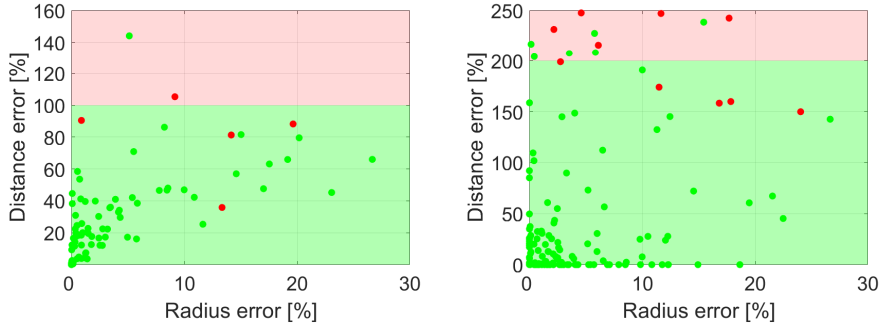
example, a center-to-center distance of 5 µm for a pore body with a radius of 40 µm results in 12.5 %. Secondly, the difference in radii is calculated and once again normalised with respect to the pore radius. Thirdly, the volumes of the two elements are compared and normalised with respect to the pore volume. These relative errors are called distance error, radius error and volume error, respectively.

A water island is labelled as a capillary filled element if the previously explained errors remain smaller than certain predefined limits. These limits are determined by visually assessing pore bodies and throats in several sets of XCT images and heuristically choosing boundary values. These visually assessed pore bodies and throats are plotted in Figure 5.26 (a) in function of their distance and radius errors. Every marker represents a single water island which is classified as a capillary filled pore if the distance, radius and volume errors are significantly small. The green markers are labeled as capillary filled pore bodies during the visual assessment while the red markers showed to be corner islands and hence should not be labeled as capillary filled elements. Based on this visual assessment, the limits on the distance and radius errors are set to 100 % and 30 %, respectively, and the volume error should remain between 50 % and 200%. It can be seen that some elements are wrongly classified in the algorithm (i.e. green dots in the red zone or red dots in the green zone), however, since manually labeling the hundreds to thousands of pores of every XCT scan is too labor intensive, this is inevitable. Nevertheless, these wrongly classified elements typically account for less than a few percent of the total moisture in the sample.



(a) (b)

Figure 5.25: Representation of the overlapped water island network (WI) and pore network (PE) when comparing pore bodies (a) and pore throats (b).



(a) (b)

Figure 5.26: Distance error in fuction of radius error of the elements visually categorised as capillary filled pores (a) and throats (b) (green) and corner islands (red).

Identifying throats as capillary filled follows the same procedure, however, the boundary on the distance error is different. Since the radius of the throats is typically quite small, the distance error, which is normalised with respect to the element's radius, is larger than for pore bodies as indicated in Figure 5.26 (b). Therefore, the distance error is limited to 200 % which seems much, but it is relative to the small throat radius. Once again, some throats are inevitably characterised incorrectly, however, the moisture in these elements is negligible compared to the total moisture content. It is important to mention that the smallest pore throats (with the smallest throat radii) are highly influenced by segmentation errors and slight differences in network extraction. Capillary filled

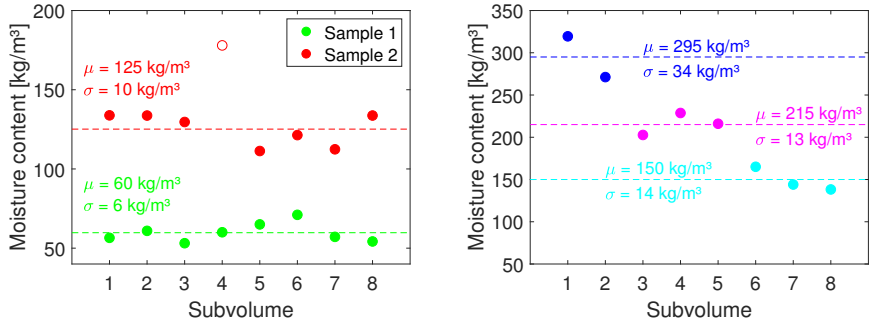
throats with radii smaller than 10 µm are therefore sometimes mislabeled as corner islands when they are capillary filled. This is important to keep in mind when analysing results.

B.3 Results

This section discusses the results obtained for both hydrophilic sintered glass as well as the sintered glass, hydrophobised with the three water repellent agents, in sections B.3.1 and B.3.2, respectively.

B.3.1 Hydrophilic sintered glass

To acquire the XCT images of hydrophilic materials, three different samples are preconditioned in the centrifuge to different moisture contents after which they are moved to the XCT apparatus. The same three samples as in Subchapter A are studied here. As explained in previous section, not the entire sample, but a 3^3 mm^3 cube in the middle of the sample is imaged from which 8 subvolumes are extracted and segmented separately to account for the computational requirements of the trainable WEKA algorithm. The moisture contents of these eight subvolumes of samples 1,2 and 3 are repeated in Figure 5.27. The average moisture contents of the grouped subvolumes (µ) as well as their standard deviation (σ) are indicated as well. In this subchapter, they are grouped according to similar moisture content to allow all water island size distributions, displayed in this and following section, to at least be an average of the results of two different subvolumes. Doing so, the water island size distributions of the hydrophilic samples are derived for average moisture contents of 60 kg/m^3, 125 kg/m^3, 215 kg/m^3 and 295 kg/m^3. The three subvolumes of sample 3 with an average moisture content of 150 kg/m^3 are omitted to not clutter the graphic representation of the results.
It should be noted that in section A.4.1, the subvolumes of sample 3 were grouped differently (four top and four bottom subvolumes). This is because these distributions are used in Chapter 6 to microscopically validate the existing pore network model. Grouping them according to their moisture content, however, reduces the large spread on the calculated water island size distributions and hence makes it easier to compare results from hydrophilic and hydrophobised samples in this section. This different grouping does not alter any previously made conclusions, it merely clarifies the visual representation.



(a) (b)

Figure 5.27: The moisture contents of the eight subvolumes of samples 1,2 (a) and 3 (b).

Figure 5.28 shows the water island size distributions extracted from the hydrophilic samples, which are preconditioned to 60 kg/m³, 125 kg/m³, 215 kg/m³ and 295 kg/m³, together with the complete pore size distribution of the material. As explained before, the water island size distributions are always at least averaged over results of two different subvolumes. The line represents the average distribution and all individual results are comprised within the shaded area. When the material desaturates, the largest elements have the tendency to empty first as can be seen by the disappearing of the biggest water islands. Upon emptying, some pore bodies and throats retain moisture in their corners and form so-called corner islands as illustrated on Figure 5.21. This explains why the amount of water islands with radii smaller than 10 µm in the unsaturated samples surpasses the amount of pore bodies and throats in the pore network (represented by the black curve) with these dimensions. This was already noticed in Subchapter A.

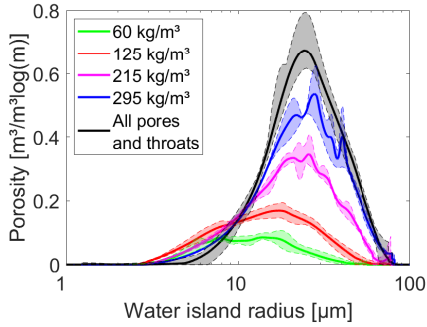


Figure 5.28: The water island size distributions, composed using all water islands of the hydrophilic samples, preconditioned to different moisture contents, together with all pores and throats in the pore network.

Using the algorithm described in Section B.2.2, the capillary filled pore bodies and throats are labeled and the water island size distributions of solely the capillary filled elements are composed. Figures 5.29 (a) and (b) represent the water island size distributions composed of the capillary filled pore bodies and throats, respectively. The pore bodies' desaturation process seems to be mostly dependent on the water island size. Therefore, the biggest water islands (or more specifically the pores with the largest absolute capillary pressure) generally empty first. On the other hand, the throats follow a more random drying sequence where small and large elements empty interchangeably. After studying the XCT images, it is inferred that this is caused by the omission of isolated capillary filled throats, which can be explained as follows. Per definition, a throat connects two pore bodies which have larger dimensions than the throat itself. This means that it often occurs that the two pore bodies empty prior to the throat. As a result, several isolated filled throats should be present in the pore network connected to two empty pore bodies. However, these types of isolated filled throats are rather scarce as shown by the XCT images acquired in this subchapter as well as in other literature [84,203]. Therefore, regardless of the throat's radius, the order in which they empty during a desaturation process is influenced by the moment at which their two connecting pore bodies empty rather than their proper size or threshold capillary pressure.
Studying the desaturation process of both pore bodies and throats separately also heavily depends on the pore network extraction and how the continuum pore space is divided into pore bodies and pore throats. Therefore, the previous explanation of isolated filled throats is only really valid for this specific pore network, extracted with PNextract. If the pore network would be extracted using a different algorithm or a different material would be studied, these

isolated throats might be present to a lesser amount.

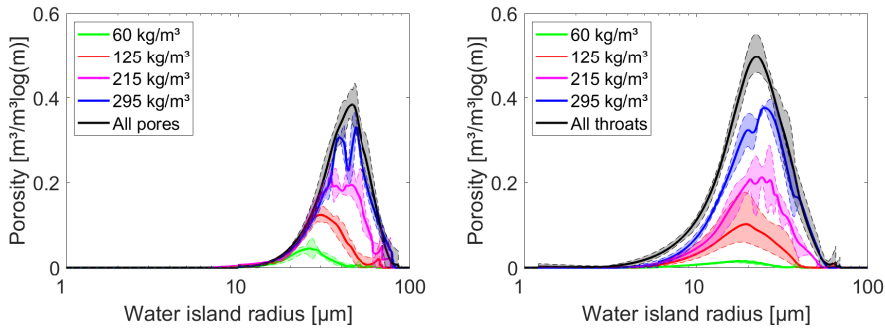


Figure 5.29: The water island size distributions, composed using the capillary filled pore bodies (a) and throats (b) of the hydrophilic samples, preconditioned to different moisture contents.

B.3.2 Hydrophobised sintered glass

This section shows the water island size distributions extracted from the samples hydrophobised with water repellent agents A, B and LM at different saturation states. These distributions are acquired exactly as explained in previous section and all displayed results are therefore the average of the results of at least two subvolumes of a sample. Figure 5.30 shows the water island size distributions obtained from samples hydrophobised with all three water repellent agents (b-d) as well as the water island size distribution obtained from the hydrophilic samples (a), which was already displayed in Figure 5.28. Two main differences can be noted between the distributions of hydrophilic and hydrophobised materials. Firstly, when the hydrophobic elements empty, water is less likely to form corner islands in the pore body and throat corners. This is shown by the lower amount of small water islands (with radii less than 10 µm) in figures b-d compared to figure a. Since these corner islands require a hydrophilic surface to adhere to, it makes sense that the hydrophobisation procedure makes their presence less likely.

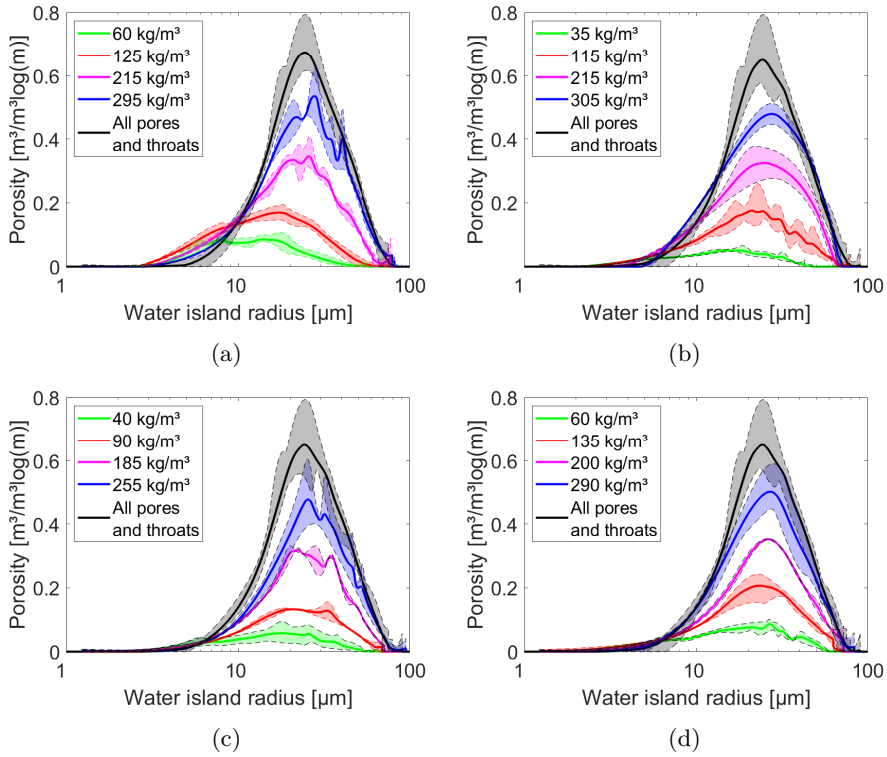


Figure 5.30: The water island size distributions, composed using all water islands, of the hydrophilic samples (a) and the samples hydrophobised using water repellent agents A (b), B (c) and LM (d), preconditioned to different moisture contents.

Secondly, while it is shown in previous section that the drying sequence of pore bodies in hydrophilic samples is governed by their sizes (or more specifically by their threshold capillary pressures), the pore bodies in the hydrophobised materials empty in a more random order. This is confirmed by the water island size distributions composed of only the capillary filled pore bodies and throats of the sample, hydrophobised with water repellent agent A, in Figure 5.31. While the results derived from the hydrophilic samples already showed that the drying sequence of throats is more random, Figure 5.31 (a) shows that drying of the hydrophobised pore bodies is similarly less governed by their size. The same conclusions can be drawn from the samples hydrophobised with the other water repellent agents, the results of which are collected in Appendix 5.B.1.
This more random drying order agrees with experimental and simulational

studies in literature where hydrophobised materials experience less of a capillary fingering drying pattern, and hence have less trapped liquid water clusters, but more of a drying front [200,203,204]. Therefore, the position of the elements with respect to the drying front governs their potential to empty, more than their size, shape and/or threshold capillary pressure. The materials studied in literature [200,203,204] typically exist of pore networks where all pore bodies and throats are rendered hydrophobic. Since the drying sequence of the materials in this subchapter occurs similarly to the materials in these studies, it is possible that the emulsion droplets of all three water repellent agents, used in this PhD, are also capable of entering most (if not all) pore bodies or throats of the sintered glass filter. The next section elaborates further on the presence of any hydrophilic or partially hydrophobised pore network elements.

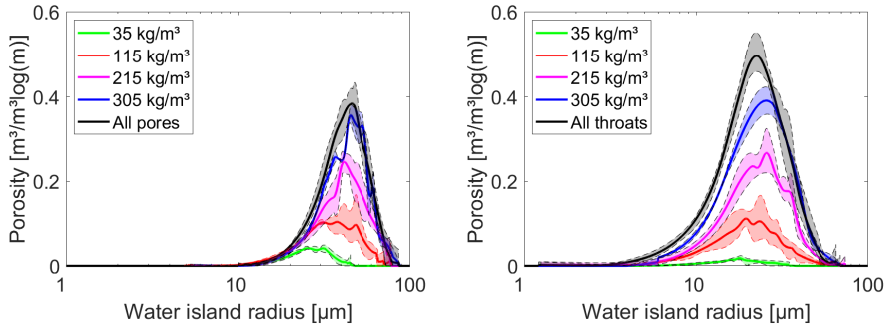


Figure 5.31: The water island size distributions composed using the capillary filled pore bodies (a) and throats (b) of the samples hydrophobised with water repellent agent A, preconditioned to different moisture contents.

B.4 Location of hydrophilic pore bodies and throats

The main goal of this subchapter is to locate the hydrophilic water storage sites in a hydrophobised sintered glass filter. As explained in Section B.2, it is assumed that moisture storage largely depends on the manner in which elements become hydrophobised. In hydrophilic pore bodies and throats, water can fill the entire element, while in partially hydrophobised pore bodies and throats, water islands can solely attach to the hydrophilic part of the pore surfaces as shown in Figure 5.21 (c). This section discusses the presence of both completely hydrophilic as well as partially hydrophobised pore bodies and throats in the hydrophobised sintered glass.

B.4.1 Hydrophilic pore network elements

Figure 5.32 shows the moisture retention curves of the three types of hydrophobised sintered glass, determined with steady state centrifugation as described in Chapter 4. The reference moisture retention curve of hydrophilic sintered glass, measured using the well-known MIP experiment in Chapter 4, is also shown. Every data point displayed in the figure represents the average and standard deviation of four different samples. It is clear that the moisture retention curves shift to smaller absolute capillary pressures when they are hydrophobised. This means that these samples start to desaturate at lower rotational velocities inside the centrifuge. Smaller pressures are required to force water from the hydrophobised pore bodies and throats because they actively repel water. The degree to which the curves are moved to smaller absolute capillary pressures scales with the contact angles measured on the hydrophobised samples and hence with their degree of hydrophobicity ($\theta_{\text{hydrophilic}} < \theta_{\text{B}} < \theta_{\text{A}} \approx \theta_{\text{LM}}$).

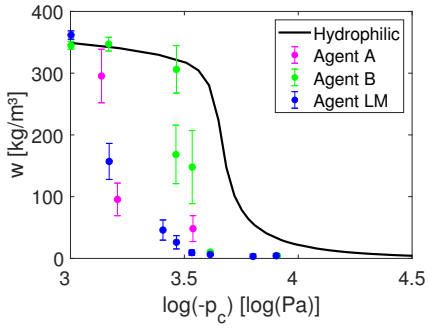


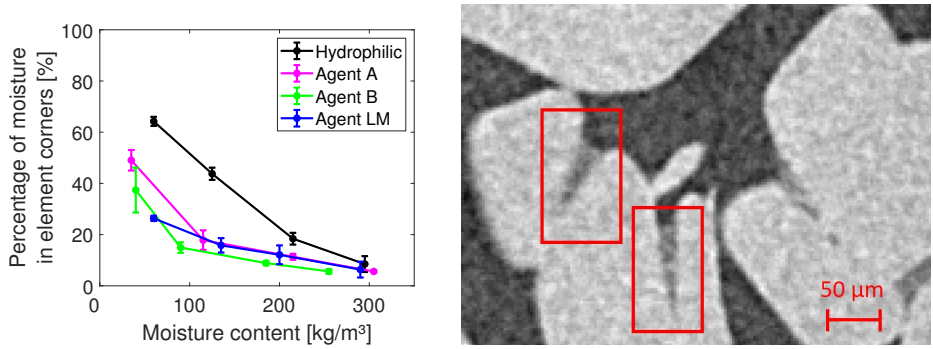
Figure 5.32: The moisture retention curve of hydrophilic samples, derived using MIP, and of hydrophobised samples, derived using steady state centrifugation.

Interestingly, all hydrophobised samples almost completely empty before any substantial desaturation occurs in hydrophilic samples (around 3.6 log(Pa)). Every pore body and throat in a hydrophobised sample, which empties at absolute capillary pressures below 3.6 log(Pa), is therefore assumed to be at least partially hydrophobic. If not, they would have remained water-filled. Based on these moisture retention curves and the fact that the images of hydrophobised samples in Section B.3 showed a similar drying pattern as materials with only fully hydrophobised pore bodies and throats [200,203,204], it can be concluded that the emulsion droplets of all three water repellent agents can enter most, if not all, pore network elements of sintered glass. According to the hydrodynamic radii of the different water repellent agents in Figure 5.23, this is possible although it was expected that some pores would remain hydrophilic in the

samples hydrophobised with the laboratory made water repellent agent. This agent also has a fraction of smaller emulsion droplets in the nanometer range, however, and hence it is possible that these entered the smallest pore network elements. Unfortunately, developing a water repellent agent which solely forms emulsion droplets in the micrometer range proved excessively difficult.
Since the presence of the water repellent agent in the pores is not visualised directly, it is possible that some isolated pores do remain hydrophilic and/or are blocked by the water repellent agent. However, since these would not guarantee a continuous liquid flow path throughout the sample, their influence on moisture storage and transport are negligible [69]. Extending this analysis to more common building materials with finer pore systems is required in the future.

B.4.2 Partially hydrophobised pore network elements

Previous results have made it clear that the only place for moisture to be stored in these hydrophobised materials is in the hydrophilic corners of partially hydrophobised pore bodies and throats as illustrated in Figure 5.21 (c). The discussion in Section B.3.2 and the results in Figure 5.30 have shown, however, that many of these corner islands disappear when materials are hydrophobised. To investigate the presence of corner islands, the algorithm described in Section B.2.2 is used to label the water islands as filled elements or water in element corners. Figure 5.33 (a) shows the percentage of the sample's total moisture content stored in corners of pore bodies and throats in function of the total moisture content determined from the XCT images of hydrophilic and hydrophobised samples. While the amount of moisture stored in corners is evidently lower in hydrophobised samples, corner islands are not completely eliminated. It should be kept in mind that the labeling algorithm, described in Section B.2.2, is not without errors, especially for small throats. All percentages in 5.33 (a) are therefore somewhat overestimated.
Nevertheless, Figure 5.33 (a) together with the XCT images does show that some water islands can reside in hydrophilic corners of partially hydrophobised pore bodies and throats. Examples of such corner islands are provided in Figure 5.33 (b). This could explain the slight increase in weight during capillary absorption experiments [6,9,17,32,43,51], in which water is transported via vapour diffusion through the pore network and stored in these hydrophilic corners. These corner islands remain isolated occurrences, however, and therefore do not form a continuous liquid corner flow network throughout the sample (like in hydrophilic materials [69]). Their impact on macroscopic moisture storage and transport is therefore limited [69]. This also agrees with the results in Chapter 4, where the absence of liquid moisture flow in hydrophobised materials was noted.



(a) (b)

Figure 5.33: The percentage of the total moisture content stored as corner islands with respect to the overall moisture content for both hydrophilic and hydrophobised samples (a) and examples of such corner islands noticed in the hydrophobised samples (b).

B.5 Summary

This subchapter investigates the microscopic moisture storage in the pore network of hydrophobised materials using XCT imaging. The aim of this investigation is to locate hydrophilic sites in the pore structure of hydrophobised materials which allow moisture storage. To do so, different water repellent agents are investigated. Two main conclusions are produced by this investigation. Firstly, the emulsion droplets, formed during the polymerisation process of the agents, are capable of entering most, if not all, pore bodies and throats of the sintered glass. All pore bodies and throats are therefore assumed to become at least partially hydrophobised.

Secondly, even though hardly any pore network elements remain entirely hydrophilic, some moisture storage proved possible in the hydrophilic pore corners of partially hydrophobised pore network elements. Compared to hydrophilic samples, however, these corner islands are more sparse. The presence of almost no filled pore bodies and throats, together with sparsely distributed corner islands throughout the pore network, does not guarantee a continuous liquid flow path. Moisture transport is therefore dominated by the much slower vapour flow.

It should be mentioned that this study is centered around sintered glass, which is not a typical building material. Its entire network can be visualised using XCT images while the network of more common building materials cannot. Therefore, the investigation should be extended to other materials like ceramic brick or lime mortar once advancements are made with respect to the full-scale

imaging of pore structures of building materials.

Appendix 5.B.1 Water island size distributions of capillary filled pore bodies and throats

The water island size distributions, composed of only the capillary filled pore bodies and throats of the samples hydrophobised with agents B and LM, can be found in Figures 5.34 and 5.35, respectively.

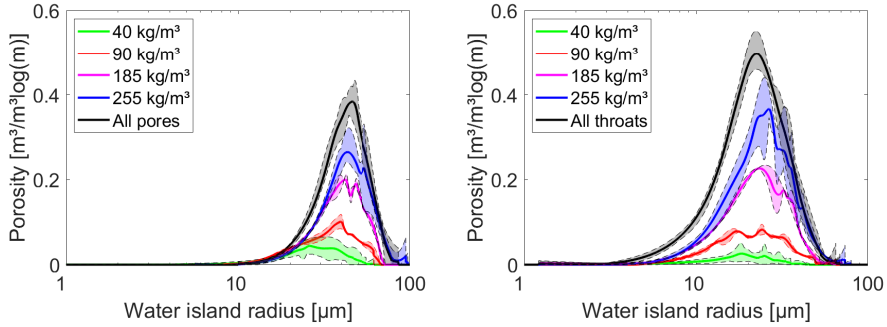


Figure 5.34: The water island size distributions, composed using the capillary filled pore bodies (a) and throats (b) of the samples hydrophobised with water repellent agent B, preconditioned to different moisture contents.

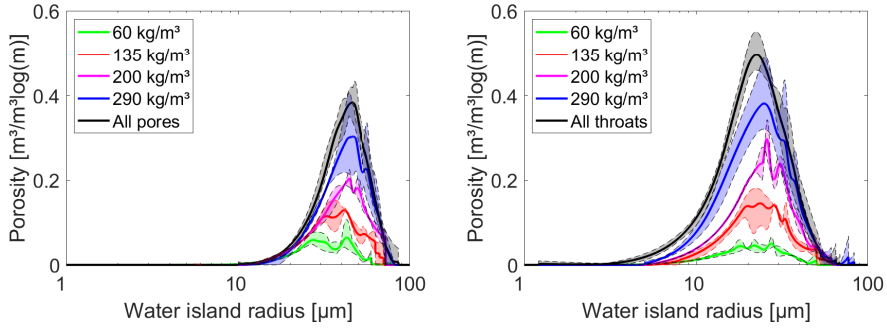


Figure 5.35: The water island size distributions, composed using the capillary filled pore bodies (a) and throats (b) of the samples hydrophobised with water repellent agent LM, preconditioned to different moisture contents.

Chapter 6

Pore network modeling of hygric properties

This chapter handles the prime objective of this PhD thesis: the adaptation and validation of the existing hydrophilically-oriented pore network model (PNM) for the hygric property determination of hydrophobised building materials. The existing hydrophilically-oriented PNM, extensively described in Chapter 3, has previously been validated in Islahuddin and Janssen [23] by comparing the simulated hygric properties with experimentally determined properties. Although this macroscopic validation is crucial to obtain a successful PNM, research has shown that this does not necessarily entail a correct simulation of the microscopic moisture behaviour at pore-scale [62,63]. To this aim, Subchapter A compares the microscopic moisture behaviour in the hydrophilic sintered glass filter, derived from the X-ray computed tomography (XCT) images in Chapter 5, with the simulated microscopic moisture behaviour obtained from PNM simulations. This section aims to microscopically validate the PNM and, resultantly, to also formulate improvements.
Subchapter B then adapts the existing PNM, using the conclusions drawn in Chapter 5, for the hygric property determination of hydrophobised building materials. The outcomes of this adapted PNM (i.e. the simulated hygric properties of hydrophobised building materials), are then validated macroscopically, using the experimentally determined hygric properties of Chapter 4. After validation, the simulated hygric properties of these hydrophobised materials are used in a hygrothermal simulation model to simulate the capillary absorption experiments. This is done with the aim of formulating guidelines to choose a suitable water repellent agent for a certain building material.

Subchapter A is an extended version of journal paper 6.1 below and parts of Subchapter B stem from the conference paper 6.2 below.

Paper 6.1: D. Deckers, H. Janssen. Microscopic validation of a pore network model for hygric properties of porous materials. Transp. Porous Media, 151: 119–140, 2024. doi: 10.1007/s11242-023-02035-y

Paper 6.2: D. Deckers, H. Janssen. The influence of hydrophilic pores on the moisture behaviour in hydrophobised building materials. Proceedings of the 9th International Building Physics Conference, 2024, Toronto, Canada.

A Pore network modeling in hydrophilic porous materials

A.1 Introduction

Regardless of the research area for which a pore network model (PNM) is developed, it is typically validated by comparing measured and simulated macroscopic material properties, such as liquid permeability, moisture retention, ... [23,24,59]. This is also the case for the existing hydrophilically-oriented PNM of Islahuddin and Janssen [23] on which this dissertation is based. Since these PNMs describe microscopic moisture storage and transport processes, however, the validation of a PNM with macroscopic properties does not guarantee a correct representation of the moisture behaviour on a microscopic scale in the individual pores [62,63]. To remedy this, several studies monitor the experimental fluid flow in 2D micromodels to validate their PNMs [69,70]. A comparison at the pore-scale level of the simulated fluid flow in real three-dimensional porous media, however, is still largely missing [62–64,66,205,206]. The studies that do concern themselves with real media typically focus on saturated liquid flow problems, where one liquid (e.g. brine) displaces a second one (e.g. oil), rather than unsaturated flow problems where gas (vapour in air) and liquid (water) coexist, as handled in this thesis. For example, Bultreys et al. [63] imaged the imbibition process of brine displacing decane in water-wet quarry stones and compared these images to the simulated fluid flow.

This subchapter therefore targets the microscopic validation of the previously macroscopically validated PNM for hygric property determination of porous materials [23]. This is done by comparing the microscopic moisture behaviour, visualised using X-ray computed tomography (XCT) images of real three-dimensional porous media in Chapter 5, with the outcomes of the PNM. Several samples are preconditioned to different saturation states to investigate the

correct implementation of the microscopic moisture behaviour over the entire saturation range. To do so, this section is structured as follows. Section A.2 explains how the moisture storage is implemented in the PNM. Section A.3 then compares the results obtained from the PNM with the X-ray computed tomography images described in Chapter 5 and indicates the shortcomings of the PNM. Next, Section A.4 formulates possible improvements to the PNM. Finally, Section A.5 discusses the limitations of the PNM and Section A.6 summarises the most important conclusions.

A.2 Materials and methods

The PNM used in this paper has previously been macroscopically validated [23] by comparing measured and simulated hygric properties of a porous materials. However, as stated in the introduction, previous studies [62,63] have shown that a macroscopic validation does not necessary verify a correct implementation of the microscopic moisture behaviour at pore level. Therefore, the overall goal of this subchapter is to validate the hydrophilically-oriented PNM in a microscopic manner, by comparing the simulated water storage in the individual pores with XCT images made of samples at different stages during the drying process. To do so, the water phase is extracted from the XCT images and the volume of all water islands is plotted against their radius to form a water island size distribution. These distributions are similar to pore size distributions, but only the water phase is considered rather than the entire void space. These water island size distributions were already extracted from XCT images in Chapter 5. The following discussion explains how these distributions are obtained from PNM simulations. First the characterisation of the pore networks of ceramic brick and sintered glass, used as input to the simulations, is described. Next, the extraction of the water island size distributions from the simulations is illustrated. As a reminder, Figure 6.1 shows the different ways in which water can be stored in hydrophilic materials. Once again, liquid films are not incorporated in the water island size distribution, but they are modeled in the PNM as explained in Chapter 3.

A.2.1 Pore network characterisation

The two materials used throughout this dissertation (i.e. the sintered glass filter and the Vandersanden ceramic brick) are discussed in detail in Chapter 2 and throughout the other chapters of this dissertation. Here, they are used for PNM simulations, which require the materials' pore networks as input. These pore networks exist of lists of pore bodies and throats with their topological (e.g. positions and connections) and geometrical (e.g. radii, volumes, shape factors) information and they can be obtained in various ways, as described in Chapter 3. Since the entire pore structure of sintered glass can be visualised

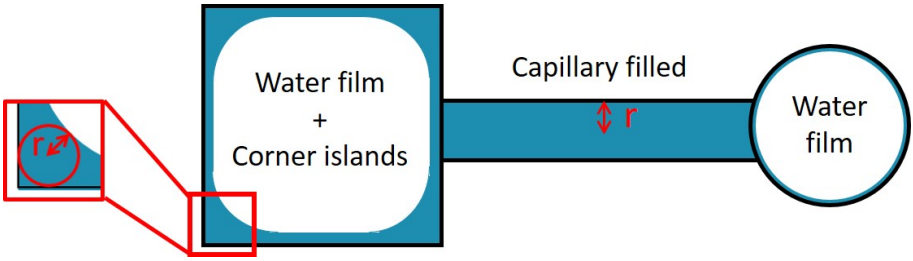


Figure 6.1: An example of the storage mechanisms of water in pores and throats and the radii of the water islands.

with XCT images, its pore network can be extracted directly from these images. Chapter 5 handles the acquisition and segmentation of these images as well as the extraction of pore networks from the processed images in great detail. To account for material heterogeneity, a pore network is extracted from three different sintered glass samples and these three pore networks are used to perform simulations with the PNM.

Since ceramic bricks are composed of nano- and micrometer scale pore bodies and throats [75], complete visualisation of the pore structure with a single imaging method is not possible. Therefore, statistical information of the pore network is gathered at various scales from different imaging methods, after which the brick's pore network is stochastically generated using this multi-scale statistic information. The statistic information on which the pore network generation of ceramic brick is based is shown in Appendix 6.B.1. Once more, three different pore networks are generated and used throughout the simulations. The stochastic generator, used to obtain these pore networks, is an extension of the work in [75,76] and it is validated and applied in [76] for sintered glass. It should be mentioned, however, that this stochastic generator is still being developed and hence the pore networks of brick are the current state-of-the art. A further discussion of the representativeness of these networks of the material's true pore structure is provided in Section B.3.

Since Subchapter A focuses on the microscopic validation of the existing hydrophilically-oriented PNM, it requires imaging the microscopic moisture behaviour in the pore system of the material of interest. Due to spatial limitations of existing visualisation techniques, this is currently only possible for sintered glass and hence the ceramic brick is not used in the simulations of this subchapter. When advancements are made in the research area of microscopy, however, this microscopic validation should be repeated for ceramic brick as well as other common building materials.

A.2.2 Water island size distributions extracted from PNM simulations

A detailed explanation of the PNM and its macroscopic validation can be found in Chapter 3 and [23], respectively. However, some post-processing is required to derive the water island size distributions, used for comparison with the XCT images, from the simulation results of the PNM. After the PNM simulations, all pore bodies and throats are classified as capillary filled or empty and the volume of moisture in each element is individually calculated. To compose the water island size distributions, however, the radii of the water islands, illustrated in figure 6.1, are also required. In capillary filled elements, the water islands' radii equal the radii of the pore bodies or throats themselves and they are hence easily derived from the extracted pore network. The radii of corner islands, however, are not computed in the original PNM. The amount of moisture in pore corners is represented by the calculated corner volume fraction (see Equation 3.3 in Chapter 3), which denotes the fraction of the pore's volume that is filled by moisture in corner islands. This moisture volume in pore corners is subsequently used to determine the conductances in the pore network, which are required to calculate the moisture permeability of the material. The radius of these corner islands is therefore not required for the hygric property determination. The microscopic validation in this chapter, however, requires the extraction of water islands size distributions from the PNM simulations and hence both radii and volumes of corner islands are required.

To calculate the radii of these corner islands, an assumption about their shape therefore has to be made. In this dissertation, it is assumed that all water islands in pore corners, in both triangular as well as square pores, can be represented by equilateral triangles. Since more than 85% of pore bodies and throats of the extracted pore networks are classified as triangular by their shape factor G (see Chapter 3), this corner shape represents reality relatively well. The total moisture volume in a single pore, calculated using the corner volume fraction, is equally divided amongst the pore's corners. The volume in every corner then equals the volume of the equilateral triangle ($V_{corner} = \sqrt{3}/4 * H^2 * L$) in Figure 6.2, with L being the porelength in the third dimension obtained from the pore network extraction. This allows calculating the height H of the triangle and subsequently the radius r of the inscribed circle (and hence of the corner island).

The same analysis is also performed for corners shaped like isosceles triangles with a varying pore corner angle (α). The inscribed maximal spheres in these isosceles triangles are smaller and therefore so are the water island radii. A goniometric calculation shows that the corner island radii are reduced by a maximum of 1.7 for very sharp (10°) and very obtuse (140°) angles, which has a limited effect on the overall results as shown further in section A.3. A final possible remark is that the real corner islands exist of a curved air/water interface rather that a straight one as shown in Figure 6.2. Since results of the

PNM are compared to XCT images, where pixelation also blurs this curved interface, the assumption of a straight water/air interface does not induce large errors.

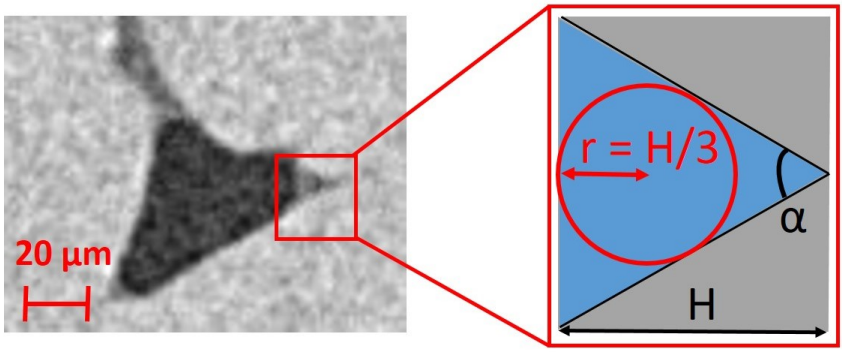


Figure 6.2: An illustration of the assumed shape of a water island in a pore corner.

A.3 Results

This subchapter aims at microscopically validating the hydrophilically-oriented PNM by comparing the simulated water island size distributions at various saturation states to the results obtained from XCT images, discussed in Chapter 5. To do so, the water island size distributions acquired from PNM simulations are first discussed in Section A.3.1, after which they are compared to the results obtained from XCT images in Section A.3.2, wherein subsequently shortcomings of the PNM are indicated.

A.3.1 Water island size distributions simulated with the PNM

The XCT images, investigated in Section A.4 of Chapter 5, resulted in water island size distributions obtained for samples preconditioned to four different moisture contents: 60 kg/m^3, 125 kg/m^3, 165 kg/m^3 and 255 kg/m^3. To allow comparing the results from the PNM with these XCT images, the same four moisture contents are assessed. To do so, the PNM simulates the drainage process, illustrated in Chapter 3, until samples acquire these moisture contents. This means that the reigning capillary pressure does not necessarily agree with the one imposed by the centrifuge on the experimental samples. This is worth noting since the capillary pressure influences corner island and water film formation as explained in Chapter 3. Matching the capillary pressures of the

samples in the PNM with the one calculated for the centrifuge preconditioning (using Equation 4.2 in Chapter 4) would result in samples with different moisture contents and resultantly, comparison of the experimental and simulated water island size distributions becomes difficult. It is therefore chosen to match the moisture contents of the experimental samples using the PNM simulations since they are easily derived from gravimetric measurements after centrifugation.
The water island size distributions, simulated with the PNM for the four moisture contents of interest, are shown in Figure 6.3. The simulations are performed on three different pore networks and the average distribution (line) as well as the shaded area encompassing all distributions are shown. As explained in Section A.2.2, composing the water island size distributions requires assuming the pore corner shape to calculate the radius of the water islands in these corners. This radius is largest for a corner shaped like an equilateral triangle and decreases when this triangle transforms into an isosceles triangle, making the angle sharper or more obtuse. The results in Figure 6.3 show the extreme cases where the radii of the water islands in the pore corners are largest (equilateral triangles) and smallest (isosceles triangle). The latter assumes that all pore corners have an angle of 10° or 140°. In reality, the wide array of pore corner shapes will transform the distinct peak of small water islands into a more broad distribution that extends between the two extremes displayed in Figure 6.3. Since even these two extreme situations are not that different, the comparison of the results from the PNM with the XCT images is solely based on the assumption of equilateral corner islands to not overcomplicate the results' visual representation.
Chapter 3 explains that the hydrophilically-oriented PNM assumes perfect wetting of the pore structure. The influence of wettability on the water island size distributions is investigated by performing the same simulations, with equilateral triangular corners, for contact angles of 0° and 60°. Figure 6.3 shows that a deviation from perfect wetting causes more of the total moisture to be stored in pore corners and less in capillary filled elements. As a result, the largest water islands disappear from the distributions. Further comparison of the PNM with XCT images shall prove that deviating from the perfect wetting case and storing more moisture in pore corners does not guarantee a better fit with results derived from the XCT images. Nevertheless, it is interesting to keep the distributions derived with higher contact angles in mind.

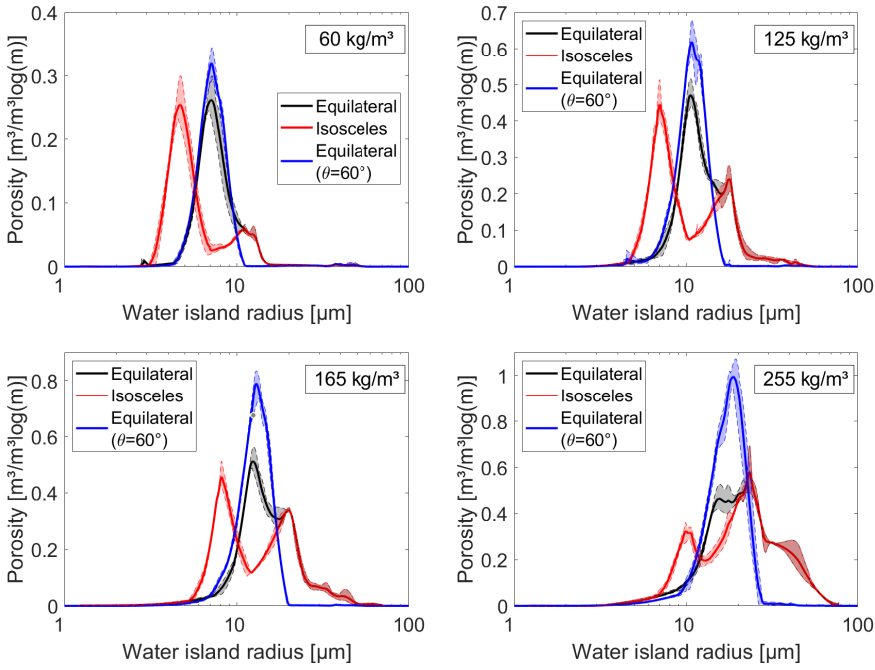


Figure 6.3: The water island size distributions calculated using the PNM for samples with a moisture content of 60 kg/m^3, 125 kg/m^3, 165 kg/m^3 and 255 kg/m^3 and with the assumption of equilateral (both for contact angles equal to 0 °and 60 °) and isosceles water islands in the pore corners.

A.3.2 Comparison of the results from the PNM and the XCT images

The water island size distributions acquired from the XCT images as well as simulated with the PNM are compared in Figure 6.4. Overall, both techniques record the presence of equally large water islands and at first glance, the PNM therefore approaches the distributions obtained from the XCT images in an acceptable manner, especially when the sample contains a high moisture content (255 kg/m^3). However, the comparison worsens when the moisture content decreases. The largest water islands from XCT are missing in the results from the PNM and instead there is an abundance of small water islands, possibly caused by an overestimation of the amount of water stored in the pore corners.

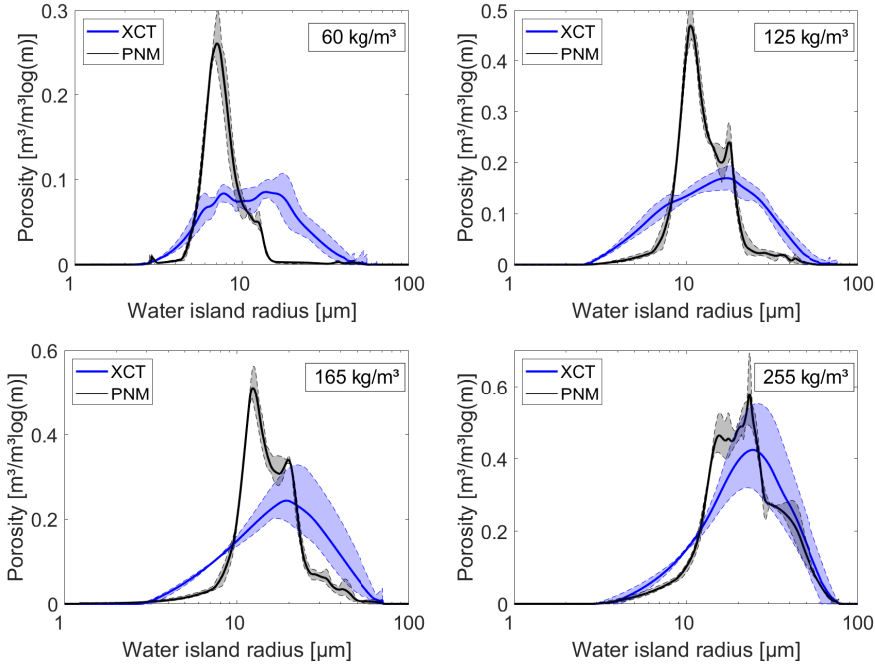
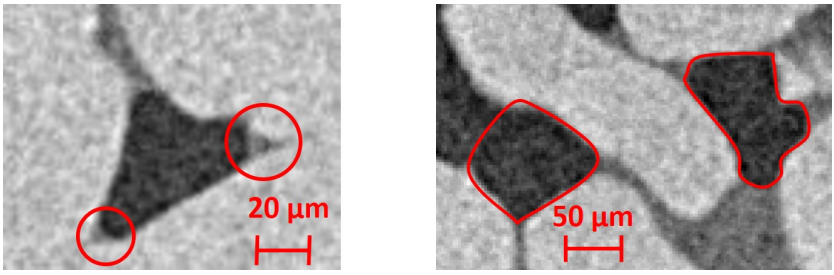


Figure 6.4: The water island size distributions calculated using the PNM and derived from the XCT images for samples with moisture contents of 60 kg/m^3, 125 kg/m^3, 165 kg/m^3 and 255 kg/m^3.

According to the PNM, samples with a moisture content of 60 kg/m^3, 125 kg/m^3, 165 kg/m^3 and 255 kg/m^3 store 72 %, 53%, 39% and 14 % of this moisture in pore corners, respectively. This is a result of the fact that the PNM assumes that every single (non-circular) empty element stores water in its corners and that these water islands keep growing for increasing capillary pressures (as can be deduced from Equation 3.3 in Chapter 3). A closer look at the results from the PNM shows that the average radius of a water island in a single corner increases from 7 µm to 15 µm when the sample's moisture content increases from 60 kg/m^3 to 255 kg/m^3. It is important to note that this is the radius of a water island in a single corner of an element and that three or four of these corner islands can therefore coexist in such elements. The current implementation of the PNM makes it possible for some pores, classified as empty, to still contain enough moisture in their corners to fill 80 % of the pore volume.

To investigate whether these large corner islands actually occur in porous media, the XCT images are reanalyzed. Figure 6.5 shows examples of typical pores

with (a) and without (b) corner islands. The corner islands in Figure 6.5 (a) are encircled and the other water island, connected to this pore, is a capillary filled throat. It is important to mention that these figures are 2D representations of 3D pore bodies and throats and they should therefore be treated solely as examples. The pores without corner islands do border on pools of water, but these are all capillary filled pore throats connecting different pore bodies. The assumption of corner islands in every single pore body or throat, as implemented by the PNM, is therefore not valid. The non-existence of these corner islands in some elements is consistent with micromodel experiments on both drainage [207] as well as imbibition [70] of water in porous media.
A further investigation of the pore with corner islands is performed by first isolating it from the segmented XCT images after which its pore network and its water island network are extracted using PNextract [97]. From the geometrical information of both extracted networks, the total pore volume as well as the total moisture volume is retrieved and the volume fraction, occupied by the liquid corner islands, can be deduced. This procedure is repeated for three different corner islands and the volume fractions equal 3 %, 6 % and 8 %, nowhere near the volume fractions calculated with the PNM. Although the analysis is limited to three pores, the XCT images are extensively investigated to make sure that these three corners are representative of the others rather than outliers. The current implementation of the PNM hence overestimates the amount of moisture which can be stored in pore corners. This conclusion is currently only valid for the studied sintered glass and future validation on other materials is necessary.

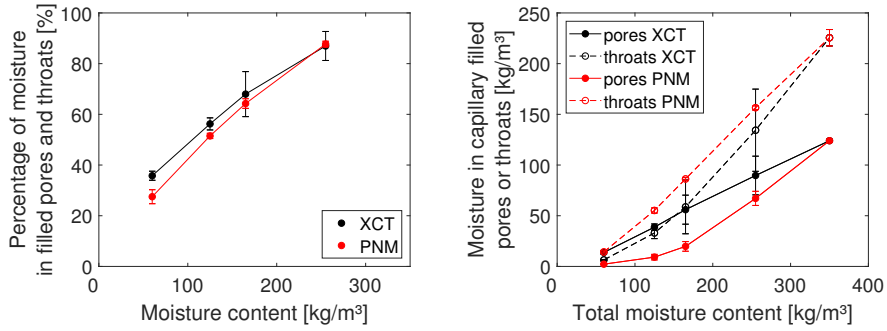


(a) (b)

Figure 6.5: Examples of empty pores with (a) and without (b) corner islands.

With the help of the algorithm described in Section B.2.2 of Chapter 5, the water islands, extracted from XCT images, are subdivided into capillary filled elements or corner islands. The same classification is also performed for the results extracted from the PNM. Figure 6.6 (a) shows the percentage of the sample's total moisture stored in filled elements in function of the sample's

total moisture content (i.e. 60, 125, 165 or 255 kg/m³). It is important to keep in mind that some of the smallest capillary filled throats in the XCT image can be mislabeled as corner islands as explained in Section B.2.2 of Chapter 5. The percentages calculated from the XCT images are therefore slight underestimations. Figure 6.6 (a) once more confirms that the PNM simulates too much moisture in the element corners. This phenomenon is more pronounced for lower total moisture contents since more empty elements, in which corner islands can be stored in the PNM, are present. Calculating the corner volume fractions purely based on the pore's geometrical properties and the reigning capillary pressure, as done in the current PNM [122], is hence not sufficient.



(a) (b)

Figure 6.6: The percentage of the moisture in filled elements (a) and the amount of moisture in filled pores and filled throats in funtion of the sample's total moisture content (b) for the results acquired from XCT images and PNM simulations.

Besides distinguishing between moisture in capillary filled elements and corner islands, one can also distinguish between moisture in filled pore bodies and filled pore throats. This sheds light on the correctness of the invasion percolation algorithm, which models the emptying sequence of all pore network elements. Figure 6.6 (b) shows the amount of moisture stored in capillary filled pore bodies or throats, separately, in function of the sample's total moisture content in both the XCT images and PNM simulations. By reading this figure from high to low moisture content, one can follow the emptying sequence of pore bodies and throats. This shows that the amount of moisture in the filled pore bodies is consistently underestimated in the PNM. In other words, the pore bodies empty too quickly during the modeled drying process. Since the percolation algorithm is more likely to empty the largest elements first, the (larger) pore bodies are regularly emptied before the (smaller) pore throats. Resultantly, pore throats,

which per definition connect two bigger pore bodies, often remain filled while the pore bodies empty. These types of isolated filled throats are sporadically visible in the XCT images as shown in Figure 6.7. Although this image shows quite a lot of these isolated throats, it should be mentioned that this example is a single slice of a 3D image and often these throats are still connected to filled pore bodies in the third dimension. The amount of isolated filled throats is therefore overestimated in the PNM simulations due to the nature of the simplified invasion percolation algorithm.

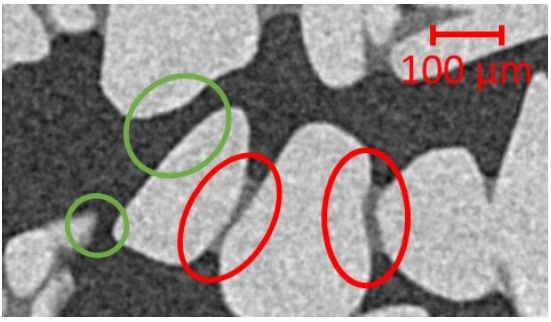


Figure 6.7: An XCT image with examples of isolated filled throats (red) and empty throats (green).

The isolated filled throats, shown in Figure 6.7, are per definition in contact with the air phase on both sides. Therefore, it is possible that some of these isolated filled throats evaporate over time. Alternatively, some moisture redistribution from these isolated throats to pore corners can also occur. Experimental [203] and numerical [84] studies on convective drying of porous media show that almost no isolated filled throats remain in such drying processes. The current invasion percolation algorithm therefore does not fully replicate the material's drying behaviour, possibly because evaporation and/or moisture redistribution are not modeled in the PNM. It should be mentioned that the presence of such isolated filled throats is also heavily dependent on the pore network extraction, in which the continuum pore space has to be divided into individual pore bodies and throats [86,87]. In other words, using a different pore network extraction method might increase or decrease the amount of isolated filled throats present in the pore network. Nevertheless, the invasion percolation algorithm is slightly adapted in next section to limit the amount of isolated filled throats with the aim of investigation the impact of this percolation algorithm on both the microscopic and macroscopic moisture behaviour.
Although perfect representations of both the drying sequence of the pore network elements as well as the amount of moisture stored in element corners cannot be obtained without more detailed simulations, the next section formulates

recommendations to improve the current implementation of the PNM. The impact of these simple changes to the PNM on the microscopic moisture behaviour is investigated and the resulting macroscopic hygric properties are compared to the original PNM outcomes.

A.4 Recommendations for possible model improvement

This section formulates possible changes to the PNM which solve the problems identified in previous section and investigates their impact on the microscopic and macroscopic level. The two main problems are the overestimation of the amount of water in the corner islands and the implementation of the simplified invasion percolation algorithm, which are handled in Sections A.4.1 and A.4.2, respectively. Section A.4.3 then more closely investigates the best PNM implementations of the previous sections. Finally, Section A.4.4 investigates the impact of the implemented changes on the simulated hygric properties. Since previous section showed that water island size distributions, simulated using the three pore networks, are very similar, only the average water island size distributions are shown in this section to not clutter the figures. It should be mentioned that the recommended model improvements in this section are solely focused on the moisture behaviour in sintered glass. Their applicability needs to be checked for other materials with finer pore systems (e.g. ceramic brick or lime mortar) in future work when advancements in imaging techniques allow it.

A.4.1 Overestimation of the corner islands

The current implementation of corner islands in the PNM assumes that all (non-circular) elements possess corner islands, of which the amount of moisture in such corners is only limited by the elements' volumes. Limiting the amount of moisture, stored in such corner islands, can hence easily be done by either limiting the amount of moisture in each corner or by removing the corner islands from certain pore bodies and throats. The former is implemented in the PNM by limiting the pore volume which can be occupied by the corner islands to a predefined percentage (i.e. a predefined maximum volume fraction $S_{c,max}$). In other words, the volume of the water islands in element corners is still calculated according to 3.3 in Chapter 3, but it is limited to 1%, 10% or 100% of the element's volume.

Removing the corner islands from several pore network elements is more difficult. From current XCT images, it is unclear which elements are capable of storing such corner islands and which are not. Mostly because the necessary transformation from pore space to a stick-and-ball pore network makes it difficult to assign corner islands to single elements. The pore space of sintered glass is typically composed of three times as many pore throats as pore bodies. As a result, 70-80 % of the water in element corners is located in throat corners.

Additionally, these throats are simplified as having a constant cross-section across their length. The corner islands are therefore also assumed to extend over the throat's entire length and hence there is a continuous (fast) liquid flow path across each element. Previous studies have highlighted the impact of these fast continuous flow paths on the macroscopic permeability [69]. Pore body and throat corner islands, however, are typically local irregularities, as shown on Figure 6.5 and are hence less likely to exist over the entire throat's length. To mimic the extreme case of discontinuous corner flows, the PNM is changed to remove all corner islands from pore throats. Although this is a drastic change to the implementation of the PNM, it is implemented here to investigate the impact of the extreme case of discontinuous corner flows on the hygric properties of the PNM. The corner islands in pore bodies are calculated as in Equation 3.3, however, also with $S_{c,max}$ set to 1%, 10% or 100%.

Figure 6.8 shows the simulated water island size distributions with $S_{c,max}$ equal to 1 %, 10 % and 100%, with (–) and without (- -) corner islands in the pore throats. When the volume fraction of corner islands is limited to 10% and corner islands can exist in pore throats (red line), results of the PNM agree well with the XCT images for the three samples with the highest moisture contents. Simulations for the sample preconditioned to 60 kg/m^3, however, still overestimate the contribution of the small corner islands. Limiting the volume fraction to 1% has an adverse effect on the distributions to the point where the amount and size of corner islands is now underestimated for all saturation states besides 255 kg/m^3. In this extreme case, corner islands hardly exist, which does not agree with XCT images. It is possible to further optimize the maximum volume fraction to guarantee the optimum fit for the sample preconditioned to 60 kg/m^3, however, one should keep in mind that solely limiting this $S_{c,max}$ does not mimic reality.

When corner islands are removed from throat corners (dotted lines), the amount of water islands smaller than 10 µm are underestimated in all samples. Seeing as the pore network of sintered glass exists of three times as many pore throats as pore bodies and the ability of moisture storage in these throat corners is removed, a large part of the moisture stored in small corner islands is missing. Removing corner islands from pore throats therefore does not necessarily improve the PNM. Nevertheless, this extreme case is further used to investigate the impact of discontinuous corner flows on the macroscopic hygric properties of a sample in Section A.4.4.

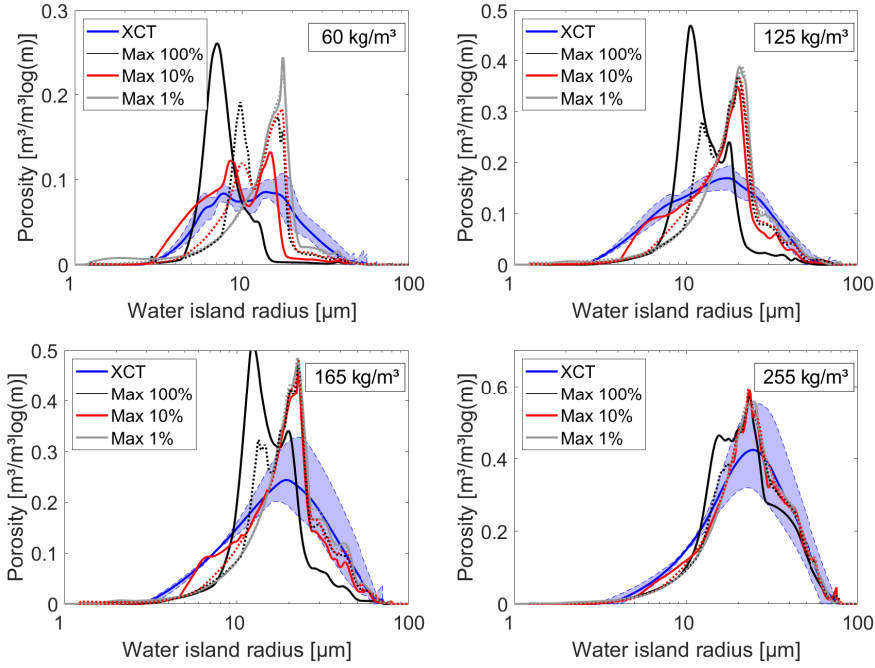


Figure 6.8: The water island size distributions calculated using the PNM and derived from the XCT images for samples with a moisture content of 60 kg/m^3, 125 kg/m^3, 165 kg/m^3 and 255 kg/m^3 and maximum corner volume fractions of 1 %, 10% and 100 %, with (–) and without (- -) throat corner islands.

A.4.2 Adapted invasion percolation algorithm

The current implementation of the invasion percolation (IP) algorithm always empties the biggest element, viable to be emptied next, at every step. This results in many isolated filled throats which are connected to two empty pore bodies. As explained in Section A.3.2, these isolated filled throats are rather scarce occurrences in the XCT images. Therefore, the extreme case is investigated, where no isolated filled throats can exist. This change is implemented by locating and emptying any filled throats which become isolated every time a pore body is emptied in the percolation algorithm. It should be mentioned that this adaptation of the PNM is not based on a physical phenomenon, but that it is simply implemented here to investigate and illustrate the influence of the percolation algorithm on the results of the PNM. As explained before, this presence of isolated filled throats can be influenced by the non-unique pore network extraction of sintered glass [86,87] and this

phenomenon could therefore be much less present if a different extraction algorithm (or a different material) would be used.

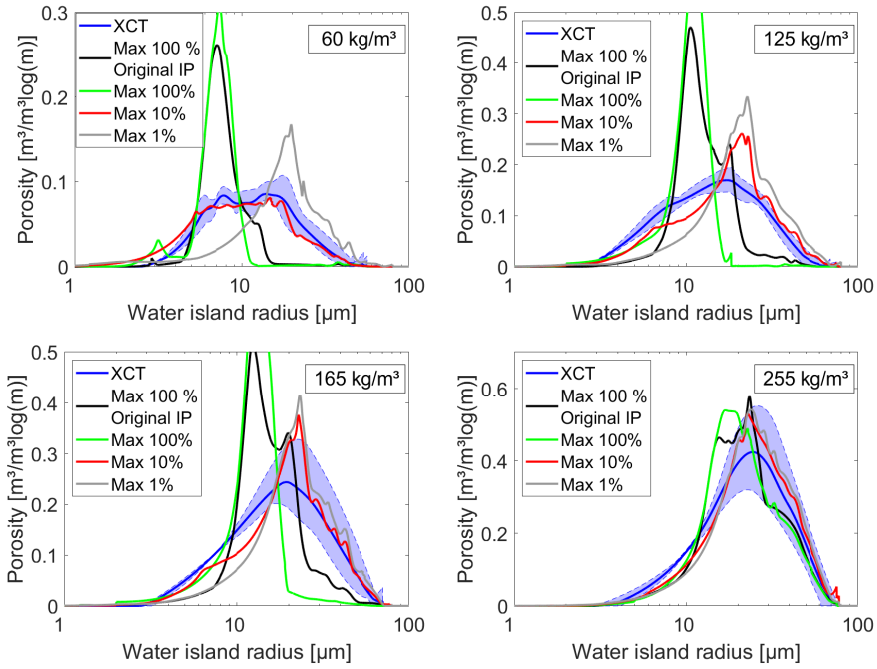


Figure 6.9: The water island size distributions calculated using the PNM and derived from the XCT images for samples with a moisture content of 60 kg/m^3, 125 kg/m^3, 165 kg/m^3 and 255 kg/m^3 and maximum corner volume fractions of 1 %, 10% and 100 %, with the adapted invasion percolation algorithm.

Figure 6.9 shows the water island size distributions extracted from simulations using the adapted invasion percolation algorithm with $S_{c,max}$ equal to 1%, 10% or 100%. The distributions, extracted using the original invasion percolation (IP) algorithm with a maximum corner fraction of 100 % and already displayed in Figure 6.4, are also shown for reference. The adapted percolation algorithm causes throats to empty quicker than in the original implementation. When these throats empty, water islands are assumed to be stored in their corners. If the volume fraction of these corner islands is not limited (i.e. $S_{c,max}$=100%) the majority of the moisture in a sample is stored in the throat corners, especially at low overall moisture contents. This causes the samples, preconditioned to 60 kg/m³ and 125 kg/m³, to store 84.7 % and 84.5 % of their moisture in throat corners. Limiting these volume fractions is therefore required. An $S_{c,max}$ of 10% shows good agreement with the results obtained from XCT images, while

an $S_{c,max}$ of 1% once again underestimates the amount of moisture stored in corners.

A.4.3 Best PNM implementations

From all the different PNM implementations, there are two which agree best with XCT images. Firstly, the PNM with $S_{c,max}$ equal to 10 % and the ability to store moisture in throat corners (the red curves in Figure 6.8). Secondly, the PNM with the adapted invasion percolation (IP) algorithm and $S_{c,max}$ equal to 10 % (the red curves in Figure 6.9). For a further investigation, Figure 6.10 shows the amount of moisture in the capillary filled pores and throats, separately, in function of the total moisture content of the sample, similarly to Figure 6.6. The PNM with $S_{c,max}$ of 100% are the results derived from the original PNM and they are given as reference. The PNM with the adapted invasion percolation algorithm and a $S_{c,max}$ equal to 10% predicts approximately the same amount of moisture in the filled pore bodies as the XCT images. The amount of moisture in filled pore throats, however, is still underestimated. It should be mentioned that the results from the XCT images mislabel some filled pore throats with radii smaller than 10 µm as explained in Section B.2.2 of Chapter 5 and hence the amount of moisture in filled pore throats is slightly underestimated in XCT images.
Although the PNM with the adapted invasion percolation algorithm and a $S_{c,max}$ equal to 10% performs best, it is definitely not perfect. This PNM implementation still assumes corner islands to be present in all (non-circular) elements. Also, some isolated throats were proven to still exist in materials while they are completely eliminated from this implementation. One should keep in mind that a perfect match between XCT images and PNM results is unlikely because of the necessary simplifications made in the PNM. Next section investigates the impact of these PNM adaptations on the simulated hygric properties.

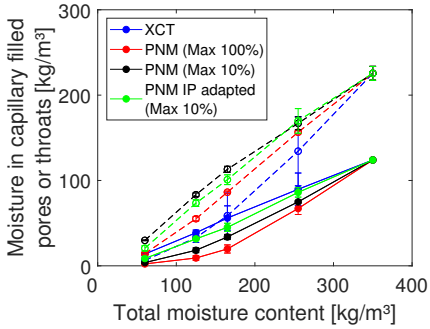


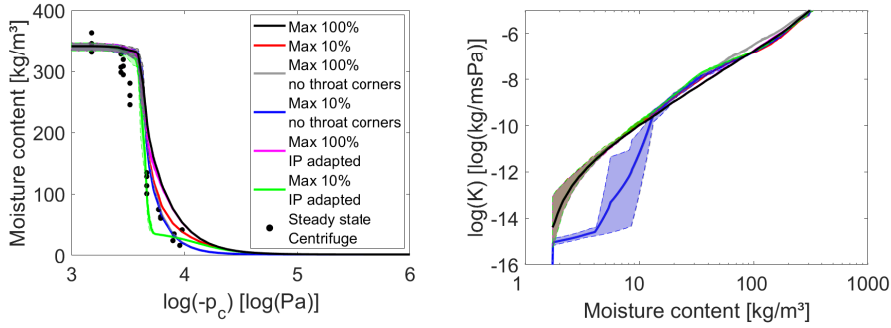
Figure 6.10: The amount of moisture in filled pore bodies (–) and throats (- -) derived from XCT images, the original PNM (i.e. with a maximum corner island volume fraction of 100 %), the PNM with a maximum corner island volume fraction of 10 % and the PNM with the adapted invasion percolation (IP) algorithm and a maximum corner island volume fraction of 10 %.

A.4.4 Impact on macroscopic hygric properties

Previous section investigates a wide array of changes to the PNM at a microscopic level. However, since the main goal of the PNM remains the simulation of the hygric properties of building materials, the impact of these changes on a macroscopic level is arguably more important. Figure 6.11 shows both the moisture retention curves (a) and the liquid permeability curves (b), simulated with the original as well as the adapted PNM's. This includes the PNM with the original percolation algorithm, with and without throat corner islands, and with a $S_{c,max}$ of 10 % and 100 % and the PNM with the adapted percolation algorithm (IP adapted) with an $S_{c,max}$ of 10 % and 100 %. The results with $S_{c,max}$ equal to 1 % are omitted because they already showed large discrepancies at microscopic level with the XCT results. Since a maximum volume fraction of 1 % is very low, one can approximate these results by simply omitting the corner flows in the model. Islahuddin et al. [23] already showed that this has a significant (and unrealistic) impact on the hygric properties. It should be noted that the PNM with the original percolation algorithm and an $S_{c,max}$ of 100 % (red curves) is the original implementation and these hygric properties have therefore previously been validated in Islahuddin and Janssen [23].

Although the microscopic analysis showed significant discrepancies between simulated water island size distributions of the different PNM implementations, the variation of the hygric properties is smaller. The moisture retention curve varies most, while the liquid permeability remains almost constant. Only at low overall moisture contents, when throat corner islands are completely removed, the moisture permeability is significantly affected by the discontinuous corner

flows. This is consistent with previous research [69] where it is shown that completely eliminating the continuous corner flow does not agree with reality. The moisture retention curves all agree to some extent with the results from the steady state centrifuge experiment, discussed in Chapter 4, however, differences amongst the PNM implementations can still be noted.



(a) (b)

Figure 6.11: The moisture retention (a) and permeability (b) curves simulated with the different versions of the PNM and the moisture retention curve derived from the steady state centrifuge experiment in Chapter 4.

A.5 Discussion

Two main problem areas in the implementation of the PNM are identified in the results section. The first problem is that the moisture stored in pore body and throat corners is currently overestimated. A different way of determining in which pore corner water can be stored as well as the amount of water that can be stored in such corners is hence necessary. Consulting the literature shows that the accurate simulation of these corner islands is typically based on more complex (dynamic) models, capable of simulating the moisture supplied to and evaporated from these corners [27,69,208]. Zhao et al. [27] for example use a hybrid simulation approach which tracks the progression of the drying front by performing lattice-Boltzmann simulations (i.e. direct modeling) in the voxels surrounding the water interface and pore network simulations in the voxels further away. This allows a better computation of the formation of the corner islands at the expense of an increased computation time. As explained in Chapter 3, however, the pore networks, which are representative of the building materials, are typically too large for the increased computation time of dynamic and direct (or even hybrid) modeling approaches. The quasi-static pore network

modeling approach, as implemented in the PNM in this dissertation, therefore remains the desired, if not the only viable, computational method.
In such a quasi-static approach, the sizes of corner islands are typically calculated based on the pore's geometry and the imposed capillary pressure as indicated by equation 3.3. Other quasi-static approaches in literature, which simulate corner storage, are based on the same principles [28]. A different expression, which allows calculating the size of the corner islands in such a quasi-static approach, is hence vital for the model's pore level validation. Limiting the volume occupied by these corner islands to a percentage of the pore's volume, as proposed in this study, is simple in nature and has a clear effect on the water island size distributions. However, it does not necessarily agree with the actual moisture behaviour. A detailed study of the occurrence of corner islands in actual porous media using microscopy imaging methods is therefore required to further optimise such quasi-static PNM's. The currently used algorithm of Section B.2.2 in Chapter 5, however, is too sensitive to slight deviations during the pore network extraction from XCT images to designate corner islands to individual pore bodies and throats. Therefore, such a study does require a more elaborate processing of the XCT images (e.g. [63,65]). It is important to remember, however, that other simplifications in the PNM, such as the invasion percolation algorithm and the non-unique representation of the pore network [86,87], also influence the results obtained from the PNM and hence a perfect agreement with XCT images is unlikely.
The second problem area in the PNM is the current implementation of the invasion percolation algorithm. Due to its preference towards emptying the (larger) pore bodies prior to the (smaller) pore throats, it creates many isolated filled pore throats connected to empty pore bodies. XCT images, however, show that these kinds of isolated filled throats only occur sporadically. This is possibly caused by evaporation of water in these filled throats once they are no longer connected to a larger body of moisture. Chakraborty [202], for example, shows evaporative drying of such isolated throats, albeit with larger radii, in 30 minutes to an hour in a lab environment. Preconditioning of the samples in this thesis took longer than this timespan and hence evaporation of the moisture from some (if not most) of these pore throats is possible. Alternatively, it is possible that some of the moisture in these isolated filled throats is redistributed to pore and throat corners after centrifugation. Completely eliminating these isolated throats from the PNM (i.e. using the adapted percolation algorithm) also showed the best microscopic agreement with XCT results.
To solve these problems, several alternative PNM implementations are proposed. Comparison of the simulated water island size distributions with XCT images showed that limiting the maximum volume fraction of corner islands in elements to 10 % is crucial in somewhat agreeing with XCT images. Adapting the percolation algorithm to eliminate isolated filled throats also slightly improved

the microscopic moisture distribution. Eliminating all isolated filled throats, however, does not agree with the XCT results, which is why further simulations on hydrophilic media can use both models with and without the adapted percolation algorithm, in which the maximum volume fraction is always limited to 10 %. It should be noted that the different implementations of the PNM had a smaller effect on the simulated macroscopic hygric properties than on the microscopic moisture behaviour. One could therefore argue that a good microscopic agreement between distributions derived from XCT images and PNM simulations is sufficient, especially since a perfect agreement is unlikely due to the multiple necessary simplifications and assumptions implemented in the PNM.

The microscopic validation in this subchapter is solely based on microscopic images of sintered glass and hence some of these problems (e.g. isolated filled throats) could be material-specific and might not occur in other materials like ceramic brick. This microscopic validation should therefore be repeated in the future on different materials to assess the general applicability of these changes to the PNM. The simple solutions proposed in this subchapter are not in vain though, as it has been shown in literature that tailoring your PNM to some experimental properties (e.g. microscopic water island size distributions and moisture retention curves), reinforces the confidence in other simulated properties, which are much harder to measure experimentally (e.g. unsaturated permeability) [88–90]. Therefore, the better microscopic agreement between XCT images and PNM simulations after the implementation of these solutions makes the model more reliable for simulation of the macroscopic hygric properties of sintered glass.

As a last remark, it is important to highlight the importance of eventually obtaining a sufficiently validated PNM. While the need for a more efficient hygric property determination to replace the cumbersome experimental work has previously been highlighted, the information regarding water storage on a pore-by-pore basis has different interesting applications as well. This PhD dissertation has shown that it is possible to acquire such pore level information from XCT images, however, this is a time-consuming affair. A single sample, preconditioned to a certain moisture content, requires 1 day to precondition, two hours to acquire the images and 1 day to segment the images, extract the water phase and calculate the water island size distributions. Hence, after approximately two days of experimental work, a distribution is obtained for a sample preconditioned to a single moisture content. The PNM, however, requires a single simulation with a duration of 30 minutes to obtain the same water island size distributions for every possible saturation state simultaneously. The more efficient character of the PNM, combined with its lower computational demand, therefore justifies the need for the future work on pore network modeling approaches.

A.6 Summary

This subchapter microscopically validates the hydrophilically-oriented PNM by simulating water island size distributions using the PNM and comparing them with distributions obtained from XCT images. When comparing these distributions, two main problems are detected. Firstly, the amount of moisture stored as corner islands in the PNM is overestimated. The PNM implementation assumes that all pore corners contain moisture and that this amount of moisture is calculated based on the pore's geometry and the capillary pressure. This allows up to 80 % of some elements' volumes to be filled with corner islands, which does not agree with observations from the XCT images. Secondly, the invasion percolation algorithm tends to empty the (larger) pore bodies prior to the (smaller) pore throats, which creates many isolated filled throats connected to two empty pore bodies. XCT images, however, show that these isolated filled throats are a rather unique occurrence.

Both problems are addressed by creating several variations of the existing PNM and subsequently microscopically validating them using the XCT images. A reduction of the amount of moisture in the corners of empty elements has shown to be vital to approach a microscopic validation of the PNM. Limiting the volume fraction of moisture in corners to 10 % shows the best results and further simulations of sintered glass will continue using this maximum volume fraction. Additionally, adapting the PNM to remove all isolated filled throats shows a promising agreement with XCT images. Nevertheless, this does not fully agree with reality where such filled throats still occur sporadically. Validation of these models, using different materials, with other types of pore networks, remains necessary before it can be deemed fully validated.

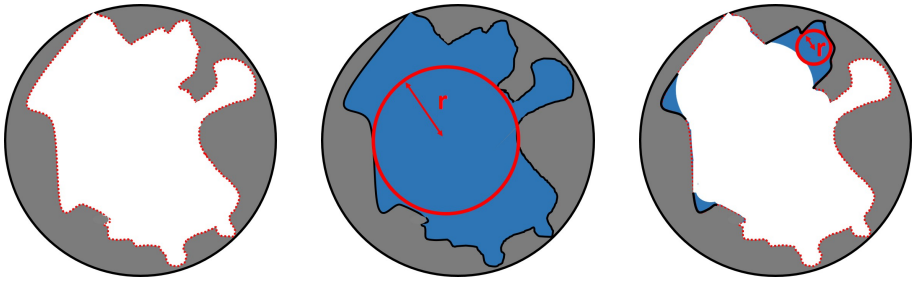
Finally, it is shown that all these different implementations have a more limited effect on the simulated macroscopic hygric properties for the investigated sintered glass. Since these properties are the main purpose of the PNM, one could argue that a perfect microscopic agreement with XCT images is not required. Additionally, such a perfect agreement remains unlikely seeing as the quasi-static pore network modeling approach requires multiple assumptions and simplifications.

B Pore network modeling in hydrophobised porous materials

B.1 Introduction

This subchapter focuses on the prime objective of this PhD thesis, the pore network modeling of hygric properties of hydrophobised building materials. The existing hydrophilically-oriented PNM of Islahuddin and Janssen [23], used in Subchapter A, is adapted for hydrophobised materials by using the conclusions of the microscopic investigation in Chapter 5, Section B. The adapted PNM is subsequently validated with the experimentally determined hygric properties of hydrophobised materials, measured in Chapter 4, Section B. To put the simulated hygric properties into perspective, they are also used to simulate the capillary absorption experiment, typically performed to assess a hydrophobisation application's efficiency, using the hygrothermal simulation model Delphin [209]. The adaptation and validation are subsequently discussed in Sections B.2 and B.3. The discussion of these results in Section B.4 and a reiteration of the most important conclusions of this part of the dissertation in Section B.5 finalise this chapter.

As a reminder, Figure 6.12 shows the different ways in which a pore body or throat can become hydrophobised [30,32]. If the emulsion droplets, formed by the polymer chains of a water repellent agent, are much smaller than the pore network element, it enters easily and renders (part of) the pore walls hydrophobic. Examples of a fully and partially hydrophobised element are shown in Figure 6.12 (a) and (c), respectively. However, if the emulsion droplets are of a similar magnitude or larger than the pore network elements, their pore walls remain unaffected and these elements therefore remain hydrophilic as in Figure 6.12 (b). Additionally, it is possible that their entrance becomes blocked by the polymer droplets hereby rendering the element completely inaccessible for moisture. For a more detailed description of the hydrophobisation application, the reader is referred to Chapter 2.



(a) (b) (c)

Figure 6.12: Examples of the cross-section of a completely hydrophobic pore (a), a completely hydrophilic pore (b) and a partially hydrophobic pore (c) with the hydrophobised pore surfaces represented by a red dotted line.

B.2 Adaptation of the hydrophilically-oriented PNM

The adaptation of the hydrophilically-oriented PNM for hygric property determination of hydrophobised materials is based on following conclusions from Chapter 5. These conclusions are valid for all tested sintered glass/water repellent agent combinations in Chapter 5 and hence the adapted model can be used for any of the tested hydrophobised materials.

- No completely hydrophilic pore bodies and throats are detected in the hydrophobised sintered glass.
- Moisture storage in hydrophilic corners of partially hydrophobised elements (i.e. as in Figure 6.12 (c)) remains possible, but the amount of corner islands is heavily reduced with respect to hydrophilic samples.
- The liquid water islands throughout the hydrophobised pore network, both in corners of partially hydrophobised elements as well as in completely hydrophilic elements, are not connected to each other and no continuous liquid flow path therefore exists in hydrophobised sintered glass.

Previous conclusions are all derived from experiments on hydrophobised sintered glass, which comprises a narrow range of pore body and throat radii. Common building materials, such as ceramic brick or lime mortar, typically exist of a pore system over several spatial scales. Therefore, the occurrence of completely hydrophilic pore bodies and throats is more likely in these materials. Unfortunately, due to the spatial limitations of imaging techniques, a microscopic study of such multiscale materials is currently not feasible. The same goes for materials in the partially hydrophobised zone of a real masonry wall, as illustrated in Chapter 3. As the water repellent agent emulsion penetrates

the pore walls, emulsion droplets attach to the pore walls and render them hydrophobic. This causes the amount of emulsion droplets which progress into the wall to diminish further into the wall and resultantly less and less pores become hydrophobised.

To account for the possible presence of such hydrophilic pore network elements in materials with fine pore systems or in partially hydrophobised materials, a hydrophobic radius (r_{hydr}) is defined in the PNM. All elements smaller than this hydrophobic radius are assumed to remain hydrophilic, while the larger elements become (at least partially) hydrophobised. This hydrophobic radius is varied ($r_{hydr,1}$-$r_{hydr,4}$ in Table 6.1) to investigate the impact of increasing amounts of hydrophilically-oriented elements in hydrophobised pore networks. The hydrophobic radii are chosen arbitrarily with respect to the pore size distribution of the simulated material and hence are different for both sintered glass and ceramic brick. The simulations with the smallest hydrophobic radius are most representative of the hydrophobised materials, studied in this thesis, where (almost) all pores are hydrophobised as shown in Chapter 5. It should be mentioned that all hydrophilic elements contribute to moisture storage and transport and no pores are therefore blocked or clogged by the water repellent agent. With regards to reducing or eliminating moisture absorption in hydrophobised materials, this is the worst case scenario since fast liquid water flow remains possible in hydrophilic elements throughout the pore network.

The hydrophilic elements still contribute to moisture storage and transport in the same way as in the hydrophilically-oriented PNM and hence moisture can exist as a liquid film on the pore surfaces, as water islands in pore corners and eventually in a capillary filled element. As explained in Subchapter A, however, the corner volume fraction in hydrophilic elements ($S_{c,max,hydrophilic}$) is always limited to 10 %. The moisture behaviour in the (partially) hydrophobised elements on the other hand, requires adaptation in the PNM, using the conclusions of Chapter 5, repeated above. Firstly, these elements are assumed to remain empty throughout the simulation since capillary filling is highly unlikely under normal environmental conditions. This is mainly demonstrated in Chapter 4, where preconditioning of samples required vacuum conditions to warrant a notable moisture uptake. Secondly, most of the pore walls in such hydrophobised pores are assumed to be rendered hydrophobic, which eliminates the formation of adsorbed surface films. Some moisture storage in corner islands, however, remains possible, albeit in lesser amounts than in hydrophilic elements. Since the exact amount of moisture, stored in such corners, is unknown, the maximum corner volume fraction ($S_{c,max,hydrophobic}$) is limited to 0%, 5% or 10% to simulate the impact of no moisture, less moisture and equally much moisture in element corners of hydrophobised elements as in hydrophilic elements. The $S_{c,max,hydrophobic}$ used in the simulations determines the name of every PNM scenario as illustrated in Table 6.1.

Finally, the microscopic validation of the hydrophilically-oriented PNM in Subchapter A has shown that this PNM assumes the existence of corner islands in all pore network elements, which does not stroke with observations in XCT images of both hydrophilic and hydrophobised materials. Therefore, the extreme case of omitting corner islands from all pore throats, in both hydrophilic and hydrophobised elements, is simulated as well. The reasoning behind this omission of corner islands is already discussed in Section A.4 and hence not repeated here. All simulated scenarios are listed in Table 6.1, where NTC stands for 'no throat corner islands'.

Table 6.1: The different scenarios implemented in the adapted PNM for the different hydrophobic radii ($r_{hydr,i}$) which will be explained further in following sections. (NTC = no throat corner islands)

	Scenario name	**Throat corner islands**	$\mathbf{S_{c,max,hydrophilic}}$	$\mathbf{S_{c,max,hydrophobic}}$
	0%	Yes	10%	0%
$\mathbf{r_{hydr,1}}$	**0% (NTC)**	No	10%	0%
$\mathbf{r_{hydr,2}}$	**5%**	Yes	10%	5%
$\mathbf{r_{hydr,3}}$	**5% (NTC)**	No	10%	5%
$\mathbf{r_{hydr,4}}$	**10%**	Yes	10%	10%
	10% (NTC)	No	10%	10%

B.3 Macroscopic validation of the adapted PNM

This section simulates the hygric properties of hydrophobised sintered glass and ceramic brick and validates them using the experimental results acquired in Chapter 4. In this chapter, the moisture retention curves were measured starting from the (forced) vacuum saturated moisture content, since other preconditioning methods are not applicable to the hydrophobised materials. This means that water is also forced into the hydrophobised pore bodies and throats, which would not occur under normal circumstances. The PNM, however, simulates spontaneous moisture storage and transport through hydrophobised materials, in which moisture storage is only possible at hydrophilic storage sites in hydrophilic and partially hydrophobised pore network elements. The moisture retention curves, measured in Chapter 4 therefore hold theoretical value, however, they cannot be used to validate the PNM in this subchapter. Due to the elimination of liquid transport in hydrophobised materials, illustrated in Chapter 4, only the vapour permeability of hydrophobised materials, measured in the cup tests, remains viable for comparison with the simulated hygric properties.
After the validation of the hygric properties of the different PNM implementations listed in Table 6.1, the properties are used as input into the hygrothermal

model Delphin to replicate the capillary absorption experiment. Since this experiment is typically regarded as a measure of a hydrophobisation application's efficiency, it will put the simulated hygric properties into perspective. By performing these simulations for the hygric properties of the different PNM implementations with varying r_{hydr}, listed in Table 6.1, it is possible to investigate the impact of an increasing amount of hydrophilically-oriented elements in hydrophobised materials on their ability to reduce or eliminate moisture absorption. To account for material heterogeneity, all simulations are performed on three different pore networks for both materials. The extraction of these pore networks is discussed in Subchapter A.

B.3.1 Sintered glass

Hygric properties. To simulate an increasing amount of hydrophilic pore bodies and throats in a hydrophobised sintered glass, r_{hydr} is taken equal to 5 µm, 10 µm, 20 µm or 25 µm. All elements with radii smaller than this value are hence assumed to remain completely hydrophilic. These hydrophobic radii cause 0.1%, 1.8%, 17.6% or 32.9% of the complete pore volume to remain hydrophilic, respectively. Figure 6.13 shows the pore size distribution of sintered glass, extracted from the three pore networks used as input to the PNM, together with the different hydrophobic radii. The average of the three pore size distributions is presented as a line while the shaded area encompasses all distributions. The percentages on the graph denote the fraction of the pore volume which remains hydrophilic for every hydrophobic radius.

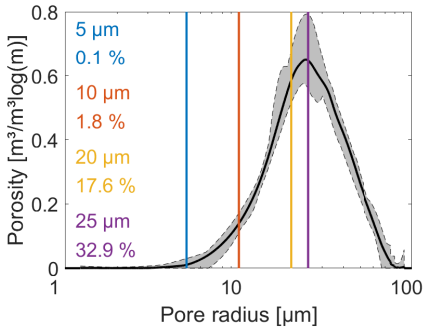


Figure 6.13: The pore size distribution of sintered glass and the hydrophobic radii (r_{hydr}). The percentages indicate the amount of pore volume which remains hydrophilic at a specific r_{hydr}.

Figure 6.14 shows the moisture retention and permeability curves of hydrophobised sintered glass, assuming a r_{hydr} equal to 10 µm (a-b) and 25 µm (c-d), respectively. Simulation results of all the variations of the PNM, listed in Table 6.1, are displayed on these figures as well as the properties simulated for hydrophilic sintered glass, derived from Subchapter A. The PNM simulation of these hygric properties from a single pore network requires several minutes for every scenario in Table 6.1. Although simulations are performed on three different pore networks, only the average curves are shown to not clutter the figures. The discussion of the capillary absorption experiments below, however, will show that there is only a minimal difference between results derived for all three networks and the average is therefore representative of all results.

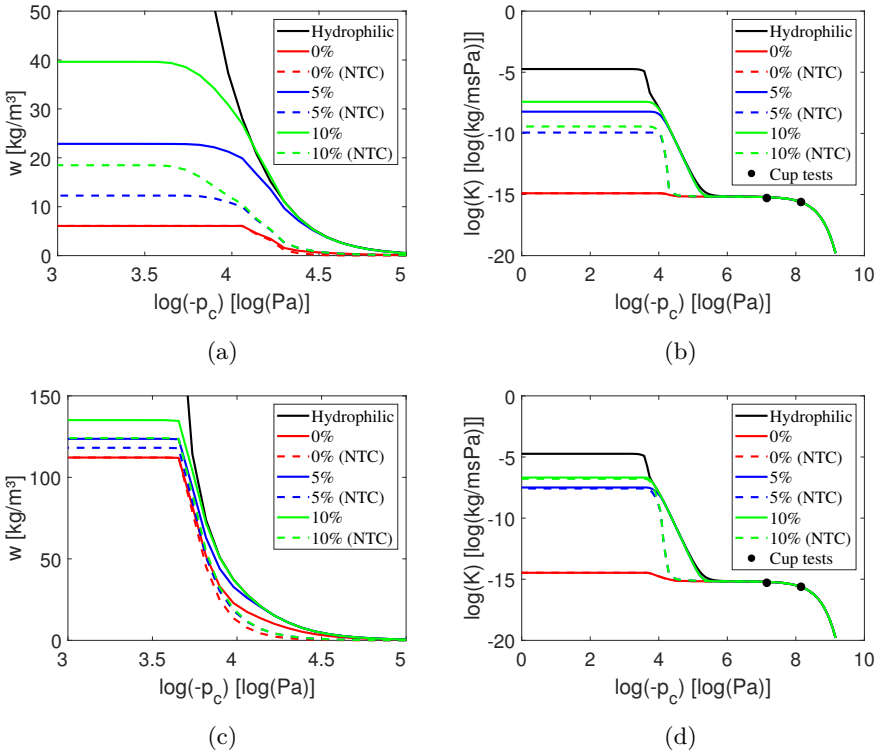


Figure 6.14: The moisture retention and permeability curves simulated with the PNM for the hydrophilic sintered glass and the hydrophobised scenarios listed in Table 6.1 with r_{hydr} equal to 10 µm (a-b) and 25 µm (c-d).

The moisture retention curves in Figure 6.14 show increasing amounts of maximum moisture storage for a larger r_{hydr}. Increasing the r_{hydr} logically results in more hydrophilically-oriented elements, which can become capillary filled, and therefore have a higher storage capacity. Moisture storage in corner islands also contributes to the maximum amount of moisture in these hydrophobised materials. When r_{hydr} is quite small, as in Figure 6.14 (a), most elements are hydrophobised and consequently they remain empty. These empty elements can store moisture in their hydrophilic corners and reducing $S_{c,max}$ (e.g. from 10% to 0 %) therefore significantly affects the amount of moisture storage. When r_{hydr} is larger (i.e. as in Figure 6.14 (c)), however, the larger share of hydrophilic elements, which can become filled, make the influence of corner storage in empty elements less impactful on the overall moisture storage.
The moisture permeability curves in Figure 6.14 show the combined liquid and vapour permeability over the entire capillary pressure range. Usually, these permeabilities are expressed in function of the moisture content, however, plotting them in function of the capillary pressure allows simultaneous visualisation of the results of the cup tests on hydrophobised materials, performed in Chapter 4. Two values are shown, representing the average of all dry-cup and wet-cup tests on the different types of hydrophobised sintered glass. Since the spread on these results is so limited, only this average is displayed. Due to the logarithmic scale on the y-axis, however, it is difficult to assess the agreement between experimental and simulated values. Therefore, this simulated permeability is transformed into vapour diffusion resistance factors (i.e. µ-values) and compared to dry-cup and wet-cup test results. Table 6.2 shows the µ-values, derived from the simulated vapour permeability, together with the experimentally measured µ-values, adopted from the cup tests in Chapter 4. The good agreement between the simulated and measured µ-values show that vapour transport is modeled satisfactorily in the adapted PNM.

Table 6.2: The experimentally measured µ-values, adopted from Chapter 4 and the simulated µ-values, derived from the moisture permeability curves of Figure 6.14 for sintered glass.

	Dry-cup test	**Wet-cup test**
Experimental	5.75 ± 0.4	6.91 ± 1.1
Simulated	6.43	5.82

Chapter 4 concluded that (almost) all moisture transport through this hydrophobised sintered glass occurs via vapour flow due to the omission of a continuous liquid flow path. The moisture permeability should therefore remain (almost) constant over the entire capillary pressure range. This of course only holds for (almost) perfectly hydrophobised materials in which (almost) all pore

bodies and throats are hydrophobised. The hydrophobised materials, studied in this dissertation, are therefore best represented by the simulations with the smallest hydrophobic radius (r_{hydr} = 5 µm), where most elements are rendered hydrophobic. Introducing more hydrophilic elements into the pore network (e.g. for materials in the partially hydrophobised zone), by increasing r_{hydr}, and allowing larger corner flows in elements, by increasing $S_{c,max}$, promotes liquid flow and increases the overall permeability. This is illustrated by the overall larger moisture permeabilities in Figure 6.14 (d) for a r_{hydr} equal to 25 µm, compared to Figure 6.14 (b). Also interesting to mention is the fact that the removal of throat corner islands, which render the corner flows discontinuous, lowers the moisture permeability.

Capillary absorption. In order to put into perspective the change in hygric properties caused by an increasing amount of hydrophilic elements in hydrophobised materials, the capillary absorption experiment is simulated. This experiment brings a sample into contact with water and tracks its water absorption rate. Since reducing this absorption rate is a primary goal of a hydrophobisation application, the capillary absorption coefficient (A_{cap}) is a popular measure for the application's efficiency and will be treated as such to assess the impact of hydrophilic elements in hydrophobised materials. Performing such experiments on the sintered glass samples, hydrophobised with all three water repellent agents used in this PhD, results in a reduction of the capillary absorption coefficient with more than 99.9 % compared to the hydrophilic material.
The simulations of this capillary absorption experiment are performed in the hygrothermal model DELPHIN, which require the simulated hygric properties of the hydrophobised materials as input. Figure 6.15 shows the simulated capillary absorption coefficients for every scenario listed in Table 6.1. These coefficients are expressed as a percentage of the hydrophilic capillary absorption coefficient, simulated using the hygric properties of hydrophilic sintered glass samples ($A_{cap,hydrophilic}$ = 4.94 kg/m²s$^{0.5}$). The limits of 1% and 10% are also highlighted for clarity.
As stated in Section B.2, the scenario with the smallest r_{hydr} (i.e. r_{hydr} = 5 µm) best describes the materials studied in this dissertation. As can be seen in Figure 6.15, this r_{hydr} guarantees reductions of the capillary absorption coefficient of at least 98 % and if the throat corner islands are removed and/or if $S_{c,max,hydrophobic}$ is set at 0%, reductions larger than 99.9 % are simulated, which agrees best with the experimentally measured values. To further investigate the impact of more hydrophilically-oriented elements in hydrophobised materials, simulations are performed for larger r_{hydr}.

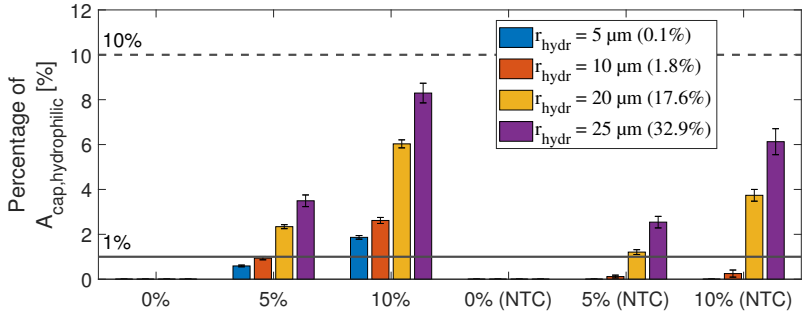


Figure 6.15: The capillary absorption coefficients, simulated with DELPHIN for the hydrophobised scenarios listed in Table 6.1, expressed as a percentage of the capillary absorption coefficient of hydrophilic sintered glass ($A_{cap,hydrophilic}$ = 4.94 kg/m²s$^{0.5}$).

The capillary absorption coefficient shows reductions of at least 92 % after hydrophobisation and these coefficients gradually increase together with r_{hydr}. Further reductions up to 97 % are also guaranteed when less than 2 % of the pore volume remains hydrophilic. Most experimental studies typically label applications of water repellent agents as successful when they achieve reductions of at least 95-97% [6,30]. This once again confirms the need to tailor the water repellent agent to the building material to make sure a sufficient amount of the pore volume can become hydrophobised. Also interesting to note is that the removal of throat corner islands in the PNM allows up to 17.6 % of the pore volume to remain hydrophilic while still ensuring reductions of over 96 %. Since the microscopic investigation in Chapter 5 has shown that discontinuous corner flows are more likely to occur in real materials, the scenarios without throat corner islands could prove to be more realistic. Regardless of the existence of throat corner islands, however, the results show no r_{hydr} above which the capillary absorption coefficient suddenly increases significantly due to the formation of a large continuous liquid flow over the sample. Of course, further increasing r_{hydr} above 25 µm will negatively affect the moisture permeability, however, leaving more than 30 % of the material's pore volume hydrophilic is simply not realistic.

Sensitivity analysis. As mentioned many times before, sintered glass is not a material which typically becomes hydrophobised and previous conclusions are therefore not immediately applicable to more common building materials. Next section therefore performs the same analysis on stochastically generated networks of ceramic brick. However, as stated in Section A.2.1, these pore networks are generated with a multiscale stochastic generator which is currently under development [75,76], which means that these networks are not yet a finished product. Therefore, some alternative (monoscale) pore networks are generated using statistical information of sintered glass. In these networks, a single pore network property is altered while the other properties remain the same, to investigate its impact on the simulated capillary absorption experiments of hydrophobised materials. A more extensive sensitivity analysis has been performed by Shi et al. [76], in which the impact of various pore network properties on the hygric properties of materials is investigated. The goal of the sensitivity analysis in this section is to identify pore network properties which have a large impact on the changing capillary absorption coefficient after hydrophobisation to hereby isolate the properties which require attention in the construction of the brick's pore network.

Two properties are targeted; the porosity and the coordination number (i.e. the amount of connections between pore bodies). These properties are chosen since they inherently have a large impact on the capillary absorption coefficient of hydrophilic materials. Reducing the pore body and throat radii also affects the material's permeability heavily, but for a material with a finer pore system, the reader is referred to next section on ceramic brick. The porosity of the original sintered glass network equals $36.5\% \pm 0.7\%$. Networks are therefore generated with porosities of 20% and 50% to represent less porous and more porous materials, respectively. The average coordination number of sintered glass is originally equal to 6. Networks are therefore generated with coordination numbers of 4 and 9 to represent less and better connected porous materials, respectively. All the different scenarios of Table 6.1 are once more tested for these four alternative types of pore networks (higher and lower porosity, and better and less connected). Results for the sintered glass network with a smaller coordination number, and the sintered glass with a higher porosity are shown in Figures 6.16 and 6.17, respectively. The capillary absorption coefficients are again represented as a percentage of their hydrophilic capillary absorption coefficient. By comparing the capillary absorption coefficients of these adapted networks to the original sintered glass (in Figure 6.15), it is shown that the exact same conclusions are valid. This is also the case for the other alternative sintered glass networks (less porous and better connected networks) and they are therefore not shown here. Both porosity and coordination number therefore do not notably affect the conclusions of this study and hence good assumptions of the ceramic brick's porosity and coordination number in next section are

sufficient.

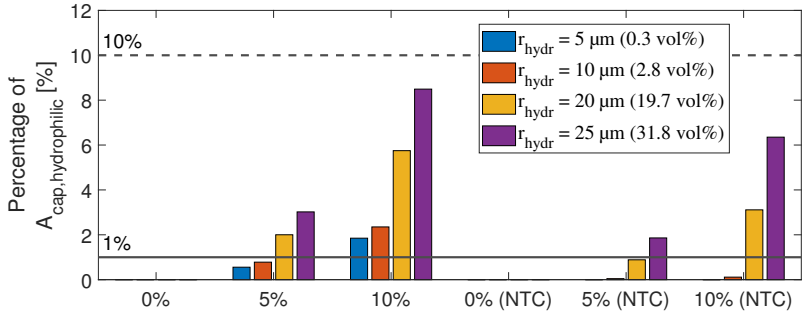


Figure 6.16: The capillary absorption coefficients, simulated with DELPHIN for the hydrophobised scenarios listed in Table 6.1, expressed as a percentage of the capillary absorption coefficient of hydrophilic sintered glass with a smaller average coordination number of 4 ($A_{cap,hydrophilic} = 3.27$ kg/m^{2}s$^{0.5}$).

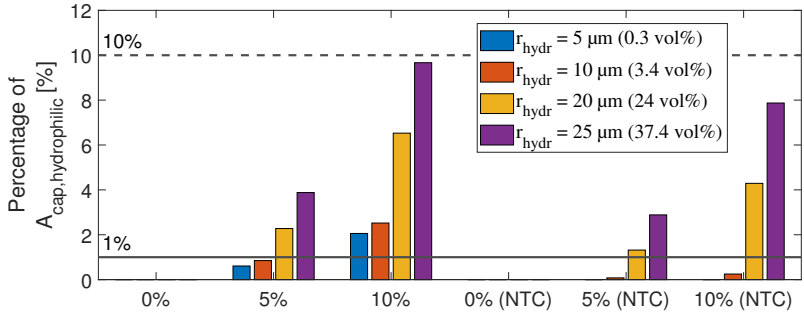
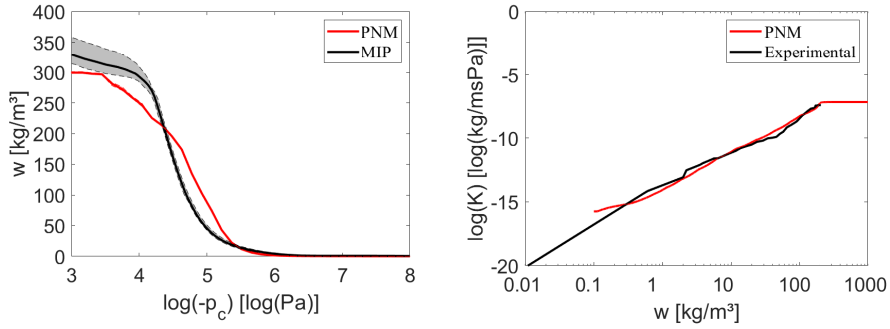


Figure 6.17: The capillary absorption coefficients, simulated with DELPHIN for the hydrophobised scenarios listed in Table 6.1, expressed as a percentage of the capillary absorption coefficient of hydrophilic sintered glass with a higher porosity of 50 % ($A_{cap,hydrophilic} = 5.74$ kg/m^{2}s$^{0.5}$).

B.3.2 Ceramic brick

Hygric properties. The same analysis as in previous section is performed here on the pore networks of ceramic brick. As explained in Section A.2.1, these pore networks are derived from a stochastic generator which is still under development. The pore networks, used in the simulations, are therefore the current state-of-the-art. More information about the pore network properties used in the stochastic generator can be found in Appendix 6.B.1. The hygric properties, simulated with the hydrophilically-oriented PNM, are shown in Figure 6.18 together with experimentally measured properties. The experimental moisture retention curve is derived from mercury intrusion porosimetry measurements, previously discussed in Chapter 4, and the moisture permeability curve is adopted from [44]. Although the simulated moisture permeability somewhat agrees with the measured curve, the moisture retention curve still shows a large discrepancy. The current version of the pore network of ceramic brick is therefore not completely representative of the true pore structure. Due to lack of another network, however, it is used in this study. Validation of the conclusions of this section using the final version of the stochastically generated pore network remains future work.



(a) (b)

Figure 6.18: The moisture retention curve simulated with the PNM together with the curves derived from MIP measurements (a) and the moisture permeability curve simulated with the PNM together with the experimentally measured permeability curve adopted from [44] (b).

Since the brick's pore network is different to sintered glass, the hydrophobic radii also need to be altered. Figure 6.19 shows the pore size distribution of ceramic brick, extracted from the three stochastically generated pore networks. The chosen r_{hydr} are 0.5 µm, 0.75 µm, 1 µm and 2 µm which leave 1 %, 6.2 %, 16.6 % and 33.8 % of the total pore volume hydrophilic, respectively.

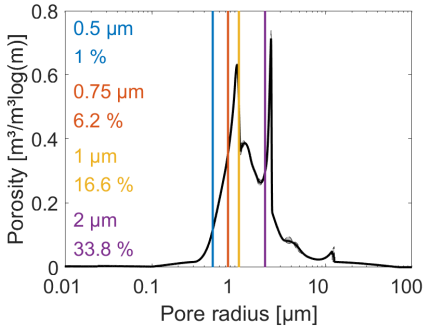


Figure 6.19: The pore size distribution of the generated pore network of ceramic brick and the hydrophobic radii (r_{hydr}). The percentages indicate the amount of pore volume which remains hydrophilic at a specific r_{hydr}.

Figure 6.20 shows the moisture retention and permeability curves for the hydrophobised ceramic brick with r_{hydr} equal to 0.75 µm (a-b) and 2 µm (c-d), respectively. The PNM simulation of these hygric properties for a single pore network requires 1-2 hours for every scenario in Table 6.1. The same overall conclusions are valid as for the sintered glass. Firstly, the storage capacity of the hydrophobised materials increases with increasing r_{hydr} and $S_{c,max}$. Secondly, removing the throat corner islands reduces the overall moisture permeability, however, this effect is less pronounced than for sintered glass. Since the logarithmic y-axis possibly does not show the disagreement between the cup tests and the simulated moisture permeability curves, Table 6.3 once again shows the measured and simulated µ-values of the dry-cup and wet-cup tests. Even though the cup test results seem to agree well with the moisture permeability curves in Figure 6.20, the PNM clearly underestimates the µ-values. This is possibly caused by the imperfect representation of the pore network of ceramic brick as some problem areas of this pore network extraction of brick are still being worked on. Therefore, the analysis of the results on ceramic brick have to be seen here as an indication of the true moisture behaviour. Future validation of any conclusions in this section using the final version of the brick's pore network remains necessary.

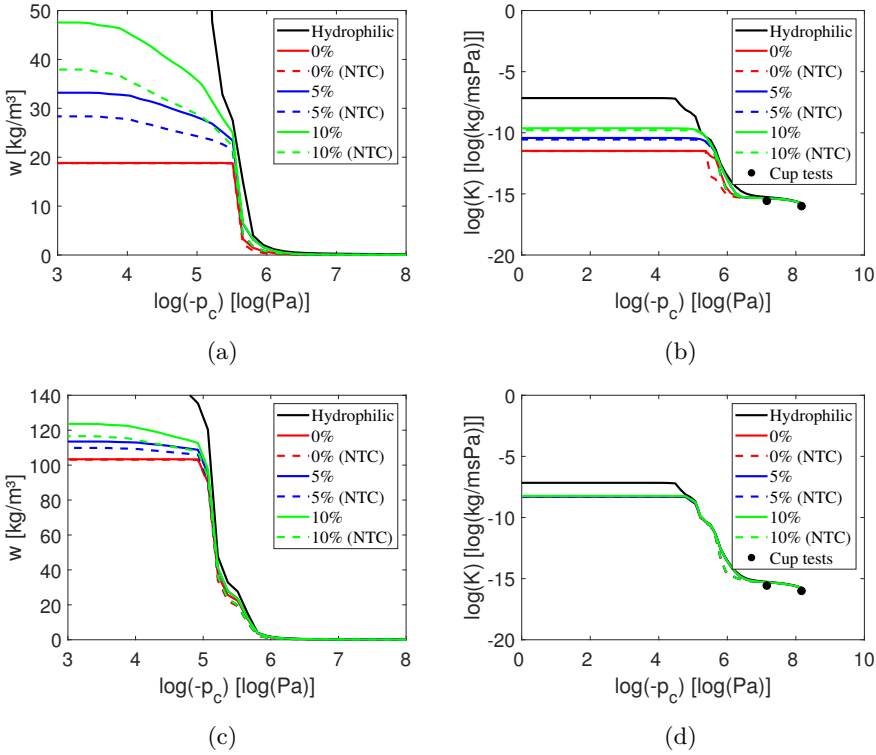


Figure 6.20: The moisture retention and permeability curves simulated with the PNM for the hydrophilic ceramic brick and the hydrophobised scenarios listed in Table 6.1 with r_{hydr} equal to 0.75 µm (a-b) and 2 µm (c-d).

Table 6.3: The experimentally measured µ-values, adopted from Chapter 4 and the simulated µ-values, derived from the moisture permeability curves of Figure 6.14 for ceramic brick.

	Dry-cup test	**Wet-cup test**
Experimental	13.4 ± 0.6	13 ± 1.8
Simulated	7.98	7.95

Capillary absorption. Using the simulated hygric properties, the capillary absorption experiment is replicated in Delphin and the capillary absorption coefficient is calculated. The experiments are also performed on the brick, hydrophobised with all three water repellent agents used in this PhD, which resulted in reductions of the capillary absorption coefficient of more than 99.9% compared to the hydrophilic material. The simulated coefficients are shown in Figure 6.21, expressed as a percentage of the simulated capillary absorption coefficient of hydrophilic ceramic brick ($A_{cap,hydrophilic}$ = 1.2 kg/m^{2}s$^{0.5}$). A reduction of the capillary absorption coefficient of more than 99.9 % is only reached for some PNM implementations when r_{hydr} is 0.5 µm and resultantly the largest share of the pore network volume has been rendered hydrophobic. This hints towards the fact that (almost) all pores in the hydrophobised ceramic brick, used in the experiments of Chapter 4, are rendered hydrophobic. It should be mentioned, however, that this conclusion cannot be made solely based on these simulated capillary absorption coefficients since they rely on a flawed representation of the brick's pore structure. To further investigate the impact of an increasing amount of hydrophilically-oriented pores in (partially) hydrophobised brick, r_{hydr} is varied.

As stated before, experimental studies typically label applications of water repellent agents successful when they reduce the capillary absorption coefficient by at least 95-97% [6,30]. This is guaranteed for a r_{hydr} of 0.75 µm when 6.2% of the pore volume remains hydrophilic. Also, when r_{hydr} is increased to 1 µm, a reduction of 95 % is achieved when $S_{c,max,hydrophobic}$ remains limited to 5 %. Since corner storage in hydrophobised elements has been proven to be present to a lesser extent than in hydrophilic elements, where $S_{c,max,hydrophilic}$ is limited to 10%, an $S_{c,max,hydrophobic}$ of 5 % is not a bad assumption. Interesting to note is that the capillary absorption coefficient increases drastically when r_{hydr} goes from 1 µm to 2 µm, which differs from the gradual evolution seen for the sintered glass in Figure 6.15. This has to be avoided at all cost in real-life applications. The discussion section elaborates further on this sudden increase.

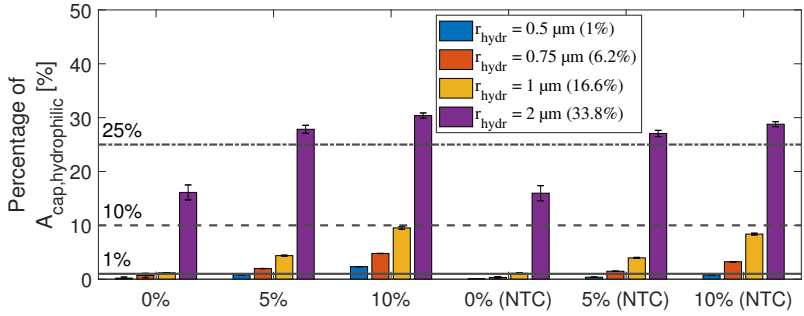


Figure 6.21: The capillary absorption coefficients, simulated with DELPHIN for the hydrophobised scenarios listed in Table 6.1, expressed as a percentage of the capillary absorption coefficient of hydrophilic ceramic brick ($A_{cap,hydrophilic}$ = 1.2 kg/m^{2}s$^{0.5}$).

B.4 Discussion

This subchapter simulates the hygric properties of hydrophobised sintered glass and ceramic brick with the adapted PNM after which these properties are used to model a capillary absorption experiment. Due to some uncertainty on the microscopic moisture behaviour in hydrophobised materials, more specifically in hydrophobised ceramic brick, several different variations of the PNM, listed in Table 6.1, are created. The PNM which most closely resembles the conclusions of Chapter 5 is the one with the smallest hydrophobic radius, where almost no pore network elements remain hydrophilic. In this case, liquid moisture flow is eliminated and transport only occurs through vapour flow. Additionally, moisture storage is only possible in hydrophilic corners of hydrophobised materials and possibly some isolated hydrophilic elements, which are scattered over the pore network. Storage therefore becomes negligible on a macroscopic scale. Figures 6.15 and 6.21 show that this (best) implementation of the PNM, with the smallest hydrophobic radius, reduces the capillary absorption coefficient to less than 2 % of its hydrophilic counterpart, something which is measured in capillary absorption experiments as well [5,6].

The presence of (almost) no hydrophilically-oriented pore bodies and throats in a hydrophobised material is derived from a microscopic investigation on sintered glass. More of such hydrophilically-oriented elements may be present in other materials, such as ceramic brick which comprises pore bodies and throats of different spatial scales, or in partially hydrophobised materials. To account for the possible presence of hydrophilic elements, the analysis in Section B.3 is repeated for several hydrophobic radii. Figure 6.22 shows the capillary absorption coefficients of Figures 6.15 and 6.21 as a function of the percentage

of the pore volume which remains hydrophilic in sintered glass (a) and ceramic brick (b). While A_{cap} increases linearly with the percentage of hydrophilic volume in sintered glass, there seems to be a sudden increase of this coefficient in ceramic brick when changing the percentage of hydrophilic pore volume from 16.6% to 33.8% (i.e. r_{hydr} from 1 µm to 2 µm).
This sudden increase can be attributed to the presence of nanoscale pore bodies and throats in ceramic brick which have a higher chance of remaining hydrophilic due to their small radii. These can act as parallel liquid flow paths between two pore bodies as illustrated in Figure 6.23, while not contributing notably to the volume of hydrophilically-oriented elements. The sudden increase of the capillary absorption coefficient in Figure 6.22 then indicates the existence of a connected liquid flow cluster from one side of the sample to the other through hydrophilically-oriented pore bodies and throats. The importance of this smaller porous system in the calculation of the moisture permeability was already noted for hydrophilic materials in literature [25].

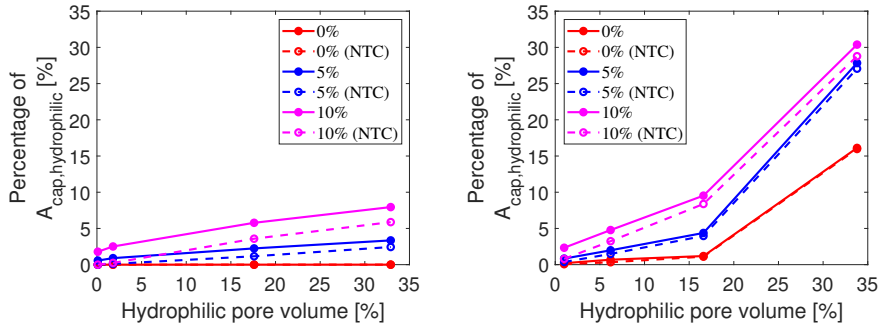


Figure 6.22: The simulated capillary absorption coefficients of all PNM implementations of sintered glass (a) and ceramic brick (b) in function of the percentage of pore volume which remains hydrophilic.

Such fast liquid flow path through a hydrophobised material should be avoided at all cost. From DLS experiments, described in Chapter 3, it is known that commercially available water repellent agents are typically composed of polymers with hydrodynamic radii smaller than several hundreds of nanometers. In this thesis, the largest measured emulsion droplet size of commercial water repellent agents is 400 nm. This is even smaller than the proposed hydrophobic radii in Section B.3, which explains why these water repellent agents almost completely eliminate liquid flow in the experiments in Chapter 4. While the few hydrophilic elements in the sintered glass and the ceramic brick, hydrophobised with common water repellent agents, will not affect the moisture flow notably,

these common agents might fail at hydrophobising other materials with finer pore systems to a sufficient degree, like lime mortar or other bricks. Therefore, measuring the pore size distribution of the material to be hydrophobised as well as the hydrodynamic radius of the water repellent agent's emulsion droplets is advised to prevent faulty hydrophobisation applications.

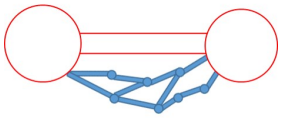


Figure 6.23: Representation of the impact of hydrophilic (black) nanoscale pore bodies and throats which connect larger hydrophobised (red) pore bodies.

The previously drawn conclusions are based on hygric properties simulated with a PNM, which relies on several necessary simplifications and assumptions. Additionally, the simulations on ceramic brick are still performed with an imperfect pore network representation. This brings along an inevitable degree of doubt. Nevertheless, the need for a proper choice of water repellent agent, which hydrophobises as much elements as possible, is highlighted. Choosing the water repellent agent with the smallest emulsion droplets will not always guarantee the highest reduction of the capillary absorption coefficient though, since other factors such as the side groups on the polymer droplets, the penetration depth of water repellent agents, and many more, also influence the efficiency of a hydrophobisation application. Especially the penetration depth of water repellent agents and the way in which the hygric properties are adapted in the partially hydrophobised zone (see Chapter 2), require a more in-depth study.

B.5 Summary

This section adapts the existing hydrophilically-oriented PNM for hygric property determination of hydrophobised materials using the conclusions drawn in Chapter 5. Since these conclusions are derived from a microscopic investigation on hydrophobised sintered glass, they are not directly applicable to other more common building materials like ceramic brick. Therefore, different variations of the PNM are created by varying the hydrophobic radius, which labels the elements as either hydrophilic or hydrophobised and hereby investigates the impact of increasing amounts of hydophilically-oriented pores in hydrophobised materials.
These adapted variations of the PNM are subsequently validated using the hygric properties of hydrophobised materials, measured in Chapter 4. Since the PNM simulates spontaneous moisture transport through hydrophobised materials, however, only results from the cup tests can be used for the validation. The

μ-values, derived from dry-cup and wet-cup tests agree nicely with simulated values for sintered glass. The imperfect representation of the ceramic brick's pore structure, however, results in an underestimation of the simulated μ-values. Further improvements of this extracted pore network of ceramic brick are expected in the future.

The simulated hygric properties of all PNM variations are used to simulate a capillary absorption experiment in the hygrothermal model Delphin. Both simulations on sintered glass and ceramic brick show that capillary absorption coefficient reductions of 95-97 %, which is regarded as a successful hydrophobisation application, are guaranteed when less than 6 % of the pore volume remains hydrophilic. By comparing the simulated capillary absorption coefficients of both sintered glass and ceramic brick, it is also shown that the nanoscale porosity of ceramic brick, which typically remains hydrophilic due to its small radii, contribute to a fast liquid flow path over the material. This liquid flow path might cause an insufficient reduction of the capillary absorption coefficient after hydrophobisation. Choosing a water repellent agent, which renders at least part of the nanoscale porosity of building materials hydrophobic, is therefore advised.

This chapter shows the possibilities of the adapted pore network model to simulate the hygric properties of hydrophobised building materials and therefore once more highlights the importance of this dissertation. It should be mentioned that further work on this PNM is required, but this is discussed in detail in Chapter 7.

Appendix 6.B.1 Stochastic pore network generator

As explained in Chapter 3, the stochastic pore network generator used in this dissertation is developed by Claes and Janssen [75] and Shi et al. [76]. Since the model is currently still being worked on and is hence subject to change, it will not be explained in great detail in this dissertation. Only the statistical information of the pore network of ceramic brick is displayed here. For more information, the reader is referred to published [75,76] and soon to be published works [115]. The figures, shown in this appendix, are all derived from [115].
The stochastic pore network generator starts by distributing pore bodies and pore throats in a predefined network volume. The locations of the pore body centers are determined via Sobol sequences. The other network parameters, pore body and throat radii, pore body coordination number (i.e. amount of connections of pore bodies to other pore bodies) and pore throat lengths are sampled from statistical information extracted from XCT images and X-ray microscopy images at different scales [115]. Figure 6.24 shows the pore body and pore throat radii distributions, derived from three different images at various scales (PN1, PN2 and PN3). The envelope of these three distributions is then used for the pore network generation of ceramic brick.

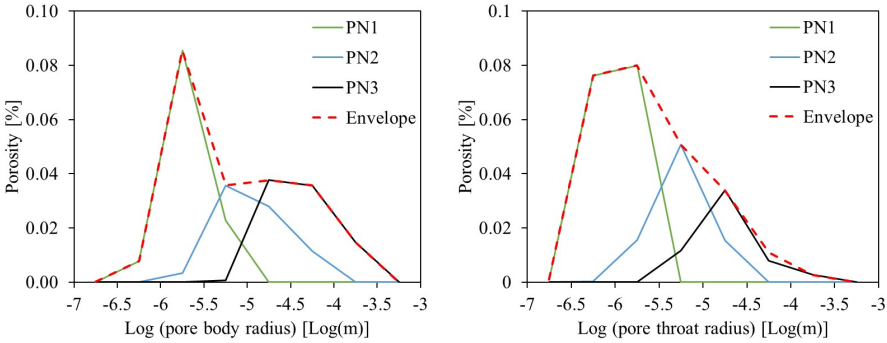
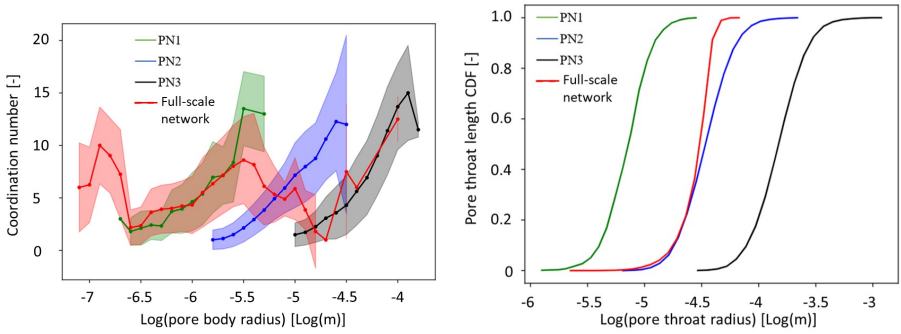


Figure 6.24: The pore body (a) and pore throat (b) radii distributions used to generate the pore network of ceramic brick derived from three individual pore networks that stem from images at different scales. [115]

The amount of pore throats is adjusted to make sure the coordination number distribution of the pore bodies mimics the ones derived from the images. Figure 6.25 (a) shows the coordination number in function of the pore body radius of the three different images as well as the eventual coordination number distribution of the full-scale pore networks, generated using the stochastic generator. The full line represents the average value, while the shaded area displays the standard

deviation. Figure 6.25 (b) shows the cumulative distribution function of the throat lengths derived from the networks extracted from the three different images (PN1-PN3) and from the eventual extracted full-scale pore network of brick. This throat length distribution only slightly agrees with a single network (PN2). This is a result of the coordinates of the pore bodies, generated by a Sobol sequence. Further research into matching these throat lengths with images at various scales is still ongoing. Other network properties, like the shape factor of elements, have shown to be less impactful on the hygric property simulation [76] and they are hence not shown here.



(a) (b)

Figure 6.25: The pore body coordination numbers (a) and pore throat lengths (b) derived from three individual pore networks that stem from images at different scales and of the full-scale pore network generated using the stochastic generator [115].

Chapter 7

Conclusions and outlook

The main aim of this dissertation is to investigate the pore-scale modeling of hygric properties of hydrophobised building materials. To do so, a previously developed hydrophilically-oriented PNM is adapted for use on hydrophobised building materials. This adaptation is based on conclusions drawn from an investigation of the microscopic moisture behaviour in hydrophobised materials, discussed in Chapter 5. The model outcomes are then validated using experimentally determined hygric properties of hydrophobised building materials, measured in Chapter 4. The summary and discussion of the research in this dissertation can be found in Section 1. The main conclusions are then reiterated in Section 2. Finally, the limitations of this study and perspectives for future work are provided in Section 3.

1 Summary and discussion

1.1 Chapter 4: Experimental hygric property determination

This chapter focuses on the hygric property determination of hydrophobised materials, which are used in Chapter 6 to validate the adapted PNM. As explained in detail in Chapter 2, commonly used experimental techniques for hygric property determination have had mixed success for the hygric property determination of these hydrophobised materials. While cup tests remain capable of quantifying the vapour permeability of such materials, no existing methods prove suitable for the measurement of the moisture storage properties (i.e. moisture retention curve) and the liquid permeability and hence there are very limited reports in literature about hydrophobised materials' hygric properties. To this aim, the steady state centrifuge experiment and the adapted cup tests are developed.

Subchapter A is fully dedicated to the design, validation and application of the steady state centrifuge technique. While this technique is often used in the research area of earth sciences [130,131,135–137], its applicability on building materials is hardly investigated [143]. Due to its popularity in earth sciences, multiple centrifuge designs already exist and hence it is possible to simply use a commercially available centrifuge. Nevertheless, a centrifuge is designed in-house since it allows more freedom in both the initial design as well as possible alterations afterwards. During this trial-and-error design, heat generation by the motor and the resulting unwanted evaporation of moisture from the samples during rotation prove the main problem. Local motor cooling with a large ventilator and the design of sample holders, which shield the samples from the surrounding air, manage to eliminate the unwanted evaporation from the samples for rotational velocities smaller than 1250 RPM and corresponding capillary pressures below 5.1 log(Pa). Higher velocities, which allow preconditioning samples to larger absolute capillary pressures and lower moisture contents, would require more invasive heat reducing solutions, like water- or oil-cooled motors, as well as stronger sample holders, which do not break under the induced pressures.

This steady state centrifuge technique is subsequently successfully validated using three well-characterised materials (two ceramic bricks and one sintered glass), by comparing the measured moisture retention curve with the curves derived from mercury intrusion porosimetry measurements. The main advantage of this measuring technique over other experimental methods (i.e. pressure plates and MIP) is the possibility to measure moisture retention curves starting from the more realistic capillary moisture content within a limited timeframe. When moisture retention curves from the vacuum saturated moisture content are desired, MIP remains faster and (a little) more accurate, however, it still requires toxic mercury and the resulting moisture retention curves are more dependent on certain assumptions (e.g. contact angle between mercury and pore walls) [148]. This steady state centrifuge technique is therefore a valuable addition to the gamma of hygric property measurement techniques.

Next, Subchapter B is dedicated to the hygric property determination of hydrophobised materials. First, the moisture storage properties (i.e. the moisture retention curves) are measured using the steady state centrifuge technique, designed and validated in Subchapter A. The most important effect of these agents on the moisture retention curve is the horizontal displacement of this curve to lower absolute capillary pressures compared to the hydrophilic materials. This means that the hydrophobic nature of the pore walls in hydrophobised materials causes moisture to expel from the pore network under the influence of a smaller centrifugal force. It should be mentioned that the moisture retention curves of hydrophobised materials, measured in this subchapter, are derived from initially vacuum saturated samples. Preconditioning samples to these

moisture contents requires vacuum conditions, however, which do not occur in reality. In realistic conditions, where samples can only absorb moisture via spontaneous absorption, hydrophobised materials remain nearly dry, as shown in the adapted cup tests. These moisture retention curves, measured using this steady state centrifuge technique, therefore contribute mostly to the theoretical understanding of moisture storage in such hydrophobised materials, but they cannot be used as material properties in hygrothermal simulation models.
Next, the vapour permeability of hydrophobised materials is measured using the well-known cup test. Both dry-cup and wet-cup tests are executed according to the ISO 12572 standard [47]. While these tests are often destructive, the cups in this dissertation are constructed with a detachable lid, which allows performing both tests on the same sample. The measured vapour diffusion resistance factors slightly increase compared to the hydrophilic samples. Also, the hygrocopicity of the hydrophobised materials is further reduced, causing the vapour diffusion resistance factors to be less dependent on the relative humidity conditions. Both of these conclusions have been noted previously in literature [3,5,6,8,9,17,30,32,50,51].
Finally, the liquid permeability of hydrophobised materials is quantified using adapted cup tests in which the sample is brought into contact with a water reservoir inside the cup. The moisture flow through the sample is then tracked via periodic weight measurements and compared to the theoretically calculated vapour flow, which occurs in absence of any liquid flow. These adapted cup tests are performed on sintered glass and ceramic brick, hydrophobised with the two commercial water repellent agents (agents A and B). While samples, hydrophobised with agent B, show a moisture flow governed solely by vapour transport, agent A causes periods of fast moisture flow (i.e. combined liquid and vapour flow) alternated with periods of only vapour transport. In these periods of fast moisture flow, some parts of the sample visibly contain higher moisture contents, hereby inducing a liquid flow path. Over time, the moisture in these wet zones evaporates and the moisture flow rate once more decreases to the theoretically calculated vapour flow rate. It is therefore assumed that, under normal working circumstances, hydrophobised samples solely permit vapour transport, something which is further validated in the microscopic investigation of Chapter 5. A possible reason for the temporarily induced liquid flow is the presence of emulsifiers which diminish the hydrophobic effect of the agents. During the period of combined vapour and liquid flow, these emulsifiers are washed away, hereby making further liquid flow more unlikely. This is backed up by other studies in literature where repeated water exposure rendered the hydrophobised materials more water-repellent [6,7].
This chapter presents the hygric properties of hydrophobised building materials. The main conclusion is that such samples only transport moisture through vapour transport, even if they are placed in direct contact with a free water

surface. Hardly any spontaneous absorption of moisture occurs and therefore, under normal circumstances, almost no moisture is stored in these materials. To model such a fully hydrophobised material in a hygrothermal model, it is sufficient to significantly lower the material's storage capacity and only allow vapour transport. These conclusions are of course only applicable to the hydrophobised materials studied in this dissertation. Other materials with finer pore systems (e.g. lime mortar) require further experimentation. Also, only fully hydrophobised materials are investigated while it is widely accepted that the hydrophobisation application in a wall creates both a fully and partially hydrophobised zone, as shown in Chapter 2. The partially hydrophobised materials will also prove important in fully understanding the moisture behaviour in hydrophobised walls and hence require further investigation.

1.2 Chapter 5: Investigation of microscopic moisture behaviour

Chapter 5 investigates the microscopic moisture behaviour in both hydrophilic and hydrophobised porous materials. The first part of this subchapter compares the applicability of two techniques (i.e. XCT imaging and NMR relaxometry) to investigate the microscopic moisture behaviour in hydrophilic porous materials. Due to the limits on the spatial resolution of the XCT images, this technique is only applicable to visualise moisture in pores of the micrometer range (i.e. with radii larger than ca. 1 µm). NMR relaxometry on the other hand is investigated as a possible alternative to XCT imaging in more common building materials, like ceramic brick, due to its ability to measure the presence of water islands in micro- and nanometer scale pore bodies and throats. To do so, both techniques are applied to hydrophilic sintered glass samples and the extracted water island size distributions are compared to each other to assess both their capabilities and limitations. The technique(s) which have proven suitable for the investigation of the moisture behaviour in porous materials can then be used to investigate the microscopic moisture behaviour in hydrophobised materials in Subchapter B.

While the extraction of water island size distributions from XCT images is easily understood, transforming the measured magnetic signals from NMR measurements into such distributions proves much more difficult. Firstly, transforming the continuous magnetic signal into a distribution of transverse relaxation times is a commonly known ill-posed inversion problem. This means that no unique correct solution to this problem exists. The calculated distributions can therefore be heavily influenced by the chosen inversion method as well as the signal-to-noise ratio of the magnetic signal. Secondly, the transformation of a transverse relaxation time distribution into a water island size distribution requires multiple assumptions (no or weak diffusional coupling,

little paramagnetic impurities, calculation of the surface relaxivity). If these assumptions are not applicable to the studied material, this can also distort the final water island size distributions.

By comparing the water island size distributions of saturated samples as well as two unsaturated samples, extracted from both XCT images and NMR measurements, it becomes clear that the NMR measurements focus on the largest water islands, residing in the capillary filled pore bodies and throats. The smaller water islands, stored in corners of pore bodies and throats, seem to be out of the NMR's measuring range. Since these corner flows have shown to be imperative to simulate moisture transport in previous research [23,69], their omission from the distributions is problematic. Due to this omission as well as all the above-mentioned assumptions required to obtain the water island size distributions, NMR relaxometry is deemed unsuitable for the investigation of the microscopic moisture behaviour. The little literature on NMR measurements of unsaturated materials [161,191] shows that there is still much work to do to fundamentally understand proton relaxation in corner islands. This is out of the scope of this dissertation. The investigation of the moisture behaviour in hydrophobised materials is therefore solely based on XCT images, which means that this technique's spatial resolution limits the investigation to hydrophobised sintered glass.

Subchapter B hence uses XCT imaging to extract the water island size distributions of hydrophobised sintered glass samples, preconditioned to different saturation states, and compares them with distributions extracted from hydrophilic samples. This investigation focuses on identifying the remaining storage sites in hydrophobised materials. From these distributions, two main conclusions are drawn. Firstly, (almost) all pore bodies and throats in the hydrophobised sintered glass samples are assumed to at least become partially hydrophobised. This conclusion is derived from the desorption sequence of pore bodies and throats in the hydrophobised materials, which follow a more random drying order, with less of a capillary fingering drying pattern and more of a drying front. This drying sequence is similar to existing studies on networks which only contain hydrophobised pore bodies and throats [200,203,204]. Also, the moisture retention curves, derived from the steady state centrifuge experiment in Chapter 4, show that the hydrophobised sintered glass samples empty completely at velocities for which the hydrophilic sintered glass hardly desaturates. Therefore, most (if not all) pore network elements need to be at least partially hydrophobised.

Secondly, due to the absence of completely hydrophilic pore network elements in the hydrophobised pore network, moisture can only be stored in corners of hydrophobised elements. The water island size distributions and XCT images show that this type of corner storage remains possible, albeit in lesser amounts compared to the hydrophilic samples. Due to the little amount of corner storage

and the little to no filled hydrophilic elements, there is no continuous liquid flow through the sample and hence vapour transport remains the only possible moisture transport mechanism. This absence of liquid flow was also noted in the adapted cup tests of Chapter 4. The conclusions of this subchapter are used to adapt the hydrophilically-oriented PNM in Chapter 6 for hygric property determination of hydrophobised porous materials.
Such possible hydrophilic storage sites in hydrophobised materials have been noted previously in literature. Barnat-Hunek and Smarzewski [198] use scanning electron microscopy (SEM) images to visualise the water repellent agent in hydrophobised ceramic bricks. They notice a continuous silicon coating on the grains with some cracks where the material possibly remains hydrophilic. These cracks could be the hydrophilic corners where some moisture storage remains possible. Also, measurements with hygroscopic desiccators show that moisture storage in the hygroscopic region of hydrophobised materials, where moisture is stored in small capillary filled elements and in pore corners, is reduced, but still remains possible, as explained in Chapter 2. Both these microscopic [198] and macroscopic [8,9,30,32,46] investigations therefore show that some hydrophilic storage sites can exist in hydrophobised materials. Blocked and/or clogged pores, which were noticed in [197] are not seen in the hydrophobised sintered glass. This is possibly due to the larger pore system of sintered glass, where all pores can be penetrated by the water repellent agent. The same investigation therefore needs to be repeated on materials with finer pore systems (i.e. ceramic brick and lime mortar) once imaging techniques allow it.

1.3 Chapter 6: Pore network modeling of hygric properties

This final chapter revolves around the main objective of this dissertation, i.e. the pore network modeling of hygric properties of hydrophobised building materials. Before focusing on these hydrophobised materials, however, the existing hydrophilically-oriented PNM is microscopically validated with the XCT images, acquired in Chapter 5, Subchapter A. In doing so, the limitations of the PNM are highlighted and recommendations for model improvement are formulated.
Subchapter A compares the water island size distributions, extracted from the XCT images of hydrophilic sintered glass, with the same distributions, simulated with the PNM, to microscopically validate the existing model. In doing so, two main problems are highlighted. Firstly, the PNM assumes that all pore bodies and throats, labelled as rectangular or triangular, are capable of storing moisture in their irregularly shaped corners. The amount of moisture in these corners also continuously increases with increasing capillary pressure. This amounts to a severe overestimation of the amount of moisture stored in such element corners. Secondly, it is shown that the invasion percolation algorithm, implemented in the PNM, preferentially empties pore bodies over pore throats in the drying

sequence due to the overall larger size of these elements. This results in the existence of multiple filled pore throats, which are connected to two empty pore bodies, which is rarely noticed in the XCT images. It should be mentioned that the presence of such isolated filled throats, however, is influenced by the extraction of the pore network from the material's continuous pore structure [86,87] and using a different pore network extraction algorithm might cause less of these isolated filled throats to occur. This problem might therefore be specific to this material and the used extraction algorithm.

Based on these problems, recommendations for model improvement are formulated and different model implementations are created. The water island size distributions, resulting from these different versions of the PNM, are then compared with the distributions extracted from XCT images to assess their microscopic impact. The amount of moisture in the element corners is reduced by either limiting the volume of moisture stored in element corners to a certain percentage of that element's total volume or by eliminating the corner islands from all pore throats. The isolated filled throats are removed from the PNM by emptying a pore throat once its two connecting pore bodies are emptied. By comparing the simulated water island size distributions with results from the XCT images, it becomes clear that limiting the maximum volume fraction of corner islands in all elements to 10 % is necessary to achieve an acceptable microscopical agreement between XCT images and PNM simulations. This maximum volume fraction of 10 % is therefore used in any future simulations with the PNM. The removal of isolated filled throats also provide a slightly better microscopic agreement between distributions from XCT images and PNM simulations. Since XCT images still show the existence of some isolated filled throats, however, this change does not completely stroke with reality. It is important to mention that the impact of these changes to the PNM have a large impact on the extracted microscopic water island size distributions, but a smaller impact on the macroscopic hygric properties. Only completely removing throat corner islands from pore throats, and hereby interrupting the corner flow between every pore body, has a significant effect on the moisture permeability. Since the simulation of the macroscopic hygric properties is the main goal of the PNM, one could argue that striving for an acceptable microscopic validation, rather than a perfect one, is sufficient, especially since this pore network modeling approach already relies on multiple assumptions and simplifications.

Above-mentioned changes to the PNM are derived from a microscopic study on sintered glass and they are hence not uniformly applicable to all materials. In other words, the PNM is tailored to some experimental properties of this sintered glass (e.g. microscopic water island distributions and moisture retention curves). Research has shown that this tailoring reinforces the confidence in other simulated properties, which are much harder to measure experimentally

(e.g. unsaturated permeability) [88–90]. Future microscopic validation of the PNM on other materials are required to indicate whether these changes are universally applicable or material-specific.

Subchapter B subsequently handles the pore network modeling of hygric properties of hydrophobised building materials. First, the existing hydrophilically-oriented pore network model is adapted for hydrophobised materials using the conclusions drawn in Chapter 5. This results in a PNM where almost all elements are hydrophobised and moisture storage in element corners remains possible, albeit to a lesser degree than in hydrophilic elements. Since these conclusions are based on a microscopic investigation of moisture behaviour in sintered glass, however, they are not directly applicable to more common building materials like ceramic bricks. In such bricks, more hydrophilic elements might be present due to the overall smaller size of its pore bodies and throats, as also shown by the measured moisture retention curves in Chapter 4. The same goes for partially hydrophobised materials, where more hydrophilically-oriented elements can be found. To this aim, the hydrophobic radius, below which all elements are assumed to remain hydrophilic, is implemented in the PNM. This hydrophobic radius is varied to represent an increasing amount of hydrophilically-oriented pore bodies and throats in the pore network. Also, the maximum volume fraction of water islands in hydrophobised element corners, which is set to 10 % in hydrophilic elements as shown in Section A, is varied between 0%, 5% or 10% to represent no moisture, less moisture and equally much moisture in element corners of hydrophobised elements as in hydrophilic elements. Finally, the discontinuous liquid flows in porous materials are also represented by modeling the extreme case where corner islands are removed from all pore throats.

The hygric properties of both hydrophobised sintered glass and ceramic brick are simulated using all variations of the PNM and they are validated with the hygric properties acquired in Chapter 4. Since spontaneous moisture storage and transport is modeled, the experimentally determined moisture retention curves, acquired from the saturated moisture content in Chapter 4, cannot be used. Therefore, only the vapour permeabilities, measured with the cup tests, remain viable for comparison. These vapour permeabilities provide a good agreement with the modeled hygric properties of sintered glass, however, they do not approach the vapour permeability of ceramic brick. This is attributed to the imperfect pore network representation of ceramic brick, derived from the stochastic generator [76,115,116], which is still under construction. Any conclusions drawn from the simulations with the pore network of ceramic brick therefore still require validation once the final version of the brick's pore network is extracted.

To investigate the impact of an increasing amount of hydrophilic elements in a hydrophobised material, the hygric properties are simulated for different

hydrophobic radii after which these properties are used to simulate the capillary absorption experiment in the hygrothermal model Delphin. The capillary absorption coefficient, derived from this experiment, is generally used as a measure of the hydrophobisation application's efficiency and is also treated as such in this subchapter. For both materials, capillary absorption coefficients are reduced by at least 95-97 %, which is generally regarded as successful, when less than 6 % of the pore volume remains hydrophilic. For sintered glass and ceramic brick, this translates to a hydrophobic radius of 10 µm and 0.75 µm, respectively. In other words, if the polymers of water repellent agents manage to hydrophobise all elements larger than these radii, the absorption of moisture is sufficiently reduced. Since the DLS measurements recorded hydrodynamic radii of commercial water repellent agents smaller than 0.4 µm, these water repellent agents are suited for the hydrophobisation of the investigated building materials. This also explains the removal of a continuous liquid flow across the sample as measured in the adapted cup tests of Chapter 4.
It is also interesting to note the sudden increase of the capillary absorption coefficient in ceramic brick when the hydrophobic radius is increased from 1 µm to 2 µm. This is attributed to the nanoscale porosity in the brick, which remains hydrophilic due to its small size and forms liquid flow paths between elements which are otherwise only connected via hydrophobised elements. Such high capillary absorption coefficients should be avoided at all cost, which again points out the need to tailor the water repellent agent to the building material. It is therefore advised to at least estimate the pore size distribution of materials and the emulsion droplet size of water repellent agents, before deciding which product to use.

2 Conclusions

The main conclusions of this PhD thesis are reiterated in this section. These conclusions are all applicable to the materials studied in this thesis and they are hence not generally applicable to all hydrophobised materials. Generalising these conclusions requires future research, which is explained in Section 3.

- The developed steady state centrifuge experiment has shown to be a valuable addition to the existing experimental techniques for moisture retention curve determination of hydrophilic materials. Moisture retention curves can be determined up to capillary pressures of ca. 5.1 log(Pa) within a limited timeframe and with a sufficient degree of accuracy. While MIP testing is still faster and a little more accurate, the steady state centrifuge's potential to measure moisture retention curves starting from the more realistic capillary moisture content, makes this technique worth using. This technique has also shown to be applicable for the moisture

retention curve determination of hydrophobised materials. These curves take significantly longer to measure, however, and are currently only measured from the saturated moisture content, which requires unrealistic vacuum conditions to precondition the samples.

- The hygric property measurement of the fully hydrophobised materials used in this dissertation has proven that hardly any moisture can be stored in these materials under normal environmental conditions. As a result, there is no continuous liquid flow across the fully hydrophobised material and moisture transport is dominated by vapour flow. Extension of these conclusions to hydrophobised materials with finer pore systems (e.g. lime mortar) and partially hydrophobised materials, however, does require further testing using the same experimental methods as in Chapter 4.

- Nuclear magnetic resonance relaxometry proves unable to investigate the microscopic moisture behaviour in porous materials as intended in this dissertation. The extracted water island size distributions focus on the largest water islands in the capillary filled pore network elements and the corner islands are largely ignored. Additionally, the magnetic signals require elaborate post-processing, which is heavily influenced by the used inversion algorithms and the applicability of several assumptions (i.e. no or weak diffusional coupling, little paramagnetic impurities, calculation of the surface relaxivity).

- The microscopic investigation of the moisture behaviour in hydrophobised materials shows that there are little to no completely hydrophilic elements in the studied materials. Moisture storage remains possible in some hydrophilic corners of hydrophobised pore network elements albeit to a lesser degree than in hydrophilic materials. These water islands do not form a continuous liquid flow path through the sample, however, and hence this once more confirms that moisture flow through these samples is dominated by vapour flow.

- The microscopic validation of the existing hydrophilically-oriented PNM has highlighted some problems (overestimation of water in pore corners, presence of isolated filled throats) which were solved with rather simple changes to the PNM. Especially, limiting the corner volume fraction of these corner islands to 10 % proves necessary. These changes are derived from a study on sintered glass, however, and they are therefore not universally applicable to all materials.

- The PNM, adapted with the conclusions of Chapter 5, has been used to simulate hygric properties of materials with varying amounts of

hydrophilically-oriented pore network elements with the help of a fictive hydrophobic radius. If the smallest hydrophobic radius is used, (almost) all elements become hydrophobised and the simulated capillary absorption coefficient approximates the experimental values of both sintered glass and ceramic brick well. The different hydrophobic radii have also shown that capillary absorption coefficient reductions of 95-97 %, which are typically required for successful hydrophobisation applications, are guaranteed for both materials if less than 6 % of their pore volume remains hydrophilic.

- Simulations of the capillary absorption coefficient of hydrophobised materials with increasing amounts of hydrophilically-oriented elements have noted the importance of the nanoscale porosity in ceramic brick. These smaller pores are most likely to remain hydrophilic due to the water repellent agent's inability to enter them and they can therefore cause liquid flow paths across the material. Choosing a water repellent agent which is capable of hydrophobising at least part of the nanoscale porosity is therefore advised.

3 Limitations and future work

This final part of the dissertation discusses the main limitations of this PhD thesis and provides an outlook on possible follow-up research. This section focuses on the general limitations of this work. Some specific problem areas (e.g. the limited rotational velocity of the centrifuge), are already discussed in the individual chapters and they are therefore not repeated here.

The main limitation of this dissertation is that most of its work is focused on sintered glass, which is not a typical building material. It exists of a rather narrow range of pore sizes in the micrometer range in comparison to the more common building materials, comprising pore bodies and throats over several spatial scales. In chapter 5, the investigation of hydrophilic storage sites in the hydrophobised sintered glass showed no completely hydrophilic pore bodies or throats in the material. However, such hydrophilically-oriented elements could be present in other building materials which also contain pores in the nanometer range. Extending this microscopic investigation to other materials, to validate the conclusions drawn in Chapter 5, therefore remains crucial. This is of course only possible when progress is made in the research area of microscopy and the smaller pore bodies and throats of these materials can be visualised.

This investigation of the microscopic moisture behaviour in other building materials would also allow further microscopically validating the PNM. Currently, this PNM is microscopically and macroscopically validated in Chapter 6 using results from sintered glass. The limitations of the PNM, with regards to the percolation algorithm and the calculation of the moisture storage and transport

in pore corners, are illustrated during this validation. Currently, crude solutions to these problems, which provide an acceptable microscopic and macroscopic validation of the PNM for hygric property determination in sintered glass, are implemented. It is possible though that these problems of the PNM are only applicable to the studied sintered glass. The simple solutions, implemented in the PNM in Chapter 6 might therefore cause the model to be fitted to this material. Microscopically validating this model with other materials therefore also remains necessary before the PNM can be deemed fully validated.

This dissertation also only focuses on fully hydrophobised materials. As explained in Chapter 2, however, when a water repellent agent penetrates a masonry wall, it forms a fully hydrophobised zone near the application surface, with a partially hydrophobised zone spreading much further into the materials, in which the hydrophobic effect is less pronounced. No hygric properties of such partially hydrophobised materials are measured as of yet nor do any other studies of the moisture behaviour in such partially hydrophobised zones exist to the author's knowledge. Modeling such partially hydrophobised materials therefore remains difficult at the moment. Repeating this entire study for partially hydrophobised samples, which can be created by exposing samples to a more diluted water/agent emulsion or by cutting the samples directly from the partially hydrophobised zone of a hydrophobised wall, is therefore crucial to obtain hygric properties which allow simulating the complete hydrophobised masonry wall in a real-life application. Also, a detailed investigation towards the physics of polymer transport through the pore network of materials can prove useful to identify how the water repellent agent truly penetrates the masonry walls, hereby creating fully and partially hydrophobised zones.

Once hygric properties of ceramic brick as well as mortar, in both the fully and partially hydrophobised zones, are available, hygrothermal simulation models can use these properties to more accurately simulate the moisture behaviour in hydrophobised masonry walls. For now, this dissertation has shown that the ceramic brick in the fully hydrophobised zone can be approximated by (almost) completely eliminating the liquid flow and only permitting vapour transport through the material as well as heavily reducing the storage capacity. However, solely modeling this fully hydrophobised zone does not stroke with reality and more information on the partially hydrophobised zone as well as the hydrophobised mortar is required.

A final remark is that this PhD thesis revolves around the development of a PNM for the hygric property determination of hydrophobised materials. In this PNM, a pore network, which is representative of the material, is used as input and all pore network elements are classified as being hydrophilic or hydrophobised. The conclusions of the PNM simulations in Chapter 6 then show that the reduction of the moisture absorption of such materials is directly linked to the amount of pore network elements which become hydrophobised. There are other factors,

however, which can also influence the moisture behaviour at the pore level, like cracks in a material which promote moisture transport or the diminishing water repellent effect due to weathering of the hydrophobised facade. Simply choosing a water repellent agent which hydrophobises all of the pore bodies and throats in a material might therefore not be sufficient to reduce the water absorption. One should also look at the state of the masonry wall as well as the durability of the used agents. This PhD thesis mainly focuses on the ideal scenario (i.e. undamaged, fully hydrophobised materials) to display the possibilities of this quasi-static pore network modeling approach. Before this modeling approach can be used for any hydrophobised facade, much more research needs to go into investigating different (fully and partially) hydrophobised materials as well as more specific cases like weathered hydrophobised materials.

Bibliography

[1] M. Braubach. Children living in homes with problems of damp, 2009. https://studylib.net/doc/18264409/children-living-in-homes-with-problems-of-damp, Accessed on 17/01/2024.

[2] G. R. Finken, S. P. Bjarløv, and R. H. Peuhkuri. Effect of façade impregnation on feasibility of capillary active thermal internal insulation for a historic dormitory–a hygrothermal simulation study. *Constr. Build. Mater.*, 113:202–214, 2016. doi: 10.1016/j.conbuildmat.2016.03.019.

[3] K. Fukui, C. Iba, and S. Hokoi. Moisture behavior inside building materials treated with silane water repellent. *Energy Procedia*, 132:735–740, 2017. doi: 10.1016/j.egypro.2017.10.018.

[4] A. A. Hamid and P. Wallentén. Hygrothermal assessment of internally added thermal insulation on external brick walls in swedish multifamily buildings. *Build. Environ.*, 123:351–362, 2017. doi: 10.1016/j.buildenv.2017.05.019.

[5] T. K. Hansen, S. P. Bjarløv, R. H. Peuhkuri, and K. K. Hansen. Performance of hydrophobized historic solid masonry–experimental approach. *Constr. Build. Mater.*, 188:695–708, 2018. doi: 10.1016/j.conbuildmat.2018.08.145.

[6] V. Soulios, E. J. de Place Hansen, C. Feng, and H. Janssen. Hygric behavior of hydrophobized brick and mortar samples. *Build. Environ.*, 176:106843, 2020. doi: 10.1016/j.buildenv.2020.106843.

[7] V. Soulios, E. J. de Place Hansen, R. H. Peuhkuri, E. Møller, and A. Ghanbari-Siahkali. Durability of the hydrophobic treatment on brick and mortar. *Build. Environ.*, 201:107994, 2021. doi: 10.1016/j.buildenv.2020.106843.

[8] C. Feng and H. Janssen. Impact of water repellent agent concentration on the effect of hydrophobization on building materials. *J. Build. Eng.*, 39:102284, 2021. doi: 10.1016/j.jobe.2021.102284.

[9] X. Li, Q. Zhong, M. Tang, Y. Gao, and C. Feng. Experimental and numerical analysis of the hygric performance of earthen buildings after façade hydrophobization treatment. *Case Stud. Constr. Mater.*, page e02217, 2023. doi: 10.1016/j.cscm.2023.e02217.

[10] E. Vereecken, L. Van Gelder, H. Janssen, and S. Roels. Interior insulation for wall retrofitting–a probabilistic analysis of energy savings and hygrothermal risks. *Energy Build.*, 89:231–244, 2015. doi: 10.1016/j.enbuild.2014.12.031.

[11] T. Cambray, V. Marincioni, and H. Altamirano. An overview of hydrophobic treatments and their application with internal wall insulation. *UCL Open: Environment Preprint*, 2022.

[12] E. Vereecken, D. Deckers, H. Janssen, and S. Roels. Field study on hydrophobised internally insulated masonry walls. *DBMC 2020, Barcelona*, pages 1–8, 2020. doi: 10.23967/dbmc.2020.067.

[13] E. Vereecken and S. Roels. Hygrothermal performance of internally insulated masonry walls with embedded wooden beam heads: A field study on the impact of hydrophobisation. In *J. Phys. Conf. Ser.*, volume 2069, page 012019. IOP Publishing, 2021. doi: 10.1088/1742-6596/2069/1/012019.

[14] V. Soulios, E. J. de Place Hansen, and R. H. Peuhkuri. Hygrothermal performance of hydrophobized and internally insulated masonry walls-simulating the impact of hydrophobization based on experimental results. *Build. Environ.*, 187:107410, 2021. doi: 10.1016/j.buildenv.2020.107410.

[15] E. J. de Place Hansen, T. K. Hansen, and V. Soulios. Deep renovation of an old single-family house including application of an water repellent agent–a case story. In *IOP Conf. Ser. Earth Environ. Sci.*, volume 863, page 012034. IOP Publishing, 2021. doi: 10.1088/1755-1315/863/1/012034.

[16] RIBuild. Ribuild makes historic buildings more energy efficient. https://www.ribuild.eu/references, Accessed on 17/01/2024.

[17] E. Barbieri, F. Trevisiol, C. Pizzigatti, G. Bitelli, and E. Franzoni. Evaluating water-repellents applied to brick masonry: An experimental study by thermal imaging and water transport properties' characterization. *Constr. Build. Mater.*, 356:129319, 2022. doi: 10.1016/j.conbuildmat.2022.129319.

[18] A. E. Charola. Water-repellent treatments for building stones: A practical overview. *APT Bulletin: The Journal of Preservation Technology*, 26 (2/3):10–17, 1995. doi: 10.2307/1504480.

[19] T. Van Besien, S. Roels, and J. Carmeliet. A laboratory study of the efficiency of a hydrophobic treatment of cracked porous building materials. In *Research in Building Physics*, pages 301–306. CRC Press, 2003. doi: 10.1201/9781003078852-42.

[20] B. Lubelli, R. P. J. van Hees, C. Groot, and J. Gunneweg. Risks of the use of water repellents on salt contaminated masonry: the case of a windmill in the netherlands/risiken beim hydrophobieren von salzhaltigem mauerweric fallstudie anhand einer windmühle in den niederlanden. *Restoration Build. Monuments*, 13(5):319–330, 2007. doi: 10.1515/rbm-2007-6154.

[21] E. Wendler and E. von Plehwe-Leisen. Water repellent treatment of porous materials. a new edition of the wta leaflet. In *Proceedings of the 5th International Conference on Water Repellent Treatment of Building Materials*, pages 155–168, 2008.

[22] V. Metavitsiadis, V. Soulios, H. Janssen, and S. Roels. Wall hydrophobization and internal insulation: the impact of impregnation strength and depth on moisture levels and moisture damages. In *Proceedings of Hydrophobe VIII in Hongkong, China*, pages 69–76, 2017.

[23] M. Islahuddin and H. Janssen. Pore-structure-based determination of unsaturated hygric properties of porous materials. *Transp. Porous Media*, 130(3):675–698, 2019. doi: 10.1007/s11242-019-01334-7.

[24] S. Babaei, S. C. Seetharam, A. Dizier, G. Steenackers, and B. Craeye. Permeability of cementitious materials using a multiscale pore network model. *Constr. Build. Mater.*, 312:125298, 2021. doi: 10.1016/j.conbuildmat.2021.125298.

[25] T. Bultreys, L. Van Hoorebeke, and V. Cnudde. Multi-scale, micro-computed tomography-based pore network models to simulate drainage in heterogeneous rocks. *Adv. Water Resour.*, 78:36–49, 2015. doi: 10.1016/j.advwatres.2015.02.003.

[26] P. K. Sinha and C. Wang. Pore-network modeling of liquid water transport in gas diffusion layer of a polymer electrolyte fuel cell. *Electrochim. Acta*, 52(28):7936–7945, 2007. doi: 10.1016/j.electacta.2007.06.061.

[27] J. Zhao, F. Qin, Q. Kang, D. Derome, and J. Carmeliet. Pore-scale simulation of drying in porous media using a hybrid lattice boltzmann: pore network model. *Dry. Technol.*, 40(4):719–734, 2022. doi: 10.1080/07373937.2021.1933017.

[28] S. Lal, M. Prat, M. Plamondon, L. Poulikakos, M. N. Partl, D. Derome, and J. Carmeliet. A cluster-based pore network model of drying with corner

liquid films, with application to a macroporous material. *Int. J. Heat Mass Transf.*, 140:620–633, 2019. doi: 10.1016/j.ijheatmasstransfer.2019.06.016.

[29] K. Namoulniara, P. Y. Mahieux, J. Lux, A. Aït-Mokhtar, and P. H. Turcry. Efficiency of water repellent surface treatment: Experiments on low performance concrete and numerical investigation with pore network model. *Constr. Build. Mater.*, 227:116638, 2019. doi: 10.1016/j.conbuildmat.2019.08.019.

[30] J. Carmeliet, G. Houvenaghel, J. Van Schijndel, and S. Roels. Moisture phenomena in hydrophobic porous building material part 1: measurements and physical interpretations/wechselwirkung hydrophobierter poröser werkstoffe des bauwesens mit feuchtigkeit, teil 1: messungen und physikalische interpretationen. *Restoration Build. Monuments*, 8(2-3): 165–184, 2002. doi: 10.1515/rbm-2002-5660.

[31] Sika AG. Sika technology and concepts for hydrophobic impregnations. https://www.sika.com/content/dam/dms/corporate/b/glo-hydrophobic-impregnation.pdf, 2015. Online; accessed 31 October 2023.

[32] X. Chen, T. De Kock, V. Cnudde, and N. Van Den Bossche. The influence of material characteristics and environmental circumstances on the efficiency of water repellent treatments of historic facades. *Constr. Build. Mater.*, 386:131610, 2023. doi: 10.1016/j.conbuildmat.2023.131610.

[33] J. MacMullen, Z. Zhang, J. Radulovic, C. Herodotou, M. Totomis, H. N. Dhakal, and N. Bennett. Titanium dioxide and zinc oxide nano-particulate enhanced oil-in-water (o/w) facade emulsions for improved masonry thermal insulation and protection. *Energy Build.*, 52:86–92, 2012. doi: 10.1016/j.enbuild.2012.05.027.

[34] B. Lubelli and R. P. J. van Hees. Evaluation of the effect of nano-coatings with water repellent properties on the absorption and drying behaviour of brick. In *6th International Conference on Water Repellent Treatment of Building Materials; Aedificatio Publishers: Freiburg, Germany*, pages 125–136, 2011.

[35] E. McGettigan. Factors affecting the selection of water-repellent treatments. *APT Bulletin: The Journal of Preservation Technology*, 26(4):22–26, 1995. doi: 10.2307/1504446.

[36] A. Izaguirre, J. Lanas, and J. I. Alvarez. Effect of water-repellent admixtures on the behaviour of aerial lime-based mortars. *Cem. Concr. Res.*, 39(11):1095–1104, 2009. doi: 10.1016/j.cemconres.2009.07.026.

[37] H. Mayer. Masonry protection with silanes, siloxanes and silicone resins. *Surface coatings international*, 81(2):89–93, 1998. doi: 10.1007/BF02692337.

[38] M. Roos, F. König, S. Stadtmüller, and B. Weyershausen. Evolution of silicone based water repellents for modern building protection. In *Proceedings of the 5th International Conference on Water Repellent Treatment of Building Materials, Brussels, Belgium*, pages 15–16, 2008.

[39] A. E. Charola. Water repellents and other "protective" treatments: A critical review. hydrophobe iii–3rd international conference on surface technology with water repellent agents, 2001.

[40] J. MacMullen, Z. Zhang, E. Rirsch, H. N. Dhakal, and N. Bennett. Brick and mortar treatment by cream emulsion for improved water repellence and thermal insulation. *Energy Build.*, 43(7):1560–1565, 2011. doi: 10.1016/j.enbuild.2011.02.014.

[41] D. Deckers, E. Vereecken, S. Roels, and H. Janssen. Influence of the disparities between lab and in-situ application on the penetration depth of a hydrophobic agent. In *J. Phys. Conf. Ser.*, volume 2069, page 012048. IOP Publishing, 2021. doi: 10.1088/1742-6596/2069/1/012048.

[42] F. Braun and J. Orlowsky. Non-destructive detection of the efficiency of long-term weathered hydrophobic natural stones using single-sided nmr. *J. Cult. Herit.*, 41:51–60, 2020. doi: 10.1016/j.culher.2019.07.005.

[43] J. Zhao and F. Meissener. Experimental investigation of moisture properties of historic building material with hydrophobization treatment. *Energy Procedia*, 132:261–266, 2017. doi: 10.1016/j.egypro.2017.09.716.

[44] C. Feng and H. Janssen. Hygric properties of porous building materials (vii): Full-range benchmark characterizations of three materials. *Build. Environ.*, 195:107727, 2021. doi: 10.1016/j.buildenv.2021.107727.

[45] Building Physics and Sustainable Design, KU Leuven. Test setups hygrothermal laboratory, 2016. Personal communication.

[46] Z. Pavlík, M. Keppert, M. Pavlíková, and R. Černỳ. Investigation of the effectiveness of siloxane hydrophobic injection for renovation of damp brick masonry. *Int. J. Chem. Mol. Nucl. Mater. Metall. Eng*, 6:123–126, 2012.

[47] ISO12572:2016(E). Hygrothermal performance of building materials and products - determination of water vapor transmission properties - cup method, 2016.

[48] C. Feng, H. Janssen, Y. Feng, and Q. Meng. Hygric properties of porous building materials: Analysis of measurement repeatability and reproducibility. *Build. Environ.*, 85:160–172, 2015. doi: 10.1016/j.buildenv.2014.11.036.

[49] C. Feng and H. Janssen. Hygric properties of porous building materials (ii): Analysis of temperature influence. *Build. Environ.*, 99:107–118, 2016. doi: 10.1016/j.buildenv.2016.01.016.

[50] Y. D. Aktas, H. Zhu, D. D'Ayala, and C. Weeks. Impact of surface waterproofing on the performance of brick masonry through the moisture exposure life-cycle. *Build. Environ.*, 197:107844, 2021. doi: 10.1016/j.buildenv.2021.107844.

[51] J. Engel, P. Heinze, and R. Plagge. Adapting hydrophobizing impregnation agents to the object. *Restoration Build. Monuments*, 20(6):433–440, 2014. doi: 10.1515/rbm14.20.6-0042.

[52] J. Carmeliet, T. van Besien, and S. Roels. Moisture phenomena in hydrophobic porous building material part 2: Measurements and modelling/wechselwirkung hydrophobierter poröser werkstoffe des bauwesens mit feuchtigkeit, teil 2: Messungen und modellbildung. *Restoration Build. Monuments*, 8(2-3):185–204, 2002. doi: 10.1515/rbm-2002-5661.

[53] Vandersanden. Robusta. https://www.vandersanden.com/nl-be/products-and-solutions/robusta, 2023. Online; accessed 28 November 2023.

[54] S. Roels, E. Vereecken, M. H. L. Stappers, and W. J. Quist. Hygrothermal properties relationships in historic bricks. In *2nd International Conference on Moisture in Buildings 2023*. ScienceOpen, 2023. doi: 10.14293/ICMB230017.

[55] ROBU. Vitrapor glass filters. https://www.robuglas.com/en/service/technical-data/porosity-of-vitraporr-glass-filters.html, 2023. Online; accessed 28 November 2023.

[56] S. Claes, W. Van De Walle, M. Islahuddin, and H. Janssen. The application of computed tomography for characterizing the pore structure of building materials. *J. Build. Phys.*, 43(4):254–276, 2020. doi: 10.1177/17442591198809.

[57] J. MacMullen, J. Radulovic, Z. Zhang, H. N. Dhakal, L. Daniels, J. Elford, M. A. Leost, and N. Bennett. Masonry remediation and protection by aqueous silane/siloxane macroemulsions incorporating colloidal titanium dioxide and zinc oxide nanoparticulates: Mechanisms,

performance and benefits. *Constr. Build. Mater.*, 49:93–100, 2013. doi: 10.1016/j.conbuildmat.2013.08.019.

[58] I. Fatt. The network model of porous media. *Transactions of the AIME*, 207(01):144–181, 1956. doi: 10.2118/574-G.

[59] J. Carmeliet, F. Descamps, and G. Houvenaghel. A multiscale network model for simulating moisture transfer properties of porous media. *Transp. Porous Media*, 35:67–88, 1999. doi: 10.1023/A:1006500716417.

[60] M. A. Ioannidis and I. Chatzis. Network modelling of pore structure and transport properties of porous media. *Chem. Eng. Sci.*, 48(5):951–972, 1993. doi: 10.1016/0009-2509(93)80333-L.

[61] J. Arns, V. Robins, A. P. Sheppard, R. M. Sok, W. V. Pinczewski, and M. A. Knackstedt. Effect of network topology on relative permeability. *Transp. Porous Media*, 55(1):21–46, 2004. doi: 10.1023/B:TIPM.0000007252.68488.43.

[62] A. Q. Raeini, J. Yang, I. Bondino, T. Bultreys, M. J. Blunt, and B. Bijeljic. Validating the generalized pore network model using micro-ct images of two-phase flow. *Transp. Porous Media*, 130(2):405–424, 2019. doi: 10.1007/s11242-019-01317-8.

[63] T. Bultreys, K. Singh, A. Q. Raeini, L. C. Ruspini, P. Øren, S. Berg, M. Rücker, B. Bijeljic, and M. J. Blunt. Verifying pore network models of imbibition in rocks using time-resolved synchrotron imaging. *Water Resour. Res.*, 56(6):e2019WR026587, 2020. doi: 10.1029/2019WR026587.

[64] S. Berg, M. Rücker, H. Ott, A. Georgiadis, H. Van der Linde, F. Enzmann, M. Kersten, R. T. Armstrong, S. De With, J. Becker, and A. Wiegmann. Connected pathway relative permeability from pore-scale imaging of imbibition. *Adv. Water Resour.*, 90:24–35, 2016. doi: 10.1016/j.advwatres.2016.01.010.

[65] T. Bultreys, Q. Lin, Y. Gao, A. Q. Raeini, A. AlRatrout, B. Bijeljic, and M. J. Blunt. Validation of model predictions of pore-scale fluid distributions during two-phase flow. *Phys. Rev. E*, 97(5):053104, 2018. doi: 10.1103/PhysRevE.97.053104.

[66] T. Akai, A. M. Alhammadi, M. J. Blunt, and B. Bijeljic. Modeling oil recovery in mixed-wet rocks: pore-scale comparison between experiment and simulation. *Transp. Porous Media*, 127:393–414, 2019. doi: 10.1007/s11242-018-1198-8.

[67] A. S. Al-Kharusi and M. J. Blunt. Network extraction from sandstone and carbonate pore space images. *J. Pet. Eng.*, 56(4):219–231, 2007. doi: 10.1016/j.petrol.2006.09.003.

[68] M.J. Blunt. *Multiphase flow in permeable media: A pore-scale perspective.* Cambridge university press, 2017.

[69] R. Wu, T. Zhang, C. Ye, C. Y. Zhao, E. Tsotsas, and A. Kharaghani. Pore network model of evaporation in porous media with continuous and discontinuous corner films. *Phys. Rev. Fluids*, 5(1):014307, 2020. doi: 10.1103/PhysRevFluids.5.014307.

[70] J. Zhao, F. Qin, Q. Kang, C. Qin, D. Derome, and J. Carmeliet. A dynamic pore network model for imbibition simulation considering corner film flow. *Water Resour. Res.*, 58(7):e2022WR032332, 2022. doi: 10.1029/2022WR032332.

[71] K. Xu, J. Daian, and D. Quenard. Multiscale structures to describe porous media part i: theoretical background and invasion by fluids. *Transp. Porous Media*, 26:51–73, 1997. doi: 10.1023/A:1006557915438.

[72] D. A. Quenard, K. Xu, H. M. Künzel, D. P. Bentz, and N. S. Martys. Microstructure and transport properties of porous building materials. *Mater. Struct.*, 31:317–324, 1998. doi: 10.1007/BF02480673.

[73] M. Koster, J. Hannawald, and W. Brameshuber. Simulation of water permeability and water vapor diffusion through hardened cement paste. *Comput. Mech.*, 37:163–172, 2006. doi: 10.1007/s00466-005-0687-0.

[74] S. Babaei, S. C. Seetharam, U. Muehlich, A. Dizier, G. Steenackers, and B. Craeye. A multiscale framework to estimate water sorption isotherms for opc-based materials. *Cem. Concr. Compos.*, 105:103415, 2020. doi: 10.1016/j.cemconcomp.2019.103415.

[75] S. Claes and H. Janssen. Stochastic generation of multiscale 3d pore network models of building materials. In *E3S Web of Conferences*, volume 172, page 08002. EDP Sciences, 2020. doi: 10.1051/e3sconf/202017208002.

[76] S. Shi, J. Soete, and H. Janssen. Influence of pore network parameters on hygric property prediction for porous building materials. *Transp. Porous Media*, 2024. doi: 10.1007/s11242-024-02076-x.

[77] Z. Jiang, M. I. J. Van Dijke, K. S. Sorbie, and G. D. Couples. Representation of multiscale heterogeneity via multiscale pore networks. *Water Resour. Res.*, 49(9):5437–5449, 2013. doi: 10.1002/wrcr.20304.

[78] T. Bultreys, W. De Boever, and V. Cnudde. Imaging and image-based fluid transport modeling at the pore scale in geological materials: A practical introduction to the current state-of-the-art. *Earth Sci. Rev.*, 155: 93–128, 2016. doi: 10.1016/j.earscirev.2016.02.001.

[79] A. R. Kovscek, H. Wong, and C. J. Radke. A pore-level scenario for the development of mixed wettability in oil reservoirs. *AIChE J.*, 39(6): 1072–1085, 1993.

[80] P. H. Valvatne and M. J. Blunt. Predictive pore-scale modeling of two-phase flow in mixed wet media. *Water resour. res.*, 40(7), 2004.

[81] P. Øren, S. Bakke, and O. J. Arntzen. Extending predictive capabilities to network models. *SPE J.*, 3(04):324–336, 1998.

[82] J. Zhao, F. Qin, R. Fischer, Q. Kang, D. Derome, and J. Carmeliet. Spontaneous imbibition in a square tube with corner films: theoretical model and numerical simulation. *Water Resour. Res.*, 57(2): e2020WR029190, 2021. doi: 10.1029/2020WR029190.

[83] B. Ahrenholz, J. Tölke, P. Lehmann, A. Peters, A. Kaestner, M. Krafczyk, and W. Durner. Prediction of capillary hysteresis in a porous material using lattice-boltzmann methods and comparison to experimental data and a morphological pore network model. *Adv. Water Resour.*, 31(9): 1151–1173, 2008. doi: 10.1016/j.advwatres.2008.03.009.

[84] L. Fei, F. Qin, J. Zhao, D. Derome, and J. Carmeliet. Pore-scale study on convective drying of porous media. *Langmuir*, 38(19):6023–6035, 2022. doi: 10.1021/acs.langmuir.2c00267.

[85] T. Ramstad, C. F. Berg, and K. Thompson. Pore-scale simulations of single-and two-phase flow in porous media: approaches and applications. *Transp. Porous Media*, 130:77–104, 2019. doi: 10.1007/s11242-019-01289-9.

[86] A. Hunt, R. Ewing, and B. Ghanbarian. *Percolation theory for flow in porous media*, volume 880. Springer, 2014.

[87] J. Arns, A. P. Sheppard, C. H. Arns, M. A. Knackstedt, A. Yelkhovsky, and W. V. Pinczewski. Pore-level validation of representative pore networks obtained from micro-ct images. In *Proceedings of the international symposium of the society of core analysts*, pages 1–12. Citeseer, 2007.

[88] C. Caubit, G. Hamon, A. P. Sheppard, and P. Øren. Evaluation of the reliability of prediction of petrophysical data through imagery and pore network modelling. *Petrophysics-The SPWLA Journal of Formation Evaluation and Reservoir Description*, 50(04), 2009.

[89] K. S. Sorbie and A. Skauge. Can network modeling predict two-phase flow functions? *Petrophysics*, 53(06):401–409, 2012.

[90] L. C. Ruspini, P. Øren, S. Berg, S. Masalmeh, T. Bultreys, C. Taberner, T. Sorop, F. Marcelis, M. Appel, J. Freeman, et al. Multiscale digital rock analysis for complex rocks. *Transp. Porous Media*, 139(2):301–325, 2021.

[91] S. Konangi, N. K. Palakurthi, N. K. Karadimitriou, K. Comer, and U. Ghia. Comparison of pore-scale capillary pressure to macroscale capillary pressure using direct numerical simulations of drainage under dynamic and quasi-static conditions. *Adv. Water Resour.*, 147:103792, 2021. doi: 10.1016/j.advwatres.2020.103792.

[92] V. Joekar-Niasar and S. M. Hassanizadeh. Analysis of fundamentals of two-phase flow in porous media using dynamic pore-network models: A review. *Crit. Rev. Environ. Sci. Technol.*, 42(18):1895–1976, 2012. doi: 10.1080/10643389.2011.574101.

[93] H. Janssen, G. A. Scheffler, and R. Plagge. Experimental study of dynamic effects in moisture transfer in building materials. *Int. J. Heat Mass Transf.*, 98:141–149, 2016. doi: 10.1016/j.ijheatmasstransfer.2016.03.031.

[94] M. Islahuddin and H. Janssen. Hygric property estimation of porous building materials with multiscale pore structures. *Energy Procedia*, 132: 273–278, 2017. doi: 10.1016/j.egypro.2017.09.722.

[95] Q. Xiong, T. G. Baychev, and A. P. Jivkov. Review of pore network modelling of porous media: Experimental characterisations, network constructions and applications to reactive transport. *J. Contam. Hydrol.*, 192:101–117, 2016. doi: 10.1016/j.jconhyd.2016.07.002.

[96] H. Dong and M. J. Blunt. Pore-network extraction from micro-computerized-tomography images. *Phys. R. E*, 80(3):036307, 2009. doi: 10.1103/PhysRevE.80.036307.

[97] A. Q. Raeini, B. Bijeljic, and M. J. Blunt. Generalized network modeling: Network extraction as a coarse-scale discretization of the void space of porous media. *Phys. Rev. E*, 96(1):013312, 2017. doi: 10.1103/PhysRevE.96.013312.

[98] C. L. Y. Yeong and S. Torquato. Reconstructing random media. *Phys. Rev. E*, 57(1):495, 1998. doi: 10.1103/PhysRevE.57.495.

[99] C. L. Y. Yeong and S. Torquato. Reconstructing random media ii. three-dimensional media from two-dimensional cuts. *Phys. Rev. E*, 58(1): 224–233, 1998. doi: 10.1103/PhysRevE.58.224.

[100] M. A. Ioannidis and I. Chatzis. On the geometry and topology of 3d stochastic porous media. *J. Colloid Interface Sci.*, 229(2):323–334, 2000. doi: 10.1006/jcis.2000.7055.

[101] H. Okabe and M. J. Blunt. Pore space reconstruction using multiple-point statistics. *J. Pet. Eng.*, 46(1-2):121–137, 2005. doi: 10.1016/j.petrol.2004.08.002.

[102] Y. Wu, C. Lin, L. Ren, W. Yan, S. An, B. Chen, Y. Wang, X. Zhang, C. You, and Y. Zhang. Reconstruction of 3d porous media using multiple-point statistics based on a 3d training image. *J. Nat. Gas Sci. Eng.*, 51:129–140, 2018. doi: 10.1016/j.jngse.2017.12.032.

[103] S. Bryant and M. Blunt. Prediction of relative permeability in simple porous media. *Phys. Rev. A*, 46(4):2004, 1992. doi: 10.1103/PhysRevA.46.2004.

[104] S. Bakke and P. Øren. 3-d pore-scale modelling of sandstones and flow simulations in the pore networks. *Spe J.*, 2(02):136–149, 1997. doi: 10.2118/35479-PA.

[105] D. B. Silin, G. Jin, and T. W. Patzek. Robust determination of the pore space morphology in sedimentary rocks. In *SPE Annual Technical Conference and Exhibition*. OnePetro, 2003. doi: 10.2118/84296-MS.

[106] D. Silin and T. Patzek. Pore space morphology analysis using maximal inscribed spheres. *Phys. A: Stat. Mech. Appl.*, 371(2):336–360, 2006. doi: 10.1016/j.physa.2006.04.048.

[107] F. Arand and J. Hesser. Accurate and efficient maximal ball algorithm for pore network extraction. *Comput. Geosci.*, 101:28–37, 2017. doi: 10.1016/j.cageo.2017.01.004.

[108] C. A. Baldwin, A. J. Sederman, M. D. Mantle, P. Alexander, and L. F. Gladden. Determination and characterization of the structure of a pore space from 3d volume images. *J. Colloid Interface Sci.*, 181(1):79–92, 1996. doi: 10.1006/jcis.1996.0358.

[109] W. B. Lindquist and A. Venkatarangan. Investigating 3d geometry of porous media from high resolution images. *Phys. Chem. Earth*, 24(7):593–599, 1999. doi: 10.1016/S1464-1895(99)00085-X.

[110] W. B. Lindquist, A. Venkatarangan, J. Dunsmuir, and T. Wong. Pore and throat size distributions measured from synchrotron x-ray tomographic images of fontainebleau sandstones. *J. Geophys. Res. Solid Earth*, 105(B9):21509–21527, 2000. doi: 10.1029/2000JB900208.

[111] R. I. Al-Raoush and C. S. Willson. Extraction of physically realistic pore network properties from three-dimensional synchrotron x-ray microtomography images of unconsolidated porous media systems. *J. Hydrol.*, 300(1-4):44–64, 2005. doi: 10.1016/j.jhydrol.2004.05.005.

[112] A. Rabbani, S. Jamshidi, and S. Salehi. An automated simple algorithm for realistic pore network extraction from micro-tomography images. *J. Pet. Eng.*, 123:164–171, 2014. doi: 10.1016/j.petrol.2014.08.020.

[113] P. Øren and S. Bakke. Reconstruction of berea sandstone and pore-scale modelling of wettability effects. *J. Pet. Eng.*, 39(3-4):177–199, 2003. doi: 10.1016/S0920-4105(03)00062-7.

[114] A. Raoof and S. M. Hassanizadeh. A new method for generating pore-network models of porous media. *Transp. Porous Media*, 81(3):391–407, 2010. doi: 10.1007/s11242-009-9412-3.

[115] C. Shi, J. Soete, and H. Janssen. Toward stochastic full-scale pore network generation for porous building materials. In *Accepted for publication at International Building Physics Conference 2024 in Toronto, Canada*, 2024.

[116] S. Claes and H. Janssen. Towards stochastic generation of 3d pore network models of building materials. In *MATEC Web of Conferences*, volume 282, page 02022. EDP Sciences, 2019. doi: 10.1051/matecconf/201928202022.

[117] G. Scott, K. Wu, and Y. Zhou. Multi-scale image-based pore space characterisation and pore network generation: Case study of a north sea sandstone reservoir. *Transp. Porous Media*, 129:855–884, 2019. doi: 10.1007/s11242-019-01309-8.

[118] D. Deckers and H. Janssen. Development and validation of the steady state centrifuge experiment for the moisture retention curve of porous building materials. *J. Build. Phys.*, 47(1):36–61, 2023. doi: 10.1177/1744259123117877.

[119] R. Badmann, N. Stockhausen, and M. J. Setzer. The statistical thickness and the chemical potential of adsorbed water films. *J. Colloid Interface Sci.*, 82(2):534–542, 1981. doi: 10.1016/0021-9797(81)90395-7.

[120] R. P. Mayer and R. A. Stowe. Mercury porosimetry—breakthrough pressure for penetration between packed spheres. *J. Colloid Sci.*, 20(8):893–911, 1965. doi: 10.1016/0095-8522(65)90061-9.

[121] H. M. Princen. Capillary phenomena in assemblies of parallel cylinders: I. capillary rise between two cylinders. *J. Colloid Sci.*, 30(1):69–75, 1969. doi: 10.1016/0021-9797(69)90379-8.

[122] G. Mason and N. R. Morrow. Capillary behavior of a perfectly wetting liquid in irregular triangular tubes. *J. Colloid Sci.*, 141(1):262–274, 1991. doi: 10.1016/0021-9797(91)90321-X.

[123] T. W. Patzek and J. G. Kristensen. Shape factor correlations of hydraulic conductance in noncircular capillaries: Ii. two-phase creeping flow. *J. Colloid Interface Sci.*, 236(2):305–317, 2001. doi: 10.1006/jcis.2000.7414.

[124] H. Janssen, B. Blocken, S. Roels, and J. Carmeliet. Wind-driven rain as a boundary condition for ham simulations: analysis of simplified modelling approaches. *Build. Environ.*, 42(4):1555–1567, 2007. doi: 10.1016/j.buildenv.2006.10.001.

[125] S. K. Asphaug, B. Time, and T. Kvande. Hygrothermal simulations of thermally insulated basement envelopes-importance of boundary conditions below grade. *Build. Environ.*, 199:107920, 2021. doi: 10.1016/j.buildenv.2021.107920.

[126] M. Van Belleghem, H. Steeman, M. Steeman, A. Janssens, and M. De Paepe. Sensitivity analysis of cfd coupled non-isothermal heat and moisture modelling. *Build. Environ.*, 45(11):2485–2496, 2010. doi: 10.1016/j.buildenv.2010.05.011.

[127] T. Defraeye, B. Blocken, and J. Carmeliet. Influence of uncertainty in heat–moisture transport properties on convective drying of porous materials by numerical modelling. *Chem. Eng. Res. Des.*, 91(1):36–42, 2013. doi: 10.1016/j.cherd.2012.06.011.

[128] M. Van Belleghem, M. Steeman, H. Janssen, A. Janssens, and M. De Paepe. Validation of a coupled heat, vapour and liquid moisture transport model for porous materials implemented in cfd. *Build. Environ.*, 81:340–353, 2014. doi: 10.1016/j.buildenv.2014.06.024.

[129] J. Šimůnek and J. R. Nimmo. Estimating soil hydraulic parameters from transient flow experiments in a centrifuge using parameter optimization technique. *Water Resour. Res.*, 41(W04015), 2005. doi: 10.1029/2004WR003379.

[130] J. C. Lozano, P. Blanco Rodríguez, F. Vera Tomé, R. Maldonado, A. S. Medeiros, and C. Prieto. A system for obtaining soil solution extracts and soil water retention curves using a bench centrifuge with fixed angle rotors. *Geoderma*, 361(114063), 2020. doi: 10.1016/j.geoderma.2019.114063.

[131] R. M. Khanzode, S. K. Vanapalli, and D. G. Fredlund. Measurement of soil-water characteristic curves for fine-grained soils using a small-scale centrifuge. *Can. Geotech. J.*, 39:1209–1217, 2002. doi: 10.1139/t02-060.

[132] J. S. McCartney and J. G. Zornberg. Centrifuge permeameter for unsaturated soils. II: Measurement of the hydraulic characteristics of an unsaturated clay. *J. of Geotech. and Geoenviron. Eng.*, 136(8):1064–1076, 2010. doi: 10.1061/(ASCE)GT.1943-5606.0000320.

[133] C. Feng and H. Janssen. Hygric properties of porous building materials (iv): Semi-permeable membrane and psychrometer methods for measuring moisture storage curves. *Build. Environ.*, 152:39–49, 2019. doi: 10.1016/j.buildenv.2019.01.054.

[134] C. Feng, A. S. Guimarães, N. Ramos, L. Sun, D. Gawin, P. Konca, C. Hall, J. Zhao, H. Hirsch, J. Grunewald, et al. Hygric properties of porous building materials (vi): A round robin campaign. *Build. Environ.*, 185:107242, 2020. doi: 10.1016/j.buildenv.2020.107242.

[135] Q. Chen and B. J. Balcom. Measurement of rock-core capillary pressure curves using a single-speed centrifuge and one-dimensional magnetic resonance imaging. *J. Chem. Phys.*, 122(214720), 2005. doi: 10.1063/1.1924547.

[136] A. Reatto-Braga, E. Medrado da Silva, A. Bruand, E. de Souza Martins, and J. Lima. Validity of the centrifuge method for determining the water retention properties of tropical soils. *Soil Sci. Soc. Am. J.*, 72(6):1547–1553, 2008. doi: 10.2136/sssaj2007.0355N.

[137] S. E. Vero, M. G. Healy, T. Henry, R. E. Creamer, T. G. Ibrahim, P. J. Forrestal, K. G. Richards, and O. Fenton. A methodological framework to determine optimum durations for the construction of soil water characteristic curves using centrifugation. *Irish J. Agric. Food Res.*, 55(2):91–99, 2016. doi: 10.1515/ijafr-2016-0009.

[138] J. R. Nimmo, J. Rubin, and D. P. Hammermeister. Unsaturated flow in a centrifugal field: Measurement of hydraulic conductivity and testing of darcy's law. *Water Resour. Res.*, 23(1):124–134, 1987. doi: 10.1029/WR023i001p00124.

[139] J. R. Nimmo. Experimental testing of transient unsaturated flow theory at low water content in a centrifugal field. *Water Resour. Res.*, 26(9):1951–1960, 1990. doi: 10.1029/WR026i009p01951.

[140] H. Nakajima and A. T. Stadler. Centrifuge modeling of one-step outflow tests for unsaturated parameter estimations. *Hydrol. Earth Syst. Sci.*, 10(5):715–729, 2006. doi: 10.5194/hess-10-715-2006.

[141] B. Malengier, G. Di Emidio, H. Peiffer, and M. C. Ciocci. Unsaturated permeability and retention curve determination from in-flight weight

measurements in a bench-scale centrifuge. *Geotech. Test. J.*, 38(2): 20140121, 2015. doi: 10.1520/GTJ20140121.

[142] A. C. Turturro and M. C. Caputo. Mercury intrusion porosimetry and centrifuge methods for extended-range retention curves of soil and porous rock samples. *Vadose Zone J.*, 21(1), 2022. doi: 10.1002/vzj2.20176.

[143] E. Vereecken, S. Roels, and H. Janssen. Centrifuge experiments for the determination of the moisture storage and transport properties in the overhygroscopic range. In MATEC Web of Conferences, editor, *Proceedings of the 4th Central European Symposium on Building Physics (CESBP 2019)*, volume 282(02035), 2019. doi: 10.1051/matecconf/201928202035.

[144] E. Vereecken, S. Roels, and H. Janssen. Inverse hygric property determination based on dynamic measurements and swarm-intelligence optimisers. *Build. Environ.*, 131:184–196, 2018. doi: 10.1016/j.buildenv.2017.12.030.

[145] R. Gardner. A method of measuring the capillary tension of soil moisture over a wide moisture range. *Soil Sci.*, 43(4):277–284, 1937. doi: 10.1097/00010694-193704000-00004.

[146] SEW Eurodrive. CM3C63 – CM3C100 Synchronous Servomotors. https://download.sew-eurodrive.com/download/pdf/29194652.pdf, 2020. Online; accessed 26 April 2023.

[147] S. Roels, J. Carmeliet, H. Hens, O. Adan, H. Brocken, R. Czerny, C. Hall, A. Hamilton, K. Kumaran, Z. Pavlik, et al. Hamstad work package 1: Final report-moisture transfer properties and materials characterisation. *EU Contract GRD1-1999-200072003*, 2003.

[148] R. A. Cook and K. C. Hover. Mercury porosimetry of cement-based materials and associated correction factors. *Constr. Build. Mater.*, 7(4): 231–240, 1993. doi: 10.1016/0950-0618(93)90007-Y.

[149] W. Sonderegger and P. Niemz. Thermal conductivity and water vapour transmission properties of wood-based materials. *Aur. J. Wood Wood Prod.*, 67(3):313–321, 2009. doi: 10.1007/s00107-008-0304-y.

[150] M. Tziotziou, E. Karakosta, I. Karatasios, G. Diamantopoulos, A. Sapalidis, M. Fardis, P. Maravelaki-Kalaitzaki, G. Papavassiliou, and V. Kilikoglou. Application of 1h nmr to hydration and porosity studies of lime–pozzolan mixtures. *Microporous Mesoporous Mater.*, 139(1-3):16–24, 2011. doi: 10.1016/j.micromeso.2010.10.010.

[151] P. Ren, C. Feng, and H. Janssen. Hygric properties of porous building materials (v): Comparison of different methods to determine moisture diffusivity. *Build. Environ.*, 164:106344, 2019. doi: 10.1016/j.buildenv.2019.106344.

[152] R. M. E. Valckenborg. *NMR on Technological Porous Materials*. Technische Universiteit Eindhoven, 2001. doi: 10.6100/IR548383.

[153] G. R. Coates, L. Xiao, and M. G. Prammer. *NMR logging Principles and Applications*. Gulf Professional Publishing, 2001.

[154] B. Liu, X. Jiang, L. Bai, and R. Lu. Investigation of oil and water migrations in lacustrine oil shales using 20 mhz 2d nmr relaxometry techniques. *Pet. Sci.*, 19(3):1007–1018, 2022. doi: 10.1016/j.petsci.2021.10.011.

[155] S. Sharma, F. Casanova, W. Wache, A. Segre, and B. Blümich. Analysis of historical porous building materials by the nmr-mouse. *Magn. Reson. Imaging*, 21(3-4):249–255, 2003. doi: 10.1016/s0730-725x(03)00132-2.

[156] A. C. A. Muller, K. L. Scrivener, A. M. Gajewicz, and P. J. McDonald. Densification of c–s–h measured by 1h nmr relaxometry. *J. Phys. Chem. C.*, 117(1):403–412, 2013. doi: 10.1021/jp3102964.

[157] L. Liu, Z. He, X. Cai, and S. Fu. Application of low-field nmr to the pore structure of concrete. *Appl. Magn. Reson.*, 52:15–31, 2021. doi: 10.1007/s00723-020-01229-7.

[158] L. Pel, K. Hazrati, K. Kopinga, and J. Marchand. Water absorption in mortar determined by nmr. *Magn. Reson. Imaging*, 16(5-6):525–528, 1998. doi: 10.1016/S0730-725X(98)00061-7.

[159] R. M. E. Valckenborg, L. Pel, K. Hazrati, K. Kopinga, and J. Marchand. Pore water distribution in mortar during drying as determined by nmr. *Mater. Struct.*, 34:599–604, 2001. doi: 10.1007/BF02482126.

[160] G. H. A. Van der Heijden, H. P. Huinink, L. Pel, and K. Kopinga. Non-isothermal drying of fired-clay brick, an nmr study. *Chem. Eng. Sci.*, 64 (12):3010–3018, 2009. doi: 10.1016/j.ces.2009.03.012.

[161] S. M. Munsch, C. Strangfeld, and S. Kruschwitz. Determining the pore size distribution in synthetic and building materials using 1d nmr. *Diffus. Fundam.*, 31(2):1–9, 2019.

[162] E. Fukushima and S. B. W. Roeder. *Experimental Pulse NMR: A Nuts and Bolts Approach*. CRC Press, 1993.

[163] K. R. Brownstein and C. E. Tarr. Importance of classical diffusion in nmr studies of water in biological cells. *Phys. Rev. A*, 19(6):2446 – 2453, 1979. doi: 10.1103/PhysRevA.19.2446.

[164] F. Benavides, R. Leiderman, A. Souza, G. Carneiro, and R. Bagueira. Estimating the surface relaxivity as a function of pore size from nmr T_2 distributions and micro-tomography images. *Comput. and Geosci.*, 106: 200 – 208, 2017. doi: 10.1016/j.cageo.2017.06.016.

[165] P. R. J. Connolly, W. Yan, D. Zhang, M. Mahmoud, M. Verrall, M. Lebedev, S. Iglauer, P. J. Metaxas, E. F. May, and M. L. Johns. Simulation and experimental measurements of internal magnetic field gradients and NMR transverse relaxation times (T_2) in sandstone rocks. *J. Pet. Sci. Eng.*, 175:985 – 997, 2019. doi: 10.1016/j.petrol.2019.01.036.

[166] R. Xie, L. Xiao, K. Dunn, and S. Fu. Determination of T_2 distribution in the presence of significant internal field gradients. *J. Geophys. Eng.*, 10 (054008), 2013. doi: 10.1088/1742-2132/10/5/054008.

[167] F. Benavides, R. Leiderman, A. Souza, G. Carneiro, and R. Bagueira de Vasconcellos Azeredo. Pore size distribution from NMR and image based methods: A comparative study. *J. Pet. Sci. Eng.*, 184(106321), 2020. doi: 10.1016/j.petrol.2019.106321.

[168] K. Keating and R. Knight. The effect of spatial variation in surface relaxivity on nuclear magnetic resonance relaxation rates. *Geophys.*, 77 (5):365–377, 2012. doi: 10.1190/GEO2011-0462.1.

[169] S. Ryu. Effect of inhomogeneous surface relaxivity, pore geometry and internal field gradient on nmr logging: Exact and perturbative theories and numerical investigations. In *SPWLA Annual Logging Symposium*, pages SPWLA–2009. SPWLA, 2009. doi: 10.48550/arXiv.0906.5327.

[170] S. Ghomeshi, S. ad Kryuchkov and A. Kantzas. An investigation into the effects of pore connectivity on T_2 NMR relaxation. *J. Magn. Reson.*, 289: 79 – 91, 2018. doi: 10.1016/j.jmr.2018.02.007.

[171] H. Y. Carr and E. M. Purcell. Effects of diffusion on free precession in nuclear magnetic resonance experiments. *Phys. Rev.*, 94(3):630 – 638, 1954. doi: 10.1103/PhysRev.94.630.

[172] M. Saidian and M. Prasad. Effect of mineralogy on nuclear magnetic resonance surface relaxivity: A case study of middle bakken and three forks formations. *Fuel*, 161:197–206, 2015. doi: 10.1016/j.fuel.2015.08.014.

[173] S. W. Provencher. A constrained regularization method for inverting data represented by linear algebraic or integral equations. *Comput. Phys. Commun.*, 27:213 – 227, 1982. doi: 10.1016/0010-4655(82)90173-4.

[174] K. P. Whittall. *Analysis of NMR Relaxation Data*, pages 44 – 67. Elsevier, 1996. doi: 10.1016/S0922-3487(96)80040-2.

[175] M. N. Testamanti and R. Rezaee. Considerations for the acquisition and inversion of NMR t_2 data in shales. *J. Pet. Sci. Eng.*, 174:177–188, 2019. doi: 10.1016/j.petrol.2018.10.109.

[176] F. Mariette, J. P. Guillement, C. Tellier, and P. Marchal. *Continuous Relaxation Time Distribution Decomposition by MEM*, pages 218 – 235. Elsevier, 1996. doi: 10.1016/S0922-3487(96)80047-5.

[177] É. Chouzenoux, S. Moussaoui, J. Idier, and F. Mariette. Efficient maximum entropy reconstruction of nuclear magnetic resonance T_1-T_2 spectra. *IEEE Trans. Signal Process.*, 58(12):6040–6051, 2010. doi: 10.1109/TSP.2010.2071870.

[178] Y. Zou, R. Xie, Y. Ding, and A. Arad. Inversion of nuclear magnetic resonance echo data based on maximum entropy. *Geophys.*, 81(1):1–8, 2016. doi: 10.1190/GEO2015-0200.1.

[179] P. Berman, O. Levi, Y. Parmet, M. Saunders, and Z. Wiesman. Laplace inversion of low-resolution NMR relaxometry data using sparse representation methods. *Concepts Mag. Reson. Part A Bridg. Educ. Res.*, 42(3):72–88, 2013. doi: 10.1002/cmr.a.21263.

[180] J. Guo, R. Xie, Y. Zou, G. Jin, L. Gao, and C. Xu. A new method for NMR data inversion based on double-parameter regularization. *Geophys.*, 83(5):39–49, 2018. doi: 10.1190/GEO2017-0394.1.

[181] Y. Zou, R. Xie, and A. Arad. Numerical estimation of choice of the regularization parameter for NMR T_2 inversion. *Pet. Sci.*, 13:237–246, 2016. doi: 10.1007/s12182-016-0093-6.

[182] S. M. Nagel, C. Strangfeld, and S. Kruschwitz. Interpretation of nmr signals from partly saturated sandstones. In *2021 13th International Conference on Electromagnetic Wave Interaction with Water and Moist Substances (ISEMA)*, pages 1–5. IEEE, 2021. doi: 10.1109/ISEMA49699.2021.9508337.

[183] KU Leuven XCT Core Facility. https://xct.kuleuven.be, 2023. Online; accessed 14 March 2023.

[184] D. Wildenschild, C. M. P Vaz, M. L. Rivers, D. Rikard, and B. S. B. Christensen. Using x-ray computed tomography in hydrology: systems, resolutions, and limitations. *J. Hydrol.*, 267(3-4):285–297, 2002. doi: 10.1016/S0022-1694(02)00157-9.

[185] A. Kaestner, E. Lehmann, and M. Stampanoni. Imaging and image processing in porous media research. *Adv. Water Resour.*, 31(9):1174–1187, 2008. doi: 10.1016/j.advwatres.2008.01.022.

[186] L. V. Pengfei, Y. Liu, Z. Wang, S. Liu, L. Jiang, J. Chen, and Y. Song. In situ local contact angle measurement in a co2–brine–sand system using microfocused x-ray ct. *Langmuir*, 33(14):3358–3366, 2017.

[187] I. Arganda-Carreras, V. Kaynig, C. Rueden, K. W. Eliceiri, J. Schindelin, A. Cardona, and H. Sebastian Seung. Trainable weka segmentation: a machine learning tool for microscopy pixel classification. *Bioinform.*, 33 (15):2424–2426, 2017. doi: 10.1093/bioinformatics/btx180.

[188] KU Leuven Materials and Constructions. https://bwk.kuleuven.be/mat, 2024. Online; accessed 1 July 2024.

[189] P. Fantazzini and R. J. S. Brown. Initially linear echo-spacing dependence of $1/T_2$ measurements in many porous media with pore-scale inhomogeneous fields. *J. Magn. Reson.*, 177:228 – 235, 2005. doi: 10.1016/j.jmr.2005.08.001.

[190] O. Mohnke. Jointly deriving nmr surface relaxivity and pore size distributions by nmr relaxation experiments on partially desaturated rocks. *Water Resour. Res.*, 50(6):5309–5321, 2014. doi: 10.1002/2014WR015282.

[191] O. Mohnke, R. Jorand, C. Nordlund, and N. Klitzsch. Understanding nmr relaxometry of partially water-saturated rocks. *Hydrol. Earth Syst. Sci.*, 19(6):2763–2773, 2015. doi: 10.5194/hess-19-2763-2015.

[192] J. Guo, R. Xie, Y. Zou, G. Jin, L. Gao, and C. Xu. A new method for nmr data inversion based on double-parameter regularization. *Geophys.*, 83(5):JM39–JM49, 2018. doi: 10.1190/geo2017-0394.1.

[193] R. Salazar-Tio and B. Sun. Monte carlo optimization-inversion methods for nmr. *Petrophysics-The SPWLA Journal of Formation Evaluation and Reservoir Description*, 51(03), 2010.

[194] K. Dunn and G. A. LaTorraca. The inversion of nmr log data sets with different measurement errors. *J. Magn. Reson.*, 140(1):153–161, 1999. doi: 10.1006/jmre.1999.1837.

[195] K. Keating and R. Knight. A laboratory study to determine the effect of iron oxides on proton nmr measurements. *Geophys.*, 72(1):E27–E32, 2007. doi: 10.1190/1.2399445.

[196] H. De Clercq and E. De Witte. Reactivity of silicon based water repellent agents at different application conditions-part i: reactivity of model compounds/reaktivität von hydrophobierungsmitteln auf silikonbasis bei unterschiedlichen applikationsbedingungen-teil i: Reaktivität von modellverbindungen. *Restoration Build. Monuments*, 7(1):63–78, 2001. doi: 10.1515/rbm-2001-5541.

[197] V. Cnudde, J. P. Cnudde, C. Dupuis, and P. J. S. Jacobs. X-ray micro-ct used for the localization of water repellents and consolidants inside natural building stones. *Mater. Charact.*, 53(2-4):259–271, 2004. doi: 10.1016/j.matchar.2004.08.011.

[198] D. Barnat-Hunek and P. Smarzewski. Increased water repellence of ceramic buildings by hydrophobisation using high concentration of organic solvents. *Energy Build.*, 103:249–260, 2015. doi: 10.1016/j.enbuild.2015.06.048.

[199] H. Chraibi, M. Prat, and O. Chapuis. Influence of contact angle on slow evaporation in two-dimensional porous media. *Phys. Rev. E*, 79(2):026313, 2009. doi: 10.1103/PhysRevE.79.026313.

[200] M. Prat. Pore network models of drying, contact angle, and film flows. *Chem. Eng. Technol.*, 34(7):1029–1038, 2011. doi: 10.1002/ceat.201100056.

[201] R. Wu, C. Y. Zhao, E. Tsotsas, and A. Kharaghani. Convective drying in thin hydrophobic porous media. *Int. J. Heat Mass Transf.*, 112:630–642, 2017. doi: 10.1016/j.ijheatmasstransfer.2017.05.023.

[202] P. P. Chakraborty, M. Ross, H. Bindra, and M. M. Derby. Evaporative drying from hydrophilic or hydrophobic homogeneous porous columns: Consequences of wettability, porous structure and hydraulic connectivity. *Transp. Porous Media*, 143(3):551–578, 2022. doi: 10.1007/s11242-022-01775-7.

[203] M. Nasir, Z. Li, M. A. Mahardika, W. Wang, Y. She, K. Wang, A. Patmonoaji, S. Matsushita, and T. Suekane. Pore-scale investigation of wettability effects on drying process of three-dimensional porous medium. *Int. Commun. Heat Mass Transf.*, 140:106527, 2023. doi: 10.1016/j.icheatmasstransfer.2022.106527.

[204] O. Chapuis and M. Prat. Influence of wettability conditions on slow evaporation in two-dimensional porous media. *Phys. Rev. E*, 75(4):046311, 2007. doi: 10.1103/PhysRevE.75.046311.

[205] S. Foroughi, B. Bijeljic, Q. Lin, A. Q. Raeini, and M. J. Blunt. Pore-by-pore modeling, analysis, and prediction of two-phase flow in mixed-wet rocks. *Phys. Rev. E*, 102(2):023302, 2020. doi: 10.1103/PhysRevE.102.023302.

[206] S. Foroughi, B. Bijeljic, and M. J. Blunt. Pore-by-pore modelling, validation and prediction of waterflooding in oil-wet rocks using dynamic synchrotron data. *Transp. Porous Media*, 138(2):285–308, 2021. doi: 10.1007/s11242-021-01609-y.

[207] J. B. Laurindo and M. Prat. Numerical and experimental network study of evaporation in capillary porous media. drying rates. *Chem. Eng. Sci.*, 53(12):2257–2269, 1998. doi: 10.1016/S0009-2509(96)00341-7.

[208] M. Prat. On the influence of pore shape, contact angle and film flows on drying of capillary porous media. *Int. J. Heat Mass Transf.*, 50(7-8):1455–1468, 2007. doi: 10.1016/j.ijheatmasstransfer.2006.09.001.

[209] Bauklimatik Dresden. Delphin. https://bauklimatik-dresden.de/delphin/, 2024. Online; accessed 8 February 2024.

Curriculum

Daan Deckers (25th of June 1996, Genk, Belgium) obtained his bachelor's (2014-2017) as a civil engineer at the Faculty of Engineering Science of the KU Leuven. In 2019, he graduated at the same university as a master of science in Civil Engineering with a specialisation in Building Technologies where his master thesis revolved around 'Assessing the impact of a hydrophobic treatment on the moisture response of an internally insulated massive wall'. This thesis helped him develop great interest in both research as well as the topic of hydrophobisation in the built environment and how it fits into the search for more sustainable building practices. This led to him starting his PhD, centered around the use of water repellent agents, on the first of October in 2019.
Daan was a PhD student at the Building Physics and Sustainable Design section of the KU Leuven from 2019-2024. In the first year of his PhD, he prepared an application for a grant at the Research Foundation – Flanders (FWO), which was eventually granted. Simultaneously, he initiated the development of new experimental setups for hygric property determination of hydrophobised building materials. In 2020, he started as a fundamental research fellow of the FWO, and continued his PhD research with the pore-scale modeling of hygric properties of hydrophobised building materials as main aim. During his years as a doctoral student, Daan participated in hygrothermal expertises for several different companies in which he deepened his interest towards Heat, Air and Moisture transport in the built environment. Daan was also a teaching assistant for 5 years in which he supervised the exercise sessions of the 'Building Physics' course of prof. dr. ir. Hans Janssen. Moreover, he guided several students towards successful completion of their master theses.
Daan has been the lead author in four papers which were published in peer-reviewed journals, and he contributed in five research papers presented at international conferences, four of which he presented himself. In doing so, Daan won the 'Best PhD paper award' at the 13th Nordic Symposium on Building Physics, held in June 2023 in Aalborg, Denmark.

List of publications

Journal papers

- D. Deckers, H. Janssen. Development and validation of the steady state centrifuge experiment for the moisture retention curve of porous building materials. J. Build. Physics, 47(1): 36-61, 2023. doi: 10.1177/17442591231178778
- D. Deckers, H. Janssen. Microscopic validation of a pore network model for hygric properties of porous materials. Transp. Porous Media, 151: 119–140, 2024. doi: 10.1007/s11242-023-02035-y
- D. Deckers, H. Janssen. Microscopic Moisture Localisation in Unsaturated Materials Using Nuclear Magnetic Resonance Relaxometry. J. Build. Physics, 2024. doi: 10.1177/17442591231219931
- D. Deckers, Y. Zhu, E. Koos, H. Janssen. Microscopic localisation of hydrophilically oriented pore bodies and throats in hydrophobised porous materials. Transp. Porous Media, 151: 773–793, 2024. doi: 10.1007/s11242-024-02069-w

Peer-reviewed conference proceedings

- E. Vereecken, D. Deckers, H. Janssen and S. Roels. Field study on hydrophobised internally insulated masonry walls. Proceedings of the XVth International Conference on Durability of Building Materials and Components, 2020, Barcelona, Spain. doi: 10.23967/dbmc.2020.067.
- D. Deckers, E. Vereecken, S. Roels. and H. Janssen. Influence of the disparities between lab and in-situ application on the penetration depth of a hydrophobic agent. Proceedings of the 8th International Building Physics Conference, 2021, Copenhagen, Denmark. doi: 10.1088/1742-6596/2069/1/012048

- D. Deckers, H. Janssen. The Development of a Laboratory Centrifuge for the Measurement of the Moisture Storage Properties of Porous Building Materials. Proceedings of the 5th Central European Symposium on Building Physics, 2022, Bratislava, Slovakia. doi: 10.1063/5.0171115
- D. Deckers, H. Janssen. Moisture localisation in unsaturated materials using nuclear magnetic resonance experiments, X-ray computed tomography and pore network modeling. Proceedings of the 13th Nordic Symposium on Building Physics, 2023, Aalborg, Denmark. doi: 10.1088/1742-6596/2654/1/012035
- D. Deckers, H. Janssen. The influence of hydrophilic pores on the moisture behaviour in hydrophobised building materials. Proceedings of the 9th International Building Physics Conference, 2024, Toronto, Canada.

Research reports

- H. Janssen, D. Deckers, E. Vereecken, C. Feng, V. Soulios, A. Vanek, T. K. Hansen. Robust Internal Thermal Insulation of Historic Buildings - Impact of water repellent agents on hygric properties of porous building materials. 1–159, 2020.



FACULTY OF ENGINEERING SCIENCE
DEPARTMENT OF CIVIL ENGINEERING
BUILDING PHYSICS AND SUSTAINABLE DESIGN
Kasteelpark Arenberg 40
B-3001 Leuven
daan.deckers@kuleuven.be